2013

Scattering properties of dust in Orion and Epsilon Eridani exoplanetary system

https://hdl.handle.net/2144/14082

BOSTON UNIVERSITY

GRADUATE SCHOOL OF ARTS AND SCIENCES

Dissertation

SCATTERING PROPERTIES OF DUST IN ORION AND THE EPSILON ERIDANI EXOPLANETARY SYSTEM

by

CHRISTOPHER B. MENDILLO

ScB, Brown University, 2005

Submitted in partial fulfillment of the

requirements for the degree of

Doctor of Philosophy

2013

Approved by

First Reader [redacted]

Supriya Chakrabarti, Ph.D.
Adjunct Professor of Astronomy

Second Reader [redacted]

Timothy A. Cook, Ph.D.
Adjunct Professor of Astronomy

Third Reader [redacted]

Dan P. Clemens, Ph.D.
Professor of Astronomy

Acknowledgments

I'd like to begin by thanking my two advisors, Supriya Chakrabarti and Tim Cook for the incredible amount of guidance they have given me over the years. It would be impossible to estimate how many hours Tim and I spent in his office going over and over the details of PICTURE and SPINR. Tim and Sup were always fully involved with our research and willing to discuss any issue for hours on end. In addition to my advisors, I would like to thank the rest of my dissertation committee: Dan Clemens, John Clarke, Karl Gordon and Paul Withers. Thank you especially to Dan Clemens for his immense amount of help organizing my prospectus and dissertation into a scientifically coherent body of work.

Next, I have to thank Brian Hicks, as in the other half of Chris and Brian, the two guys no one at Wallops Flight Facility can tell apart. I spent more time together with Brian building PICTURE than I think I've spent with any other human on the planet. Brian, you are an optics wizard and a surgeon with a belt sander. I'd also like to thank the rest of my labmates: Paul Jung, Jason Martel, Ewan Douglas and Meredith Danowski. I'd like to acknowledge John Atkinson and Nick McConnell for their early work on the PICTURE pointing system.

A full list of everyone that worked on PICTURE would take up this entire page. I'd like to thank everyone at JPL, MIT, Goddard Space Flight Center and Wallops Flight Facility. Special thanks are in order to Ben Lane at Draper Laboratory. Ben helped with all aspects of PICTURE, especially the development of the fine pointing system and the wavefront sensing software.

Thank you to Kevin France for his help modeling the molecular hydrogen background in the SPINR data. Thank you to Nikole Lewis for her continued guidance with the SPINR analysis, even long after she left the department.

To wrap up my academic acknowledgments, I'd like to thank my undergraduate advisor, Ian Dell'Antonio at Brown University for introducing me to astronomical research and coaching me through the process of applying to graduate school.

I'd now like to thank all of my friends. If you stay in school forever, you are lucky to have at least three main groups of friends: high school friends, college friends and grad school friends. I am extremely lucky to have remained very close with all of them throughout the years. First, I'll say thank you simply to The Family, the loving moniker that applies to all my close friends from home. Thanks to my friends from Brown: Charlie, James, Rob, Dan and Aaron. Thanks to my newest friends from BU: Ned, Luke, Brian, Loren, Susanna and Tony. I would like to formally acknowledge my band, The Last Front, for being the finest purveyors of space-punk in the history of music. Long live its once and forever members: Ned, Kevin and Juan.

Finally, thank you to my family. To my mom and dad, my step-mom Robin, Hollie and Joe, Ben and Bella, and my wife Lumina, thank you for all of your love and support over 25 years of school and 30 years of life.

SCATTERING PROPERTIES OF DUST IN ORION AND THE EPSILON ERIDANI EXOPLANETARY SYSTEM

(Order No.)

CHRISTOPHER B. MENDILLO

Boston University, Graduate School of Arts and Sciences, 2013

Major Professor: Supriya Chakrabarti, Adjunct Professor of Astronomy

ABSTRACT

Dust grain properties were investigated in two very different Galactic environments: the interstellar medium and an exoplanetary system. Two sounding rocket missions were developed to study these regions.

Wide-field observations of the Orion OB stellar association were performed in the far-ultraviolet using the *Spectrograph for Photometric Imaging with Numeric Reconstruction* (SPINR) sounding rocket. These observations reveal the diffuse signature of starlight scattering off interstellar dust grains. The spectral-imaging data were used along with a three-dimensional radiative transfer model to measure the dust scattering parameters: the grain albedo ($\boldsymbol{a}$) and the scattering asymmetry ($\boldsymbol{g}$). The measured parameters are consistent with previous measurements made toward Orion. A sharp increase in albedo was measured at ~1330 Å. This feature is not explained by current grain models.

The constructed three-dimensional model of Orion includes a two-component dust distribution. The foreground distribution is responsible for the small amount of visible reddening measured toward the bright stars in the Orion constellation.

The background distribution represents the Orion Molecular Cloud, which dominates observations of dust emission in the infrared. This model was used to show that backscattered light from the molecular cloud alone cannot produce the observed scattered light distribution. The foreground dust, though optically thin in the visible, significantly contributes to the scattered light in the far-ultraviolet. This suggests that observations of Orion in the infrared and far-ultraviolet may probe entirely different dust populations.

The *Planetary Imaging Concept Testbed Using a Rocket Experiment* (PICTURE) sounding rocket was developed to characterize dust grains in the nearby ϵ Eridani exoplanetary system. This is a young, dusty system with a Jupiter-massed planet orbiting at $\sim$3.4 AU (astronomical units). PICTURE sought to capture a direct, visible-light image of dust-scattered starlight in this system with the aid of a high-contrast nulling coronagraph. The design and laboratory testing of the PICTURE science payload is presented. Although the mission returned no science data, several important technological advances were made to enable future direct imaging missions. Most notably, PICTURE demonstrated 5.1 milliarcsecond pointing stability using a fast optical tracking system.

Contents

List of Tables

List of Figures

List of Abbreviations

2MASS	Two Micron All Sky Survey
C-PZT	Calibration PZT
COBE	Cosmic Background Explorer
DIRTY	DustI Radiative Transfer, Yeah!
E(B-V)	reddening excess
FUSE	Far Ultraviolet Spectroscopic Explorer
GALEX	GALaxy Evolution Explorer
HIPPARCOS	HIgh Precision PArallax COllecting Satellite
HST	Hubble Space Telescope
IRAS	InfraRed Astronomical Satellite
IUE	International Ultraviolet Explorer
N-PZT	Nuller PZT
P-PZT	Pinhole PZT
P-V	peak-to-valley
PICTURE	Planetary Imaging Concept Testbed Using a Rocket Experiment
SHARPI	Solar High Angular Resolution Photometric Imager
SPEAR	Spectroscopy of Plasma Evolution from Astrophysical Radiation
SPINR	Spectrograph for Photometric Imaging with Numeric Reconstruction
TPF-C	Terrestrial Planet Finder Coronagraph
ACS	Attitude Control System
ACS	Advanced Camera for Surveys

ADC	analog-to-digital converter
ADI	angular differential imaging
ADU	analog-to-digital units
AO	adaptive optics
ARC	Astronomical Research Cameras
BMC	Boston Micromachines
CCD	charged coupled device
CHARA	Center for High Angular Resolution Astronomy
CIF	calibration interferometer
CU	Continuum Unit
DAC	digital-to-analog converter
DGL	diffuse galactic light
DIO	digital input/output
DM	deformable mirror
EGP	extrasolar giant planet
ETA	Estimated True Attitude
ETS	Estimated True Stability
EUV	extreme-ultraviolet
FOV	field of view
FPGA	field-programmable gate array
FPS	Fine Pointing System
FSM	fast steering mirror
FUV	far-ultraviolet
GSFC	Goddard Space Flight Center
HG	Henyey-Greenstein
IDL	Interactive Data Language

IRS	Spitzer Infrared Spectrograph
ISM	interstellar medium
IWA	inner working angle
JPL	Jet Propulsion Laboratory
KIN	Keck Interferometer Nuller
LSB	least significant bit
LSF	line spread function
mas	milliarcsecond
MEMS	Microelectromechanical Systems
MIF	main ionization front
MIPS	Multiband Imaging Photometer for Spitzer
NASA	National Aeronautics and Space Administration
NEA	noise equivalent angle
NICMOS	Near Infrared Camera and Multi-Object Spectrometer
NIF	nulling interferometer
OMC	Orion Molecular Cloud
OPD	optical path difference
PAH	polycyclic aromatic hydrocarbon
PDR	photodissociation region
PI	Physik Instrumente
PID	Proportional + Integral + Differential
PSD	power spectral density
PSF	point spread function
PZT	piezoelectric transducer
RMS	root mean square
SCI	science camera

SNR	signal-to-noise ratio
SST	Spitzer Space Telescope
STIS	Space Telescope Imaging Spectrograph
TATT	Telescope Alignment Transfer Tool
TESS	tomographic extreme-ultraviolet spectrograph
TTP	tip-tilt-piston
ULE	ultra-low expansion
VLT	Very Large Telescope
VNC	Visible Nulling Coronagraph
VNC, nuller	Visible Nulling Coronagraph
WCS	Wavefront Control System
WFE	wavefront error
WFF	Wallops Flight Facility
WFS	wavefront sensor
WSMR	White Sands Missile Range

Chapter 1

Introduction

This dissertation will describe my efforts to characterize dust grains in two very different environments within our Galaxy: the interstellar medium (ISM) and exoplanetary systems. I will attempt to answer the following questions about these two environments:

- *What are the physical properties of dust grains in the ISM?*
- *What is the distribution and brightness of dust grains in exoplanetary systems?*

Motivation for these questions:

Interstellar dust grains play a vital role in the continuing evolution of our Galaxy. Dust grains form in the cool outer envelopes of giant evolved stars as well as in planetary nebulae, novae and supernovae. These grains constitute the solid matter component of the interstellar medium and are composed of the heavy elements and compounds needed to form terrestrial planets and life. Apart from their direct role in the construction of solid matter, interstellar dust grains also greatly influence the chemical and physical evolution of the Galaxy through their strong interaction with the ionizing and dissociative far-ultraviolet (FUV) radiation fields of massive stars. Dust grains absorb FUV radiation, allowing molecular gas-phase chemistry to proceed in the ISM unimpeded by these destructive photons. Dust shields the cold dense cores of interstellar clouds from external radiative heating allowing them to collapse and form new stars. Dust also limits the amount of FUV radiation that escapes from the Galaxy and contributes to ionizing the intergalactic medium.

The same dust grains that regulate the chemical evolution of our Galaxy also obscure, confuse and contaminate our observations of objects within and beyond the Galaxy. All astronomically observed objects are viewed through some amount of dust. Through the process of extinction, the absorption and scattering of light in a wavelength dependent manner, dust imprints its own signature on the spectrum of a background object. This spectral fingerprint must be removed to correctly characterize the underlying spectrum. In visible light, dust blocks our view towards embedded objects of interest such as the star forming cores of molecular clouds. In fact, much of the galactic plane, including the galactic center, is completely obscured by dust. This has led observations to move towards longer wavelengths, the infrared and submillimeter, where dust extinction is less efficient.

Dust grains also pervade our Solar System and the thousands of exoplanetary habitats that have been discovered over the past two decades. Exozodiacal dust, the by-product of colliding asteroids and shedding comets, is the exo-analog of our own zodiacal dust. This dust thermally emits in the mid and far-infrared and reflects visible starlight to form the dominant astrophysical background against which exoplanets are imaged. Characterizing this background in both wavelength regimes will aid the development of future exoplanet imaging missions, which will attempt to directly image and characterize extremely faint Earth-like exoplanets in the dusty habitable zones of their host stars. Measurements of the exozodiacal dust morphology will also inform models of planet formation and migration and may lead to the indirect detection of exoplanets.

The physical properties of dust grains: chemical composition, size distribution, shape, spatial distribution, temperature, etc. all influence the myriad functions and observational characteristics of dust. Continued study of these grains in both Earth-bound and astrophysical laboratories will greatly improve our understanding of the chemical and structural evolution of our Galaxy.

1.1 Dust in the Interstellar Medium

1.1.1 Observational Techniques

The physical properties of dust grains in the ISM can be inferred through a number of observational techniques. The gas phase depletion of heavy elements in interstellar clouds, as compared to the measured abundances in nearby stars, provides indirect evidence for the deposition or "freezing-out" of these elements onto dust grains. Dust grains can be probed more directly by measuring their influence on the radiation fields of distant sources. These studies focus on three observable consequences of the interaction between radiation and dust grains: absorption, scattering and polarization.

When a photon encounters a dust grain, it can either be absorbed or scattered. In either case, if the original photon was traveling from a distant source to an observer on Earth, that photon will no longer reach the observer. This process of extinction is wavelength dependent and leaves a spectral imprint on the background source through the selective removal of photons at specific wavelengths. This imprint can be used to deduce the chemical composition and size distribution of the dust grains.

The specific extinction A_λ is normally expressed in the magnitude system as:

$$A_\lambda = -2.5 \log \left(\frac{I_\lambda}{I_{\lambda,0}} \right) \tag{1.1}$$

where, $\frac{I_\lambda}{I_{\lambda,0}}$ represents the fractional attenuation of the source intensity as it passes through an absorptive and/or scattering medium. The specific reddening excess

E(λ-V) quantifies the extinction at a specific wavelength relative to the visible band.

$$E(\lambda - V) = A_\lambda - A_V \tag{1.2}$$

This quantity relates the color of the extinction. Since extinction is generally more efficient at shorter wavelengths, the effect is to cause objects to appear redder than they truly are. The B-to-V band reddening excess E(B-V), also called the selective extinction, is often used to quantify the amount of dust along the line of sight to a source. Since more dust will induce more reddening, this quantity can be used to normalize the E(λ-V) curve of an object to probe the intrinsic reddening quality of the dust. The quantity $E(\lambda - V)/E(B - V)$ is commonly referred to as simply the reddening curve. The average reddening curve for the Milky Way is shown in Figure 1.1. This curve is constructed from the empirically formed model of Fitzpatrick (1999) using the *fmrcurve.pro* Interactive Data Language (IDL) routine. This simplified model is based on a single parameter, R_V, the ratio of absolute to selective extinction (Eq. 1.3). The average value of R_V in the Milky Way is $R_V = 3.1$ (Fitzpatrick 2004).

$$R_V = \frac{A_V}{E(B - V)} \tag{1.3}$$

The R_V parameter is thought to parametrize the average grain size. Along with the Fitzpatrick (1999) model, the widely used extinction law proposed by Cardelli et al. (1989) is linearly correlated with R_V at all wavelengths. Values of $R_V > 3.1$ indicate larger-than-average dust grains and are associated with flatter-than-average reddening curves. High values of R_V are observed both in molecular clouds, where grain growth mechanisms increase the average size of grains, and in the photodissociation regions (PDRs) of hot stars, where small grains can be destroyed through photoevaporation. Both of these mechanisms have been invoked

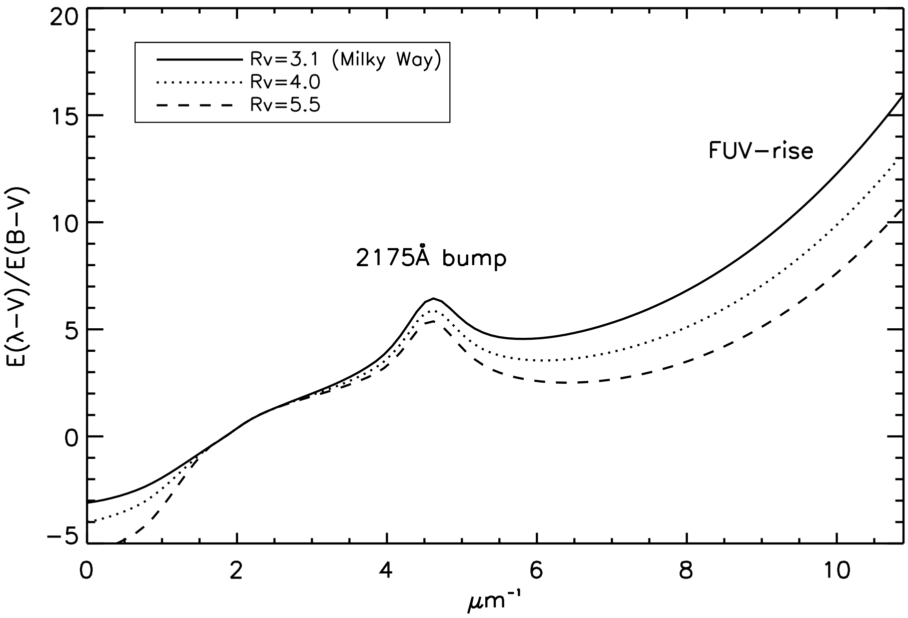

Figure 1.1: Model reddening curves for three different values of R_V. These curves are generated using the *fmrcurve.pro* IDL routine (Fitzpatrick 1999). The average Milky Way reddening corresponds to a value of $R_V = 3.1$.

to explain the anomalously large R_V value (R_V=5.5) measured towards the Orion nebula (Cardelli & Clayton 1988).

Two important features of the reddening curve shown in Figure 1.1 are immediately obvious. The so-called "2175 Å bump" is the strong extinction feature centered at 2175 Å (4.6 μm^{-1}). The "FUV-rise" is the strong increase in extinction efficiency at FUV wavelengths (7-11 μm^{-1}). The 2175 Å bump is thought to be a pure absorption feature. It is most often attributed to increased absorption by a population of small (<0.01μm) carbonaceous grains, possibly graphenes, polycyclic aromatic hydrocarbon (PAH) molecules or small graphite grains (Li & Draine 2001; Draine & Li 2007; Fischera & Dopita 2011). The FUV-rise is also thought to be caused predominantly by absorption due to reduced grain albedo in the FUV (Gordon 2004) and the increased interaction cross-section of small ($< 0.1\mu$m) dust grains, which have sizes comparable to the wavelength of FUV photons. FUV extinction measurements made using Far Ultraviolet Spectroscopic Explorer (FUSE) observations (Gordon et al. 2009) are consistent with dust grain models that explain the FUV-rise as the long-wavelength wing of an absorption feature centered at ∼720 Å. This feature correlates with a PAH resonance at 722 Å (Draine & Li 2007), which may point toward its origin; however, a turn-over in the reddening curve on the short-wave side of this feature has not yet been measured.

The extinction curve (A_λ) quantifies the number of photons that are lost at a given wavelength from a background source because they are either absorbed or scattered out of the light of sight by foreground dust grains. Of course, photons can also be scattered *into* the observer's line of sight. This light also carries information about the dust. Two scattering properties of dust grains, the albedo ($\boldsymbol{a}$) and phase function asymmetry ($\boldsymbol{g}$), determine the reflectivity and preferred direction of scattering. These parameters are set by the grain size and composition and influence the distribution of scattered light within a dust cloud. Measurements of scattered light can therefore constrain the physical properties of dust grains.

In this dissertation, I use FUV observations of scattered light across the face of an interstellar cloud to constrain the dust grain scattering parameters $\boldsymbol{a}$ and $\boldsymbol{g}$. These parameters can be connected back to the properties of the grains themselves through the use of grain composition and size-distribution models such as those found in Draine (2003) and Weingartner & Draine (2001). Observations in the FUV are difficult due to strong spectral contamination by neutral and ionized Hydrogen, which is ubiquitous in the Galaxy. These observations, however, provide crucially important data in the region of the spectrum where dust directly influences the chemical evolution and energy transport processes of our Galaxy.

1.1.2 Introduction to Dust Scattering

Modern descriptions of the electromagnetic interaction between photons and dust grains are rooted in the Mie theory of the early 20^{th} century. This theory was first formalized by Mie in 1908 and independently by Debye in 1909 (Whittet 2003). Mie theory forms a solution to Maxwell's equations for a radiation field constrained by the boundary conditions imposed by a set of small dielectric spheres (simplified models for dust grains). This solution establishes the physical backbone for dust grain scattering and absorption.

A detailed treatment of the Mie theory is presented in van de Hulst (1981). A complete description of astronomical extinction is given in Whittet (2003). I will present here a brief overview of the relevant extinction parameters to be discussed throughout this dissertation.

The emissivity of dust grains in the ultraviolet is negligible; we can then write a simplified solution to the equation of radiative transfer for a radiation field passing through a sourceless medium as:

$$I = I_0 e^{-\tau_{ext}} \tag{1.4}$$

where, I is the propagation of the initial intensity I_0 through a medium of optical depth τ_{ext}. Eq. 1.4 and Eq. 1.1 are equivalent with $A_\lambda = 1.086\,\tau_{ext}$. As a note to the reader, all parameters related to the optical properties of the dust are wavelength dependent, the λ notation has been suppressed for simplicity. The optical depth can be expressed as the integral of the extinction cross section (σ_{ext}) multiplied by the density of the material (n) along a path ds.

$$\tau_{ext} = \int n\sigma_{ext}\,\mathrm{d}s \tag{1.5}$$

The extinction cross section can be expressed as the sum of the absorption and scattering cross sections.

$$\sigma_{ext} = \sigma_{abs} + \sigma_{sca} \tag{1.6}$$

Each cross section can then be separated into a physical cross section (πr^2) multiplied by an efficiency factor Q.

$$\begin{aligned} \sigma_{abs} &= \pi r^2 Q_{abs} \\ \sigma_{sca} &= \pi r^2 Q_{sca} \end{aligned} \tag{1.7}$$

These efficiencies are functions of the grain radius, the wavelength of light and the dielectric and conductive properties of the grain material. These last two are expressed in the complex index of refraction m.

$$m = n + ik \tag{1.8}$$

Here, n relates the scattering (dielectric) properties of the material and k is the imaginary component associated with the absorptive (conductive) properties of the material. These optical constants represent the grain composition in the language of radiative transfer.

The scattering efficiency (Q_{sca}) relates nothing about the directionality of scattering. To see this dependence we must express Q_{sca} as the integral of the differential scattering efficiency $\left(\frac{\mathrm{d}Q_{sca}}{\mathrm{d}\Omega}\right)$. The differential scattering efficiency is also known as the scattering phase function (Φ) and relates the probability of scattering into a given angle.

$$Q_{sca} = \int \frac{\mathrm{d}Q_{sca}}{\mathrm{d}\Omega}\,\mathrm{d}\Omega = \int \Phi\,\mathrm{d}\Omega \tag{1.9}$$

One additional level of abstraction is required to express the scattering theory in the common astrophysical format. The extinction efficiencies (Q_{sca} and Q_{abs}) and the

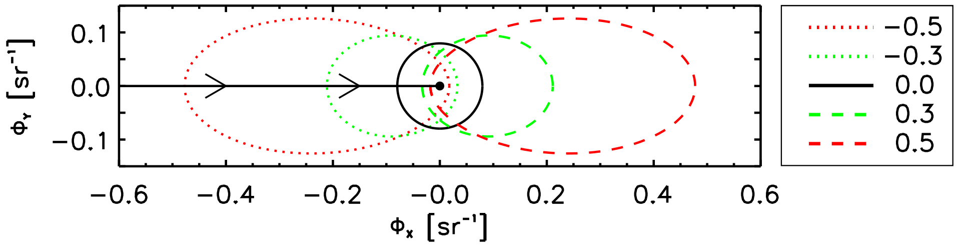

Figure 1.2: The Henyey-Greenstein phase function (Eq. 1.12) is plotted for varying $g = \langle \cos(\theta) \rangle$ in the scattering plane. The arrow shows the incident photon path.

scattering phase function (Φ) are parametrized into the single scattering albedo ($\boldsymbol{a}$), the ratio of the scattering efficiency to the total extinction efficiency (Eq. 1.10), and the phase function asymmetry parameter ($\boldsymbol{g}$), which is the cosine weighted average of the phase function (Eq. 1.11). A value of $\boldsymbol{g} = 0$ implies isotropic scattering, whereas $\boldsymbol{g} = -1$ implies pure backward scattering and $\boldsymbol{g} = 1$ implies pure forward scattering.

$$a = \frac{Q_{sca}}{Q_{ext}} \tag{1.10}$$

$$g = \langle \cos(\theta) \rangle = \frac{\int \cos(\theta)\Phi \, \mathrm{d}\Omega}{\int \Phi \, \mathrm{d}\Omega} \tag{1.11}$$

Henyey & Greenstein (1941) proposed a theoretical form for the scattering phase function. The now widely adopted Henyey-Greenstein function can be conveniently expressed in terms of its own asymmetry parameter.

$$\Phi(g, \theta) = \frac{1}{4\pi} \frac{1 - g^2}{(1 + g^2 - 2g\cos\theta)^{3/2}} \tag{1.12}$$

Here, the scattering is assumed to be azimuthally symmetric about the incident photon direction; θ is the scattering angle off of the incident direction. The Henyey-Greenstein function is plotted for different values of $\boldsymbol{g}$ in Figure 1.2.

To constrain the scattering parameters ($\boldsymbol{a}$,$\boldsymbol{g}$) using observations of scattered light, a physical model of the system must be constructed to break the degeneracy between the scattering geometry and the scattering parameters – both influence the scattered light distribution. For complex systems consisting of many stars, full three-dimensional radiative transfer models must be constructed to trace the path of each photon. This is especially true as multiple scattering effects become more dominant. The scattering parameters have been determined for many dusty systems in our Galaxy and in nearby galaxies. A brief summary of these measurements is presented in the following section.

1.1.3 Previous Measurements of the Dust Scattering Parameters

The work by Gordon (2004) provides a good summary of scattering parameter estimates made using radiative transfer models and observations of reflection nebulae, dark clouds and the diffuse galactic light (DGL). The results are collected from the past 40 years of literature and those derived from outdated or faulty methods are noted and excluded.

The results compiled by Gordon (2004) are available in ASCII format here: www.stsci.edu/∼kgordon. They are plotted in Figure 1.3. A handful of more recent measurements have been included, notably the results of Lewis et al. (2009), which were derived from Spectrograph for Photometric Imaging with Numeric Reconstruction (SPINR) observations of the Upper Scorpius region. SPINR observations of the Orion Molecular Cloud (OMC) are analyzed in this dissertation. This sounding rocket mission will be described in the following sections and chapters.

Overplotted with the collected results in Figure 1.3 are predictions made by the dust grain models of Weingartner & Draine (2001). The data and models show good agreement for $\boldsymbol{a}$ and $\boldsymbol{g}$ over most of the wavelength range. The grains produce a strong forward scattering distribution ($g \sim 0.75$) in the FUV, with the scattering becoming more isotropic at longer wavelengths. The measured albedos rise from ∼0.3 at the Lyman cut-off (912 Å) to ∼0.6 in the visible. The FUV albedo fall-off is likely responsible for producing the observed FUV-rise in Galactic extinction curves. This is thought to imply that the FUV-rise is predominantly an absorption feature (Gordon 2004).

A notable discrepancy between the measured and modeled albedos is seen between 1300-1500 Å. While the grain models predict a continuous albedo drop-off toward shorter and shorter wavelengths, the measured albedos seem to rise abruptly back to ∼0.8 at 1500 Å. The source of this feature is not well understood. Calzetti et al. (1995) attribute their measurement of high albedo at 1500 Å to an unusually flat FUV extinction curve ($R_V = 5.3$) measured along the line of sight to the observed reflection nebula, IC 435. A paucity of small grains may explain the lack of strong absorption at FUV wavelengths, however, the grain model prediction of Weingartner & Draine (2001) for a similar grain size distribution ($R_V = 5.5$) does not reproduce this feature.

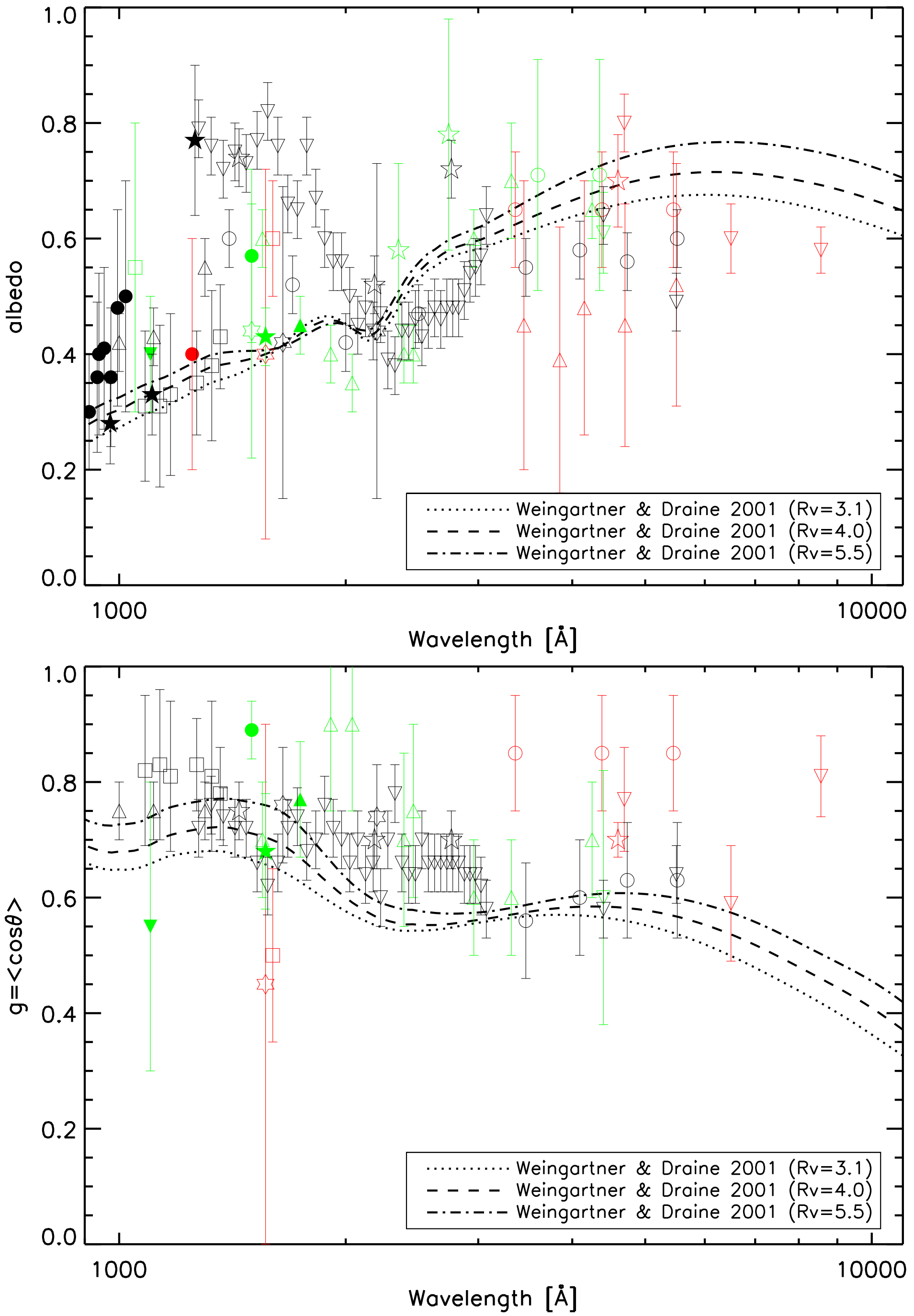

Figure 1.3: Previous measurements of the scattering parameters ($\boldsymbol{a}$,$\boldsymbol{g}$) are plotted against the grain model predictions of Weingartner & Draine (2001). The data sources are listed in Table 1.1.

Symbol	Reference	Type	Comments
○	Mattila (1970)	DC	Coalsack & Libra clouds
☆	Fitzgerald et al. (1976)	DC	Thumbprint Nebula
△	Laureijs et al. (1987)	DC	LYNDS 1642
▽	Witt et al. (1990)	DC	Bok globule
□	Hurwitz (1994)	DC	Taurus molecular cloud
✡	Haikala et al. (1995)	DC	Galactic cirrus cloud
●	Shalima & Murthy (2004)	DC	Coalsack cloud
○	Mathis (1973)	DGL	Observations by Witt (1968)
☆	Morgan et al. (1976)	DGL	TD-1 background observations
△	Lillie & Witt (1976)	DGL	OAO-2
▽	Toller (1981)	DGL	Pioneer 10
□	Murthy et al. (1993)	DGL	Voyager 2
✡	Murthy & Henry (1995)	DGL	UVX+
●	Petersohn (1997)	DGL	DE
★	Witt et al. (1997)	DGL	FAUST
▲	Schiminovich et al. (2001)	DGL	NUVIEWS
▼	Sujatha et al. (2005)	DGL	GALEX
○	Witt et al. (1982)	RN	NGC 7023
☆	Witt et al. (1992)	RN	NGC 7023
△	Witt et al. (1993)	RN	NGC 7023
▽	Calzetti et al. (1995)	RN	IC 435
□	Burgh et al. (2002)	RN	NGC 2023
✡	Gibson & Nordsieck (2003)	RN	Pleiades Nebula
●	Shalima et al. (2006)	RN	Orion Nebula
★	Lewis et al. (2009)	RN	Upper Sco. OB2

Table 1.1: Data sources for Figure 1.3. Measurements are for dark clouds (DC), the diffuse galactic light (DGL) and reflection nebulae (RN).

1.2 Dust in Planetary Systems

As planetary systems form and evolve, dust can be observed in a variety of settings. Dusty protoplanetary disks are formed first as the host star is still accreting mass. The review article by Williams & Cieza (2011) lays out a detailed description of our current understanding of this process. Disk evolution proceeds as the small (< 0.01 μm) interstellar dust grains collide and adhere to one another creating larger cross-sections for interaction with the gas, which in the early stages of disk formation, comprises 99% of the disk mass. The early disk mass is about 1% of the host star mass. Increased drag acts to decouple the grains from the motion of the gas. Grain settling along the midplane accelerates this process leading to the formation of larger grains and eventually planetesimals. As extreme-ultraviolet (EUV), FUV and X-ray radiation from the host star photoevaporates the gaseous component of the disk, small dust grains, which dominate the opacity, are removed by radiation pressure and Poynting-Robertson drag. Larger grains (> 1 μm), planetesimals and planets remain forming planetary systems and debris disks similar to our Kuiper belt. These debris disks can extend out to hundreds of AU.

Protoplanetary disk evolution is brief. The time from initial formation to arrival in the debris disk state is typically 3 Myr for solar type stars; higher mass stars lead to faster evolution (Williams & Cieza 2011). The next stage of dust evolution within planetary systems is one of continual dust processing and can last for billions of years. As comets shed their outer layers and asteroids collide and fragment, a continually replenishing blanket of exozodiacal dust settles throughout the system. Exozodiacal dust, analogous to the zodiacal dust in our own Solar System, is comprised of large (1-200 μm) grains.

Exozodiacal dust grains and interstellar dust grains are the focus of this dissertation. As with interstellar grains, scientific gains can be made by exploring both the intrinsic properties of the exozodiacal grains and the contaminating effect these grains have on other observations – namely those of extrasolar planets that cohabitate the planetary environment. The chemical composition of these grains is directly linked to the larger bodies in the system. The size distribution informs models of the various replenishment and processing mechanisms within the system. The spatial distribution of these grains reveals the center-clearing evolution of the protoplanetary disk as well as the gravitational influence of planets through the formation of dust clumps, disk warps and stable dust belts. As past observations of larger scale debris disk structures revealed the influence of unseen Jupiter-massed exoplanets (Mouillet et al. 1997; Wyatt & Dent 2002), observations of induced structures in exozodiacal dust may provide indirect methods for detecting Earth-massed planets (Stark & Kuchner 2008).

1.2.1 Observational Techniques

Planetary debris disks and exozodiacal grains undergo radiative heating from their host stars and produce excess emission relative to the stellar spectrum that can be measured from the submillimeter down into the mid-infrared. Extremely sensitive modern infrared space observatories such as the Spitzer Space Telescope (SST), the InfraRed Astronomical Satellite (IRAS) and the Herschel Space Observatory have enabled this technique to probe warm (>100 K) exozodiacal dust grains within a few AU of their host stars. Many cold (<30 K) outer debris disks have also been directly imaged in the far-infrared and submillimeter. However, in these outer regions, where large icy bodies exist, emission measurements are able to probe only the smaller grains up to a maximum radius of $a_{max} \sim 3\lambda$ (Draine 2006; Williams & Cieza 2011).

At shorter, near-infrared and optical wavelengths, light scattered by debris disks can be directly imaged to trace disk morphology. This has been accomplished using the Hubble Space Telescope (HST) in the visible and 10 m class ground-based telescopes in the near-infrared. Direct scattered-light imaging can also probe the scattering parameters ($\boldsymbol{a}$,$\boldsymbol{g}$) of dust in these systems to reveal the dust composition and size distribution.

To directly image exozodiacal dust in the inner ~10 AU of nearby stellar systems requires not only high resolution imaging, but also advanced coronagraphic techniques to suppress the overwhelming glare of the host star. The diffractive nature of telescope optics spreads the light from a star over an area hundreds of times larger than the angular extent of the stellar disk. Even at angular separations corresponding to a few AU, the stellar point spread function (PSF) can be 10^6-10^{10} times brighter than an orbiting planet or dust ring.

The following section will provide several examples of exozodiacal dust and debris disk observations made using these techniques.

1.2.2 Previous Measurements of Exozodiacal Dust and Debris Disks

The first measurement of infrared excess due to emission from a debris disk around a main-sequence star was made for Vega (Alpha Lyrae) in 1984 by Aumann et al. (1984). IRAS observations at 25, 60 and 100 μm showed significant emission in excess of the A0V intrinsic spectrum. These observations were remarkable not only because they were the first of their kind, but also because Vega had long stood as a widely adopted photometric and spectral calibration standard; indeed, Vega once defined the zero-point of the stellar magnitude system itself. The observed spectrum of Vega is dominated by dust emission in the far-infrared and exceeds the underlying stellar spectrum by a factor of ~16 at 100 μm. These observations coined the term "Vega-excess star" to describe main-sequence stars with measured mid to far-infrared excess. Later 1.3 and 3 millimeter observations reveled sub-structure in the Vega debris disk (Wilner et al. 2002). Multiband Imaging Photometer for Spitzer (MIPS) observations at 24, 70 and 160 μm made by Su et al.

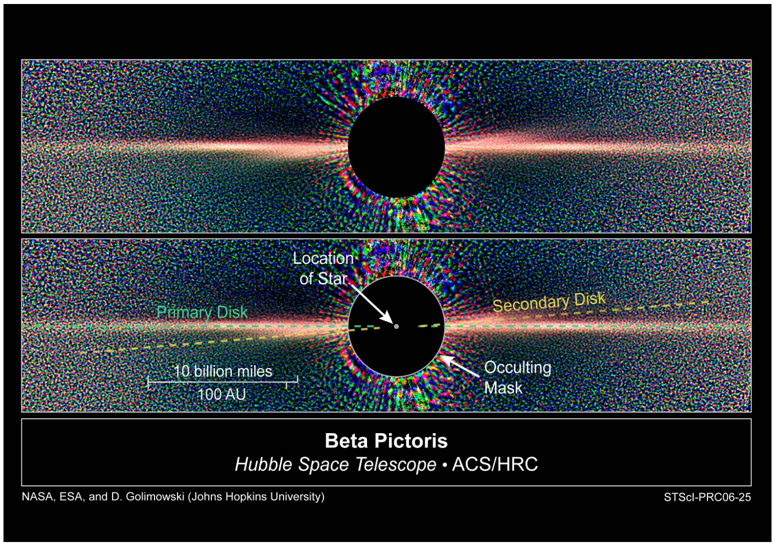

Figure 1.4: HST ACS coronagraphic image of the β Pictoris debris disk (Golimowski et al. 2006). *Image credit: NASA, ESA, D. Golimowski (Johns Hopkins University), D. Ardila (IPAC), J. Krist (JPL), M. Clampin (GSFC), H. Ford (JHU), and G. Illingworth (UCO/Lick) and the ACS Science Team.*

(2005) showed a much larger disk than was measured previously. A transient collisional event was hypothesized to produce the massive debris cloud, which extends to 815 AU at 160 μm.

Mid-infrared (5-35 μm) spectroscopic observations of some dusty systems have revealed excess emission that is the signature of warm (>50 K) exozodiacal dust located in the inner 50 AU of these systems. Lawler et al. (2009) observed 152 nearby solar-type stars with the Spitzer Infrared Spectrograph (IRS), ~1% of which showed some excess from 8.5-12 μm, and ~10% of which showed 30-34 μm excess. The 8.5-12 μm excess emission contained no spectral features like those measured towards HD 69830 by Beichman et al. (2005). These features were explained using an emission model for hot (400 K) sub-micron silicate grains with possible cometary origin. The lack of spectral features measured by Lawler et al. (2009) can be explained by larger, cooler grains, which produce broad continuum emission.

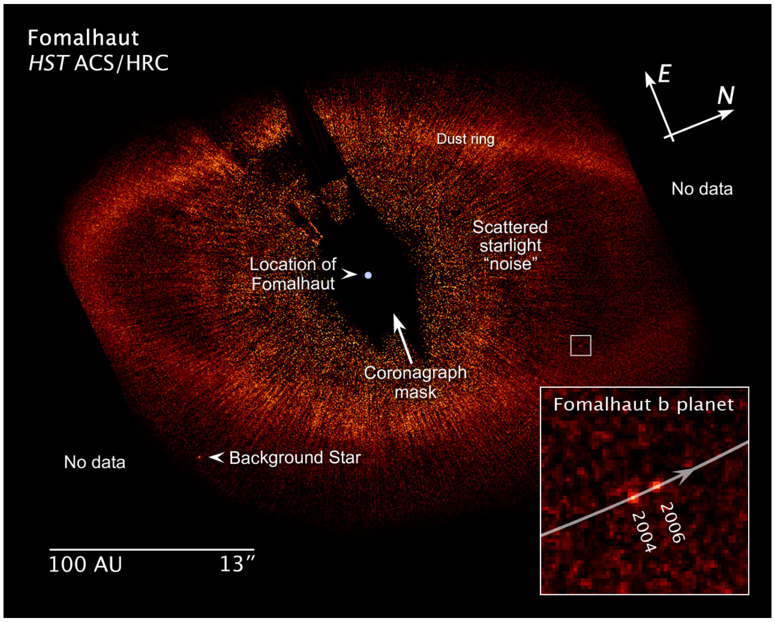

Figure 1.5: HST ACS coronagraphic image of the Fomalhaut debris disk and Fomalhaut-b planet (Kalas et al. 2005). *Image credit: NASA, ESA, P. Kalas, J. Graham, E. Chiang, E. Kite (Univ. California, Berkeley), M. Clampin (NASA/Goddard), M. Fitzgerald (Lawrence Livermore NL), K. Stapelfeldt, J. Krist (NASA/JPL)*

The edge-on debris disk around β Pictoris was also discovered using IRAS observations (Aumann 1985). Follow up ground-based coronagraphic images measured the angular extent of the disk in visible scattered light (Smith & Terrile 1984). The disk was further characterized using millimeter wave observations (Wilner et al. 2011) and HST ACS coronagraphic images (Figure 1.4) of the visible scattered light (Golimowski et al. 2006). The observed warp in the debris disk (Mouillet et al. 1997) and the inner clearing zone of the disk (Roques et al. 1994; Lagage & Pantin 1994) were used to predict the presence of a planet. This planet, β Pic b, was later imaged directly using the Very Large Telescope (VLT) at 3.78 μm (Lagrange et al. 2010).

Perhaps the most famous image to date of a debris disk is that of the disk around Fomalhaut (Figure 1.5), which was also obtained using the HST ACS coronagraphic camera (Kalas et al. 2005). The optical scattered light component of the Fomalhaut debris disk is 25 AU wide and circles the star at a radial distance of 133 AU. This image also includes a planetary candidate, Fomalhaut-b, which is believed to sheppard the exterior 50-100 $M_\oplus$ dust ring. The Fomalhaut debris disk was first discovered via its far-infrared excess, also in the IRAS study by Aumann (1985). Dynamical models by Chiang et al. (2009) offer a new method for constraining the planetary mass based on the observed morphology of the debris disk. This model predicts a mass less than 3 M_J for Fomalhaut-b.

The HR 8799 system harbors at least four giant planets, all of which have been directly imaged in the near-infrared using the Keck II and Gemini telescopes (Marois et al. 2008, 2010). The Keck II image showing all four planets is reproduced from Marois et al. (2010) in Figure 1.6. The image shown in color-scale (1 November 2009) was taken notably without the use of a coronagraph. This image is the result of a number of powerful techniques currently available to ground-based observatories. First, the planetary spot diameter is extremely small ($\sim$0.1$''$); the high-performance adaptive optics (AO) system onboard the 10 m Keck II telescope delivers near-diffraction-limited imaging in the L$'$ band (3.8μm). Second, at these longer infrared wavelengths, the emitted light from the self-luminous planet is being captured. The planet-to-star contrast ratio is more favorable than in the visible, where the reflected light is recorded. Third, these observations employ a technique known as angular differential imaging (ADI). A long series of exposures is taken as the sky rotates through the telescope field of view. Faint speckles caused by instrumental effects remain stationary in the recorded images while real astrophysical objects rotate along with the sky. This enables image post-processing software to remove the instrumental effects and reveal the faint planetary signal.

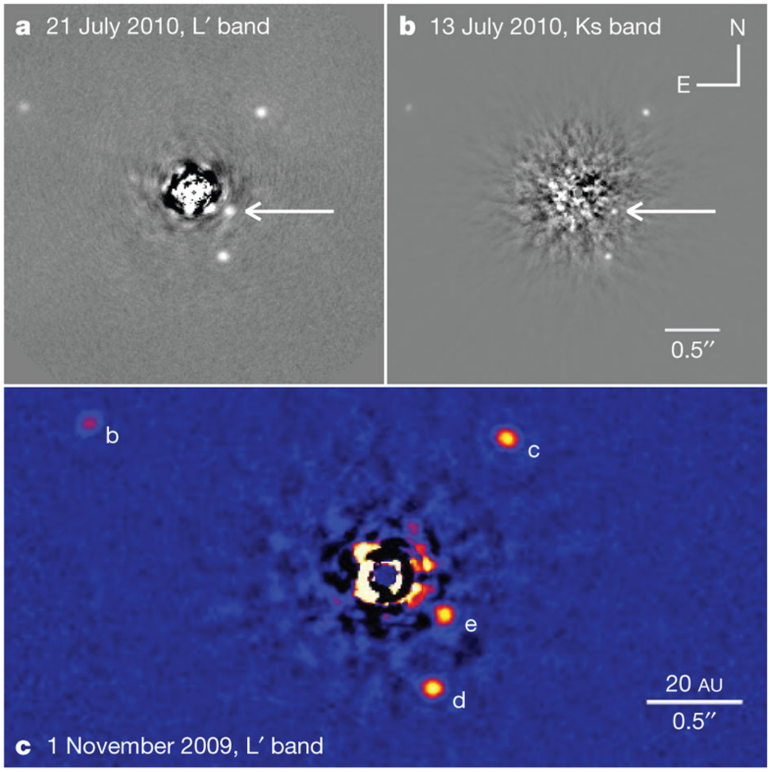

Figure 1.6: Direct image of four planets orbiting the star HR 8799. This figure is reproduced from Marois et al. (2010). The images were obtained using the Keck II telescope on three different days in the L′ and Ks bands. No coronagraphic focal plane mask was used on 1 November 2009, but a 0.4″-diameter mask was used on 13 July and 21 July 2010.

The debris disk of the multi-planet HR 8799 system was characterized by Su et al. (2009) using spectral excess measurements from the mid-infrared to the sub-millimeter. They identify a preferred model that includes three components to the dust distribution. The inner component is a warm (∼150 K) exozodiacal dust disk consisting of 1.5-4.5 μm grains. This disk extends from 6-15 AU, interior to the orbit of the innermost planet, HR 8799e. The second component is a cooler (∼45 K) planetesimal disk that extends from 90-300 AU and is made up of large 10-1000 μm grains. The third component is an outer halo of cold 1-10 μm grains that may reach out to 1000 AU.

To directly image warm exozodiacal dust in the interiors of planetary systems, observations must probe a region that is an order of magnitude closer to the host star than the debris disk region. While the HST Space Telescope Imaging Spectrograph (STIS), ACS and Near Infrared Camera and Multi-Object Spectrometer (NICMOS) coronagraphic cameras have been very successful in directly imaging visible light scattered by debris disks at many tens of AU (Schneider et al. 2009; Kalas et al. 2005; Golimowski et al. 2006; Schneider et al. 2006, eg.), attempts to capture scattered light from the inner 10 AU of dusty systems have not been successsful. Kuchner & Brown (2000) used the NICMOS camera to observe the terrestrial zones of three of the closest main-sequence stars. The stars must be extremely close to Earth in order to resolve these interior regions. These observations could not improve upon the upper limits already set by IRAS observations. No other space-based mission has a coronagraphic instrument or the angular resolution to even attempt these types of observations.

Progress in directly detecting exozodiacal dust has been made from the ground using interferometric techniques. The Center for High Angular Resolution Astronomy (CHARA) array was used by di Folco et al. (2007) to measure the 2 μm excess flux within 3 AU of the ϵ Eri and τ Ceti systems. The study resolved $\sim$1% excess emission around τ Ceti and set upper limits for ϵ Eri at an excess of <0.6%. Liu et al. (2009) set limits for exozodiacal dust brightness and morphology around 6 nearby main-sequence stars using nulling interferometric observations on the MMT 6.5 m telescope. Millan-Gabet et al. (2011) performed an exozodiacal dust survey of 25 nearby main-sequence star systems using Keck Interferometer Nuller (KIN) observations in the mid-infrared. The survey found one significant detection around η Cru, two marginal detections around γ Oph and α Aql (Altair), and 22 non-detections.

While significant progress has been made in directly imaging cold debris disks and a handful of exoplanets from the ground and space, the direct imaging of warm exozodiacal dust and exoplanets in the interior regions of nearby systems still awaits the development of an adequate high-contrast imaging instrument. The upcoming Gemini Planet Imager combines state of the art image-plane coronagraph technology with high-speed adaptive optics to achieve extreme high-contrast imaging from the ground. The instrument has already demonstrated raw contrast levels of 1×10^{-6} and 2×10^{-7} after image processing (Macintosh et al. 2012). A dedicated space mission will also be required to perform these observations in visible light and for more distant targets that require greater angular resolution than ground based AO can provide. Numerous space and balloon missions have been proposed to directly image exoplanetary systems around nearby stars (Brugarolas et al. 2010; Bryden et al. 2011; Schneider et al. 2012; Shao & Levine 2010; Matsuo et al. 2011; Liu et al. 2004, eg.). None of these missions have been selected to fly. This dissertation will describe the development of the Planetary Imaging Concept Testbed Using a Rocket Experiment (PICTURE) sounding rocket mission, the first dedicated exoplanetary imaging mission to fly in space.

1.3 Two Dusty Laboratories

Two astrophysical systems have been chosen to observationally study the properties of dust in the ISM and in planetary systems. Due to its close proximity to Earth (450 pc), well documented dust content and abundance of UV-bright O and B stars, the Orion OB association and background Orion Molecular Cloud (OMC) are an excellent laboratory for studying the interaction of dust grains and FUV radiation in the ISM. Much like Orion, the ϵ Eridani exoplanetary system provides a close-up view of an important astrophysical process that occurs throughout the Galaxy. Positioned just 3.2 pc from the Sun, ϵ Eridani is one of the closest known exoplanetary systems. Observations have shown this system contains a bright outer debris disk similar to our own Kuiper Belt and an inner population of warm exozodiacal dust grains.

1.3.1 The Orion Molecular Cloud and OB Association

The vast Orion Molecular Cloud Complex lies 450 pc from the Sun in the Galactic anti-center direction. It is positioned 15° below the Galactic plane along a sightline with very low foreground extinction and very little contamination from molecular gas associated with the Galactic plane. The molecular cloud has formed a large population of massive O and B stars, the Orion OB Stellar Association. Over the past 12 Myr, the intense ionizing and dissociative UV radiation from these stars, along with strong stellar winds and supernovae explosions, have acted to shape the physical and chemical evolution of the clouds (Wilson et al. 2005). For these reasons, the OMC has become one of the most widely studied molecular clouds in the galaxy. It offers a clear, up-close view of the interaction between massive stars and the ISM.

The three-dimensional distribution of gas, dust and stars that comprises the Orion system has been characterized with ever increasing detail over the past 50 years through the use of wide-field surveys taken over a range of wavelengths. The cloud complex contains three giant ($10^5\,M_\odot$) molecular clouds: the Orion A, Orion B and Monoceros R2 clouds. These clouds are linked by a number of filaments and smaller clouds to form one complex that fills a $20^\circ \times 10^\circ$ field on the sky. Observations of the OMC in the microwave, visible, near-infrared and far-infrared are shown in Figure 1.7.

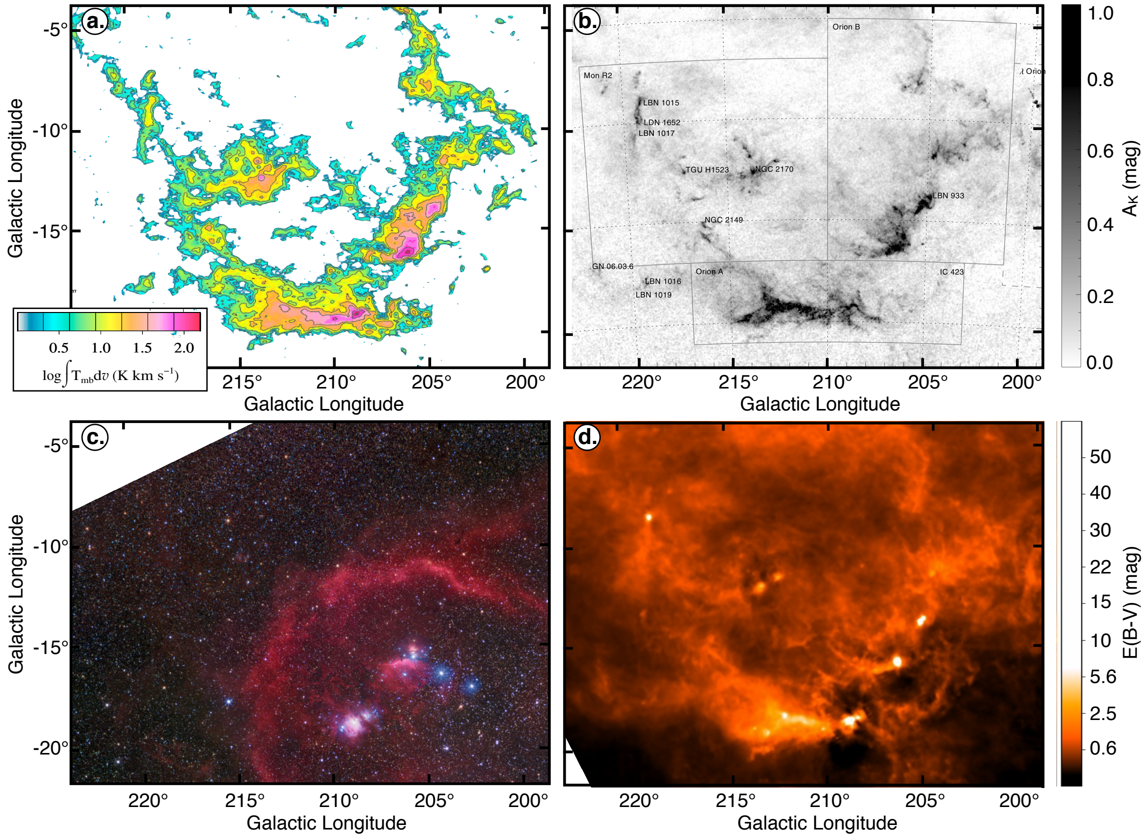

Figure 1.7: Maps of the Orion Molecular Cloud Complex in four wavelength regimes. ***a.*** The molecular gas content is traced by the ^{12}CO $J = 1 \rightarrow 0$ contours of Wilson et al. (2005). ***b.*** Near-infrared extinction is traced by Lombardi et al. (2011) using stars in the 2MASS point source catalog. The Orion A, Orion B and Monoceros R2 clouds are labeled. ***c.*** Visible-light image (H_α,L,B,V,R) of the Orion constellation (*Image credit: R.Gendler & Stéphane Guisard*). The H_α emission traces ionized gas in Barnard's Loop, an arc-shaped emission nebula that is thought to be the result of a supernova explosion. ***d.*** E(B-V) reddening map created by Schlegel et al. (1998) from far-infrared (100 μm) IRAS observations of (10-30 K) dust emission.

The molecular gas content of the entire OMC complex was mapped by Wilson et al. (2005) using microwave observations of the $J = 1 \rightarrow 0$ transition of ^{12}CO. These observations were made using the 1.2 mm wave telescope at the Harvard Smithsonian Center for Astrophysics. The measured emission map is reproduced in Figure 1.7. The ^{12}CO observations reveal the molecular mass and radial velocity of each sub-cloud. Distances are also determined to each cloud using a statistical treatment of the measured HIgh Precision PArallax COllecting Satellite (HIPPARCOS) parallax (Perryman et al. 1997) for stars in the region. Although individual stellar distances measured by HIPPARCOS are reliable out to only $\sim$200 pc, a statistical combination of measurements towards many stars paired with a model probability distribution of cloud distances can yield accurate distance estimates out to 500 pc. Using this technique, Wilson et al. (2005) calculate distances of $\sim$450 pc to the Orion A and B clouds and $\sim$800 pc to the Monoceros R2 cloud. Observational evidence for stellar wind and radiation-driven erosion and compression of the clouds is also seen in the molecular data, along with signs of triggered star formation.

Extinction studies have also been used to probe the structure of the OMC. Lombardi et al. (2011) compiled a wide-field, near-infrared extinction map of the entire OMC complex using the 2MASS point source catalog. They mapped the dust column density across the face of the OMC using point-by-point measurements towards $\sim$19 million stars. The resulting extinction map is reproduced in Figure 1.7. Distances to each cloud were determined by comparing the density of foreground stars to Galactic models. The masses and reddening laws of each cloud were also determined.

Full-sky maps of dust emission and reddening, which include the entire OMC, were constructed using IRAS and Cosmic Background Explorer (COBE) observations in the far infrared by Schlegel et al. (1998). These maps reveal the temperature profile of the OMC as a result of both internal and external heating by massive stars. The Schlegel et al. (1998) dust reddening map of the OMC is also reproduced in Figure 1.7.

A catalog of stellar properties for the Orion OB association was compiled by Brown et al. (1994). This stellar association is comprised of $\sim$400 O and B stars including the bright blue stars that form the Orion constellation – with the notable exception of Betelgeuse, a red supergiant. The Brown et al. (1994) catalog includes Walraven *(V,B,L,U,W)* photometry measured for each star by de Geus et al. (1990). These photometric measurements were used to construct reddening-independent colors using the Lub & Pel (1977) relation, which were in turn used to constrain Kurucz (1979) models to determine the effective temperature and surface gravity of each star. These stellar atmosphere models were then used as calibration standards to measure the reddening, E(B-V), and distance modulus for each star.

The discussed observations of the OMC and Orion OB association leave us with a very clear picture of the large-scale three-dimensional structure of the system. The dust is dominated by the background OMC. The FUV-bright O and B stars lie predominantly foreground to the slab-like cloud. There is very little foreground dust between the Sun and the Orion stars; most stars in the OB association have measured E(B-V) < 0.1. The Trapezium stars in the Orion Nebula (M42), including the massive Theta^1 Ori C (one of the hottest stars visible from Earth), are embedded in the front face of the OMC to a level of E(B-V)~ 0.3. Most, if not all of this reddening is produced by dust immediately in front of the stars (O'Dell 2001). The contribution of light from these stars to the observed wide-field scattered light distribution will be discussed further in Chapter 3, where a three-dimensional model of the Orion system is constructed.

1.3.2 The ϵ Eridani Exoplanetary System

Epsilon Eridani is a sun-like K2V star located 3.2 pc from Earth. The $0.83\,M_\odot$ star harbors at least one extrasolar giant planet (EGP), ϵ Eri b, which was discovered by Hatzes et al. (2000) using the radial velocity technique. This system was the closest known exoplanetary system until the recent discovery of an Earth-massed planet orbiting α Centauri B (Dumusque et al. 2012). The < 1 Gyr old ϵ Eri system exhibits the strong photospheric activity expected for a young star (Gray & Baliunas 1995). Radial velocity noise induced by this activity resulted in a failure to discover the planet in earlier observations. Hatzes et al. (2000) measured a $19\,\mathrm{m\,s^{-1}}$ amplitude radial velocity signature for the planet. Follow-up HST astrometric measurements by Benedict et al. (2006) provided a full orbital solution. The $1.55\,M_J$ planet lies in a highly eccentric ($e = 0.7$) orbit with a 6.9 year period. The system parameters are given in Table 1.2.

Parameter	Value
M_{star}	$0.83 \pm 0.03\,M_\odot$
M_b	$1.55 \pm 0.24\,M_J$
Period	6.85 ± 0.03 years
Semi-major axis	3.39 ± 0.36 AU
Eccentricity	0.702 ± 0.039
Inclination	$30.1 \pm 3.8^\circ$
Periastron separation	$0.3 \pm 0.1''$
Apastron separation	$1.8 \pm 0.4''$

Table 1.2: Orbital parameters for ϵ Eri b, as measured by Benedict et al. (2006)

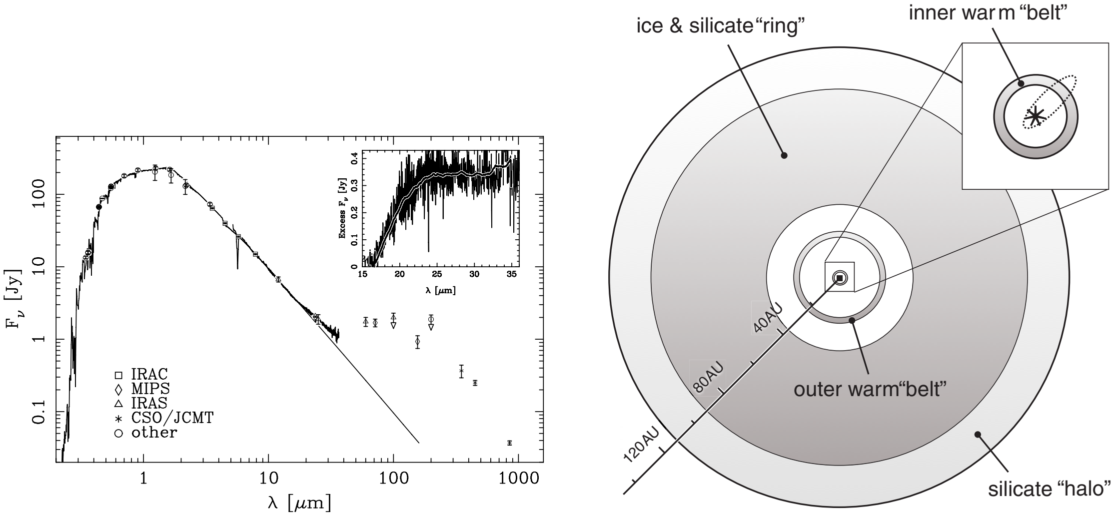

Figure 1.8: Inferred dust distribution of ϵ Eri. These figures are reproduced from Backman et al. (2009). The mid to far-infrared excess emission (*left*) is used to constrain a model of the dust distribution that includes two warm (100-150 K) dust belts at radii of 3 and 20 AU.

The ϵ Eri system contains a well characterized debris disk at 60 AU (Greaves et al. 1998, 2005). Observed infrared excess in the stellar spectrum has been used to infer the existence of two warm dust belts at 3 AU and 20 AU (Backman et al. 2009) (Figure 1.8). The 3 AU dust belt is predicted to have an integrated 2.1 μm scattered light brightness of 1.8×10^{-4} F$_*$ (Backman et al. 2009). If a maximum ring width of 0.5 AU is adopted based on the modeled minimum inner clearing radius of 2.5 AU (Liu et al. 2009), this geometry results in a ring with an average surface brightness of 2×10^{-4} F$_*$/as^2. A high-contrast coronagraph is required to directly image this inner dust belt.

1.4 Observations

Having established these two astrophysical laboratories, we may further refine the questions posed in this dissertation:

- *What are the FUV scattering properties* ($\boldsymbol{a},\boldsymbol{g}$) *of dust grains along the line of sight to the Orion OB association and background OMC?*
- *What is the morphology and visible-light brightness of exozodiacal dust in the* ϵ *Eri system?*

To detect the diffuse FUV scattered light towards Orion, we must make observations from space. FUV light is an excellent probe of interstellar dust grains due to the increased interaction cross section at these wavelengths. However, FUV light cannot penetrate Earth's atmosphere. Past and existing FUV missions such as GALaxy Evolution Explorer (GALEX) and FUSE are too sensitive to point towards the extremely bright stars in the Orion OB association and lack the large field of view needed to study the global scattering properties of dust across the face of the OMC. A wide-field, lower sensitivity, space-based instrument is required to make these observations.

To directly image the inner 10 AU ($3''$) of the ϵ Eri system in reflected visible light, a high-contrast coronagraph must be used to attenuate the overwhelming glare of the parent star. These instruments require extreme stellar wavefront stability at the level of <10 nm root mean square (RMS). Due to the refractive and turbulent qualities of the atmosphere, this level of wavefront control has not yet been demonstrated with modern AO systems on the ground. In space, an environment free from high frequency atmospheric turbulence, an adaptive optics system is left only to correct the static wavefront errors induced by the telescope and instrument optics. In this case, a small telescope can be used near its diffraction limit in the visible to probe the inner few arcseconds of a planetary system.

To perform these observations, two sounding rocket missions were designed and built by our research group at the Boston University Center for Space Physics.

1.4.1 The SPINR Rocket Mission

The Spectrograph for Photometric Imaging with Numeric Reconstruction (SPINR) sounding rocket was launched on February, 19th 1999. It recorded spectral-imaging data in the FUV (750-1450Å) over a region of sky containing the entire Orion constellation. The FUV light measured by SPINR was emitted by stars in the Orion OB association and scattered by the pervading interstellar dust. I will use SPINR data along with the DustI Radiative Transfer, Yeah! (DIRTY) radiative transfer model to probe the FUV scattering properties of dust grains in Orion.

1.4.2 The PICTURE Rocket Mission

The Planetary Imaging Concept Testbed Using a Rocket Experiment (PICTURE) sounding rocket was launched on October, 8th 2011. It attempted to directly image the exozodiacal dust disk of ϵ Eridani (K2V, 3.22 pc) down to an inner radius of 1.5 AU using a Visible Nulling Coronagraph (VNC) to attenuate the signal of the bright host star. Unfortunately, the main science telemetry transmitter on the payload failed $\sim$70 seconds after launch and all science data were lost. I will present a detailed description of the design and pre-flight testing of the PICTURE science payload. In particular, I will focus on my work developing the PICTURE fine pointing system, which achieved 5.1 milliarcsecond (mas) RMS in-flight pointing stability. I will also focus on the pre-flight laboratory testing of the PICTURE nulling interferometer and wavefront control system.

1.5 Introduction to Remaining Chapters

In the following chapters, I will describe the SPINR and PICTURE missions in detail. I will explain the work I've done using the data from these missions to answer the main science questions laid out at the start of this dissertation. Chapter 2 will discuss the SPINR instrument and a set of software tools I developed to reduce the SPINR data into calibrated data products. Chapter 3 will outline the procedure of using the SPINR data products in conjunction with the DIRTY radiative transfer model to estimate the scattering parameters of dust in Orion. Chapter 4 will describe the hardware components of the PICTURE payload, focusing on the design tolerances that were implemented in order to achieve the mission's scientific goals. Chapter 5 will present laboratory test results from the individual payload subsystems. Chapter 6 will present the PICTURE flight data and will focus primarily on the in-flight performance of the fine pointing system. In Chapter 7, a summary of the results from these chapters will be given and the implications of these results will be discussed.

Chapter 2

SPINR: Observations and Data Reduction

2.1 Science Goals and Instrument Requirements

The Spectrograph for Photometric Imaging with Numeric Reconstruction (SPINR) mission was developed to characterize the interaction between far-ultraviolet (FUV) radiation and dust grains in the interstellar medium (ISM) through wide-field spectral imaging observations of FUV dust scattering in nearby systems. The target of interest in this dissertation is the Orion OB association and background Orion Molecular Cloud (OMC), which subtends approximately 200 deg^2 on the sky, an area 32 lunar diameters in extent. As discussed in Cook et al. (2003), to record spectral imaging data across this entire region using a traditional “push-broom” spectrograph would require vast amounts of observation time and a prohibitive number of instrument pointings. The SPINR spectrograph design allows for spectral imaging over a wide field using a single instrument pointing. The following sections will describe the design of the SPINR spectrograph and the data reduction and analysis techniques I have developed to analyze the SPINR data.

2.2 SPINR Instrument Description

The SPINR instrument contains four identical tomographic extreme-ultraviolet spectrographs (TESSs) (Cotton et al. 1994, 2000) that provide spectral imaging in

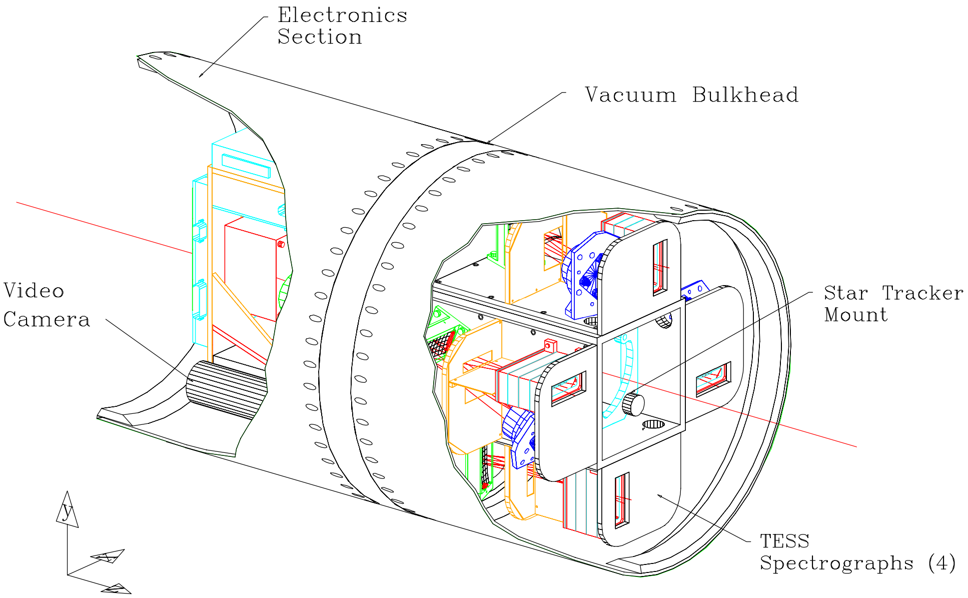

Figure 2.1: The SPINR payload carries four identical spectral imaging FUV spectrographs. The spectrographs are housed in an evacuated section of the 17″ diameter payload. The payload rotates about its long axis (red line) while pointed at the target object. *This figure is reproduced from Cook et al. (2003).*

the FUV over a 16° field of view (FOV). Four spectrographs are used for redundancy and to increase the overall sensitivity of the instrument. A schematic of the the SPINR payload is shown in Figure 2.1. The instrument and resulting data cubes are described in detail in Cook et al. (2003). Although the following sections will focus primarily on data analysis, a brief description of the instrument is warranted to aid in the understanding of the data format.

Figure 2.2 presents the design of a single SPINR spectrograph. Each spectrograph consists of an entrance aperture, a diffraction grating and a photon-counting photocathode detector.

Typical optical coatings have poor (∼50%) FUV reflectivity. The SPINR design achieves high FUV efficiency through the use of only a single optic: a toroidal diffraction grating. The toroidal grating optically compresses the image of the sky in one

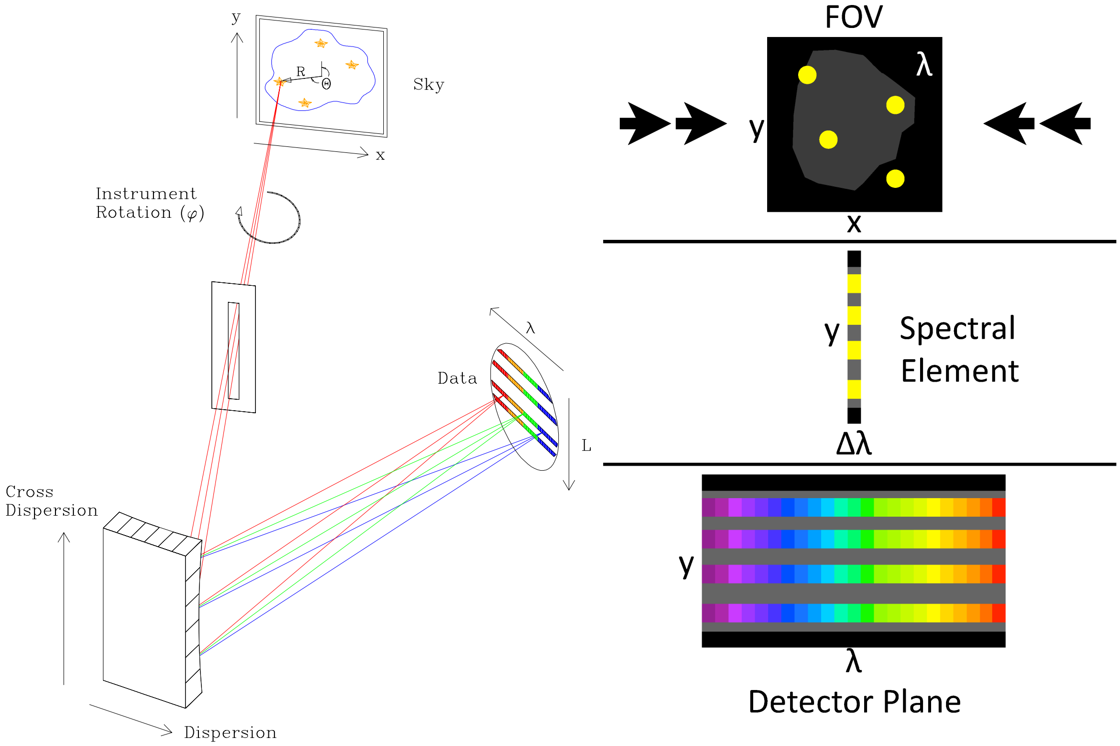

Figure 2.2: SPINR spectrograph design. The toroidal diffraction grating optically compresses the image of the sky into a single column that is then dispersed in wavelength across the detector. The spectrograph is rotated about its optical axis to recover the lost spatial dimension. *The left panel of this figure is reproduced from Cook et al. (2003).*

direction to a single column, which forms a spectral element that is then dispersed in wavelength across the detector. This spectral element is analogous to the slit of a traditional spectrograph with one key difference. A traditional slit is placed in the image plane to reject light along the axis perpendicular to the slit. The SPINR design compresses all of the light from the FOV into the slit. This greatly increases the sensitivity of the instrument at the cost of requiring more complex data analysis to determine the origin of each photon in the FOV.

Parameter (per spectrograph)	Value
System:	
Instantaneous FOV	10° × 13° (0.04 sr)
Sky coverage	16° (diameter circle)
Effective area	$1{\times}10^{-3}$ cm^2
Etendue	$4{\times}10^{-5}$ cm^{2}sr
Spectral Range	750-1450 Å
Spectral Resolution	5 Å
Spatial Resolution	$5'$
Grating:	
Rule density	3200 mm^{-1}
Optical coating	SiC
Spatial focal length	144 mm
Rowland circle diameter	150 mm
Aperture and detector:	
Aperture size	0.125 mm × 40 mm
Detector active area	36 mm (diameter)
Photocathode	KBr

Table 2.1: SPINR instrument parameters for each of the four TESS spectrographs.

To recover the compressed spatial dimension from the scene on the sky, the instrument is rotated about its optical axis. As the instrument rotates, counts from the sky coordinate system $(x_{sky}, y_{sky}, \lambda_{sky})$ are mapped into detector coordinates $(x_{det}, y_{det}, t_{det})$ to form the SPINR data cube shown in Figure 2.3. The details of this transformation will be discussed in Section 2.6. The instrument produces four simultaneous data cubes, one for each spectrograph.

The spectrograph spectral range is 750-1450 Å with 5 Å spectral resolution and $5'$ spatial resolution. The instrument has a rectangular (10° × 13°) instantaneous FOV, which sweeps out a 16° circle on the sky as the payload rotates. The short side of the FOV is limited to those angles that pass through the entrance aperture and reach the diffraction grating. The longer side is limited by size of the detector. Table 2.1 lists several relevant instrument parameters.

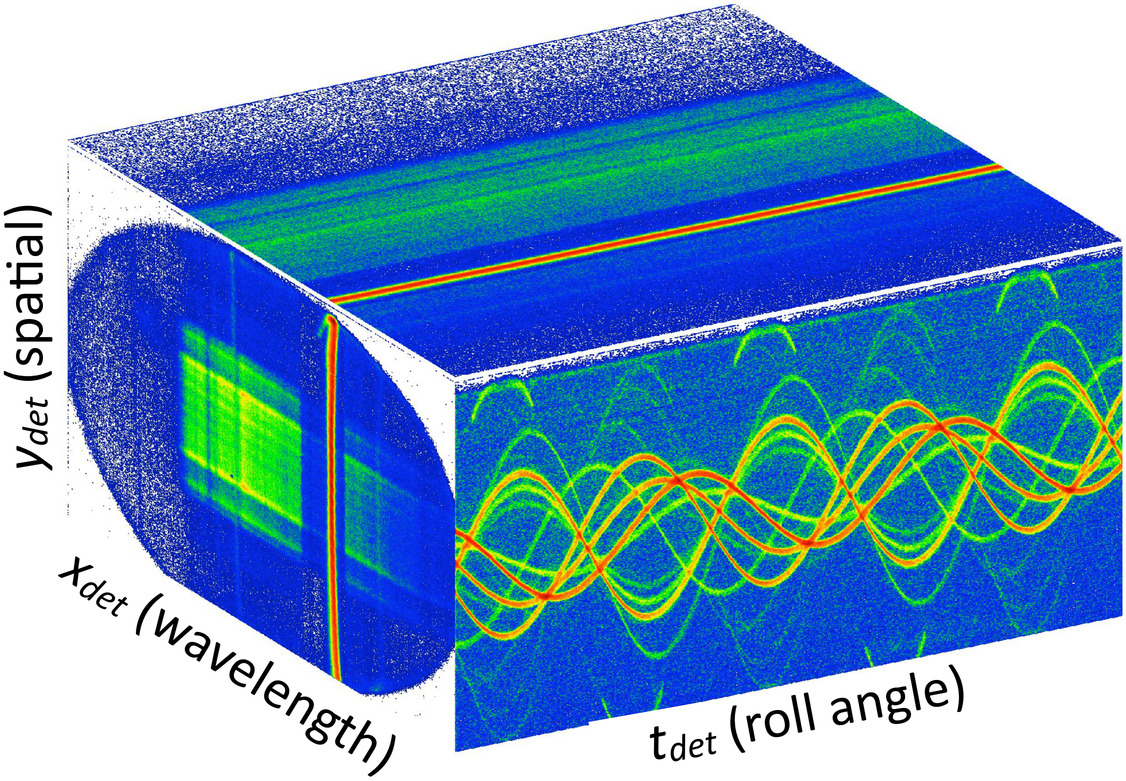

Figure 2.3: SPINR detector 0 data cube. The $(x_{det}, y_{det}, t_{det})$ data cube is constructed from a list of recorded photons. Each photon is encoded with its position on the detector (x_{det}, y_{det}) and the time it was recorded (t_{det}). Each detector axis maps to an associated physical quantity. x_{det} maps to wavelength, y_{det} maps to the 1-D spatial extent of the scene and t_{det} maps to the roll angle of the instrument. The leftmost face of the data cube shows the (x_{det}, y_{det}) plane of the detector. It is produced by summing the data cube along the t_{det} axis. The bright vertical line is created by Lyman-α photons at 1216 Å. To prevent saturation of the detector readout electronics, the detector photocathode is left uncoated beneath this bright spectral line. This region is seen as dark rectangle of reduced sensitivity. The front face of the data cube shows the (t_{det}, y_{det}) plane, which is produced by summing the data cube along the x_{det} axis. In this plane, the stars trace out sinusoids as the payload rotates. These sinusoidal patterns are discussed further in Figure 2.4

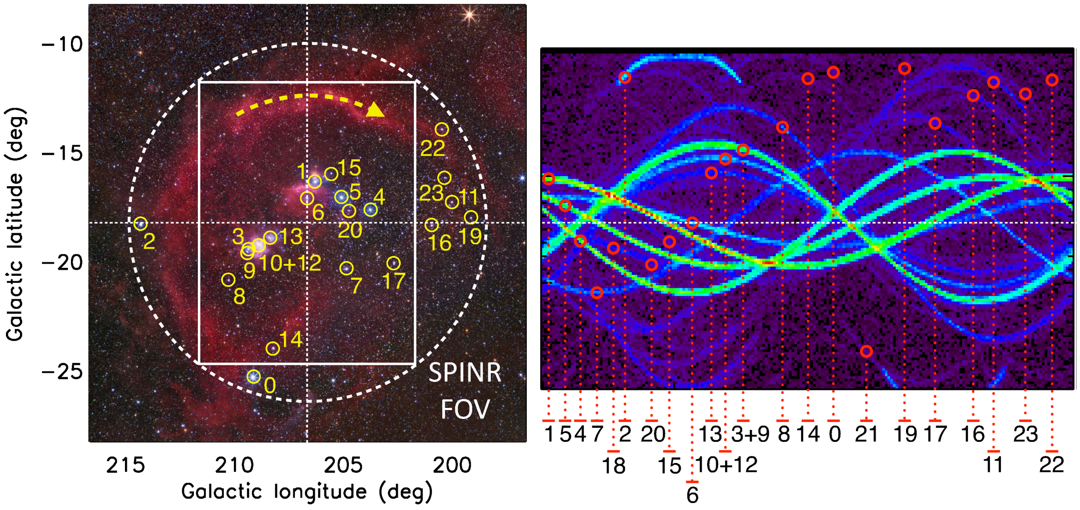

Figure 2.4: The SPINR FOV is shown for the Orion observations (*left*). The FUV-bright stars are identified. As the stars rotate clockwise around the center of the field, they trace sinusoids on the (t_{det}, y_{det}) face of the data cube (*right*). The instantaneous 10° × 13° rectangular FOV sweeps out a 16° diameter circle on the sky. Stars interior to 10° complete full sinusoids on the detector. Those beyond 10° trace partial sinusoids as the star rotates in and out of the FOV. *Background (H_α,L,B,V,R) image by R.Gendler & Stéphane Guisard.*

2.3 Orion Observation

The SPINR sounding rocket was launched on February, 19^{th} 1999. The payload collected science data for 327.3 seconds above 100 km while rolling at a period of 100 seconds (0.6 rpm) about a central pointing of (l, b)=(206.650,-18.277). After completing roughly 3 1/4 rotations, the instrument shutter door was closed as the payload began to re-enter Earth's atmosphere.

The SPINR observations of Orion are illustrated in Figure 2.4. In the reference frame of the instrument, the sky rotates clockwise through the rectangular FOV to form the sinusoidal pattern seen on the (t_{det}, y_{det}) face of the data cube. As a star exits the 10° × 13° FOV, it disappears from the data. Those stars interior to 10° are always visible and trace complete sinusoids.

2.4 Wavelength Calibration

The SPINR detectors record photon counts over a square 1024×1024 grid of pixels. In detector coordinates, the y_{det} axis maps to the cross-dispersion axis of the grating and records spatial information from the sky. The x_{det} axis maps to the dispersion axis of the grating and records spectral information. The outline of the circular photocathode is clearly seen on the (x_{det}, y_{det}) face of the data cube in Figure 2.3.

Wavelength [Å]	Species	Line Index
834	O II	0
989	O I	1
1025	Ly β	2
1216	Ly α	3
1304	O I	4

Table 2.2: SPINR telluric wavelength calibration lines.

Due to detector readout distortions and slit curvature induced by the concave diffraction grating, the wavelength of light at a point on the detector is a function of both x_{det} and y_{det}. To build a wavelength calibration function $\lambda(x_{det}, y_{det})$ for each detector, bright telluric emission lines (emitted from the Earth's geocoronal region) are mapped across the detector surface. The telluric lines used for calibration are listed in Table 2.2. The wavelength at each detector pixel is interpolated in two dimensions for pixels between the calibration lines and extrapolated to the edges of the detector. Figures 2.5 and 2.6 illustrate this process. These figures show a series of manually mapped spectral lines across each detector and the resulting $\lambda(x_{det}, y_{det})$ wavelength map contours.

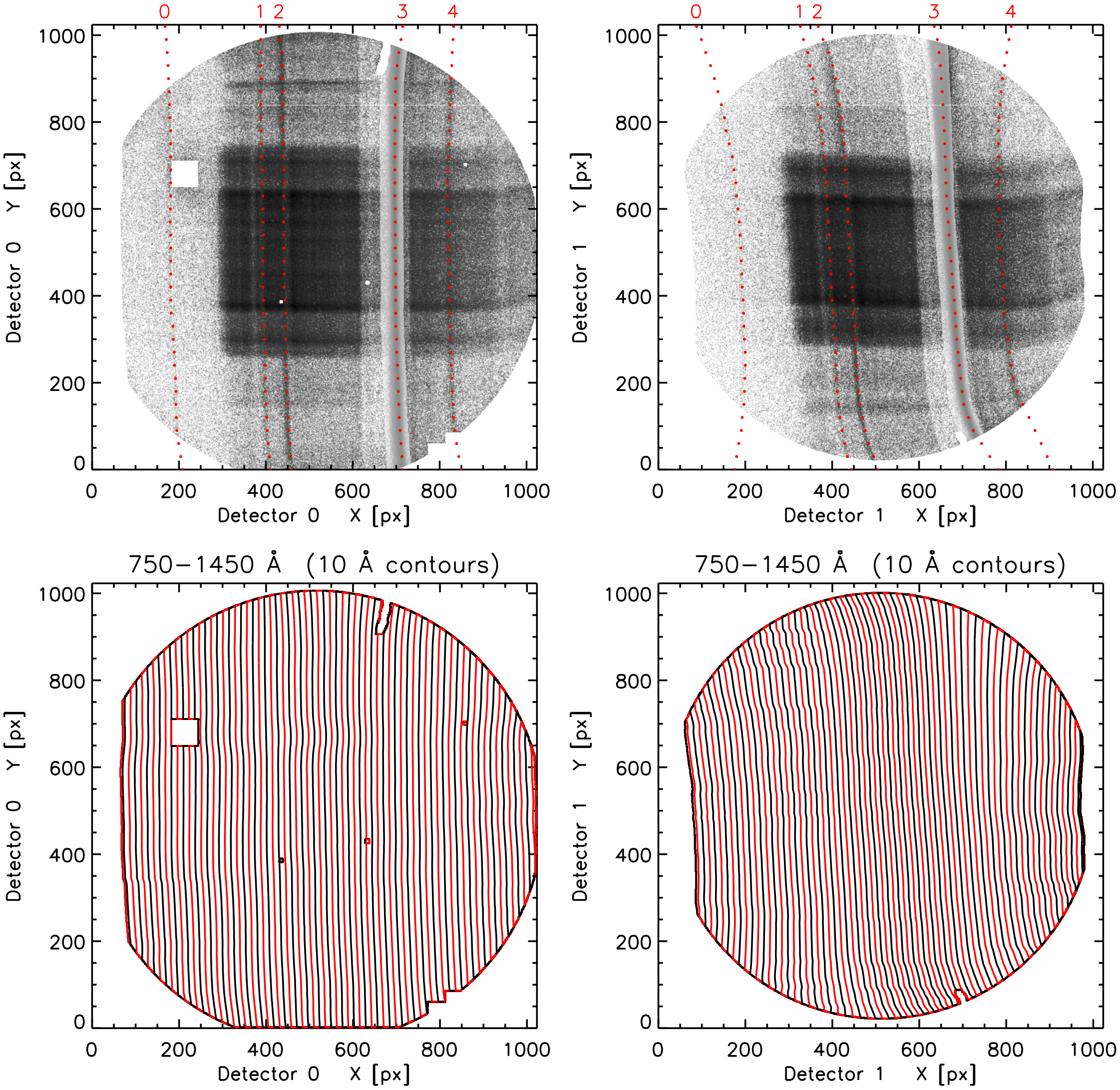

Figure 2.5: SPINR detectors 0 and 1 wavelength calibration. Bright telluric emission lines (identified in Table 2.2) are traced across the face of the detector (*top*) to create the $\lambda(x_{det}, y_{det})$ map shown in 10 Å contours (*bottom*). The wavelength contours are shown as alternating black and red lines for clarity. Bad detector areas are masked out of the data and appear as holes in the calibration map. As can be seen in images along the top, the detector photocathode is left uncoated beneath the strong Lyman-α line (#3) to reduce sensitivity and prevent saturation.

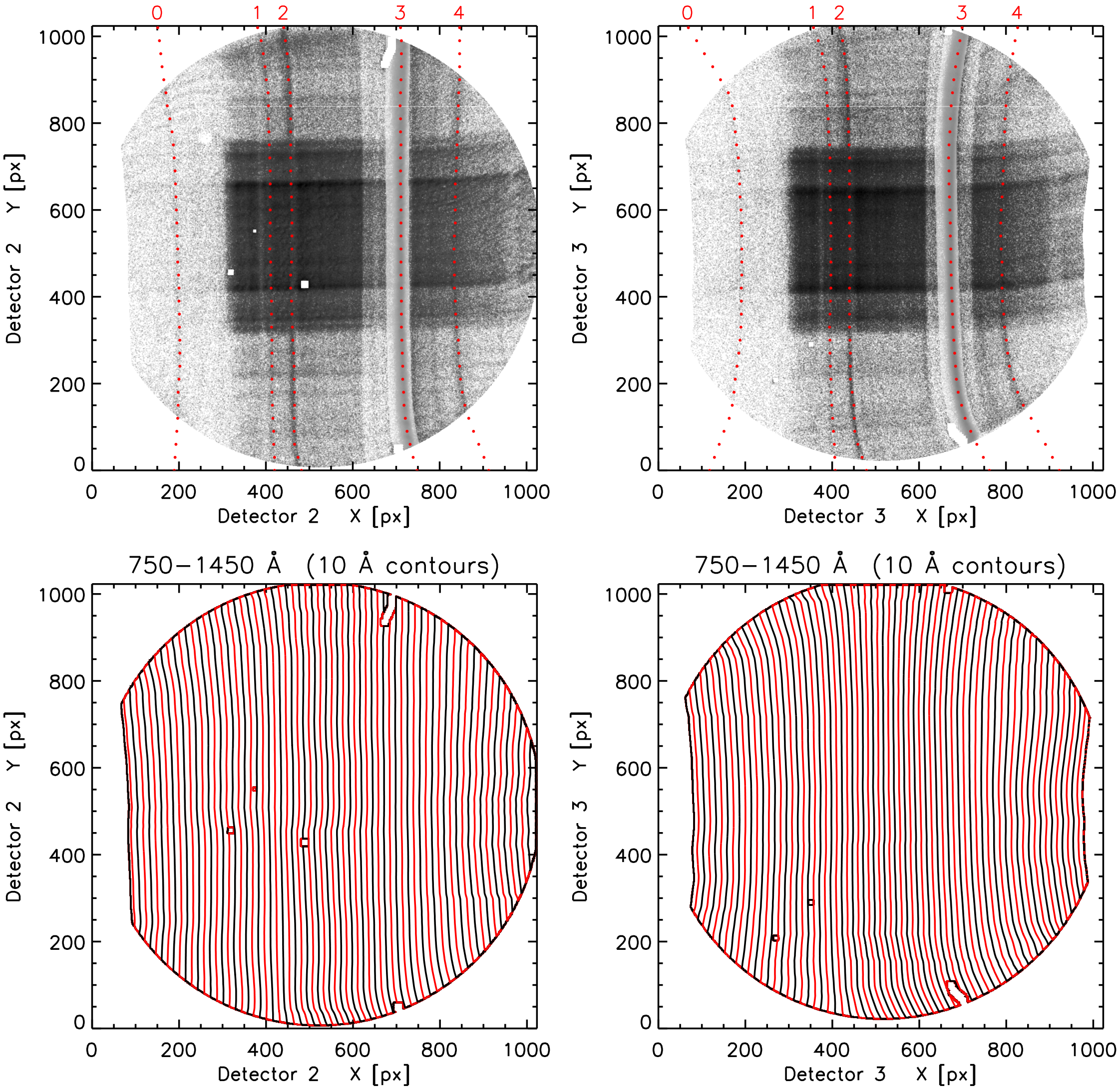

Figure 2.6: SPINR detectors 2 and 3 wavelength calibration. (See description in the caption of Figure 2.5.)

2.5 Extracting Sinograms

The simplest SPINR data products to extract are band-integrated “sinograms.” These two-dimensional (t_{det}, y_{det}) maps are created by summing the data cube over a range in wavelength. The maps have the same information content as a broadband image of the sky. Sinograms will be used in Chapter 3 to perform spatial fitting against model predictions to constrain the dust scattering parameters $(\boldsymbol{a},\boldsymbol{g})$ in Orion.

Four SPINR bands are defined for use in this work: three science bands (short, mid and long) and one background band. The band definitions are found in Table 2.3. The intensity-weighted effective wavelength (λ_{eff}) is also given for each band. It is calculated as

$$\lambda_{eff} = \frac{\sum\limits_{\Delta\lambda} \lambda C_\lambda}{\sum\limits_{\Delta\lambda} C_\lambda}, \tag{2.1}$$

where C_λ is the total number of counts on the detector in the λ wavelength bin.

Band	$\Delta\lambda$[Å]	λ_{eff} [Å]
Background	760-810	785
Short	920-1000	971
Mid	1040-1125	1090
Long	1280-1400	1330

Table 2.3: SPINR bands.

The SPINR bands are chosen to avoid the bright Lyman-α (1216 Å) and Lyman-β (1025 Å) telluric emission lines. The instrument line spread function (LSF) was measured in the lab prior to flight and is presented in Lewis et al. (2009). The LSF characterizes the wings of the Lyman-α line, which extend from 1125-1280 Å and set the respective long and short-wave boundaries of the mid and long bands.

It is important to note here that the SPINR bands are chosen to avoid regions of the spectrum that are difficult to properly calibrate. These include regions over bright telluric lines, regions at the edges of the detector and the region from 1400-1450 Å, where the detector sensitivity drops off rapidly with increasing wavelength. Throughout this work, no photon from outside these bands will be considered for scientific interpretation.

The background band is defined to measure the detector background – a combination of dark counts and grating-scattered photons. This band covers a dark area of the detector shortward of the Lyman limit (912 Å) and away from the strong telluric O II line at 834 Å.

Using the wavelength calibration function $\lambda(x_{det}, y_{det})$, the detector regions that correspond to each band are defined. These regions are shown in Figure 2.7. To build a sinogram, a detector region is extruded into the data cube, selecting a volume of data. These data are summed along the x_{det} axis, wrapped on a 100 second roll period in the t_{det} axis and binned by a factor of 8 in the y_{det} axis to produce $\sim 6'$ pixels that efficiently sample the $\sim 5'$ spatial resolution of the instrument. These operations leave a final sinogram that is 200 temporal bins by 128 spatial bins and holds all of the counts contained by the original volume of data. The 0.5 second time bins are equivalent to roll angle bins with 1.8° resolution. The SPINR band sinograms for each detector are presented in Figures 2.8-2.11.

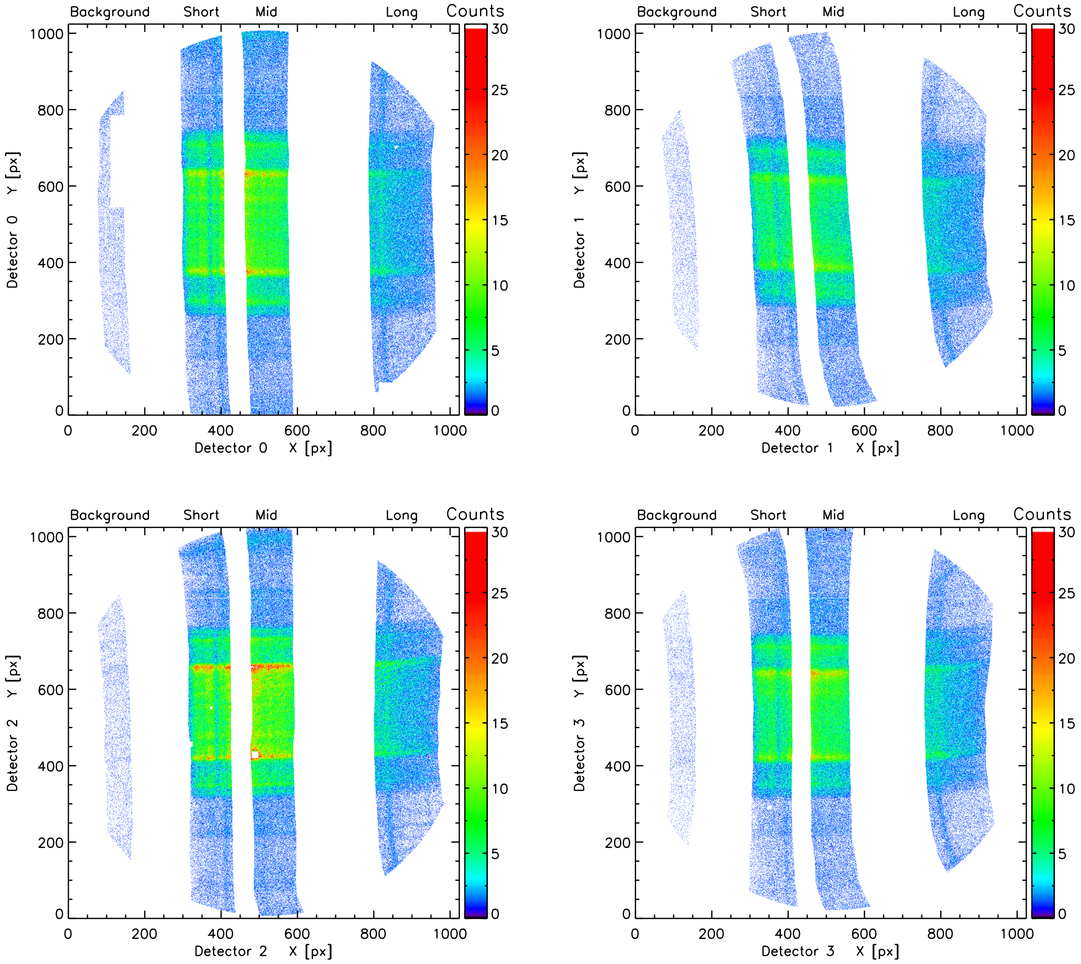

Figure 2.7: SPINR detector band regions.

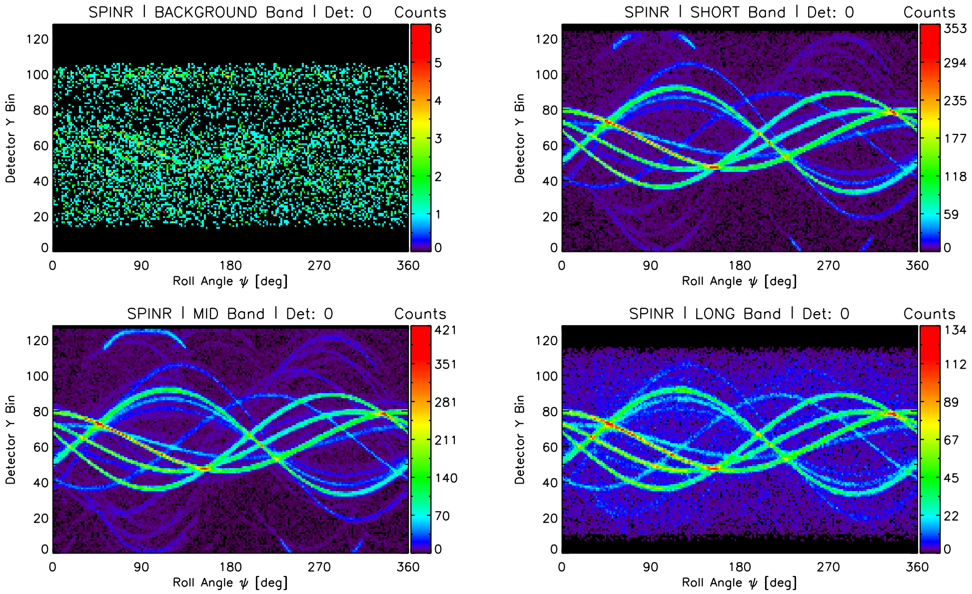

Figure 2.8: SPINR detector 0 band sinograms.

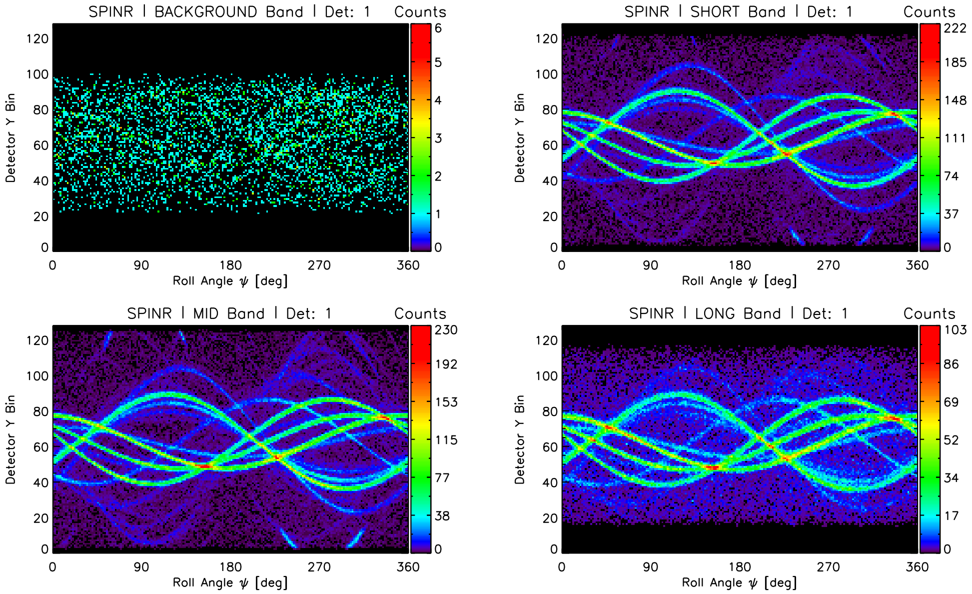

Figure 2.9: SPINR detector 1 band sinograms.

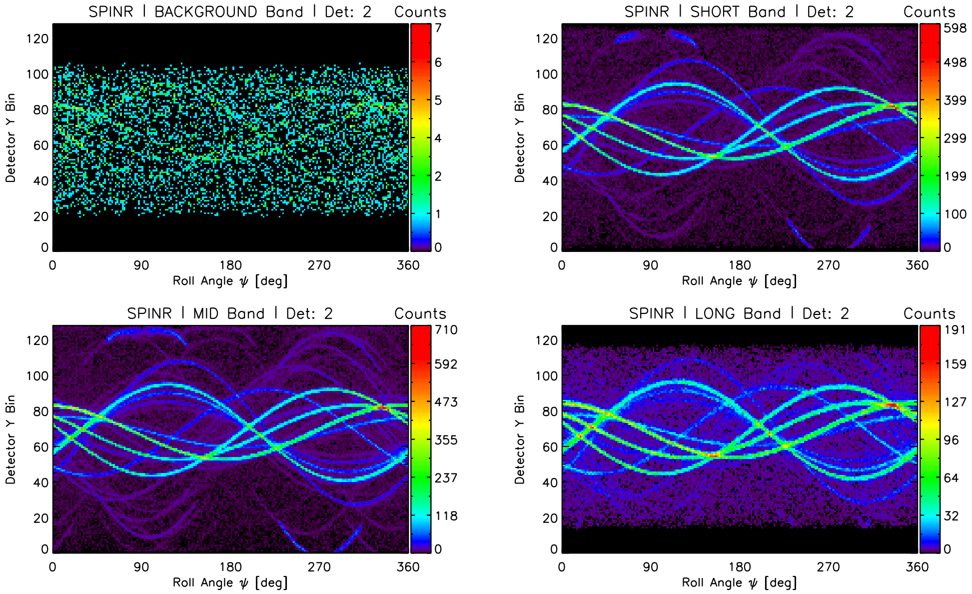

Figure 2.10: SPINR detector 2 band sinograms.

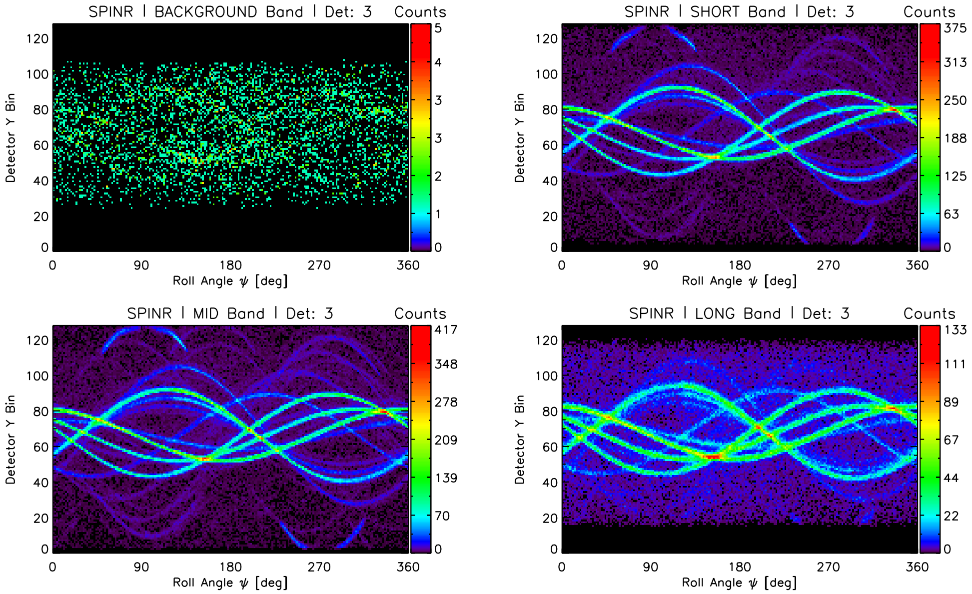

Figure 2.11: SPINR detector 3 band sinograms.

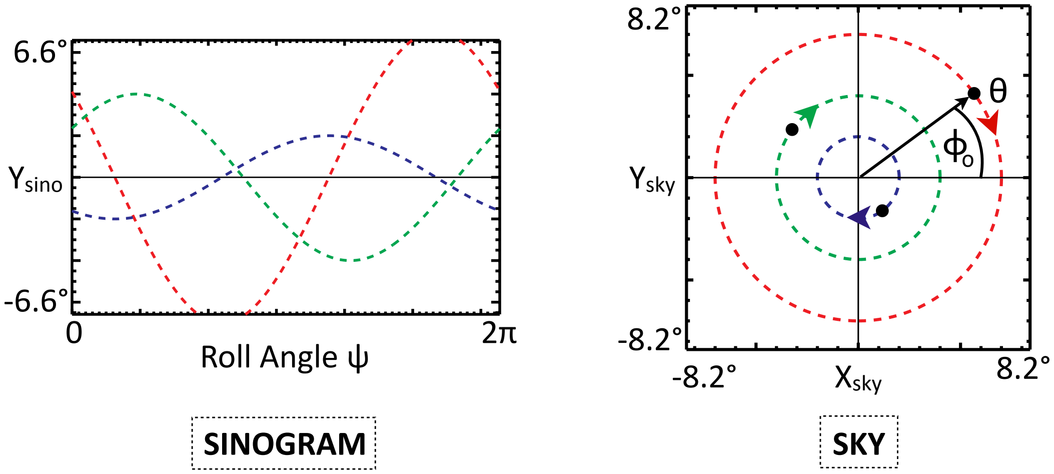

Figure 2.12: SPINR sinogram coordinate system (*left*). Sky coordinate system (*right*). A star with initial polar angle ϕ_o rotates clockwise through an angle θ as the payload rotates.

2.6 Building the SPINR Instrument Response Function

In order to relate the SPINR sinograms back to the observed scene on the sky, a model of the instrument response must be constructed. The straightforward way to approach this problem is to construct the transformation function that maps an image of the sky into a sinogram. This is straightforward because the locations of bright stars on the sky are well known, and the tracks these stars trace within a sinogram reveal the influence of the instrument. What is left is to simply characterize this influence function.

To begin, coordinate systems are established for the sky and sinogram spaces. These will be denoted (x_{sky}, y_{sky}) and (ψ_{sino}, y_{sino}) respectively. These coordinate systems are shown in Figure 2.12. The sky coordinate system is fixed in the instrument reference frame; as the instrument rotates, stars trace circles about the center of the FOV as their (x_{sky}, y_{sky}) positions change.

The instrument function creates a map from the sky into sinogram space. This is not a simple one-to-one mapping. To first order, the instrument function should compress a scene on the sky along the x_{sky} axis into a column. This represents one column of the sinogram and the position of the column is determined by the roll angle of the instrument. The instrument function should also reproduce two important second order effects. First, while the stars follow perfect circles in sky coordinates, they do not trace perfect sinusoids across the sinogram. The detector distortions discussed in Section 2.4 create a non-linear mapping between a star's y_{sky} position and its y_{sino} position. Second, as is evident in the sinograms shown in Figures 2.8-2.11, the point spread function (PSF) of a given star varies along its sinusoidal track. What is not immediately obvious from inspection of the sinograms is that the PSF varies as a function of the star's x_{sky} position. Stars with different x_{sky} positions illuminate different portions of the diffraction grating and thus exhibit different amounts of imaging aberration.

Figure 2.13 presents calibration data showing the relationship between a star's y_{sky} position and its y_{sino} position. These data points are collected directly from the sinogram maps by manually tracing the path of each star and matching each point to the known rotating position of the star on the sky. The calibration function $\mathrm{f}_{\mathrm{ysino}}(y_{sky})$ is defined as a polynomial fit (shown in red) to these data.

As the stellar tracks are followed, a Gaussian fit is made to the measured PSF. The Gaussian width values (σ_{sino}) are plotted with respect to the star's x_{sky} position in Figure 2.14. The calibration function $\mathrm{f}_{\sigma\mathrm{sino}}(x_{sky})$ is defined as a linear fit to these data. Using the same procedure, these calibration functions are defined for each of the three science bands on each detector.

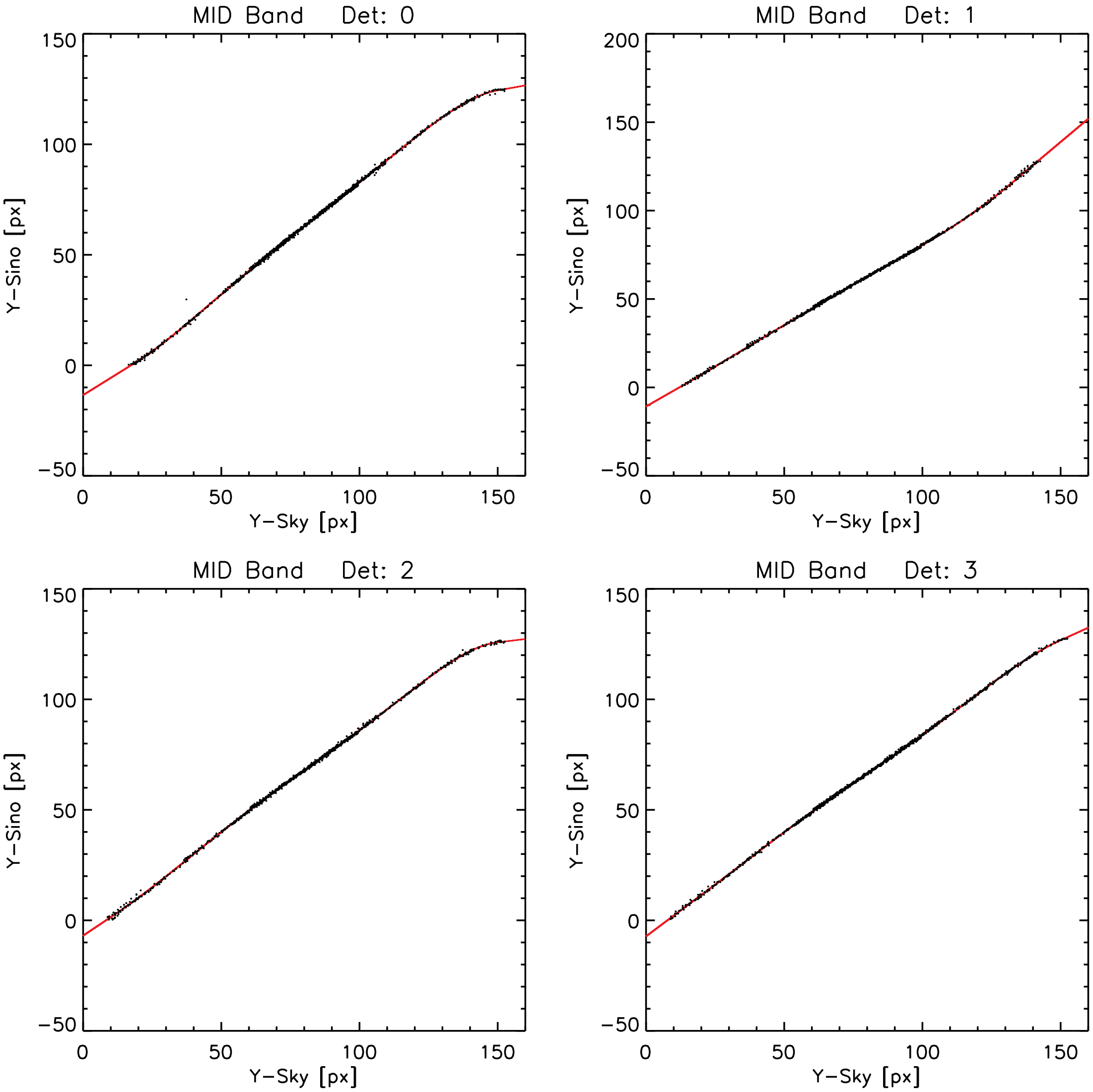

Figure 2.13: The measured y_{sino} positions of stars are plotted as a function their y_{sky} position (*black dots*). The polynomial fit shown in red is the calibration function $\mathrm{f}_{\mathrm{ysino}}(y_{sky})$.

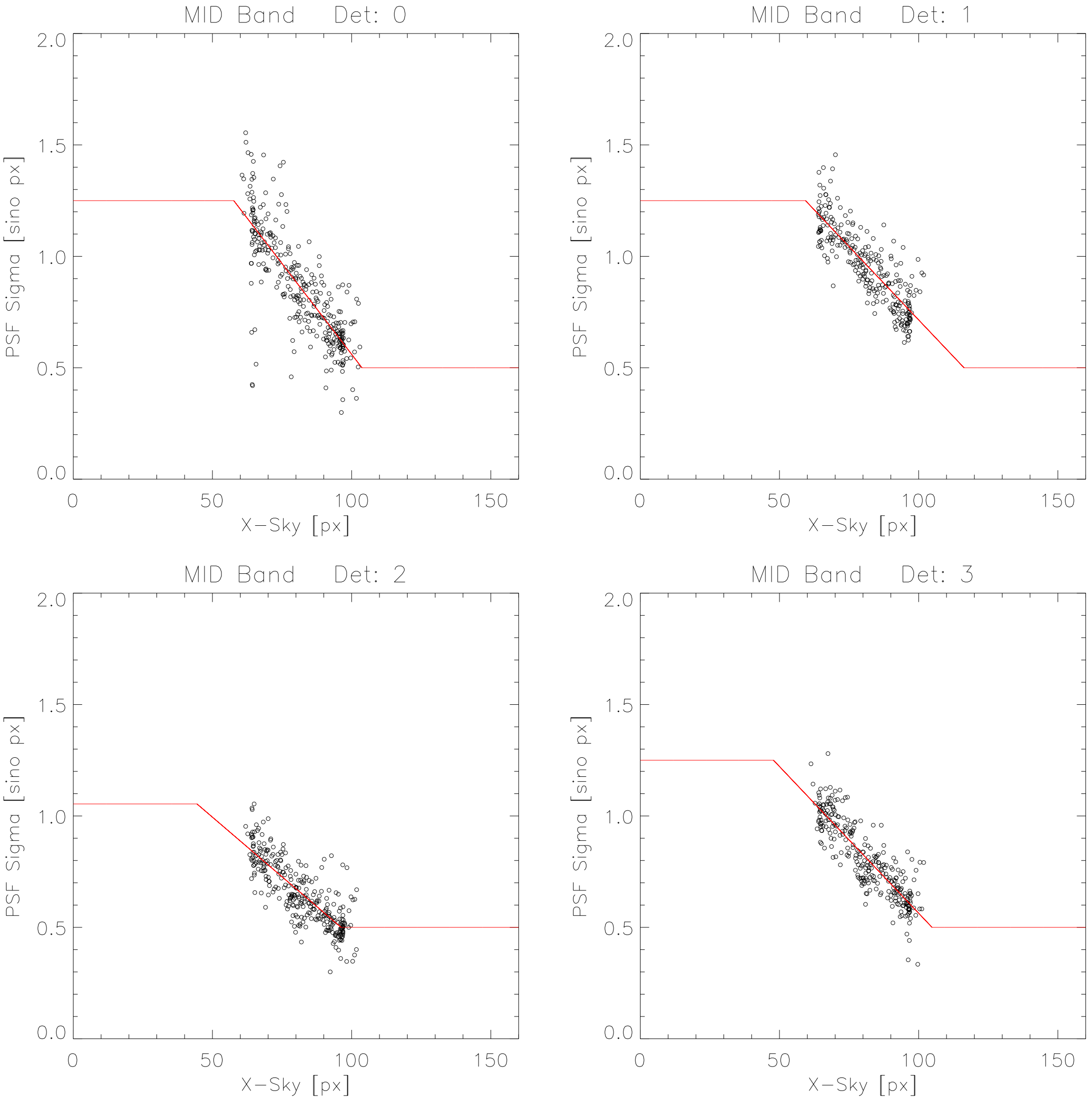

Figure 2.14: The measured Gaussian PSF σ_{sino} values are plotted as a function of stellar x_{sky} position (*black circles*) for the mid band. The linear fit shown in red is the calibration function $\mathrm{f}_{\sigma\mathrm{sino}}(x_{sky})$. The function is limited to $0.5\,\mathrm{px} \leq \mathrm{f}_{\sigma\mathrm{sino}}(x_{sky}) \leq 1.25\,\mathrm{px}$ for detectors 0, 1, and 3 and to $0.5\,\mathrm{px} \leq \mathrm{f}_{\sigma\mathrm{sino}}(x_{sky}) \leq 1.05\,\mathrm{px}$ for detector 2. These limits are chosen based on visual inspection of the data.

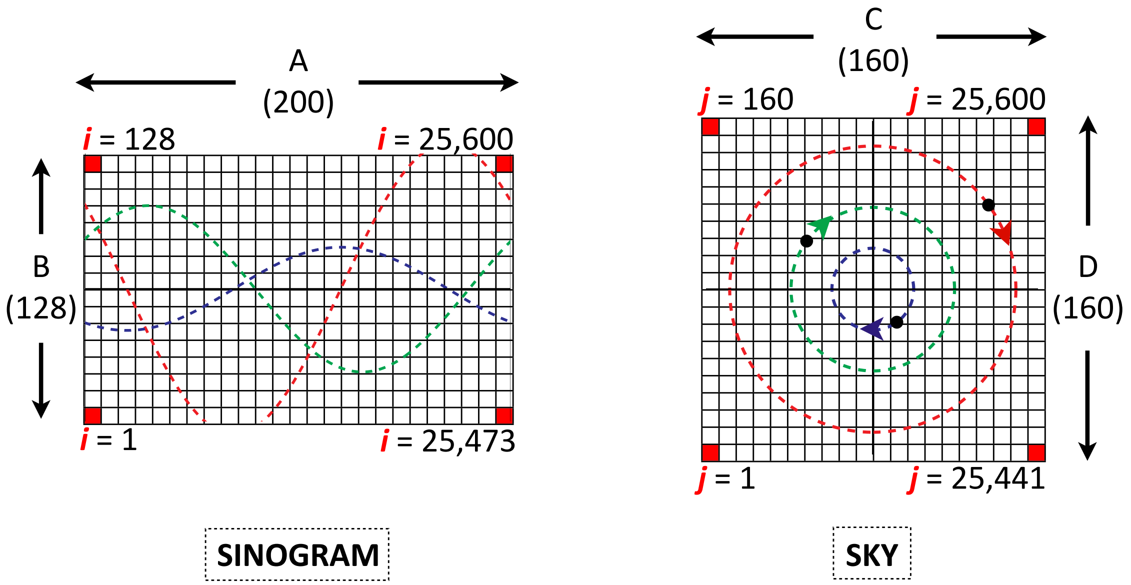

Figure 2.15: The sinogram and sky coordinate systems are reformatted into gridded cells to allow a matrix formalization of the SPINR instrument function. The grid indices are defined for both systems.

With these two calibration functions in hand, the instrument function can be defined. First the the sky and sinogram coordinate systems are discretized into pixel grids. These grids are defined in Figure 2.15. The sinogram grid dimensions are (A×B) = (200×128), which match the dimensions of the data sinograms. The sky grid dimensions are (C×D) = (160×160), which, when inscribed with a 16° FOV, match the spatial resolution of the instrument.

Next, the sinogram and sky grids are reformed into column vectors:

$$SINO_i \equiv \begin{pmatrix} sino_1 \\ sino_2 \\ \vdots \\ sino_I \end{pmatrix} \qquad SKY_j \equiv \begin{pmatrix} sky_1 \\ sky_2 \\ \vdots \\ sky_J \end{pmatrix} \tag{2.2}$$

where,

$$\begin{aligned} I &= A \times B = 25600 \\ J &= C \times D = 25600 \end{aligned} \tag{2.3}$$

The instrument function is formalized as the $(I \times J)$ transformation matrix $T_{i,j}$ that satisfies the equation:

$$SINO_i = T_{i,j} SKY_j \tag{2.4}$$

$$\begin{pmatrix} sino_1 \\ sino_2 \\ \vdots \\ sino_I \end{pmatrix} = \begin{pmatrix} T_{1,1} & T_{1,2} & \cdots & T_{1,J} \\ T_{2,1} & T_{2,2} & \cdots & T_{2,J} \\ \vdots & \vdots & \ddots & \vdots \\ T_{I,1} & T_{I,2} & \cdots & T_{I,J} \end{pmatrix} \begin{pmatrix} sky_1 \\ sky_2 \\ \vdots \\ sky_J \end{pmatrix}$$

2.6.1 Calculating the T-Matrix

To write down an expression for $T_{i,j}$, the coordinates of each sky pixel (x^j_{sky},y^j_{sky}) are first defined using j indices.

$$\begin{aligned} x^j_{sky} &= \lfloor (j-1)/D \rfloor - \frac{C}{2} \\ y^j_{sky} &= [(j-1) \bmod D] - \frac{D}{2} \end{aligned} \tag{2.5}$$

The $\lfloor\ \rfloor$ brackets abbreviate the “floor()” function from integer arithmetic; floor(x) is the largest integer less than or equal to x. The “mod” operator returns the modulus of two integers. Likewise for the sinogram grid, the sinogram y-position (y^i_{sino}) and instrument roll angle (ψ^i_{sino}) can be defined using i indices.

$$\begin{aligned} y^i_{sino} &= [(i-1) \bmod B] - \frac{B}{2} \\ \psi^i_{sino} &= \frac{2\pi}{A} \left(\lfloor (i-1)/B \rfloor \right) \end{aligned} \tag{2.6}$$

The rotation angle (θ^i_{sino}) of a point on the sky is simply the opposite of the instrument roll angle.

$$\theta^i_{sino} = -\psi^i_{sino} \tag{2.7}$$

The on-sky position ($x^{i,j}_{sky}, y^{i,j}_{sky}$) of the j^{th} image pixel rotated through the angle θ^i_{sino} can then be expressed using a rotation matrix.

$$\begin{pmatrix} x^{i,j}_{sky} \\ y^{i,j}_{sky} \end{pmatrix} = \begin{pmatrix} \cos\theta^i_{sino} & -\sin\theta^i_{sino} \\ \sin\theta^i_{sino} & \cos\theta^i_{sino} \end{pmatrix} \begin{pmatrix} x^j_{sky} \\ y^j_{sky} \end{pmatrix}. \tag{2.8}$$

The previously defined calibration functions are used to calculate the sinogram y-position ($y^{i,j}_{sino}$) and Gaussian PSF ($\sigma^{i,j}_{sino}$) for a given rotated image pixel.

$$\begin{aligned} y^{i,j}_{sino} &= \mathrm{f}_{\mathrm{ysino}}(y^{i,j}_{sky}) \\ \sigma^{i,j}_{sino} &= \mathrm{f}_{\sigma\mathrm{sino}}(x^{i,j}_{sky}) \end{aligned} \tag{2.9}$$

Finally, using a Gaussian expression for the instrument PSF, the T-matrix can be formalized.

$$T_{i,j} = \frac{1}{\sigma^{i,j}_{sino}\sqrt{2\pi}} \int_{y^i_{sino}}^{y^i_{sino}+1} \exp\left(\frac{-(y' - y^{i,j}_{sino})^2}{2(\sigma^{i,j}_{sino})^2}\right) \mathrm{d}y' \tag{2.10}$$

The integral in Eq. 2.10 represents the integration of a Gaussian PSF over a single pixel. The solution to this integral can be expressed using the Error Function.

$$T_{i,j} = \frac{1}{2}\left[\mathrm{erf}\left(\frac{y^i_{sino} + 1 - y^{i,j}_{sino}}{\sqrt{2}\sigma^{i,j}_{sino}}\right) - \mathrm{erf}\left(\frac{y^i_{sino} - y^{i,j}_{sino}}{\sqrt{2}\sigma^{i,j}_{sino}}\right)\right] \tag{2.11}$$

Using the T-matrix, any 160×160 pixel image can be transformed into a sinogram. An example set of sinograms created from test image patterns is shown in Figure 2.16. A T-matrix must be constructed for each of the three science bands and for each detector – a total of 12 matrices. Each T-matrix contains $(I \times J) = 655,360,000$ elements. The vast majority of these elements represent a portion of the trailing ex-

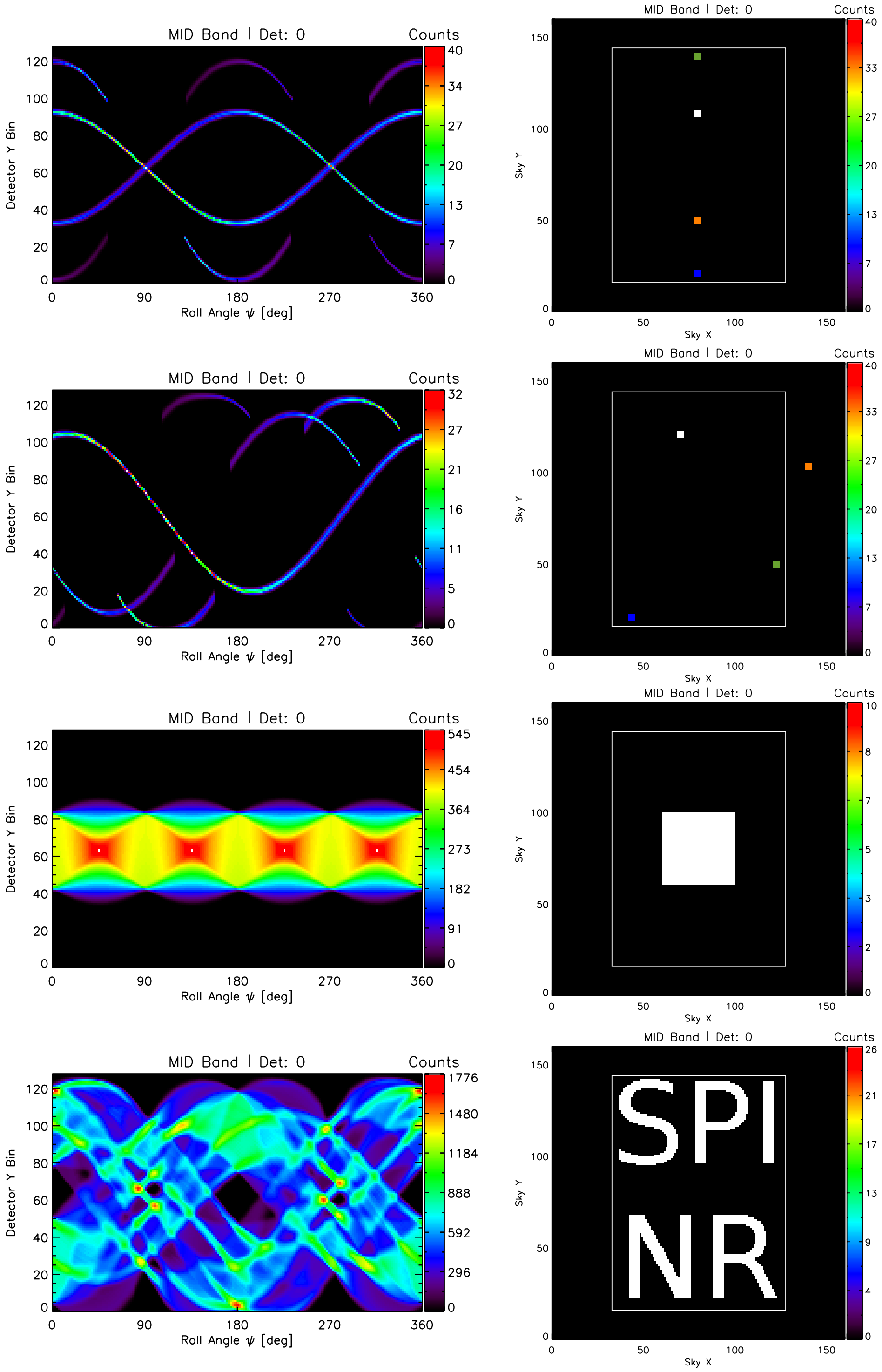

Figure 2.16: T-matrix examples. The SPINR instrument function (T-matrix) is used to transform the test pattern images (*right*) into corresponding sinograms (*left*).

ponential tail of a Gaussian function and are effectively zero-valued. Performing matrix multiplication with these elements creates a needless computational burden. To reduce the computational overhead of working with these large matrices, a sparse matrix storage system is utilized. All matrix elements above a set threshold of 0.001 are stored in a sparse matrix, which is simply a look-up table for non-zero elements. Handling functions are written to allow transparent use of the T-matrix with other non-sparse matrices. This sparse matrix formulation results in matrices with ~18,000,000 elements, a 97% reduction.

2.7 Field of View Calibration

The instrument FOV is easily calculated using the T-matrix. The angular extent of each pixel in the on-sky image from Figure 2.15 is 0.0018 rad. The angular area of a pixel is then 3.24×10^{-6} sr. Creating an image where each pixel holds this value and multiplying by the T-matrix produces a sinogram where each pixel holds the value of the area it subtends on the sky. Since the image of the sky is rotationally symmetric, the columns of this sinogram are all identical and relate the instrument FOV as a function of sinogram y_{sino} position. This relationship is plotted for all bands and all detectors in Figure 2.17. These FOV curves will be used to calibrate the SPINR data products in the following sections. The average band FOV is 0.044 sr (144 deg^2).

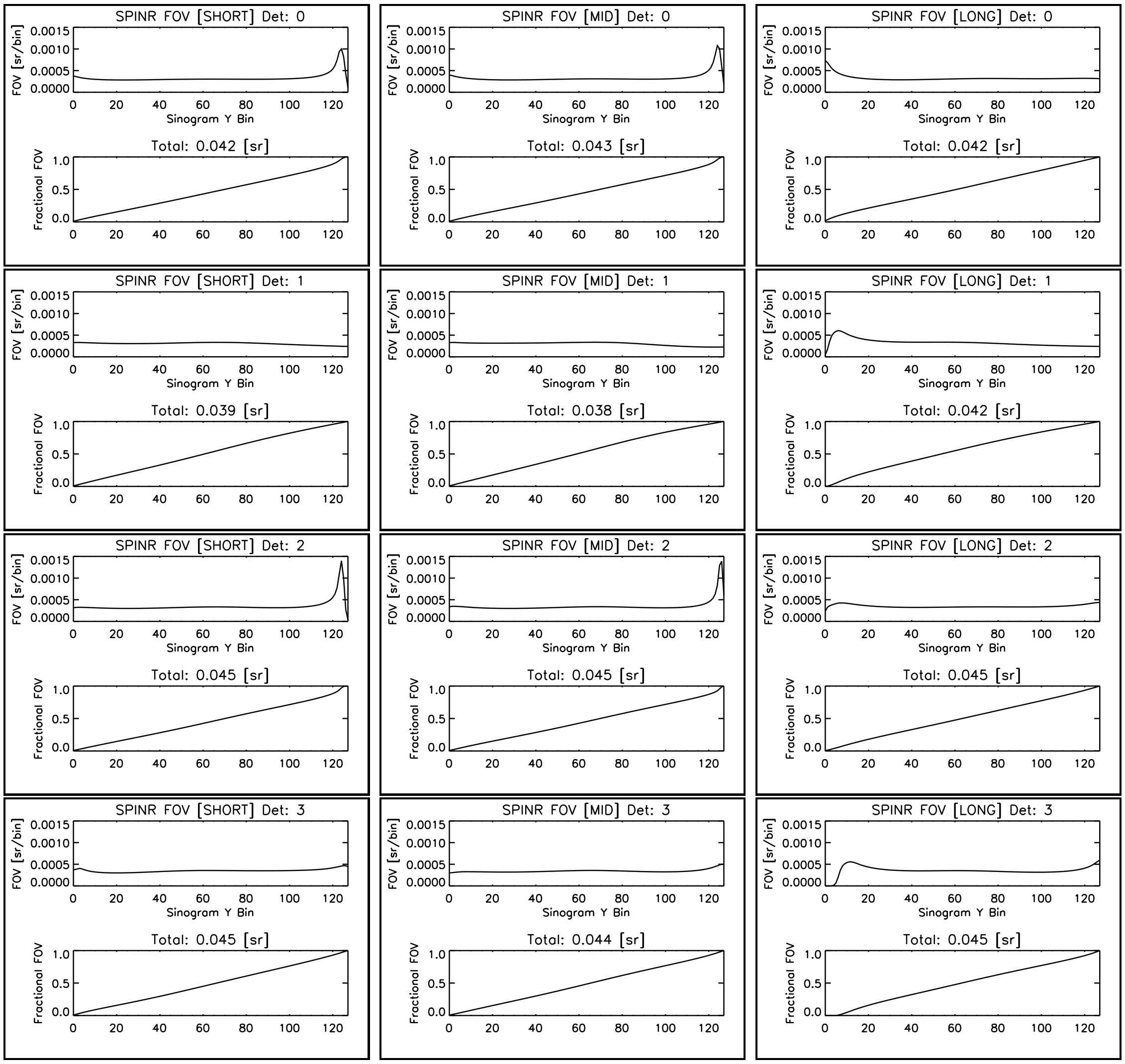

Figure 2.17: The measured FOV in each band for each detector.

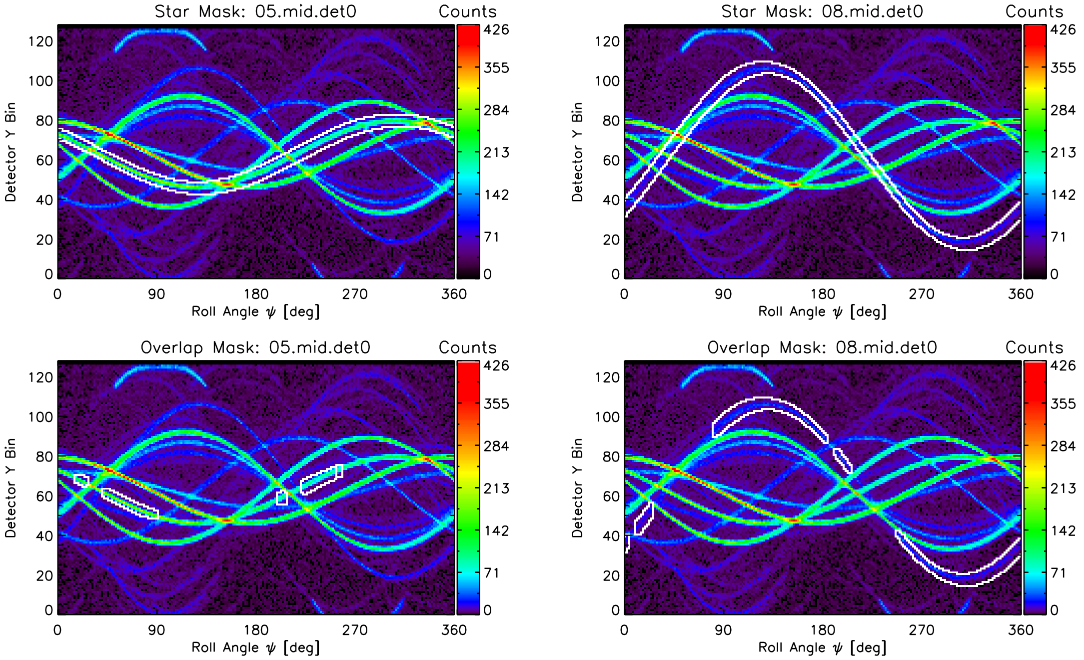

Figure 2.18: *Top:* The data selection masks for two stars are calculated using the T-matrix. *Bottom:* The same masks with regions that overlap with other bright stars removed. The data selected is interior to the white outline.

2.8 Extracting Stellar and Nebular Spectra

Using the SPINR instrument function, it is a straightforward process to accurately trace the path of a star through a sinogram. This is done by simply multiplying the T-matrix for a given band and detector by an image of the sky with only a single pixel illuminated – that which corresponds to the chosen star. Using this process, a set of data selection masks is created for each star. The masks for two stars are shown in Figure 2.18. To prevent cross-contamination between stars, regions of the stellar mask that overlap with other bright stars must be removed. Corresponding masks with these overlap regions removed are also shown in Figure 2.18.

To collect a spectrum for each star, these masks must be extruded along the wavelength (x_{det}) axis of the data cube to select a volume of data that corresponds

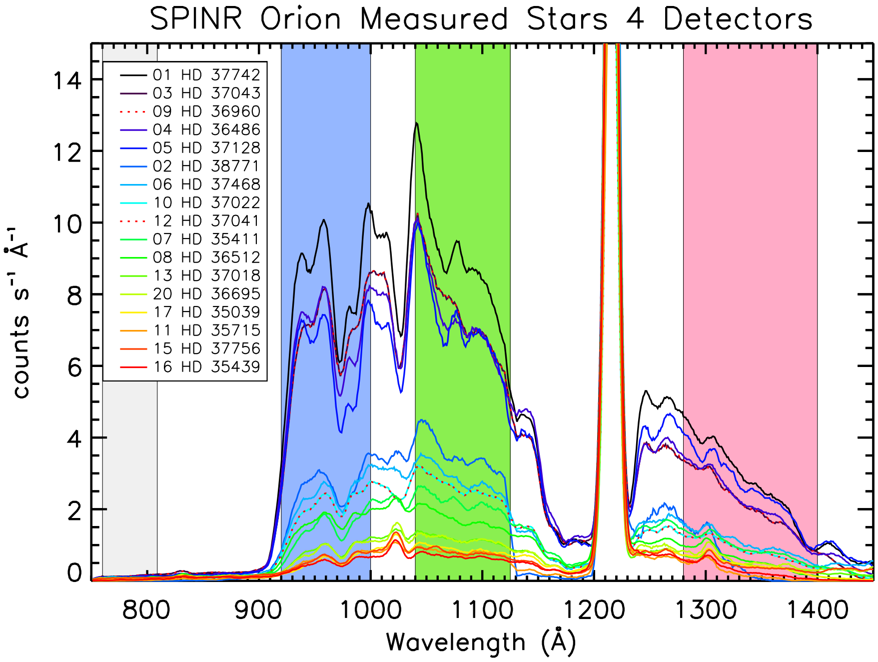

Figure 2.19: Measured SPINR spectra of 17 stars in Orion. The spectra combine the data from all four detectors and are presented in raw SPINR counts; no background sources are subtracted. The bright signal from telluric Lyman-α is visible at 1216 Å. The plot legend lists the stars in descending order of mid-band brightness. Two pairs of stars (HD 37043 and HD 36960) and (HD 37022 and HD 37041) cannot be spatially resolved and as a result have blended spectra. One star in each pair is shown as a dotted red line overlapping the other star.

to the star. For each detector, a unique mask is constructed for each of the three science bands using the three unique T-matrices. These masks are extruded within their own band and across the gaps between the bands to span the entire data cube. With this three-dimensional mask constructed, the photons within the mask can be collected and summed along the t_{det} and y_{det} axes to produce a stellar spectrum.

Stellar spectra for the 17 brightest stars in the SPINR FOV are shown in Figure 2.19. These 17 are among those designated in Figure 2.4. To be selected for spectral measurement, a star must be detected in all three SPINR science bands at a signal-to-noise ratio (SNR) greater than 3. The counts are combined from all four detectors into 1 Å-wide spectral bins. The corresponding Table 2.4 lists some general properties of these stars including their spectral type, effective temperature, reddening excess (E(B-V)), and the distance to each star in the form of their measured parallax from the HIgh Precision PArallax COllecting Satellite (HIPPARCOS) mission and their photometric distance modulus. The values in Table 2.4 are taken from the catalog compiled by Brown et al. (1994), who used the photometric survey of Warren & Hesser (1977) to study the properties of stars in the Orion OB association. The table also lists the SPINR catalog number for each star. The construction of the SPINR catalog is discussed in Section 2.10.4.

The data cube can also be separated more coarsely into stellar and nebular bins to produce total stellar and nebular spectra. To select a star for the total stellar spectrum, it must be detectable with a SNR > 1 in at least one of the three science bands. This less stringent criterion selects 42 stars including the 17 for which there are measured spectra. These stars are also listed in Table 2.4. The stellar bins are defined as the union of all bins belonging to each of these stars. The overlapping regions where stars cross are included because we are no longer concerned with star-to-star contamination. The remaining bins are classified as nebular bins. The stellar selection criterion is chosen to greatly favor over-selection of stellar pixels in order to avoid stellar contamination of the much weaker nebular signal. The complementary set of stellar and nebular masks are shown in Figure 2.20. The resulting spectra, which combine data from all four detectors, are shown in Figure 2.21.

SPINR #	ID	NAME	SpType	DM	PX [mas]	Log(T)	Log(g)	Vmag	E(B-V)	Category
0	HD 34085	beta ori	B8Iab	-	4.22	4.05	2.28	0.12	0.04	S
1	HD 37742	zeta ori	O9Iab	7.0	3.99	4.50	3.65	1.77	0.07	S
2	HD 38771	kappa ori	B0Iab	-	4.52	4.42	3.05	2.05	0.00	S
3	HD 37043	iota ori	O9III	6.6	2.46	4.51	4.07	2.77	0.05	S
4	HD 36486	delta ori	O9V	7.9	3.56	4.48	3.55	2.41	0.05	S
5	HD 37128	epsilon ori	B0Iab	-	2.43	4.45	3.00	1.70	0.00	S
6	HD 37468	sigma ori	O9.5V	8.0	2.84	4.49	4.30	3.80	0.05	S
7	HD 35411	eta ori	B0.5V	6.4	3.62	4.41	4.20	3.38	0.07	S
8	HD 36512	upsilon ori	B0V	8.1	2.11	4.50	4.11	4.62	0.03	S
9	HD 36960		B0.5V	8.6	1.75	4.45	3.90	4.78	0.02	S
10	HD 37022	theta1 ori c	O6pv	-	-	4.64	4.80	5.13	0.30	S
11	HD 35715	psi2 ori	B2IV	6.9	2.30	4.40	4.28	4.59	0.03	S
12	HD 37041	theta2 ori a	B0-B2	7.8	1.72	4.50	4.18	5.08	0.19	S
13	HD 37018	42 ori	B1V	7.1	4.15	4.41	4.18	4.59	0.06	S
14	HD 34503	tau ori	B5III	5.2	5.88	4.13	3.69	3.59	0.01	S
15	HD 37756		B2IV-V	7.1	1.56	4.33	4.05	4.95	0.02	S
16	HD 35439	psi1 ori	B1Vpe	8.3	2.94	4.46	4.26	4.87	0.09	S
17	HD 35039	22 ori	B2IV	7.4	2.53	4.30	3.80	4.70	0.04	S
18	HD 36591		B1IV	7.7	1.27	4.41	4.18	5.34	0.05	V
19	HD 35149	23 ori	B2	7.2	3.39	4.38	4.10	5.00	0.08	S
20	HD 36695		B1V	7.8	1.76	4.39	4.08	5.38	0.06	S
21	HD 39291	55 ori	B2IV-V	7.5	1.94	4.34	4.07	5.34	0.03	V
22	HD 37490	omega ori	B3IIIe	8.1	2.01	4.32	3.51	4.57	0.12	S
23	HD 36351	33 ori	B1.5V	7.0	2.08	4.33	4.30	5.46	0.03	S
24	HD 35299		B1.5V	7.4	4.03	4.37	4.27	5.70	0.02	V
25	HD 37481		B1.5IV	7.7	2.08	4.38	4.37	5.96	0.02	V
26	HD 36166		B2V	7.4	2.60	4.34	4.22	5.74	0.02	V
27	HD 37303		B1Vv	8.0	2.40	4.39	4.24	6.01	0.02	V
28	HD 37744		B1.5V	7.9	1.94	4.38	4.28	6.20	0.04	V
29	HD 35007		B3V	6.4	3.03	4.24	4.24	5.65	0.04	V
30	HD 36285		B2IV-V	7.8	2.68	4.34	4.24	6.32	0.02	V
31	HD 36779		B2.5V	7.4	2.63	4.31	4.34	6.22	0.03	V
32	HD 35588		B2.5V	7.1	2.06	4.29	4.30	6.14	0.02	V
33	HD 36430		B2V	7.1	1.85	4.28	4.34	6.20	0.02	V
35	HD 37150		B3Vv	7.7	1.84	4.31	4.30	6.51	0.02	V
36	HD 39777		B1.5V	7.9	2.18	4.33	4.28	6.54	0.03	V
50	HD 36646		B4Vn	7.4	1.18	4.24	4.28	6.63	0.06	V
55	HD 37025		B5V	7.6	-	4.22	4.26	7.18	0.02	V
57	HD 36958		B3V	7.6	-	4.23	4.38	7.31	0.09	V
63	HD 37115		B6V	7.5	-	4.20	4.39	7.16	0.04	V
73	HD 35673		B9V	5.5	6.41	4.06	4.28	6.50	0.06	V
77	HD 35501		B8V	7.6	1.84	4.12	4.14	7.42	0.05	V

Table 2.4: Properties of 42 Orion stars detected by SPINR. These stars are broken into two categories; stars marked with an “S” for “Spectrum” in the “Category” column are the 17 stars with full spectra measured by SPINR. The measured spectra for these stars are shown in Figure 2.19. Stars marked with a “V” for “Visible” are the stars that are detected in at least one of the science bands. Two distance measurements are given: the distance modulus (DM) values are calculated by Brown et al. (1994) and the parallax angles (PX) are measured by HIPPARCOS.

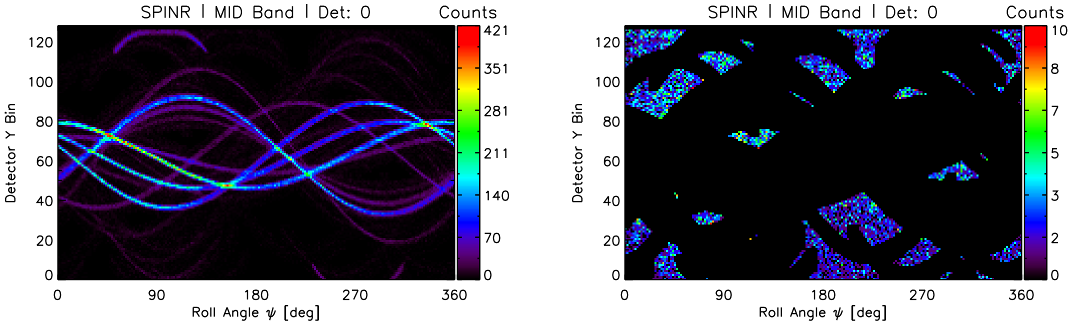

Figure 2.20: The total stellar (*left*) and nebular (*right*) sinogram masks are applied to the mid band detector 0 data.

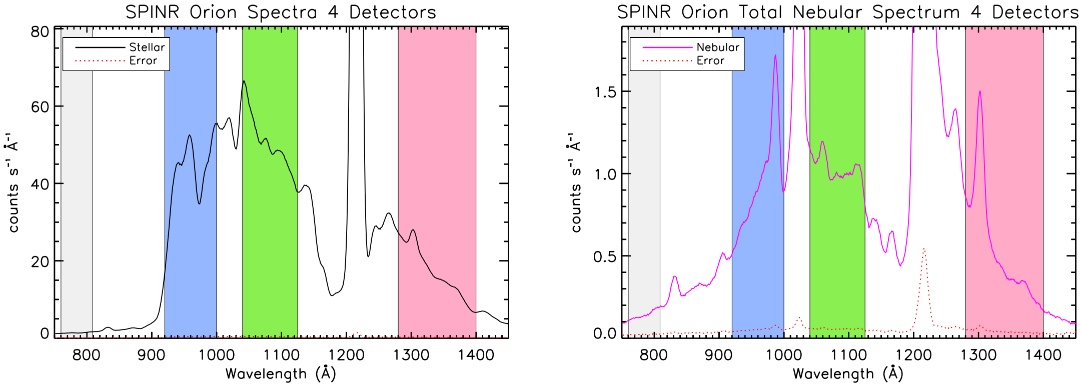

Figure 2.21: SPINR total stellar (*left*) and nebular (*right*) spectra are shown combining data from all four detectors. The spectra are presented in raw SPINR counts; no background sources are subtracted.

2.8.1 Stellar Background Subtraction

In the following section, the stellar spectra are used as calibration standards for each spectrograph. The first step in this calibration is to subtract any background signal that did not originate from the stars. As can be seen in Figure 2.21, the stellar spectrum contains excess counts in the background band, which are contributed by detector dark current and scattered light within the instrument. A second source of background counts is the nebular signal itself. Since the SPINR instrument functions to compress the entire sky into an one-dimensional spectral element, some amount of nebular signal becomes mixed in with the starlight and therefore must be subtracted.

Both of these background components can be removed accurately from the stellar spectrum in a single step by subtracting the raw nebular signal. Before subtraction, the nebular spectrum is scaled at each wavelength to reflect the difference in detector area, field of view and exposure time between the nebular and stellar spectra. The background-subtracted individual star and total stellar spectra are shown in Figure 2.22.

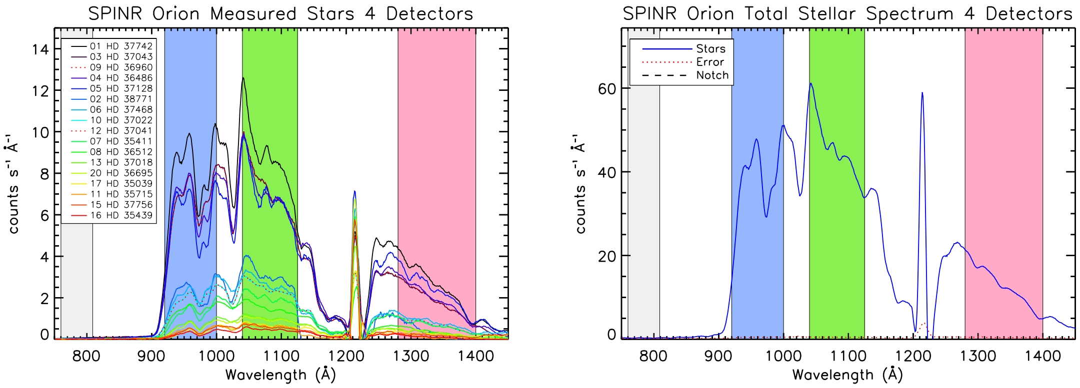

Figure 2.22: *Left:* Background-subtracted SPINR spectra of 17 stars in Orion. See Figure 2.19 for details. *Right:* Background-subtracted total stellar spectrum. These plots combining data from all four detectors.

2.9 Effective Area Calibration

A measurement of the instrument effective area is necessary to convert the raw SPINR data products into physical units, which will allow comparison with previous measurements. Three bright stars in the SPINR FOV are chosen as calibration standards. These stars are: HD 37742, HD 36486, HD 36512; SPINR catalog numbers:

1, 4, 8. Properties of these stars are given in Table 2.4. The SPINR spectra are calibrated using measured International Ultraviolet Explorer (IUE) spectra for these stars. The IUE short-wavelength spectrograph operates between 1150-2000 Å. To extend the calibration to 912 Å, a model stellar spectrum is constructed for each calibration star based on its effective temperature and surface gravity using the ATLAS9 atmospheric models of Castelli & Kurucz (2003). These model spectra are then reddened using the Fitzpatrick (1999) reddening law and scaled to match the IUE observations between 1700-1900 Å. High-resolution (0.6 Å), large-aperture IUE observations are used for the calibration. The IUE datasets are listed in Table 2.5.

SPINR #	HD	IUE Dataset
1	HD 37742	SWP52609
4	HD 36486	SWP24169
8	HD 36512	SWP40415

Table 2.5: IUE calibration data.

The calibrated model spectra are shown in Figure 2.23 alongside the SPINR observed spectra. Dividing the SPINR spectra by the model spectra produces the set of effective area measurements shown in Figure 2.24. A piecewise polynomial fit is made to these points to create an effective area curve for each detector. This curve and its uncertainty, calculated from the scatter in the data, is overplotted with the datapoints in Figure 2.24. The effective area curve is used to calibrate the spectra for individual stars and the total stellar spectrum (Figure 2.25).

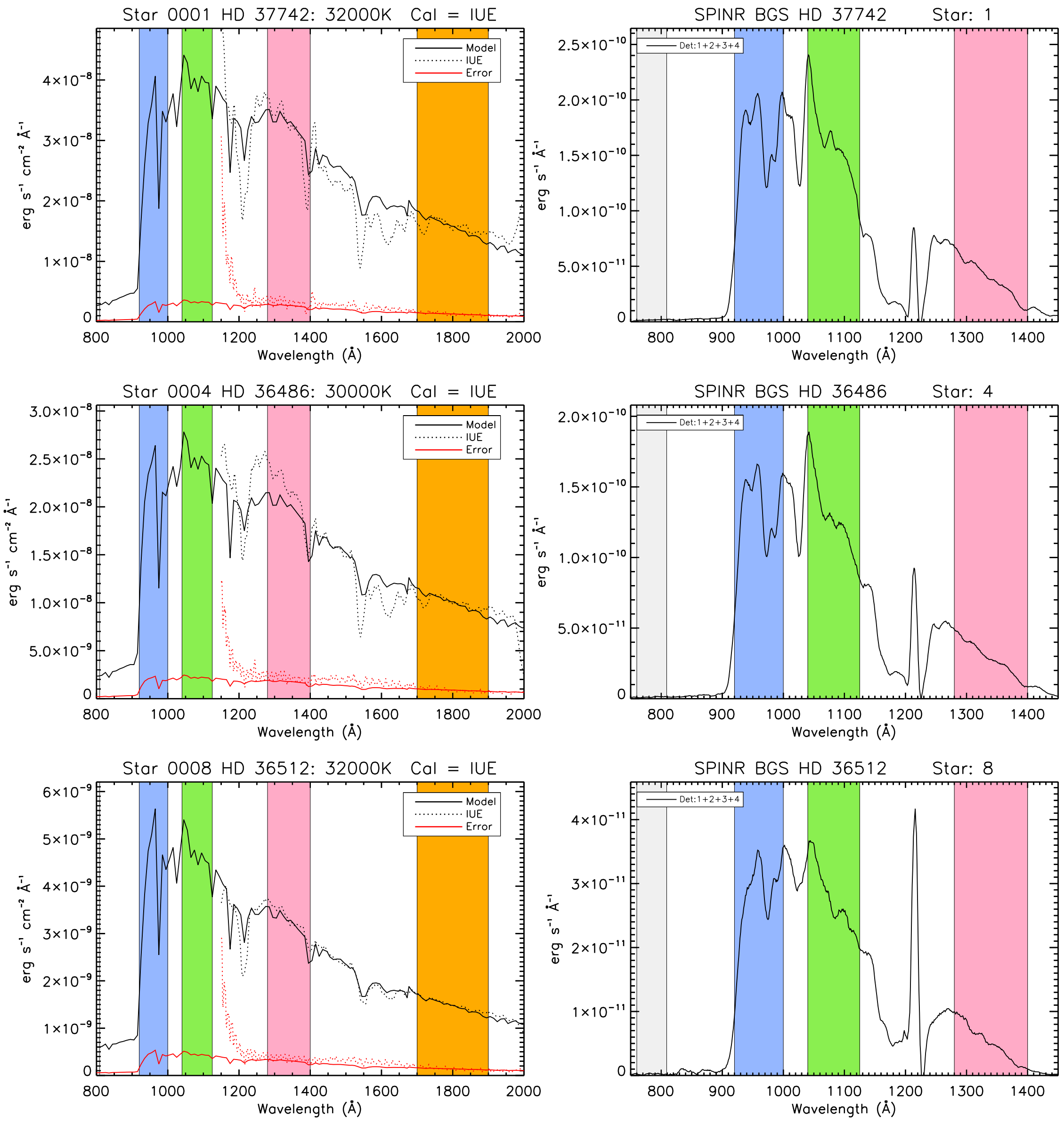

Figure 2.23: The left panels show IUE calibrated Castelli & Kurucz (2003) model spectra for the three calibration stars. The corresponding measured SPINR spectra are shown in the right panel. Dividing the SPINR spectra by the model spectra yields a measurement of the effective area of each SPINR spectrograph.

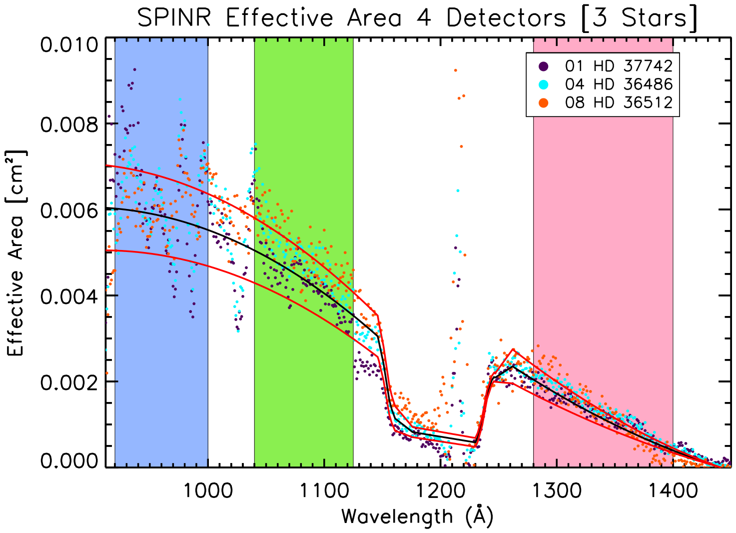

Figure 2.24: The effective area of the combined four SPINR detectors is fit as a piecewise polynomial (*black line*) to calibration data produced using the IUE calibrated Castelli & Kurucz (2003) model spectra and SPINR measured spectra from Figure 2.23. The 1-σ fit uncertainty is shown in red. This process is also performed for each detector individually.

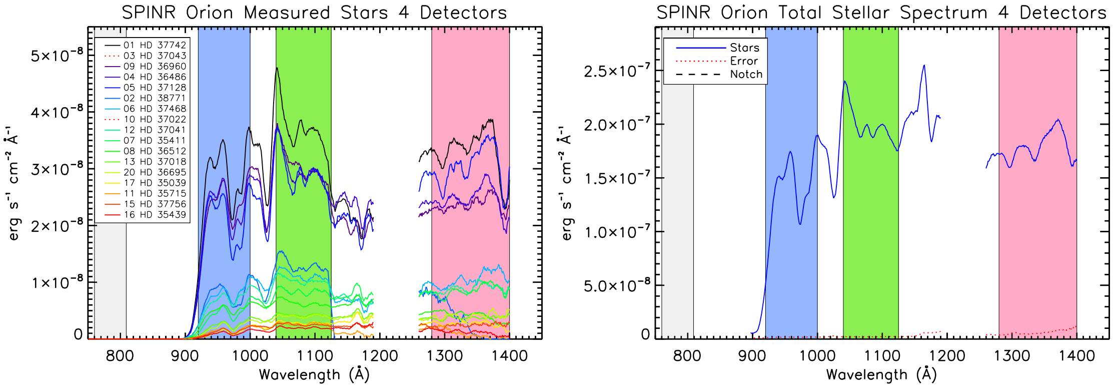

Figure 2.25: *Left:* Calibrated SPINR spectra of 17 stars in Orion. See Figure 2.19 for details. *Right:* Calibrated total stellar spectrum. These plots combining data from all four detectors.

2.10 Nebular Background Sources

The SPINR nebular spectrum and the corresponding nebular sinogram pixels contain counts that are not the result of FUV dust scattering. These contaminating background counts add on top of the true scattered light signal, producing a systematically brighter nebular signal. If left uncorrected, this would lead to the conclusion that the dust grains are more reflective than they truly are. Estimates of the background levels must be subtracted from the data to correct this bias.

The following sections will discuss estimates for each background source, which are often directly measurable from the data. Each background source has a unique distribution throughout the data cube, which is to say, each source exhibits its own spatial (on the sky) and spectral signature. Both the spatial and spectral characteristics of each background source must be estimated in order to correct the SPINR spectra and sinograms.

The starting point for this background subtraction is the raw nebular signal. With an estimate of the effective area and FOV of the four SPINR spectrographs, the measured nebular spectrum can be converted into physical units. The canonical FUV surface brightness unit is the Continuum Unit (CU), where $1\ \text{CU} = 1\ \text{count}\ \text{s}^{-1}\text{sr}^{-1}\text{cm}^{-2}\text{Å}^{-1}$. It should be noted that since the SPINR instrument is a photon counting instrument, wherever presented, the units of counts and photons are equivalent. The raw nebular spectrum is presented in both instrument units (counts $\text{s}^{-1}\text{Å}^{-1}$) and calibrated surface brightness units (CU) in Figure 2.26.

The average nebular signal in each band is given in Table 2.6. The uncertainty in the averages includes only the contribution from Poisson ($\sqrt{N}$) noise. Each background source will be summarized in a similar table and all background levels will be subtracted from these initial values. All data presented here represent the combination of data from all four detectors.

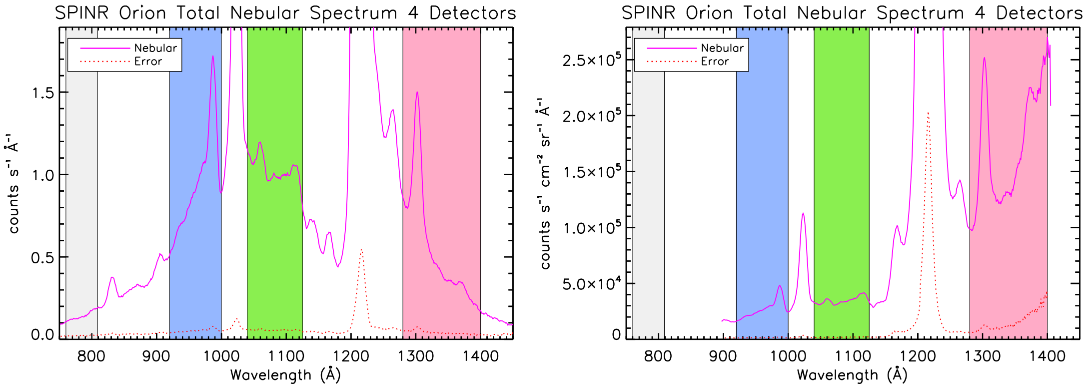

Figure 2.26: *Left:* The raw nebular spectrum in units of counts $s^{-1}Å^{-1}$. *Right:* The raw nebular spectrum in units of CU.

Band	counts $s^{-1}Å^{-1}$	CU
Short	$9.57{\pm}0.06{\times}10^{-1}$	$2.75{\pm}0.02{\times}10^{+4}$
Mid	$1.04{\pm}0.01{\times}10^{+0}$	$3.51{\pm}0.02{\times}10^{+4}$
Long	$5.53{\pm}0.04{\times}10^{-1}$	$1.72{\pm}0.02{\times}10^{+5}$

Table 2.6: SPINR Bands: raw nebular signal combined over four detectors.

2.10.1 Instrument Background

Diffraction gratings are not perfect. Each incident photon is not reflected at a singular angle that is proportional only to its wavelength. Some fraction of the photons are scattered in a non-wavelength dependent manner. There are two dominant components to the scattered light distribution: a diffuse component and a diffraction-angle-dependent component (Woods et al. 1994).

The diffuse scattering component is caused by grating surface roughness. This roughness is due to fabrication limitations and exists on microscopic scales, much smaller than the grating rule-spacing. These random surface errors scatter light uniformly across the detector.

The angularly-dependent scattering component is predicted by grating theory and follows a Lorentzian distribution in the dispersion direction (Woods et al. 1994). The cross-dispersion scatter is negligible compared to the SPINR imaging PSF.

The source of scattered light in the SPINR nebular spectrum is dominated by Lyman-α (1216 Å) photons, with a small contribution from Lyman-β (1025 Å). The Lyman-β and Lyman-α emission lines are respectively 10 and 4000 times brighter than the nebular continuum. The detector is left uncoated beneath the strong Lyman-α line, causing it to appear at reduced brightness; however, the full power at Lyman-α does illuminate the diffraction grating and is available to scatter.

Diffuse Scattered Light and Dark Current

The diffuse scattered light component is measured in the background band (760-810 Å), which, as discussed in Section 2.5, defines a region of each detector that lies in a dark section of the spectrum. Indistinguishable from the diffuse scattered light is the background caused by detector dark current; both sources are uniformly distributed on the detector. The background band count rate will be referred to as simply the "detector" background, which is approximately 4×10^{-4} counts $s^{-1}px^{-1}$. The measured rates for each detector are given in Table 2.7. The uncertainty in the background rate is set by the Poisson noise of the measured background counts.

Detector	counts $s^{-1}px^{-1}$
0	$5.9 \pm 0.2 \times10^{-4}$
1	$3.1 \pm 0.2 \times10^{-4}$
2	$4.2 \pm 0.2 \times10^{-4}$
3	$2.5 \pm 0.2 \times10^{-4}$

Table 2.7: SPINR detector background.

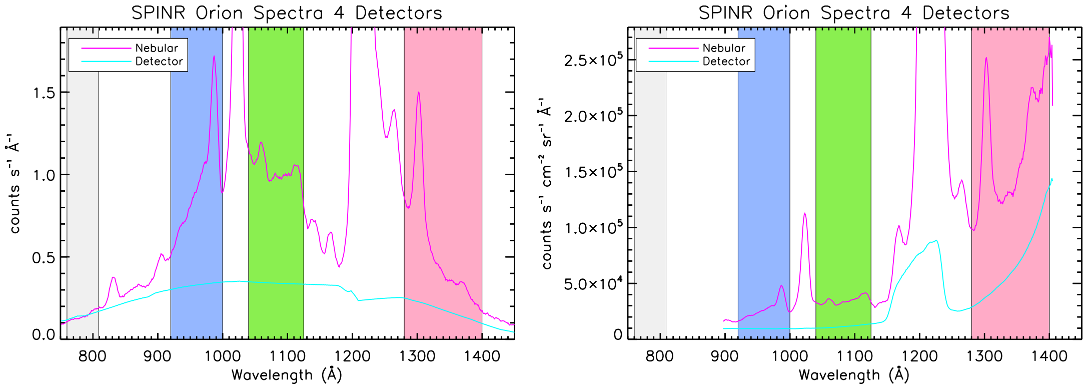

Figure 2.27: *Left:* The detector background spectrum. *Right:* The detector background plotted in physical units, as if it were a source on the sky.

The detector background is unique in the fact that it does not have a spatial (on the sky) or spectral component; it is a background in detector space. To subtract the detector background from the nebular spectrum, the background counts are collected into wavelength bins to form the detector background spectrum (shown in Figure 2.27).

The calculated average detector background in each band is given in Table 2.8. This table reports the effective surface brightness of the detector background as if it were a source on the sky.

Band	counts s^{-1}Å^{-1}	CU
Short	$3.29 \pm 0.08 \times 10^{-1}$	$9.54 \pm 0.23 \times 10^{+3}$
Mid	$3.41 \pm 0.08 \times 10^{-1}$	$1.16 \pm 0.03 \times 10^{+4}$
Long	$1.77 \pm 0.04 \times 10^{-1}$	$6.69 \pm 0.16 \times 10^{+4}$

Table 2.8: SPINR Bands: detector background combined over four detectors.

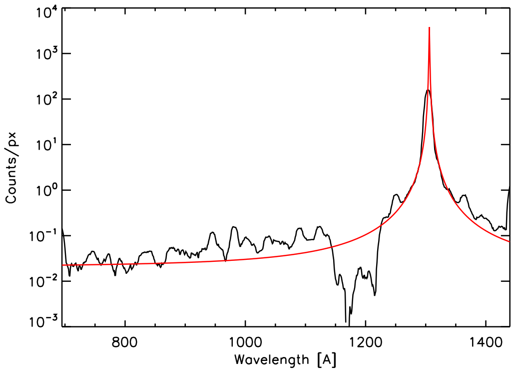

Figure 2.28: Calibration data of the O I emission line at 1304 Å. The data are contaminated by additional Oxygen lines from the source. The scattered light profile is defined as the lower envelope of the data and is fit well by a Lorentzian distribution.

Spectral Line Scatter

The SPINR diffraction gratings scatter light from individual spectral lines preferentially in the dispersion direction. Woods et al. (1994) show that this scattered light component should follow a one-dimensional Lorentzian distribution (Φ) of the form

$$\Phi(x) = \frac{1}{\pi} \frac{\frac{1}{2}\omega}{(x - x_0)^2 + (\frac{1}{2}\omega)^2}, \tag{2.12}$$

where x_0 is the line center and ω is the full width at half maximum.

Laboratory calibration data from one of the four SPINR spectrographs is shown in Figure 2.28. The scattered light profile from the O I emission line at 1304 Å is fit well by a Lorentzian distribution. With this confirmation of the functional form of the instrument line-scattering function, an estimate of the Lyman-α and Lyman-β scattering background can be calculated.

An upper limit on the Lyman-α and Lyman-β scattering profile can be easily calculated from the flight data. For each of the four detectors, a Lorentzian function is drawn spanning the Lyman-α line. The Lorentzian is scaled knowing that the

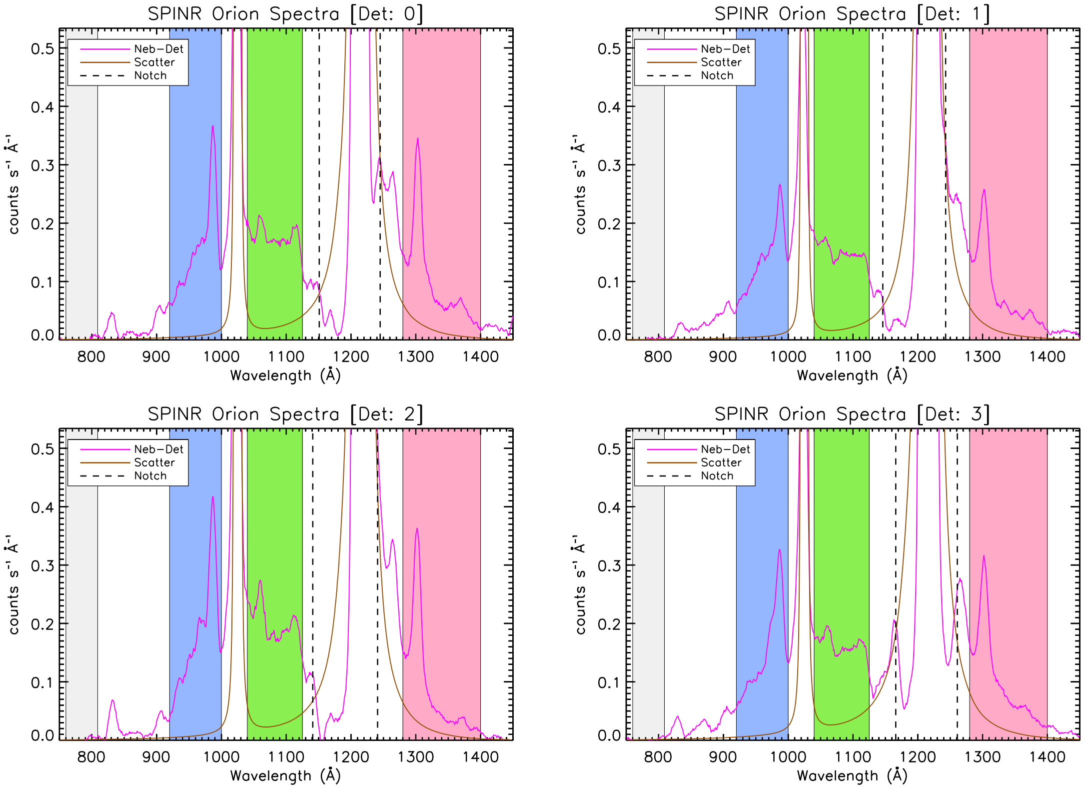

Figure 2.29: The background component due to scattered Lyman-α (1216 Å) on each detector is set to the upper limit where the scattered light profile equals the measured wings of the Lyman-α line at the point (*vertical dashed line*) where they cross back onto the coated section of the photocathode. The Lyman-β (1025 Å) component is scaled from the Lyman-α component by the line ratio measured in Chakrabarti et al. (1984). The detector background is subtracted from the nebular spectrum before the scattering profiles are defined.

scattered light profile may not exceed the measured wings of the Lyman-α line at the point where they cross back onto the coated section of the photocathode. The width (ω) is set such that the scattered light profile matches the data at this point. The uncertainty in the scattered light is set to the Poisson noise level at this point. The Lyman-α scattering profile is then scaled and translated to form the Lyman-β scattering profile. The surface brightness ratio between these two lines is measured to be 406:1 by Chakrabarti et al. (1984). The Lyman-α profile is scaled by this ratio

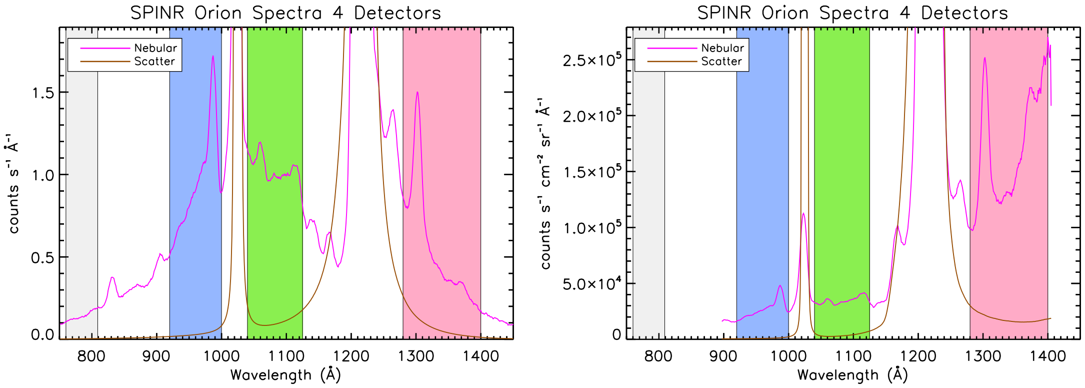

Figure 2.30: The Lyman-α and Lyman-β scattered light background combined over four detectors.

multiplied by the ratio in effective area between 1216 Å and 1025 Å. Figure 2.29 shows the total scattered light background for each of the four detectors. The combined four-detector scattered light background is plotted in Figure 2.30 and summarized in Table 2.9.

Band	counts $s^{-1}Å^{-1}$	CU
Short	$3.4\pm0.2\times10^{-2}$	$9.7\pm0.5\times10^{+2}$
Mid	$1.1\pm0.1\times10^{-1}$	$3.9\pm0.2\times10^{+3}$
Long	$7.3\pm0.4\times10^{-2}$	$1.8\pm0.1\times10^{+4}$

Table 2.9: SPINR Bands: scattered Lyman-α and Lyman-β combined over four detectors.

2.10.2 H_2 Fluorescence

Observations of molecular hydrogen (H_2) fluorescent emission in the ISM were first made in 1990 by Martin et al. (1990). Molecular hydrogen emission lines are present in the SPINR Orion nebular spectrum. To estimate the level of H_2 emission,

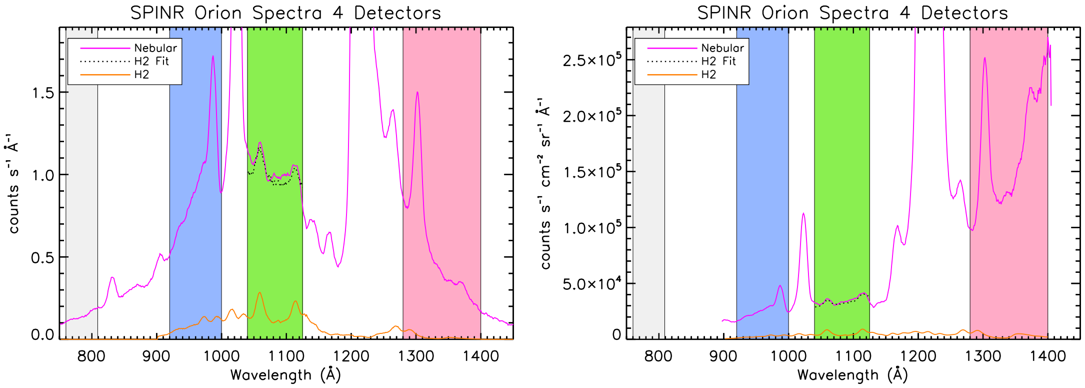

Figure 2.31: The background from H_2 fluorescent emission *(orange line)* is fit to the total nebular signal *(magenta line)* as the H_2 emission model multiplied by a scale factor and added to a linear continuum *(black dotted line)*.

the model of France & McCandliss (2005) is used. This model has been calibrated using Far Ultraviolet Spectroscopic Explorer (FUSE) observations of diffuse emission near Theta^1 Ori C (HD 37022, SPINR 10). The FUSE observations fix the model line ratios and the model is scaled to match the SPINR features. The model is fit to the SPINR mid-band data assuming a linear dust continuum beneath the H_2 features. The H_2 fit is shown in Figure 2.31. The H_2 background in each band is given in Table 2.10. The uncertainty in the H_2 background is determined by the uncertainty in the model fit parameters. The measured H_2 features are not strong enough to spatially differentiate from the FUV continuum; they will be treated as a uniform background source and subtracted as such.

The surface brightness of H_2 fluorescent emission, averaged over the SPINR field of view, is estimated to be $\sim 4\times10^3$ CU. This level is consistent with previous measurements in Orion and similar systems. The FUSE spectra used by France & McCandliss (2005) show H_2 features peaking at 1×10^5 CU. Wide-field observations of the Orion-Eridanus superbubble, taken by the Spectroscopy of Plasma

Evolution from Astrophysical Radiation (SPEAR) mission (Ryu et al. 2006; Jo et al. 2011), show H_2 emission in the range of 10^3-10^4 CU.

Band	counts $s^{-1}Å^{-1}$	CU
Short	$9.4{\pm}1.8{\times}10^{-2}$	$2.7{\pm}0.5{\times}10^{+3}$
Mid	$1.6{\pm}0.3{\times}10^{-1}$	$5.4{\pm}1.0{\times}10^{+3}$
Long	$1.5{\pm}0.3{\times}10^{-2}$	$3.6{\pm}0.7{\times}10^{+3}$

Table 2.10: SPINR Bands: H_2 background combined over four detectors.

2.10.3 Telluric Emission Lines

Bright telluric emission lines are seen as strong features in the SPINR nebular spectrum. This emission originates above the rocket altitude (∼300 km) in the Earth's high-temperature Geo-coronal region. These same lines are used to perform the instrument wavelength calibration in Section 2.4. They are removed from the nebular spectrum by assuming a linear continuum below the line and subtracting off the excess. The telluric line spectrum is shown in Figure 2.32. The spatial distribution of telluric emission is uniform across the FOV. The telluric emission line background in each band is given in Table 2.11. The uncertainty in the telluric emission is set to the Poisson noise level of the continuum beneath the line.

Band	counts $s^{-1}Å^{-1}$	CU
Short	$1.5{\pm}0.1{\times}10^{-1}$	$4.3{\pm}0.2{\times}10^{+3}$
Mid	$1.1{\pm}0.1{\times}10^{-2}$	$3.5{\pm}0.2{\times}10^{+2}$
Long	$1.2{\pm}0.1{\times}10^{-1}$	$2.7{\pm}0.1{\times}10^{+4}$

Table 2.11: SPINR Bands: telluric line background combined over four detectors.

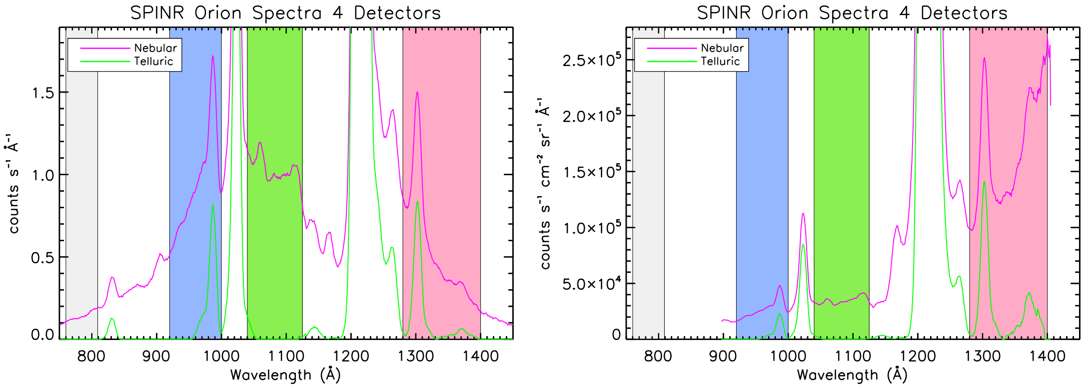

Figure 2.32: The background from telluric emission lines *(green line)* is formed by fitting a linear continuum to the total nebular signal *(magenta line)* beneath each line and subtracting the excess emission.

2.10.4 Undetected Stars

There are thousands of stars along the line of sight to Orion that are too dim to be detected in any of the SPINR bands. These stars are not included in the stellar selection mask and therefore contribute a weak FUV background to the nebular spectrum and nebular sinogram pixels. To quantify the collective contribution from these undetected stars, first a master SPINR star catalog is compiled. The base catalog combines the Brown et al. (1994) catalog of the Orion OB association members with the HIPPARCOS catalog (Perryman et al. 1997) and the TD-1 catalog (Thompson et al. 1978). For the SPINR catalog, all O, B, A and F stars stars within a 15° radius of the center of the SPINR FOV were chosen. This criteria selects 2078 stars. A map of the SPINR catalog and a histogram of the stellar V-band magnitudes are shown in Figure 2.33.

The SPINR catalog contains 2078 stars. Using the same procedure applied to measuring the instrument effective area (Section 2.9), a model spectrum is constructed for each star in the catalog. The model spectra are calibrated using the

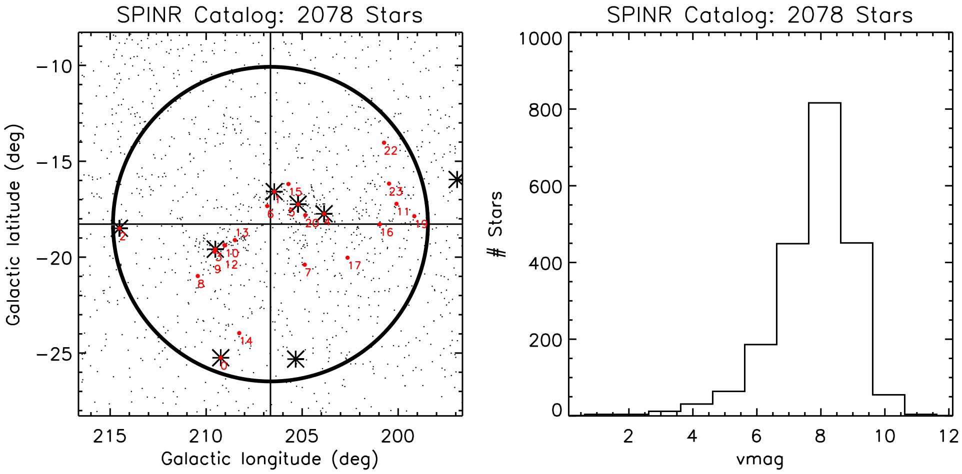

Figure 2.33: The SPINR star catalog. *Left*: The distribution of catalog stars on the sky. Red dots mark the stars with measured spectra. Asterisks mark the bright stars of the Orion constellation. *Right*: a histogram of the stellar V-band magnitudes.

measured V-band magnitude in the absence of IUE data. These model spectra are grouped by spectral type and totaled in Figure 2.34. The total count rates for each spectral type are listed in Table 2.12.

SpType	# Stars	Short counts $s^{-1}Å^{-1}$	Mid counts $s^{-1}Å^{-1}$	Long counts $s^{-1}Å^{-1}$
O	7	1.6×10^{1}	1.7×10^{1}	4.5×10^{0}
B	633	3.1×10^{1}	3.7×10^{1}	1.0×10^{1}
A	1057	1.6×10^{-3}	1.2×10^{-2}	7.0×10^{-2}
F	381	5.8×10^{-10}	2.5×10^{-8}	4.5×10^{-6}

Table 2.12: Modeled total stellar count rates for the 2078 stars in the SPINR catalog.

The count totals given in Table 2.12 and the spectra shown in Figure 2.34 relate the total stellar signal of the entire SPINR catalog. Only a small fraction of these stars, those that pass through the nebular sinogram pixels, contribute to the nebular signal. To calculate this contribution, stellar images are constructed in each band

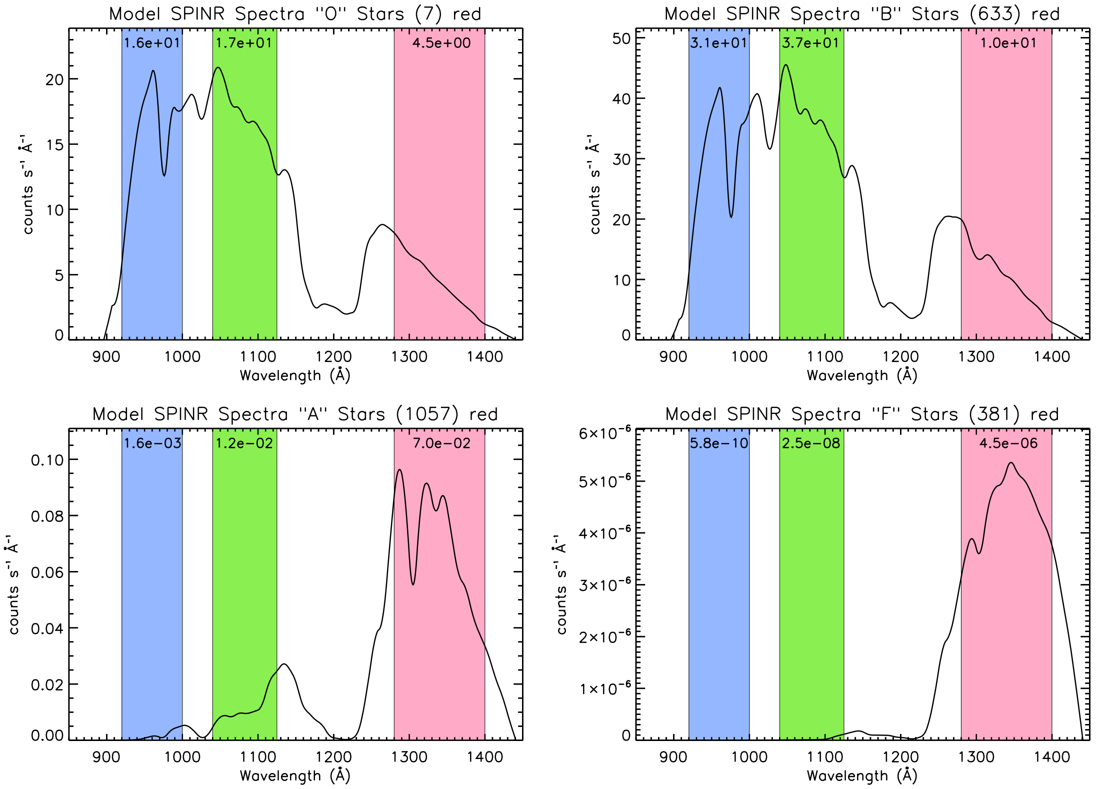

Figure 2.34: Model stellar spectra for the 2078 stars in the SPINR catalog are grouped by spectral type and summed. The average count rate is given for each band.

and converted to sinograms using the SPINR instrument function. The modeled undetected star sinograms for detector 0 are shown in Figure 2.35. The background counts from the undetected stars are totaled over the nebular pixels in each band and listed in Table 2.13. The uncertainty in the average stellar background is set to 10%, the average error between the SPINR stellar spectra and the corresponding stellar models.

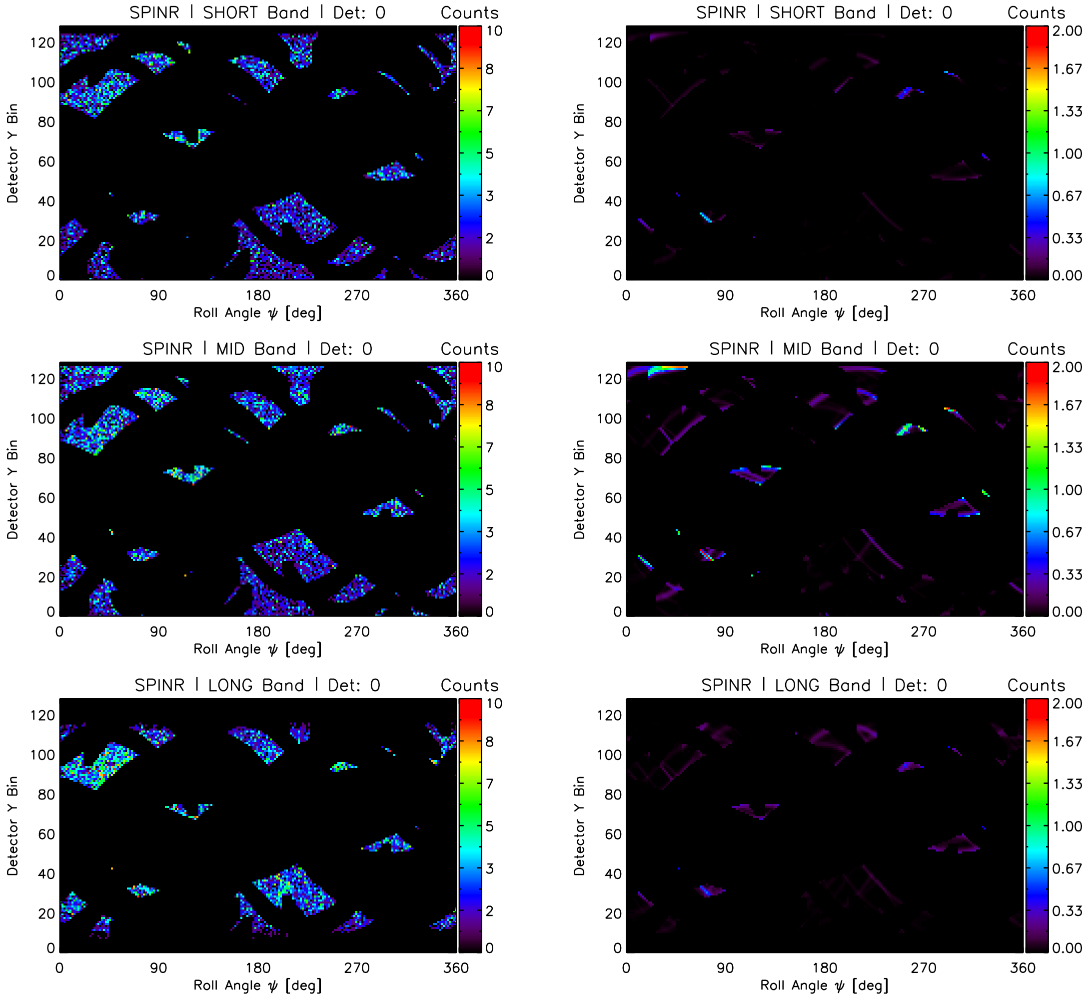

Figure 2.35: *Right:* The full SPINR catalog of 2078 stars is mapped into these calibrated sinograms to provide the spatial distribution of counts due to undetected stars. *Left:* The SPINR data are shown for comparison.

Band	counts s^{-1}Å^{-1}	CU
Short	$1.0{\pm}0.1{\times}10^{-2}$	$3.0{\pm}0.2{\times}10^{+2}$
Mid	$4.4{\pm}0.2{\times}10^{-2}$	$1.5{\pm}0.1{\times}10^{+3}$
Long	$1.2{\pm}0.1{\times}10^{-2}$	$5.7{\pm}0.3{\times}10^{+3}$

Table 2.13: SPINR Bands: undetected star background combined over four detectors.

2.10.5 Extragalactic Background

The contribution to the FUV background from extragalactic sources, predominantly spiral galaxies, has been the subject of some debate. Hurwitz (1994) provides a good overview of different estimates of the extragalactic background ranging from 0-300 CU. The value of 300±100 CU is adopted by Jo et al. (2012) and Bowyer (1991). The same value is adopted here. The extragalactic contribution to each SPINR band is given in Table 2.14. The extragalactic background is treated as a uniform source on the sky.

Band	counts $s^{-1}Å^{-1}$	CU
Short	$1.0{\pm}0.2{\times}10^{-2}$	$3.0{\pm}1.0{\times}10^{+2}$
Mid	$9.0{\pm}1.5{\times}10^{-3}$	$3.0{\pm}1.0{\times}10^{+2}$
Long	$1.1{\pm}0.2{\times}10^{-3}$	$3.0{\pm}1.0{\times}10^{+2}$

Table 2.14: SPINR Bands: extragalactic background combined over four detectors.

2.10.6 Other Background Sources

Another set of background sources that can be significant at longer wavelengths are those arising from reflected sunlight, e.g., Earthshine, Moonlight and zodiacal light. These sources reflect the stellar spectrum and are negligible shortward of 2000 Å (Murthy & Henry 1995).

2.10.7 Summary of Background Sources

A number of background sources have been discussed. The goal is to remove these sources from the nebular signal to more accurately estimate the true signal from light scattering off of dust grains. These background sources vary in wavelength and in spatial distribution across the sky. Background spectra and sinograms have been created accordingly to capture this information.

The given background levels are subtracted from the initial nebular signal; the resulting dust signal in each of the three SPINR science bands is given in Table 2.15. The discussed uncertainty in each of the background levels has been propagated through to this final result.

The average surface brightness of dust across the SPINR field of view is measured to be $\sim 2\times10^4$ CU. This value is consistent with previous measurements in the FUV. Most applicably, the wide-field (8° × 8°) observations of Orion by Onaka et al. (1984) show nebulosity ranging from 5×10^3 CU to 1×10^5 CU. This field is centered to within a degree of the SPINR field. The same FUSE observations used by France & McCandliss (2005) to estimate the H_2 emission, have been used to study the scattering properties of dust in Orion (Murthy et al. 2005; Shalima et al. 2006). These FUSE spectra, targeted near the bright Orion Nebula ($12'$ from Theta^1 Ori C), show diffuse nebular signal peaking at 3×10^5 CU.

Band	counts $s^{-1}Å^{-1}$	CU
Short	$3.3\pm0.2\times10^{-1}$	$9.4\pm0.6\times10^{+3}$
Mid	$3.6\pm0.3\times10^{-1}$	$1.2\pm0.1\times10^{+4}$
Long	$1.6\pm0.1\times10^{-1}$	$5.0\pm0.3\times10^{+4}$

Table 2.15: SPINR Bands: background-subtracted dust signal combined over four detectors.

The spectral characteristics of the discussed background sources are summarized in Figure 2.36. Each source has been subtracted from the total nebular spectrum. The resulting dust spectrum is the best estimate of the true FUV scattered light. The background spectra are averaged over each band and presented as a stack plot in

Figure 2.37. The relative contributions of each source to the total nebular signal are summarized in Table 2.16. The H_2 and telluric line emission contribute the greatest amount astrophysical background.

Source	Short [%]	Mid [%]	Long [%]
Dust	34.1	34.4	28.9
Detector	34.6	33.0	38.9
Telluric	15.7	1.0	15.9
H2	9.8	15.5	2.1
Scatter	3.5	11.0	10.7
Stars	1.1	4.2	3.3
Extra Gal.	1.1	0.9	0.2

Table 2.16: The relative contribution of each source to the total nebular signal is given for each band. The percentages are calculated in physical (CU) units averaged over four detectors.

The background sources are summed into total background sinograms and compared side-by-side with the data in Figure 2.38 and Figure 2.39. The background sinograms are not subtracted at this stage for statistical reasons. Many of the data sinograms contain pixels with zero counts. These sinograms will be re-binned more coarsely in the process of fitting models to build up enough counts to ensure the statistical uncertainty of each bin lies in the Gaussian regime – where the uncertainty is distributed randomly about the mean and the χ^2 statistic is applicable. At that point, the background sinograms will be re-binned in the same fashion and subtracted. This will be discussed further in Chapter 3.

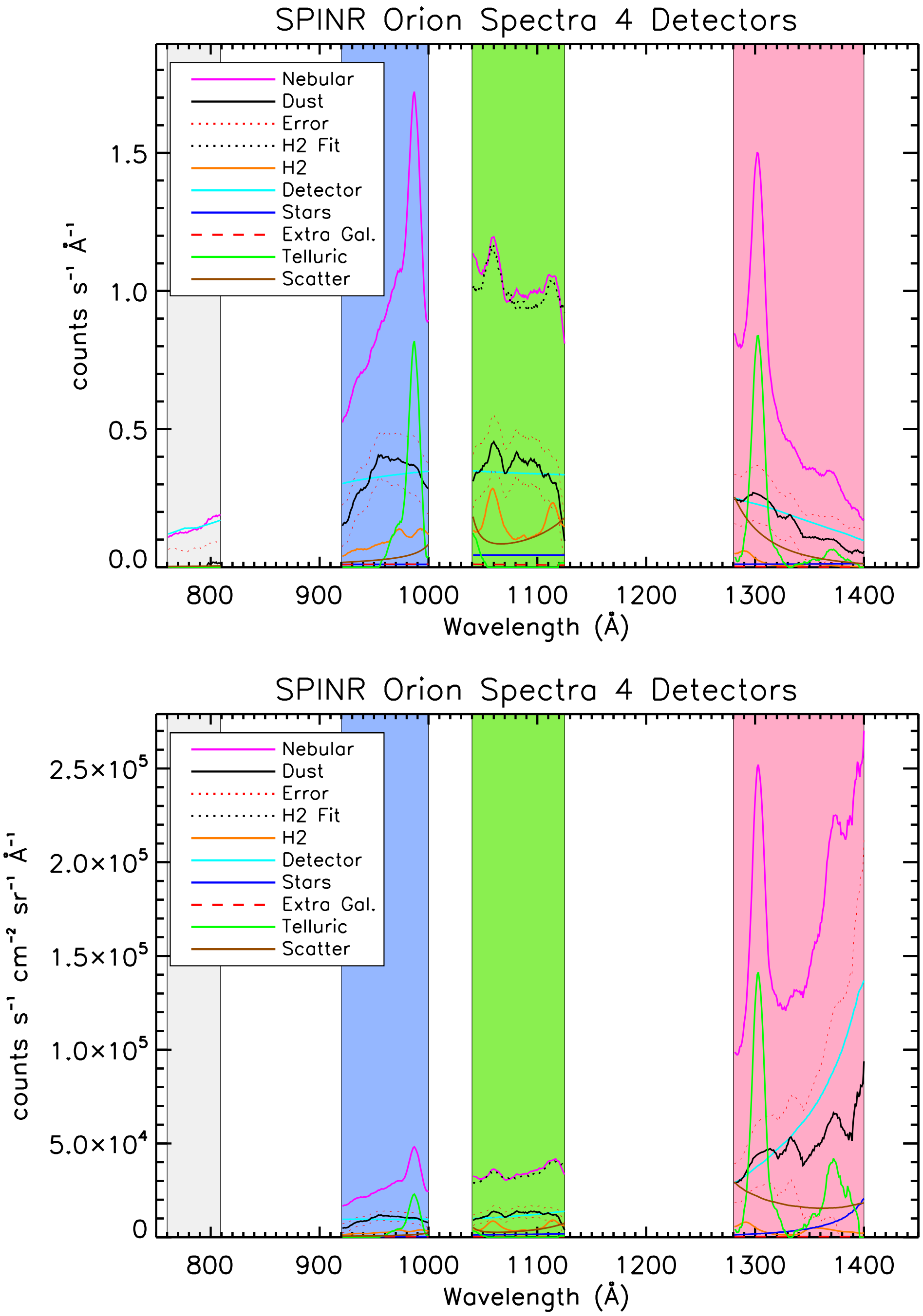

Figure 2.36: Summary of background sources in the nebular spectrum.

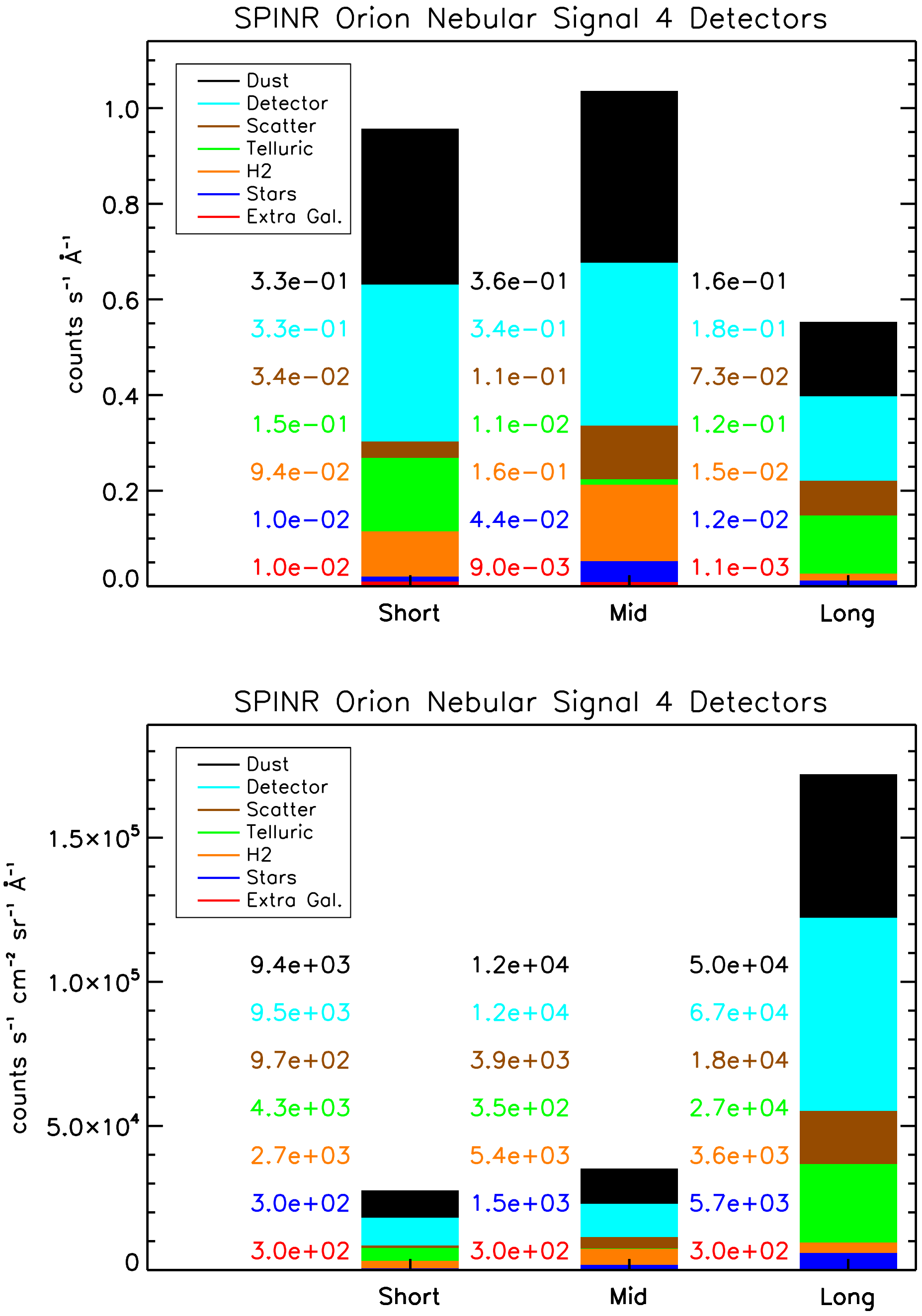

Figure 2.37: Average background levels in each band.

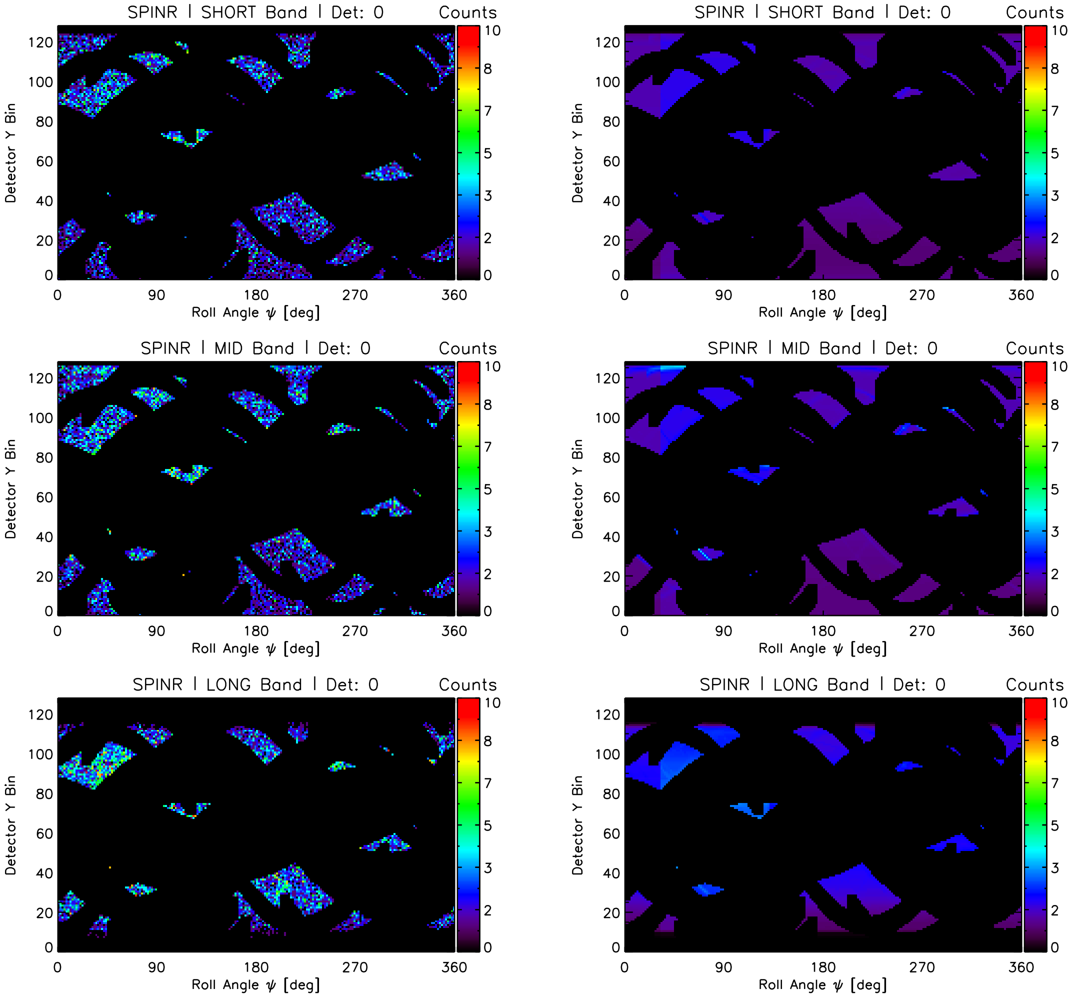

Figure 2.38: Sinograms representing each of the discussed background sources are combined to form the total background sinograms shown to the right. The data sinograms are shown to the left for comparison.

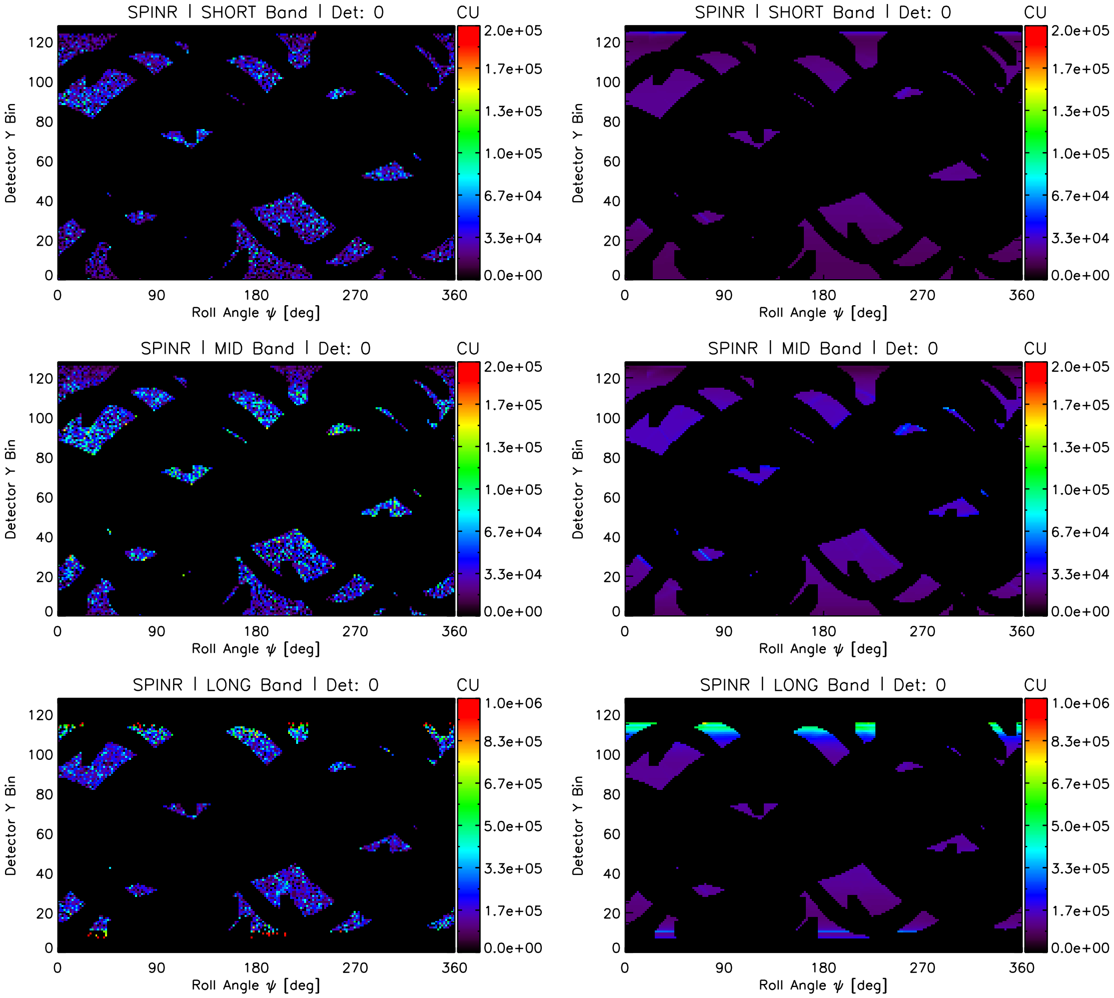

Figure 2.39: The background and data sinograms from Figure 2.38 are calibrated into physical units. Note the change in scale between plots.

2.11 Summary of SPINR Data Products

The SPINR data products are: spectra for individual stars, the total stellar spectrum, the total nebular spectrum and broadband sinogram maps. The sinograms are formed over three science bands and contain the spatial distribution of scattered light on the sky. These sinograms will be the primary data product used to constrain the scattering parameters $(\boldsymbol{a},\boldsymbol{g})$. Calibration methods have been discussed that allow these data products to be expressed in physical units for comparison to previous measurements. The construction of the SPINR instrument function, the T-matrix, allows any image of the sky to be accurately mapped into sinogram space for direct comparison with the data.

Chapter 3

SPINR: Scattering Properties of Dust Grains in Orion

3.1 Questions to be Addressed

The overarching question of this chapter is: *What are the far-ultraviolet (FUV) scattering properties of dust grains along the line of sight to the Orion OB association?* As described in Chapter 1, the dust scattering properties are parametrized as the single scattering albedo ($\boldsymbol{a}$) and the scattering phase function asymmetry parameter ($\boldsymbol{g}$). Knowledge of these parameters provides both an empirical measurement of the optical interaction between dust and FUV radiation as well as a set of constraints for models of grain composition.

To constrain $\boldsymbol{a}$ and $\boldsymbol{g}$ for a three-dimensional system of stars cospatially mixed with dust, a radiative transfer model must be used to break the degeneracy between the scattering parameters themselves and the geometry of the dust distribution; both the geometry and the scattering parameters influence the observed distribution of scattered light on the sky. The DustI Radiative Transfer, Yeah! (DIRTY) radiative transfer model is used for this purpose and is introduced in the following section.

3.2 Introduction to the DIRTY Radiative Transfer Model

The DIRTY radiative transfer model was developed by Karl Gordon and Karl Misselt (Gordon et al. 2001; Misselt et al. 2001). A brief summary follows here.

DIRTY is a Monte-Carlo method simulation that predicts the path of photons from a field of stars through an arbitrary three-dimensional dust distribution. The simulation functions within a three-dimensional box that represents a volume of interstellar space. The box is broken into a user-defined rectilinear grid of cells. Each cell can be filled with an arbitrary amount of dust. The dust is represented by the value $G = n\sigma_{ext}$, which is the product of the number density (n) and extinction cross section (σ_{ext}). More simply, G is the optical depth per unit length. This grid forms the dust distribution for the simulation. To illuminate the dust, stars of varying brightness are placed within the model along a continuous coordinate system.

In the FUV limit, where emission from dust grain heating is negligible, the DIRTY model uses only two parameters, $\boldsymbol{a}$ and $\boldsymbol{g}$. A grain-heating module is available for simulations in the infrared, where the dust emission is significant. Each simulation is considered to be monochromatic; the model corresponds to light at a specific wavelength or in a specific photometric band. To probe the spectral variance of $\boldsymbol{a}$ and $\boldsymbol{g}$, models must be run for each desired wavelength.

The path of a photon through the DIRTY model is described in complete detail in Gordon et al. (2001). The model uses a novel technique for conserving computing power. Instead of treating photons as indivisible quanta, a fraction of each photon is scattered towards the observer at each scattering event. This fraction is equal to the probability that the photon would have scattered towards the observer. This so-called "weighted" approach allows each photon to contribute to the simulated image. Computation is not wasted on photons that do not scatter towards the observer.

The model requires two additional components in order to function: a functional form for the scattering phase function (Φ) and a random number generator. The DIRTY model uses the Henyey-Greenstein (HG) (Henyey & Greenstein 1941) phase function, which was discussed in Chapter 1. This function is expressed as

$$\Phi(g,\theta) = \frac{1}{4\pi}\frac{1-g^2}{(1+g^2-2g\cos\theta)^{3/2}}. \tag{3.1}$$

The method of drawing a random scattering angle (θ') from the HG probability distribution is described in Witt et al. (1997) and Gordon et al. (2001). A random probability (ξ) that ranges between 0 and 1 is first picked using a random number generator. Setting ξ equal to the integral of the phase function over the scattering angle gives

$$\xi = \int_0^{\theta'} \frac{1}{4\pi}\frac{1-g^2}{(1+g^2-2g\cos\theta)^{3/2}}\,\mathrm{d}\theta, \tag{3.2}$$

which is then solved for the scattering angle

$$\theta' = \arccos\left(\frac{1}{2g}\left[\left(1+g^2\right) - \left(\frac{1-g^2}{1-g+2g\xi}\right)^2\right]\right). \tag{3.3}$$

This leaves an equation for a HG-distributed random scattering angle that is a function of the uniformly distributed random number ξ. The azimuthal scattering angle (ϕ') is uniformly distributed and expressed as

$$\phi' = \pi(2\eta - 1), \tag{3.4}$$

where η is a second uniformly distributed random number.

The simulations can be "observed" from any point inside or outside the model grid. The weighted contribution from model photons at each point on the sky is collected and binned into a simulated image. The angular size of the simulated image pixels is defined by the user. These image have no instrumental effects added, they represent the expected distribution of light on the sky.

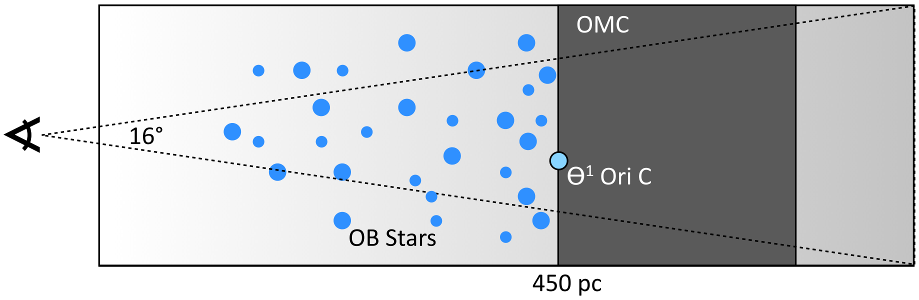

Figure 3.1: Components of the Orion model.

3.3 Description of Method

The methodology of this work is to test hypothetical dust distributions for their ability to reproduce the SPINR data. Given an arbitrary distribution of dust, simulated DIRTY images are generated over a chosen grid of $(\boldsymbol{a},\boldsymbol{g})$ points which span the range of all possible $(\boldsymbol{a},\boldsymbol{g})$ values. The SPINR instrument function is then used to spin the DIRTY images into model sinograms and a spatial fitting method is used to calculate the χ^2 goodness-of-fit statistic between the data and the model sinograms. Confidence intervals are drawn in the $(\boldsymbol{a},\boldsymbol{g})$ plane around all points that are not statistically rejected. If all $(\boldsymbol{a},\boldsymbol{g})$ values are rejected, the model dust distribution can be rejected as a whole.

To begin modeling the Orion system, its major components must be defined. These components are illustrated in Figure 3.1. The Orion system consists of the background Orion Molecular Cloud (OMC), the foreground Orion OB association, the foreground dust, which is responsible for the measured A_V towards each star, and the Orion Nebula itself. The Orion Nebula (M42) contains one of the most FUV-luminous stars visible in the night sky, Theta^1 Ori C. This massive O star sits embedded in a blister of ionized gas on the front face of the OMC. It produces an enormous amount FUV radiation and scattered light and must be given special attention in the development of realistic models.

A more general question about FUV scattering in Orion is first addressed: *Where does the FUV scattering occur?* Is the scattered light produced via backscatter from the slab-like OMC? Is it produced through forward scattering by the foreground dust grains? Is there some contribution from both dust populations? If so, which is more dominant? These questions can be recast and redirected towards specific testable models:

- *Can any model containing only background dust reproduce the SPINR data?*
- *Can any model containing only foreground dust reproduce the SPINR data?*

In asking these questions, two classes of models have been defined: background dust models and foreground dust models. These classes isolate the two dust populations so that the relative contribution of scattered light from each may be evaluated. Within each of these two classes, it is possible to construct a limiting case model, which, if rejected, would show that no model belonging to its parent class is capable of reproducing the data. In Section 3.8, a limiting case background dust model is constructed in three steps. These steps explore the uncertainty in the measured distance to each star and the amount of dust between the stars and the OMC.

After the significance of foreground and background dust is evaluated through the isolation of these two dust populations, a more realistic dust model containing both foreground and background dust will be tested. If this realistic model is not rejected, the question will then be asked: *For which values of the scattering parameters is this model allowed?* While the realistic model is not unique and certainly lacks the complexity of the true dust distribution, it represents the best estimate of the true dust distribution given the available data. The allowed $(\boldsymbol{a},\boldsymbol{g})$ values will then be interpreted as the best estimate of the true scattering parameters.

3.4 DIRTY Models: Calibration & Fitting

3.4.1 Calibrating DIRTY Models

For each of the three SPINR bands, 400 DIRTY models are run over a grid of ($\boldsymbol{a}$,$\boldsymbol{g}$) values. The ($\boldsymbol{a}$,$\boldsymbol{g}$) gridpoints run from $0.05 < (a, g) < 0.95$ with a spacing of 0.05. The DIRTY simulated image at each grid point is multiplied by the SPINR transformation matrix (see Section 2.6) to build a DIRTY "parent" sinogram. These parent sinograms are monochromatic. To construct a broadband model sinogram, a copy of the parent sinogram is created for each spectral wavelength bin across the band. The spectral bins are 1 Å wide. The parent sinograms are calibrated in each bin to match the total number of stellar counts found in the data. They are then stacked and combined to form a broadband DIRTY sinogram.

3.4.2 Sinogram Fitting Method

The χ^2 statistic is used to gauge the "goodness-of-fit" between each DIRTY model sinogram and the SPINR data. The statistic is expressed as

$$\chi^2 = \sum \frac{(C_i - B_i - M_i)^2}{\sigma_{C_i}^2 + \sigma_{B_i}^2 + \sigma_{S_i}^2} \tag{3.5}$$

where, C_i, B_i and M_i respectively represent the raw number of data counts, the number of background counts and the model count prediction in the i^{th} sinogram bin. The number of background counts in each bin is the summed contribution from the background sources listed in Section 2.10: detector background, scattered Lyman-α and Lyman-β, H_2 emission, telluric emission, undetected stars and extra-galactic background. The uncertainty in the number of raw counts is the Poisson counting error $\sigma_{C_i} = \sqrt{C_i}$ and the uncertainty in the background (σ_{B_i}) is the quadrature sum of the uncertainty in each background source.

The final uncertainty term listed in Eq. 3.5 (σ_{S_i}) is an estimate of the instrument calibration error. Since the spectrographs are calibrated independently, the variation in calibration between spectrographs offers some estimate of the accuracy of the calibration. The calibrated ratios of total dust surface brightness to total stellar flux in each band are given in Table 3.1. The dust surface brightness is the value obtained by subtracting the various background sources from the nebular signal. Given perfect calibration, these values should be consistent for each detector within the range of the quoted statistical errors. A 38% variation is measured between the detectors. This greatly outweighs the ~10% statistical errors in the individual flux ratios. A value of $\sigma_{S_i} = 0.38C_i$ is therefore adopted as the instrument calibration error in each sinogram bin. A single χ^2 value for each ($\boldsymbol{a}$,$\boldsymbol{g}$) gridpoint can then be calculated combining the data from all four spectrographs.

Spectrograph	B_d/F_s [S]	B_d/F_s [M]	B_d/F_s [L]
0	1.3±0.2 sr^{-1}	1.1±0.2 sr^{-1}	4.5±0.6sr^{-1}
1	2.3±0.2 sr^{-1}	1.9±0.3 sr^{-1}	5.3±0.5sr^{-1}
2	1.1±0.1 sr^{-1}	0.8±0.2 sr^{-1}	2.4±0.4sr^{-1}
3	1.2±0.2 sr^{-1}	1.0±0.2 sr^{-1}	4.8±0.5sr^{-1}
AVG	1.4±0.1 sr^{-1}	1.1±0.1 sr^{-1}	4.1±0.2sr^{-1}

Table 3.1: Measured dust surface brightness to stellar flux ratio for each spectrograph

An example model sinogram is shown beside its corresponding data sinogram in Figure 3.2. This model represents only one of the 400 ($\boldsymbol{a}$,$\boldsymbol{g}$) gridpoints. The normal fitting procedure would be to calculate the χ^2 value between the data and model using Eq. 3.5, summing over the nebular sinogram pixels (defined in Section 2.8). However, as discussed in Section 2.10.7, when the SPINR sinograms are binned to match the spatial resolution of the instrument, most nebular pixels still contain very few counts. Many sinogram pixels contain zero counts. These pixels behave according to Poisson statistics; repeated measurements would be distributed asymmetrically about the mean and follow a Poisson distribution. The χ^2 statistic is only applicable in the Gaussian regime, where repeated measurements are expected to be distributed symmetrically about the mean and follow a Gaussian distribution.

The χ^2 statistic is preferable to other statistics that are applicable in the Poisson regime such as the Cash C statistic (Cash 1979). The χ^2 statistic provides an absolute goodness-of-fit estimate that can be used to exclude entire classes of models and not just specific model parameters. In this work, a model "class" is defined as the structure of the model: the dust and star distribution. Differential statistics such as Cash C are calculated by subtracting the best-fit value from the value at each parameter gridpoint. They gauge only the relative goodness-of-fit assuming the best-fit model is true. The χ^2 statistic on the other hand, allows the best-fit parameters to be excluded if they fail to reproduce the data within the limits of the uncertainty. If the best-fit parameters are excluded, the entire model class is excluded. The χ^2 statistic offers a much more powerful test of each model class.

To enable the use of χ^2 on the SPINR data, the task remains to place the data uncertainty in the Gaussian regime. To accomplish this task, the data are rebinned more coarsely to increase the number of counts in each bin. The limit of the Poisson distribution, as the number of counts goes to infinity, is the Gaussian distribution. A derivation of this fact can be found in Cash (1979). In rebinning, a target of 25 counts/bin is set such that a 5σ negative excursion from the mean would remain positive. This is slightly higher than the value of 20 counts recommended by Cash (1976).

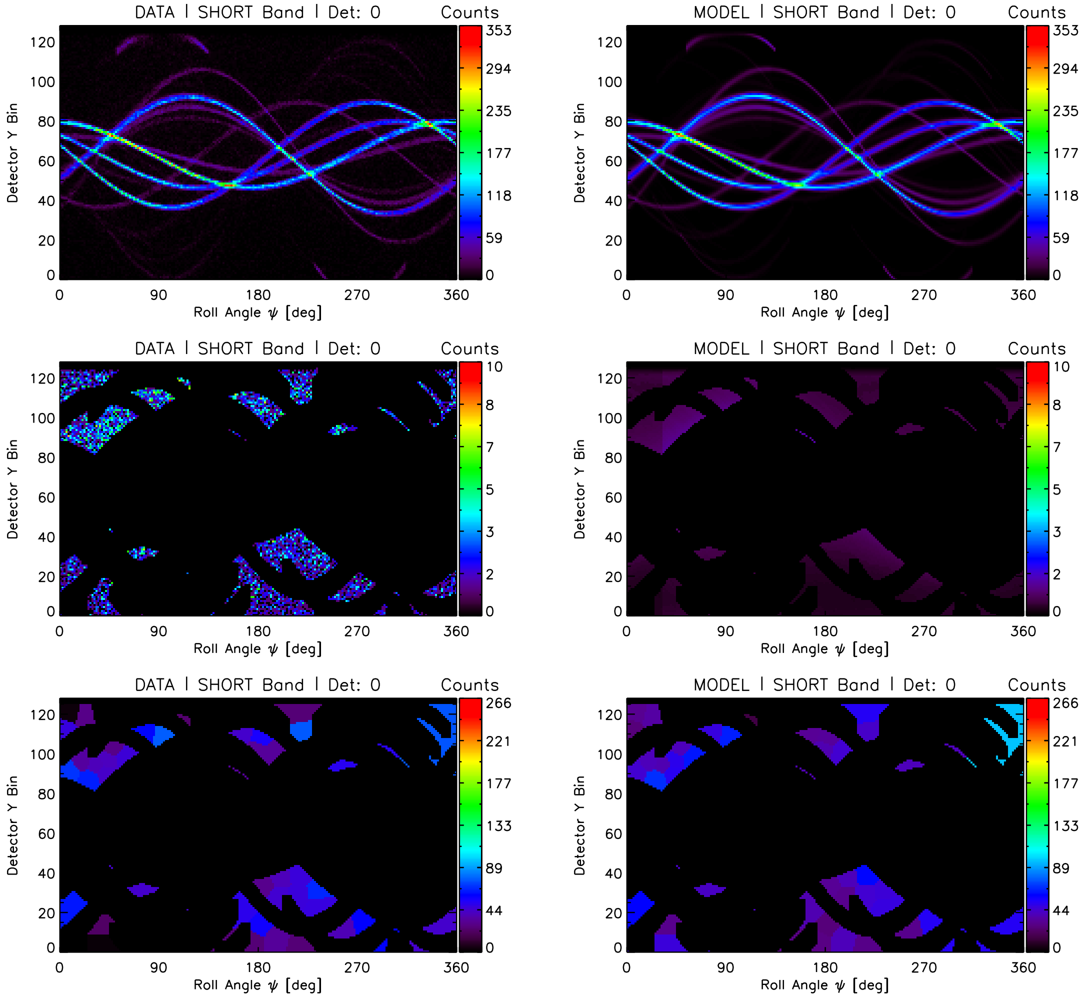

Figure 3.2: Data sinograms are shown to the left, model sinograms to the right. *Top:* The sinograms are presented at full scale, the light is dominated by the stars. *Middle:* The stars are masked out to accentuate the nebular pixels. *Bottom:* The data and model are rebinned using the Voronoi method to achieve SNR>10 *(see text)*.

The raw SPINR dataset is simply a list of recorded photons. The data can be rebinned arbitrarily without suffering the penalty of additional noise. It is for this reason that the background counts were not subtracted from the data sinograms in Section 2.10. Doing so would have led to an overestimate of the uncertainty in the rebinned sinograms. The background subtraction is performed after the data are rebinned.

The data are adaptively rebinned using the Voronoi method, which iteratively conglomerates pixels into new bins that achieve a desired SNR. The rebinning is accomplished using the *voronoi_2d_binning.pro* Interactive Data Language (IDL) routine described in Cappellari & Copin (2003). The nebular mask is applied before rebinning to conserve nebular counts. The rebinned versions of the example sinograms are also shown in Figure 3.2. To ensure each bin contains a minimum of 25 counts, the rebinning routine is run with a target SNR of 10. The model and background sinograms are rebinned identically to the data for use in calculating χ^2.

To gauge whether or not a model can be excluded by the data, the χ^2 elements of Eq. 3.5 are summed over all four detectors for each model ($\boldsymbol{a}$,$\boldsymbol{g}$) gridpoint. Contours are then drawn in the ($\boldsymbol{a}$,$\boldsymbol{g}$) plane to exclude parameters at confidence levels of 68%, 95% and 99.7%. If all parameters are excluded at 99.7%, the model class itself can be excluded.

3.5 Orion Model Geometry

The DIRTY model dust grid is 224×224×700 pc with 2×2×2 pc grid cells. The grid is placed with its long axis along the line of sight to Orion. It is centered at 400 pc along the line through the center of the SPINR field of view (FOV). A representation of the model grid is shown in Figure 3.3.

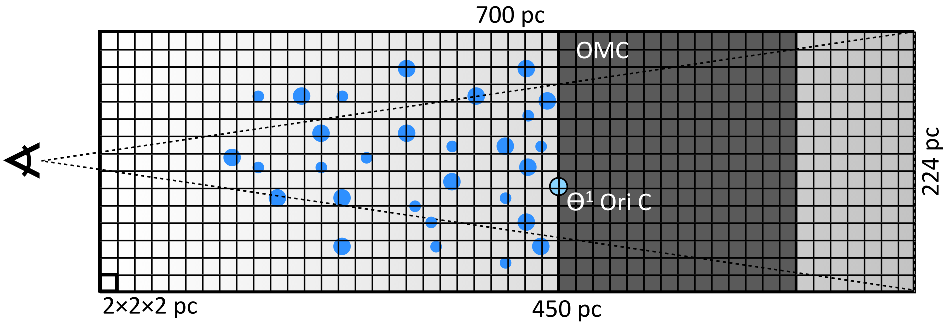

Figure 3.3: The Orion model grid is 224×224×700 pc with 2×2×2 pc grid cells. The grid cells are not shown to scale.

3.6 Background Dust Distribution

The foreground and background dust distributions are defined relative to the front face of the OMC, which is set 450 pc from the observer in compliance with the measurements of Wilson et al. (2005). A background slab of dust extending from 450-750 pc is chosen to represent the OMC. The foreground region is defined as the volume of space between the front face of the grid and the front face of the slab (50-450 pc). The physical depth of this slab is somewhat arbitrary; the optical depth of the slab in the FUV is chosen to be effectively infinite.

3.7 Foreground Dust Distribution

The volume of space foreground to the OMC contains a majority of the Orion OB association members. The measured reddening towards each of these stars confirms that there is some amount of foreground dust (Brown et al. 1994). The observed scattered light distribution depends on the physical geometry of the stars, the dust distribution and the scattering parameters of the dust. To probe only the scattering parameters, the star and dust distributions should be well constrained from additional data. I have developed an iterative method to construct a realistic foreground dust distribution constrained by both the physical location and FUV optical depth of each star. The standard extinction curves of Fitzpatrick (1999) are used to calculate the FUV optical depths of each star for each of the SPINR science bands using the measured E(B-V) and R_V values. This method is explained in the following sections.

3.7.1 Stellar Population

The foreground dust distribution is constrained by the position and optical depth of individual stars within the model grid. The master SPINR catalog containing 2078 stars is defined in Section 2.10.4. The angular position of each star is well known. The catalog collects two different measurements of stellar distance: the trigonometric parallax measured by HIgh Precision PArallax COllecting Satellite (HIPPARCOS) (Perryman et al. 1997) and the photometric distance modulus calculated by Brown et al. (1994). The HIPPARCOS measurements offer a more accurate estimate of the true stellar distance. The distance modulus is dependent on the accuracy of the assumed intrinsic stellar brightness and the extinction correction. This distance estimator is much more susceptible to systematic errors. The parallax measurements, however, are limited by the angular sensitivity of the HIPPARCOS mission. Parallax distances are chosen for stars where the fractional error in the HIPPARCOS measurement is $< 25\%$. This corresponds to a distance of $\sim$200 pc, or a parallax angle of $0.005''$. The remainder of the stars are assigned distances based on their distance modulus.

3.7.2 Optical Depth Calculation

The model reddening curves of Fitzpatrick (1999) are used to calculate the SPINR-band optical depths of each star in the master catalog. The reddening curves are produced using the *fmrcurve.pro* IDL routine. These curves, as discussed in Section 1.1.1, are determined by a single parameter, $R_V \equiv A_V/E(B-V)$. The galactic average value of R_V=3.1 is chosen for all stars in the catalog except those in the Trapezium cluster, where a value of R_V=5.5 has been measured (Cardelli & Clayton 1988; Shalima et al. 2006). Small grain destruction, caused by the extreme FUV radiation fields of these stars, has likely contributed to this anomalously high value.

To calculate the optical depth of a star, the 1-parameter reddening curve $E(\lambda-V)/E(B-V)$ is first recast.

$$\frac{E(\lambda-V)}{E(B-V)} = \frac{A_\lambda}{E(B-V)} - \frac{A_V}{E(B-V)} = \frac{A_\lambda}{E(B-V)} - R_v. \tag{3.6}$$

The specific extinction (A_λ) can then be calculated from the reddening curve.

$$A_\lambda = E(B-V)\left(\frac{E(\lambda-V)}{E(B-V)} + R_V\right) \tag{3.7}$$

The average extinction ($A_{short}, A_{mid}, A_{long}$) is calculated over each SPINR band. The optical depth is then easily calculated using the relation defined in Section 1.1.2, $\tau_{band} = A_{band}/1.086$.

Fitzpatrick (2004) concluded that the single parameter reddening model is only approximately accurate and cannot reproduce higher-order features in the measured reddening curves towards many stars. The choice of the single-parameter reddening law for this work is made out of necessity; measured reddening curves do not exist for many of the stars in the Orion OB association. To asses the uncertainty in the determined optical depths for these stars, the statistical sample of 328 reddening curves measured by Fitzpatrick & Massa (2007) are compared to the single parameter models.

Reddening curve measurements towards 328 near-main sequence B and late-type O stars were performed by Fitzpatrick & Massa (2007). These reddening curves were obtained using the "extinction without standards" method defined in

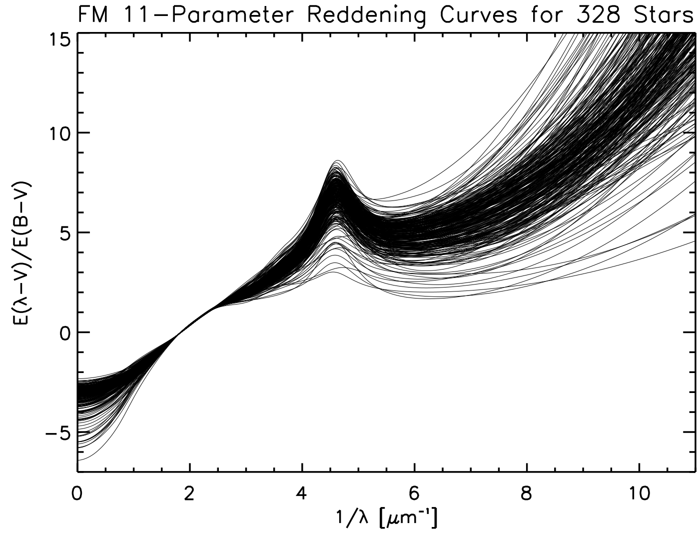

Figure 3.4: The Fitzpatrick & Massa (2007) 11-parameter model fits to 328 measured reddening curves for O and B stars.

Fitzpatrick & Massa (2005). This method is identical to the traditional "pair-method" except stellar spectrum models are used as calibration standards instead of the measured low-reddening spectra of stars with similar spectral types. The reddening curves of Fitzpatrick & Massa (2007) are parametrized by an 11-parameter fit, which captures the deviation of theses curves from the simple 1-parameter model. All 328 reddening curves are plotted in Figure 3.4.

To estimate the uncertainty and systematic error in the calculated optical depth of a star in the SPINR catalog, first the 328 Fitzpatrick & Massa (2007) 11-parameter reddening curves are regenerated from the measured parameters with only the R_V value replaced by that of the SPINR catalog star. The SPINR band optical depths are then calculated for each of the 328 reddening curves using measured E(B-V) value from the SPINR catalog and the same procedure outlined for the 1-parameter model. Finally, these optical depths are subtracted from the calculated SPINR optical depth to produce a distribution of optical depth errors. These errors estimate those that

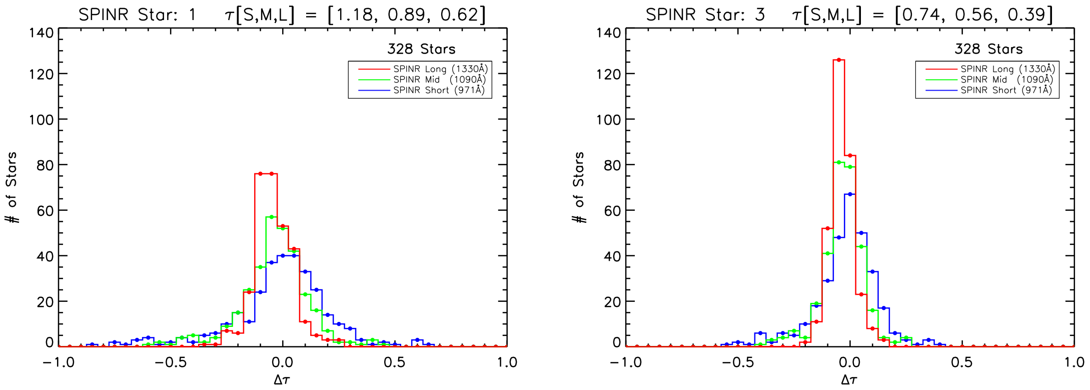

Figure 3.5: These plots show the estimated error distribution in the calculated optical depth for two stars in the SPINR catalog. Deviation of the true reddening curve from the 1-parameter model (Fitzpatrick 1999) is used to estimate the SPINR optical depth uncertainty and systematic error using 328 reddening curves constructed by Fitzpatrick & Massa (2007) (*see text*).

arise from assuming a 1-parameter reddening curve, when in fact, a variety of reddening curves exist with the same value of R_V. Two example distributions are shown in Figure 3.5. The mean and standard deviation of these distributions provides an estimate of the systematic error and uncertainty of each SPINR optical depth.

3.7.3 Star Selection

Stars are chosen from the master catalog to include in the DIRTY models based on a set of selection criteria. The aim of the selection criteria is to comply with the geometry constraints imposed by the dust distribution while preserving as much of the total FUV starlight as possible. To begin, the 42 stars that are visible in the SPINR data (see Section 2.8) are included. To this list, all stars with effective temperatures above 18,000 K are selected from the SPINR catalog. This corresponds approximately to all spectral types B4V and earlier. From this set, all stars foreground to the front edge of the OMC (450 pc) are chosen. Bright stars beyond 450 pc that lie within their 1 σ distance errors of the cloud boundary are included. These stars are placed at 449 pc within the model.

From the selected stars, those with conflicting optical depths within the model grid are thrown out. To create a foreground dust distribution, the opacity of the model grid cells along the line of sight to each star must be adjusted to produce the correct optical depth. If a high optical depth star lies closer than a low optical depth star and the two stars are separated by a small angle, the grid cells cannot reproduce both optical depths. The two stars are in conflict. This is a limitation of the finite (2 pc) cell size. With infinitely small grid cells, the optical depth to each star could be reproduced perfectly. When two stars conflict, the dimmer of the two is thrown out.

These selection criteria produce a final DIRTY star catalog containing 88 members. The master catalog contains 2078 stars; however, these 88 stars contribute the vast majority of FUV photons in Orion. These stars produce 94%, 97% and 99% of the light in the long, mid and short bands respectively. The E(B-V) values, SPINR-band optical depths and relative brightnesses are given for each of the 2078 stars in the DIRTY model input catalog in Tables 3.2 and 3.3.

SPINR #	ID	E(B-V)	B_s	τ_s	B_m	τ_m	B_l	τ_l
0	HD 34085	0.04	$0.0\times10^{+0}$	$6.3\pm1.2\times10^{-1}$	3.1×10^{-3}	$4.8\pm0.8\times10^{-1}$	5.0×10^{-2}	$3.4\pm0.5\times10^{-1}$
1	HD 37742	0.07	2.1×10^{-1}	$1.2\pm0.2\times10^{+0}$	1.7×10^{-1}	$8.9\pm1.5\times10^{-1}$	1.6×10^{-1}	$6.2\pm0.9\times10^{-1}$
2	HD 38771	0.00	4.8×10^{-2}	$0.0\pm0.0\times10^{+0}$	5.4×10^{-2}	$0.0\pm0.0\times10^{+0}$	4.2×10^{-2}	$0.0\pm0.0\times10^{+0}$
3	HD 37043	0.05	1.3×10^{-1}	$7.4\pm1.4\times10^{-1}$	1.1×10^{-1}	$5.6\pm0.9\times10^{-1}$	8.7×10^{-2}	$3.9\pm0.5\times10^{-1}$
4	HD 36486	0.05	1.4×10^{-1}	$7.9\pm1.5\times10^{-1}$	1.2×10^{-1}	$6.0\pm1.0\times10^{-1}$	1.1×10^{-1}	$4.2\pm0.6\times10^{-1}$
5	HD 37128	0.00	1.3×10^{-1}	$0.0\pm0.0\times10^{+0}$	1.2×10^{-1}	$0.0\pm0.0\times10^{+0}$	1.3×10^{-1}	$0.0\pm0.0\times10^{+0}$
6	HD 37468	0.05	4.4×10^{-2}	$7.9\pm1.5\times10^{-1}$	4.0×10^{-2}	$6.0\pm1.0\times10^{-1}$	3.8×10^{-2}	$4.2\pm0.6\times10^{-1}$
7	HD 35411	0.07	2.7×10^{-2}	$1.2\pm0.2\times10^{+0}$	3.5×10^{-2}	$8.9\pm1.5\times10^{-1}$	3.5×10^{-2}	$6.2\pm0.9\times10^{-1}$
8	HD 36512	0.03	2.9×10^{-2}	$4.4\pm0.8\times10^{-1}$	2.4×10^{-2}	$3.3\pm0.6\times10^{-1}$	1.7×10^{-2}	$2.3\pm0.3\times10^{-1}$
9	HD 36960	0.02	1.8×10^{-2}	$3.4\pm0.6\times10^{-1}$	1.7×10^{-2}	$2.6\pm0.4\times10^{-1}$	1.3×10^{-2}	$1.8\pm0.3\times10^{-1}$
10	HD 37022	0.30	4.4×10^{-2}	$4.1\pm0.9\times10^{+0}$	4.5×10^{-2}	$3.1\pm0.6\times10^{+0}$	4.2×10^{-2}	$2.4\pm0.4\times10^{+0}$
11	HD 35715	0.03	8.7×10^{-3}	$5.4\pm1.0\times10^{-1}$	1.1×10^{-2}	$4.1\pm0.7\times10^{-1}$	8.4×10^{-3}	$2.9\pm0.4\times10^{-1}$
13	HD 37018	0.06	1.4×10^{-2}	$9.4\pm1.8\times10^{-1}$	1.7×10^{-2}	$7.1\pm1.2\times10^{-1}$	1.6×10^{-2}	$4.9\pm0.7\times10^{-1}$
14	HD 34503	0.01	2.1×10^{-4}	$1.5\pm0.3\times10^{-1}$	2.3×10^{-3}	$1.1\pm0.2\times10^{-1}$	8.5×10^{-3}	$7.8\pm1.1\times10^{-2}$
15	HD 37756	0.02	7.0×10^{-3}	$2.5\pm0.5\times10^{-1}$	9.1×10^{-3}	$1.9\pm0.3\times10^{-1}$	9.5×10^{-3}	$1.3\pm0.2\times10^{-1}$
16	HD 35439	0.09	5.3×10^{-3}	$1.4\pm0.3\times10^{+0}$	7.3×10^{-3}	$1.0\pm0.2\times10^{+0}$	6.5×10^{-3}	$7.3\pm1.0\times10^{-1}$
17	HD 35039	0.04	4.9×10^{-3}	$6.4\pm1.2\times10^{-1}$	7.6×10^{-3}	$4.8\pm0.8\times10^{-1}$	6.5×10^{-3}	$3.4\pm0.5\times10^{-1}$
18	HD 36591	0.05	4.5×10^{-3}	$8.4\pm1.6\times10^{-1}$	4.9×10^{-3}	$6.3\pm1.1\times10^{-1}$	5.5×10^{-3}	$4.4\pm0.6\times10^{-1}$
20	HD 36695	0.06	5.7×10^{-3}	$9.8\pm1.9\times10^{-1}$	6.9×10^{-3}	$7.4\pm1.3\times10^{-1}$	8.1×10^{-3}	$5.2\pm0.7\times10^{-1}$
21	HD 39291	0.03	3.6×10^{-3}	$4.4\pm0.8\times10^{-1}$	5.2×10^{-3}	$3.3\pm0.6\times10^{-1}$	4.2×10^{-3}	$2.3\pm0.3\times10^{-1}$
22	HD 37490	0.12	$0.0\times10^{+0}$	$1.8\pm0.3\times10^{+0}$	3.6×10^{-4}	$1.4\pm0.2\times10^{+0}$	4.3×10^{-4}	$9.6\pm1.4\times10^{-1}$
23	HD 36351	0.03	2.0×10^{-3}	$4.4\pm0.8\times10^{-1}$	3.7×10^{-3}	$3.3\pm0.6\times10^{-1}$	3.1×10^{-3}	$2.3\pm0.3\times10^{-1}$
24	HD 35299	0.02	3.5×10^{-3}	$3.9\pm0.7\times10^{-1}$	4.5×10^{-3}	$3.0\pm0.5\times10^{-1}$	3.5×10^{-3}	$2.1\pm0.3\times10^{-1}$
25	HD 37481	0.02	3.3×10^{-3}	$2.5\pm0.5\times10^{-1}$	4.3×10^{-3}	$1.9\pm0.3\times10^{-1}$	3.1×10^{-3}	$1.3\pm0.2\times10^{-1}$
26	HD 36166	0.02	1.3×10^{-3}	$3.9\pm0.7\times10^{-1}$	1.8×10^{-3}	$3.0\pm0.5\times10^{-1}$	1.4×10^{-3}	$2.1\pm0.3\times10^{-1}$
27	HD 37303	0.02	3.5×10^{-3}	$3.9\pm0.7\times10^{-1}$	3.9×10^{-3}	$3.0\pm0.5\times10^{-1}$	2.9×10^{-3}	$2.1\pm0.3\times10^{-1}$
28	HD 37744	0.04	2.1×10^{-3}	$6.4\pm1.2\times10^{-1}$	2.7×10^{-3}	$4.8\pm0.8\times10^{-1}$	2.2×10^{-3}	$3.4\pm0.5\times10^{-1}$
29	HD 35007	0.04	1.0×10^{-3}	$6.9\pm1.3\times10^{-1}$	2.7×10^{-3}	$5.2\pm0.9\times10^{-1}$	3.1×10^{-3}	$3.6\pm0.5\times10^{-1}$
30	HD 36285	0.02	4.6×10^{-4}	$3.9\pm0.7\times10^{-1}$	6.4×10^{-4}	$3.0\pm0.5\times10^{-1}$	5.1×10^{-4}	$2.1\pm0.3\times10^{-1}$
31	HD 36779	0.03	1.2×10^{-3}	$4.9\pm0.9\times10^{-1}$	2.3×10^{-3}	$3.7\pm0.6\times10^{-1}$	2.8×10^{-3}	$2.6\pm0.4\times10^{-1}$
32	HD 35588	0.02	7.7×10^{-4}	$3.0\pm0.6\times10^{-1}$	1.4×10^{-3}	$2.2\pm0.4\times10^{-1}$	1.3×10^{-3}	$1.6\pm0.2\times10^{-1}$
33	HD 36430	0.02	6.9×10^{-4}	$2.5\pm0.5\times10^{-1}$	1.5×10^{-3}	$1.9\pm0.3\times10^{-1}$	1.3×10^{-3}	$1.3\pm0.2\times10^{-1}$
34	HD 37016	0.03	4.0×10^{-4}	$4.9\pm0.9\times10^{-1}$	1.0×10^{-3}	$3.7\pm0.6\times10^{-1}$	1.1×10^{-3}	$2.6\pm0.4\times10^{-1}$
36	HD 39777	0.03	8.6×10^{-4}	$4.9\pm0.9\times10^{-1}$	1.4×10^{-3}	$3.7\pm0.6\times10^{-1}$	1.2×10^{-3}	$2.6\pm0.4\times10^{-1}$
37	HD 35912	0.02	6.3×10^{-4}	$3.9\pm0.7\times10^{-1}$	1.2×10^{-3}	$3.0\pm0.5\times10^{-1}$	1.1×10^{-3}	$2.1\pm0.3\times10^{-1}$
38	HD 36741	0.02	8.0×10^{-4}	$3.0\pm0.6\times10^{-1}$	1.3×10^{-3}	$2.2\pm0.4\times10^{-1}$	1.1×10^{-3}	$1.6\pm0.2\times10^{-1}$
39	HD 37040	0.04	3.5×10^{-4}	$6.4\pm1.2\times10^{-1}$	7.9×10^{-4}	$4.8\pm0.8\times10^{-1}$	8.8×10^{-4}	$3.4\pm0.5\times10^{-1}$
40	HD 35575	0.02	5.5×10^{-4}	$3.9\pm0.7\times10^{-1}$	1.2×10^{-3}	$3.0\pm0.5\times10^{-1}$	1.1×10^{-3}	$2.1\pm0.3\times10^{-1}$
41	HD 37356	0.17	2.5×10^{-4}	$2.7\pm0.5\times10^{+0}$	6.2×10^{-4}	$2.1\pm0.3\times10^{+0}$	8.7×10^{-4}	$1.4\pm0.2\times10^{+0}$
42	HD 34748	0.10	4.3×10^{-4}	$1.6\pm0.3\times10^{+0}$	8.5×10^{-4}	$1.2\pm0.2\times10^{+0}$	9.2×10^{-4}	$8.3\pm1.2\times10^{-1}$
44	HD 35777	0.02	4.8×10^{-4}	$3.4\pm0.6\times10^{-1}$	1.0×10^{-3}	$2.6\pm0.4\times10^{-1}$	9.6×10^{-4}	$1.8\pm0.3\times10^{-1}$
45	HD 37017	0.07	4.7×10^{-4}	$1.0\pm0.2\times10^{+0}$	9.5×10^{-4}	$7.8\pm1.3\times10^{-1}$	8.9×10^{-4}	$5.5\pm0.8\times10^{-1}$
48	HD 35762	0.02	4.5×10^{-4}	$3.0\pm0.6\times10^{-1}$	9.6×10^{-4}	$2.2\pm0.4\times10^{-1}$	8.8×10^{-4}	$1.6\pm0.2\times10^{-1}$
50	HD 36646	0.06	1.4×10^{-4}	$9.8\pm1.9\times10^{-1}$	3.8×10^{-4}	$7.4\pm1.3\times10^{-1}$	5.2×10^{-4}	$5.2\pm0.7\times10^{-1}$

Table 3.2: DIRTY model input catalog (part 1). The optical depth (τ) and relative observed (reddened) brightness (B) is given for each of the 88 stars in each of the SPINR bands.

SPINR #	ID	E(B-V)	B_s	τ_s	B_m	τ_m	B_l	τ_l
51	HD 37397	0.03	3.0×10^{-4}	$4.4\pm0.8\times10^{-1}$	6.7×10^{-4}	$3.3\pm0.6\times10^{-1}$	6.4×10^{-4}	$2.3\pm0.3\times10^{-1}$
55	HD 37025	0.02	1.2×10^{-4}	$3.9\pm0.7\times10^{-1}$	3.0×10^{-4}	$3.0\pm0.5\times10^{-1}$	3.7×10^{-4}	$2.1\pm0.3\times10^{-1}$
57	HD 36958	0.09	6.3×10^{-5}	$1.4\pm0.3\times10^{+0}$	2.3×10^{-4}	$1.0\pm0.2\times10^{+0}$	3.7×10^{-4}	$7.3\pm1.0\times10^{-1}$
58	HD 34511	0.06	9.1×10^{-5}	$8.9\pm1.7\times10^{-1}$	2.1×10^{-4}	$6.7\pm1.1\times10^{-1}$	2.5×10^{-4}	$4.7\pm0.7\times10^{-1}$
59	HD 37889	0.08	8.2×10^{-5}	$1.3\pm0.3\times10^{+0}$	2.2×10^{-4}	$1.0\pm0.2\times10^{+0}$	2.5×10^{-4}	$7.0\pm1.0\times10^{-1}$
63	HD 37115	0.04	4.2×10^{-5}	$6.9\pm1.3\times10^{-1}$	1.5×10^{-4}	$5.2\pm0.9\times10^{-1}$	2.3×10^{-4}	$3.6\pm0.5\times10^{-1}$
66	HD 36629	0.22	3.3×10^{-5}	$3.4\pm0.6\times10^{+0}$	1.1×10^{-4}	$2.6\pm0.4\times10^{+0}$	1.7×10^{-4}	$1.8\pm0.3\times10^{+0}$
73	HD 35673	0.06	1.4×10^{-7}	$9.4\pm1.8\times10^{-1}$	6.2×10^{-6}	$7.1\pm1.2\times10^{-1}$	9.6×10^{-5}	$4.9\pm0.7\times10^{-1}$
77	HD 35501	0.05	2.5×10^{-6}	$8.4\pm1.6\times10^{-1}$	2.3×10^{-5}	$6.3\pm1.1\times10^{-1}$	9.9×10^{-5}	$4.4\pm0.6\times10^{-1}$
79	HD 35468	0.00	2.9×10^{-9}	$0.0\pm0.0\times10^{+0}$	8.1×10^{-8}	$0.0\pm0.0\times10^{+0}$	4.7×10^{-5}	$0.0\pm0.0\times10^{+0}$
80	HD 33328	0.04	1.0×10^{-2}	$6.9\pm1.3\times10^{-1}$	1.2×10^{-2}	$5.2\pm0.9\times10^{-1}$	1.1×10^{-2}	$3.6\pm0.5\times10^{-1}$
82	HD 42690	0.02	3.4×10^{-3}	$3.7\pm0.7\times10^{-1}$	5.3×10^{-3}	$2.8\pm0.5\times10^{-1}$	4.4×10^{-3}	$1.9\pm0.3\times10^{-1}$
83	HD 41335	0.18	1.0×10^{-3}	$2.9\pm0.6\times10^{+0}$	1.9×10^{-3}	$2.2\pm0.4\times10^{+0}$	2.3×10^{-3}	$1.5\pm0.2\times10^{+0}$
88	HD 41253	0.17	4.3×10^{-5}	$2.8\pm0.5\times10^{+0}$	1.3×10^{-4}	$2.1\pm0.4\times10^{+0}$	2.1×10^{-4}	$1.5\pm0.2\times10^{+0}$
265	HD 36824	0.03	4.1×10^{-4}	$5.4\pm1.0\times10^{-1}$	8.0×10^{-4}	$4.1\pm0.7\times10^{-1}$	7.9×10^{-4}	$2.9\pm0.4\times10^{-1}$
383	HD 36485	0.04	3.5×10^{-4}	$5.9\pm1.1\times10^{-1}$	8.1×10^{-4}	$4.5\pm0.8\times10^{-1}$	8.3×10^{-4}	$3.1\pm0.4\times10^{-1}$
403	HD 36827	0.03	4.4×10^{-4}	$4.9\pm0.9\times10^{-1}$	8.6×10^{-4}	$3.7\pm0.6\times10^{-1}$	8.4×10^{-4}	$2.6\pm0.4\times10^{-1}$
440	HD 37479	0.08	1.2×10^{-3}	$1.2\pm0.2\times10^{+0}$	2.0×10^{-3}	$9.3\pm1.6\times10^{-1}$	2.0×10^{-3}	$6.5\pm0.9\times10^{-1}$
489	HIP 26551	0.05	7.7×10^{-4}	$7.9\pm1.5\times10^{-1}$	1.4×10^{-3}	$6.0\pm1.0\times10^{-1}$	1.5×10^{-3}	$4.2\pm0.6\times10^{-1}$
550	HD 35337	0.02	6.1×10^{-3}	$3.0\pm0.6\times10^{-1}$	7.7×10^{-3}	$2.2\pm0.4\times10^{-1}$	5.8×10^{-3}	$1.6\pm0.2\times10^{-1}$
620	HD 36959	0.03	5.0×10^{-3}	$4.4\pm0.8\times10^{-1}$	5.9×10^{-3}	$3.3\pm0.6\times10^{-1}$	4.6×10^{-3}	$2.3\pm0.3\times10^{-1}$
639	HD 37129	0.04	2.5×10^{-4}	$5.9\pm1.1\times10^{-1}$	5.6×10^{-4}	$4.5\pm0.8\times10^{-1}$	5.5×10^{-4}	$3.1\pm0.4\times10^{-1}$
644	HD 37209	0.02	4.7×10^{-3}	$3.0\pm0.6\times10^{-1}$	5.5×10^{-3}	$2.2\pm0.4\times10^{-1}$	4.1×10^{-3}	$1.6\pm0.2\times10^{-1}$
652	HD 37334	0.03	2.9×10^{-4}	$4.4\pm0.8\times10^{-1}$	5.6×10^{-4}	$3.3\pm0.6\times10^{-1}$	5.4×10^{-4}	$2.3\pm0.3\times10^{-1}$
695	HD 38185	0.08	1.1×10^{-4}	$1.2\pm0.2\times10^{+0}$	2.4×10^{-4}	$9.3\pm1.6\times10^{-1}$	2.7×10^{-4}	$6.5\pm0.9\times10^{-1}$
1120	HD 32249	0.00	3.4×10^{-3}	$7.3\pm1.4\times10^{-2}$	6.1×10^{-3}	$5.5\pm0.9\times10^{-2}$	5.4×10^{-3}	$3.9\pm0.5\times10^{-2}$
1271	HD 34816	0.04	3.3×10^{-2}	$6.6\pm1.2\times10^{-1}$	2.8×10^{-2}	$5.0\pm0.8\times10^{-1}$	2.2×10^{-2}	$3.5\pm0.5\times10^{-1}$
1321	HD 41814	0.05	3.7×10^{-4}	$7.7\pm1.4\times10^{-1}$	7.5×10^{-4}	$5.8\pm1.0\times10^{-1}$	7.8×10^{-4}	$4.1\pm0.6\times10^{-1}$
1362	HD 34989	0.12	1.6×10^{-3}	$1.8\pm0.3\times10^{+0}$	2.4×10^{-3}	$1.4\pm0.2\times10^{+0}$	2.5×10^{-3}	$9.6\pm1.4\times10^{-1}$
1368	HD 37232	0.05	1.2×10^{-3}	$7.3\pm1.4\times10^{-1}$	1.9×10^{-3}	$5.5\pm0.9\times10^{-1}$	1.7×10^{-3}	$3.9\pm0.5\times10^{-1}$
1396	HD 44112	0.04	2.8×10^{-3}	$6.0\pm1.1\times10^{-1}$	4.6×10^{-3}	$4.6\pm0.8\times10^{-1}$	4.0×10^{-3}	$3.2\pm0.4\times10^{-1}$
1435	HD 43317	0.04	4.1×10^{-4}	$6.7\pm1.3\times10^{-1}$	8.2×10^{-4}	$5.1\pm0.9\times10^{-1}$	8.3×10^{-4}	$3.6\pm0.5\times10^{-1}$
1441	HD 36895	0.09	3.7×10^{-4}	$1.5\pm0.3\times10^{+0}$	7.1×10^{-4}	$1.1\pm0.2\times10^{+0}$	7.5×10^{-4}	$7.7\pm1.1\times10^{-1}$
1483	HD 45321	0.07	8.2×10^{-4}	$1.1\pm0.2\times10^{+0}$	1.5×10^{-3}	$8.6\pm1.5\times10^{-1}$	1.4×10^{-3}	$6.0\pm0.8\times10^{-1}$
1495	HD 45418	0.06	3.6×10^{-4}	$9.7\pm1.8\times10^{-1}$	7.7×10^{-4}	$7.3\pm1.2\times10^{-1}$	8.4×10^{-4}	$5.1\pm0.7\times10^{-1}$
1500	HD 30112	0.04	4.4×10^{-4}	$6.7\pm1.3\times10^{-1}$	7.1×10^{-4}	$5.0\pm0.9\times10^{-1}$	6.3×10^{-4}	$3.5\pm0.5\times10^{-1}$
1538	HD 45546	0.04	3.3×10^{-3}	$6.5\pm1.2\times10^{-1}$	5.4×10^{-3}	$4.9\pm0.8\times10^{-1}$	4.8×10^{-3}	$3.4\pm0.5\times10^{-1}$
1591	HD 44700	0.07	3.7×10^{-4}	$1.1\pm0.2\times10^{+0}$	8.0×10^{-4}	$8.2\pm1.4\times10^{-1}$	8.9×10^{-4}	$5.7\pm0.8\times10^{-1}$
1602	HD 32612	0.03	1.1×10^{-3}	$4.9\pm0.9\times10^{-1}$	1.7×10^{-3}	$3.7\pm0.6\times10^{-1}$	1.4×10^{-3}	$2.6\pm0.4\times10^{-1}$
1607	HD 30076	0.14	5.2×10^{-4}	$2.2\pm0.4\times10^{+0}$	1.1×10^{-3}	$1.6\pm0.3\times10^{+0}$	1.4×10^{-3}	$1.1\pm0.2\times10^{+0}$
1623	HD 45725	0.05	2.2×10^{-3}	$8.6\pm1.6\times10^{-1}$	4.6×10^{-3}	$6.5\pm1.1\times10^{-1}$	4.9×10^{-3}	$4.6\pm0.6\times10^{-1}$
1679	HD 46339	0.16	1.0×10^{-5}	$2.6\pm0.5\times10^{+0}$	3.0×10^{-5}	$2.0\pm0.3\times10^{+0}$	4.6×10^{-5}	$1.4\pm0.2\times10^{+0}$
1697	HD 31726	0.01	1.9×10^{-3}	$1.0\pm0.2\times10^{-1}$	2.7×10^{-3}	$7.6\pm1.3\times10^{-2}$	2.1×10^{-3}	$5.3\pm0.7\times10^{-2}$
1742	HD 34447	0.06	6.3×10^{-4}	$1.0\pm0.2\times10^{+0}$	1.1×10^{-3}	$7.7\pm1.3\times10^{-1}$	1.1×10^{-3}	$5.4\pm0.8\times10^{-1}$
		Total B_s:	**0.99**	**Total B_m:**	**0.97**	**Total B_l:**	**0.94**	

Table 3.3: DIRTY model input catalog (part 2). The optical depth (τ) and relative observed (reddened) brightness (B) is given for each of the 88 stars in each of the SPINR bands. The total input brightness relative to the entire 2078 element SPINR catalog is given at the bottom of each column.

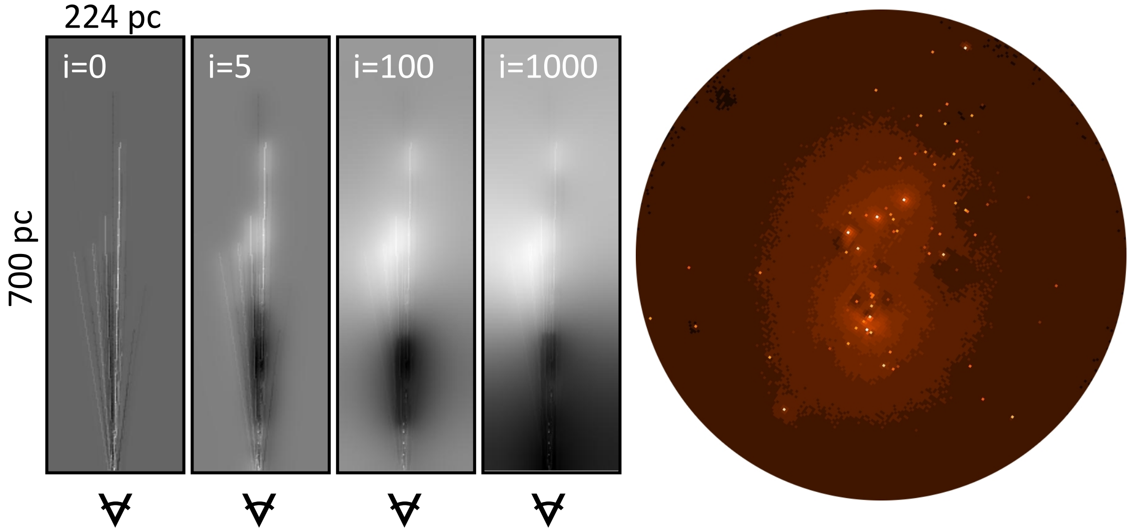

Figure 3.6: Building a 3D model of Orion (left): The 224×224×700 pc model is viewed from the top down, the observer is towards the bottom. The grayscale indicates the grid cell value of τ/pc. The grid cells are cubes, 2 pc on a side. Iterative steps are taken (from left to right) to match both the physical positions of the stars and the optical depths. The final DIRTY model image of Orion is show to the right.

3.7.4 Dust Grid Construction

I developed an iterative routine to construct a three-dimensional foreground dust distribution constrained by the physical position and optical depth of each star in the model. An illustration of the grid building process is shown in Figure 3.6. The routine begins by placing each star in the model grid at its measured (x,y,z) position. The differential path length through each grid cell is calculated along the line of sight from the observer to each star. Each grid cell holds a value corresponding to the optical depth per unit length in that cell. The grid is initialized to hold the average value for each stellar sightline.

As the algorithm iterates, grid cells along the line of sight to each star are pushed toward values that achieve the correct optical depth for that star. Cells that are unique to a stellar sightline are driven more aggressively to the ideal value than those that are shared by multiple stars. This is done to decrease the convergence time of the routine. After each iteration, a regularization algorithm is used to push each grid cell towards the average of its neighboring cells. This regularization method is controlled by the regularization gain (K_r). A value of $K_r = 1$ provides full boxcar smoothing, which is often too extreme and causes the model to diverge. A value of $K_r = 0.7$ is used to achieve a model grid that is as homogeneous as possible while still conforming to the stellar constraints. Model foreground grids are generated for each SPINR band.

3.7.5 Special Case: Theta^1 Ori C

The massive O6pe V star Theta^1 Ori C (HD 37022, SPINR #10) is a member of the Trapezium cluster and is embedded within the Orion Nebula (M42). Theta^1 Ori C is the strongest source of FUV photons in the Orion OB association. The Trapezium open cluster is extremely rich; McCaughrean & Stauffer (1994) estimate a stellar density of $\sim 5 \times 10^4$ stars pc^{-3} within the 0.1 pc diameter core of the cluster. The entire Trapezium cluster measures only a few arcminutes in diameter and fits within a single SPINR resolution element.

The three-dimensional structure of the Orion Nebula was reviewed by O'Dell (2001). Theta^1 Ori C is thought to sit $\sim$0.25 pc in front of the OMC surface, into which it is actively carving a spherical cavity through the process of photoevaporation. The OMC surface on the far side of the star is referred to as the main ionization front (MIF). The near-side material, immediately in front of Theta^1 Ori C, is referred to as the Veil. The Veil is a thin blister of gas and dust, presumably ionized on the inside; the observed material on the outside of the Veil is neutral. O'Dell (2001) concluded that the majority of extinction measured towards Theta^1 Ori C is produced locally in the Veil region.

Theta^1 Ori C is treated as a special case within the DIRTY model. Since the measured SPINR spectrum for this star is actually a blend of all the stars in Trapezium, and since most of the extinction to these stars is locally produced, the entire Trapezium cluster, including Theta^1 Ori C and the dust that produces the foreground extinction, is treated as a single reddened object and assigned the flux measured by SPINR. This object is treated the same in all models and it is not used to constrain the foreground dust distribution. Due to the confusion between sources, no attempt is made to deredden this object in any model. The object is assigned a distance of 449.75 pc to correspond with the distance to Theta^1 Ori C.

3.8 DIRTY Models: Dust Distributions and Results

In the following sections, a number of dust distributions will be examined to test the significance of foreground and background dust in the Orion system. The analysis will begin with background-only models, progress to foreground-only models, and then a realistic hybrid model containing both background and foreground dust will be examined.

3.8.1 Background Dust Model 1

Model Description

To isolate the scattered light contribution from the background OMC, this model contains only a slab of dust extending from 450 pc to 750 pc. The total slab optical depth is $\tau = 30$. The results are invariant for higher optical depths, so we may take this value as effectively infinite. The 88 DIRTY input stars are placed at their measured distances in front of the slab. Stars beyond 450 pc with 1σ distance uncertainties that could allow them to be closer than 450 pc are placed at 449 pc.

The SPINR band optical depth of each star is plotted against the model-z component of the stellar distance in Figure 3.7. For stars with parallax distance measurements, the distance uncertainties are taken directly from the HIPPARCOS catalog (Perryman et al. 1997). Stars with distances determined by the distance modulus assume an error of 0.3 mag, as quoted in the Brown et al. (1994) Orion OB association catalog. Also included in Figure 3.7 are total integrated optical depth maps from the observer's point of view. The maps are generated in DIRTY model image coordinates.

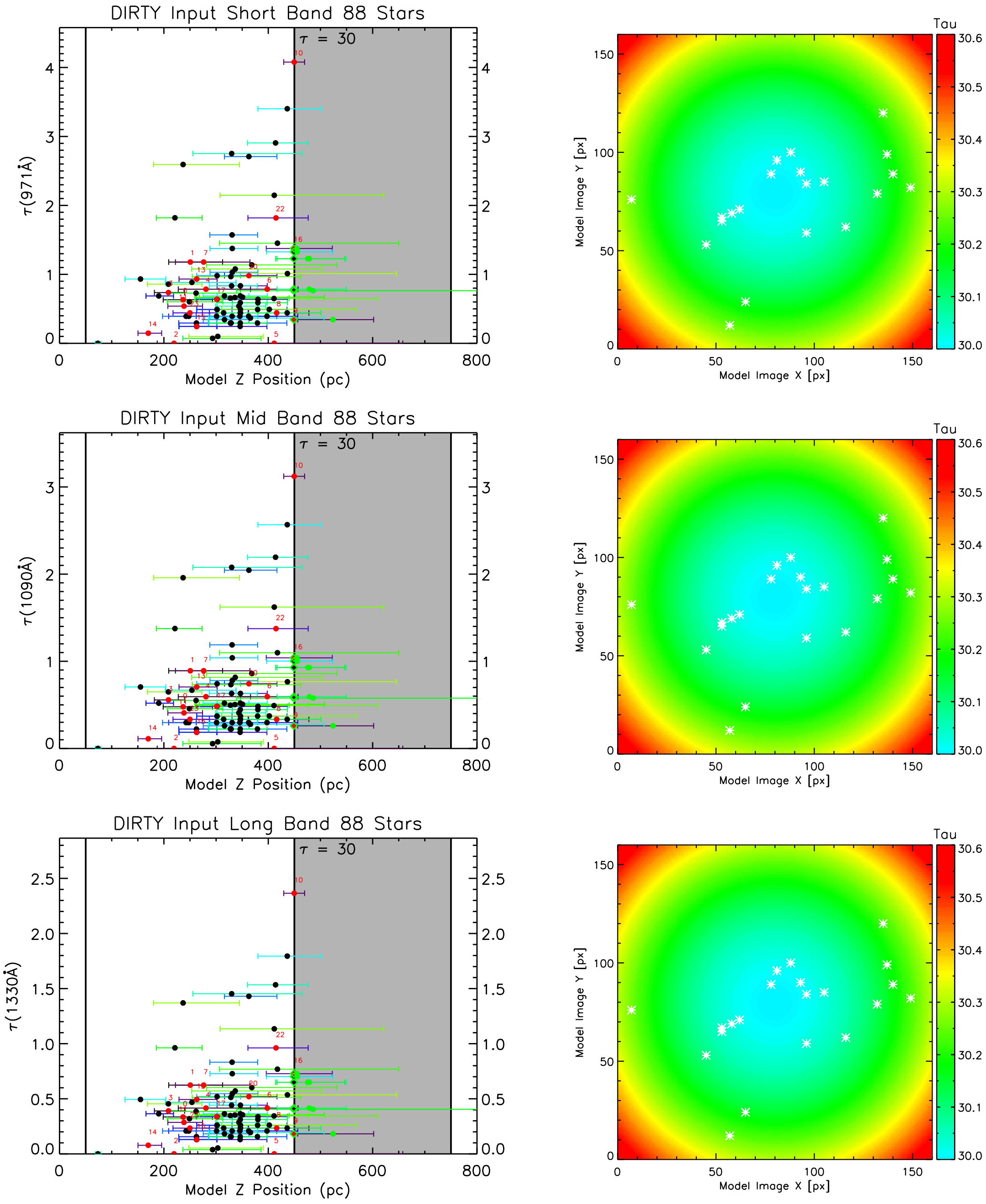

Figure 3.7: Background dust model 1. *Left:* Stellar distance vs. optical depth in each SPINR band. Black dots mark the position of each star in the model. Stars with measured spectra are shown in red. Green dots show the original position of stars that have been moved to a new position marked by a green diamond. *Right:* Optical depth maps of each dust distribution from the observer's point of view. The bright Orion stars are shown in white.

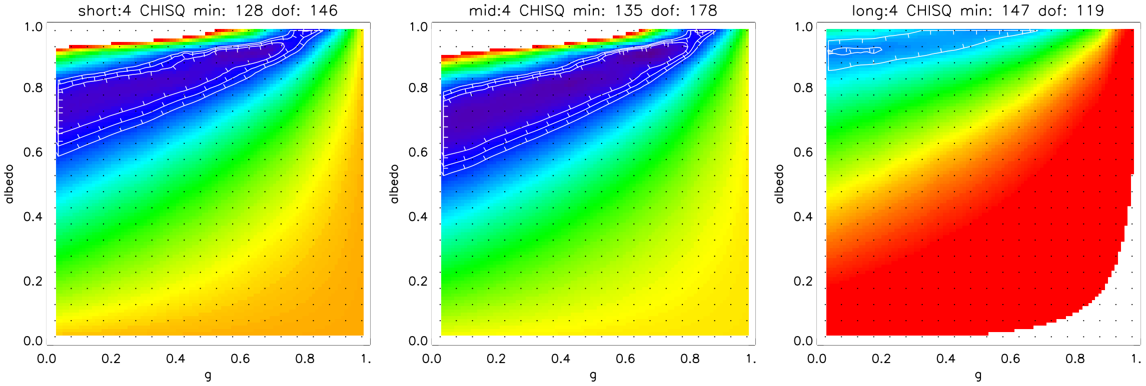

Figure 3.8: Background dust model 1: ($\boldsymbol{a}$,$\boldsymbol{g}$) confidence contours (68%, 95%, 99.7%) are plotted over the χ^2 map. *Left:* Short band. *Middle:* Mid band. *Right:* Long band. The χ^2 values are non-reduced. The minimum value and the total degrees of freedom are given at the top of each plot. The 400 ($\boldsymbol{a}$,$\boldsymbol{g}$) gridpoints are marked with black dots. The χ^2 map is interpolated in two dimensions between the gridpoints. Map values shown as white are rejected with better than 5σ confidence.

Model Results

DIRTY simulations are run for each SPINR band over the 400-point ($\boldsymbol{a}$,$\boldsymbol{g}$) grid. Although negative $\boldsymbol{g}$ values are physically possible, only positive values of $\boldsymbol{g}$ are considered. The overwhelming majority of observations and grain model predictions indicate that interstellar grains are highly forward-scattering ($g > 0$). In Figure 3.8, confidence contours are plotted in the ($\boldsymbol{a}$,$\boldsymbol{g}$) plane based on the calculated χ^2 values across all four spectrographs. The best-fit model sinograms are compared to the data in Figures 3.9, 3.10 and 3.11.

For this background-only model, high albedos (> 0.6) are able to reproduce the data in all three bands. An important characteristic of backscatter models is seen clearly. Models with more forward-throwing grains (higher $\boldsymbol{g}$ values) require higher albedos to reproduce the scattered light distribution. This relationship suggests that the observed photons are singly scattered. Multiple scattering tends to wash out the

$\boldsymbol{g}$ dependence. In the single-scattering limit, as backscatter becomes less and less probable, the albedo must increase to reflect the same amount of light. Also, given the high optical depth of the background slab, a photon that initially scatters away from the observer will likely be absorbed in the slab. This likelihood increases with increasing $\boldsymbol{g}$. Due to their strong $\boldsymbol{g}$ dependence, potential backscatter geometries such as Orion have been sought out to gain sensitivity to this parameter.

If prior measurements of $(\boldsymbol{a},\boldsymbol{g})$ are considered, the majority of evidence discussed in Section 1.1.3 suggests highly forward-scattering grains ($g > 0.75$) in the FUV and low albedos ($\sim$0.4) in the short and mid bands. If $\boldsymbol{g}$ parameters greater than 0.75 are considered, albedos above 0.9 are required in the short and mid bands, and no albedo is able to reproduce the data in the long band. This model class can then be entirely excluded for strongly forward-scattering grains.

If prior measurements of $\boldsymbol{g}$ are disregarded and isotropically scattering grains ($g = 0$) are considered, the best fit albedo values are 0.73 ± 0.05 at 971 Å, 0.68 ± 0.08 at 1090 Å, and 0.90 ± 0.05 at 1330 Å. Even for $g = 0$, the mid and short band albedos are significantly higher than previous albedo measurements.

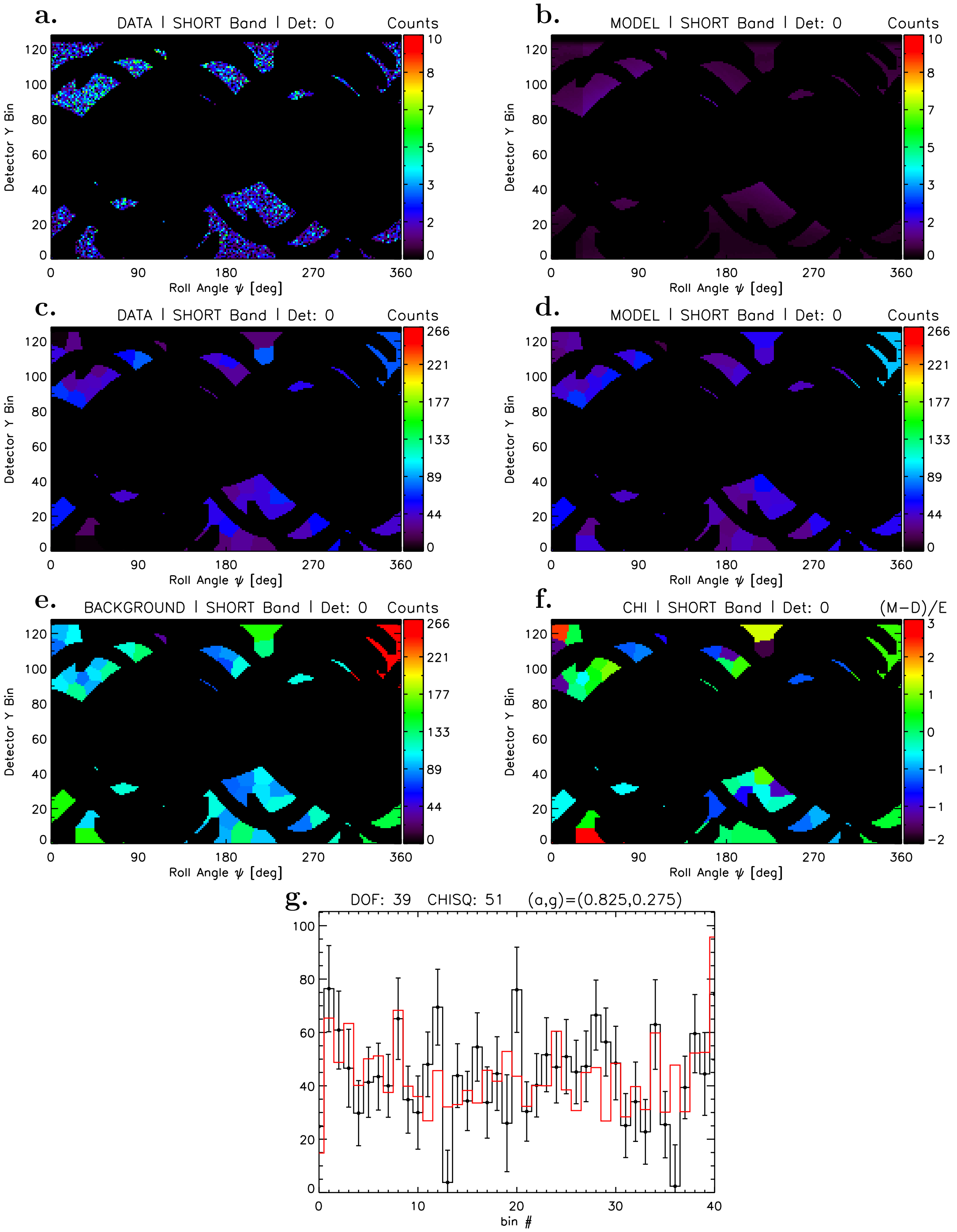

Figure 3.9: Best-fit, short-band, detector 0 model. **a.** Raw-data (unbinned). **b.** Best-fit model (unbinned). **c.** Background-subtracted data (binned). **d.** Best-fit model (binned). **e.** Background (binned). **f.** χ^2 elements (Data-Model)/Error. **g.** Binned count values for the data (*black*) and model (*red*). The degrees of freedom, non-reduced $\chi^2$and best-fit ($\boldsymbol{a}$,$\boldsymbol{g}$) values are shown along the top.

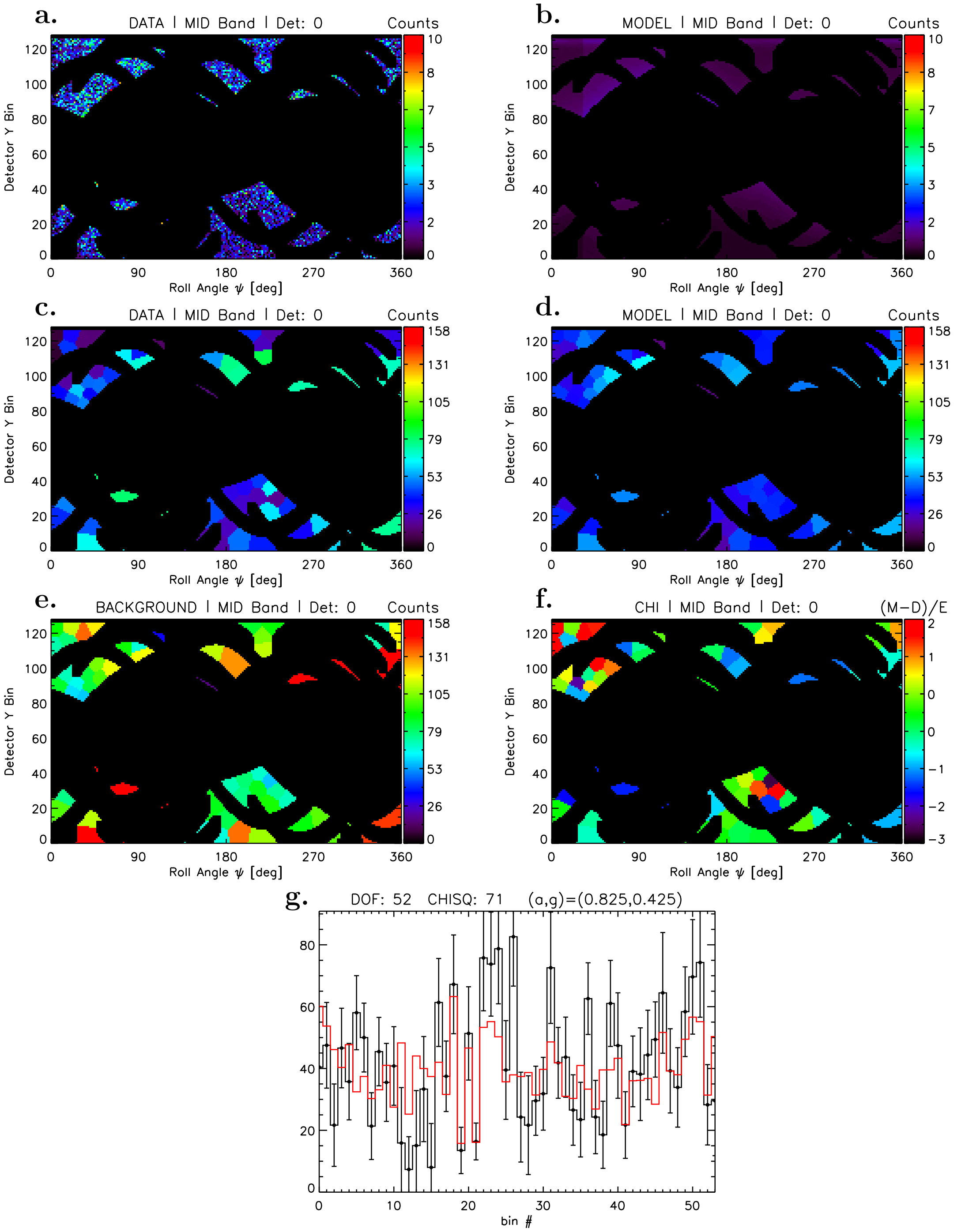

Figure 3.10: Best-fit, mid-band, detector 0 model. **a.** Raw-data (unbinned). **b.** Best-fit model (unbinned). **c.** Background-subtracted data (binned). **d.** Best-fit model (binned). **e.** Background (binned). **f.** χ^2 elements (Data-Model)/Error. **g.** Binned count values for the data (*black*) and model (*red*). The degrees of freedom, non-reduced $\chi^2$and best-fit ($\boldsymbol{a}$,$\boldsymbol{g}$) values are shown along the top.

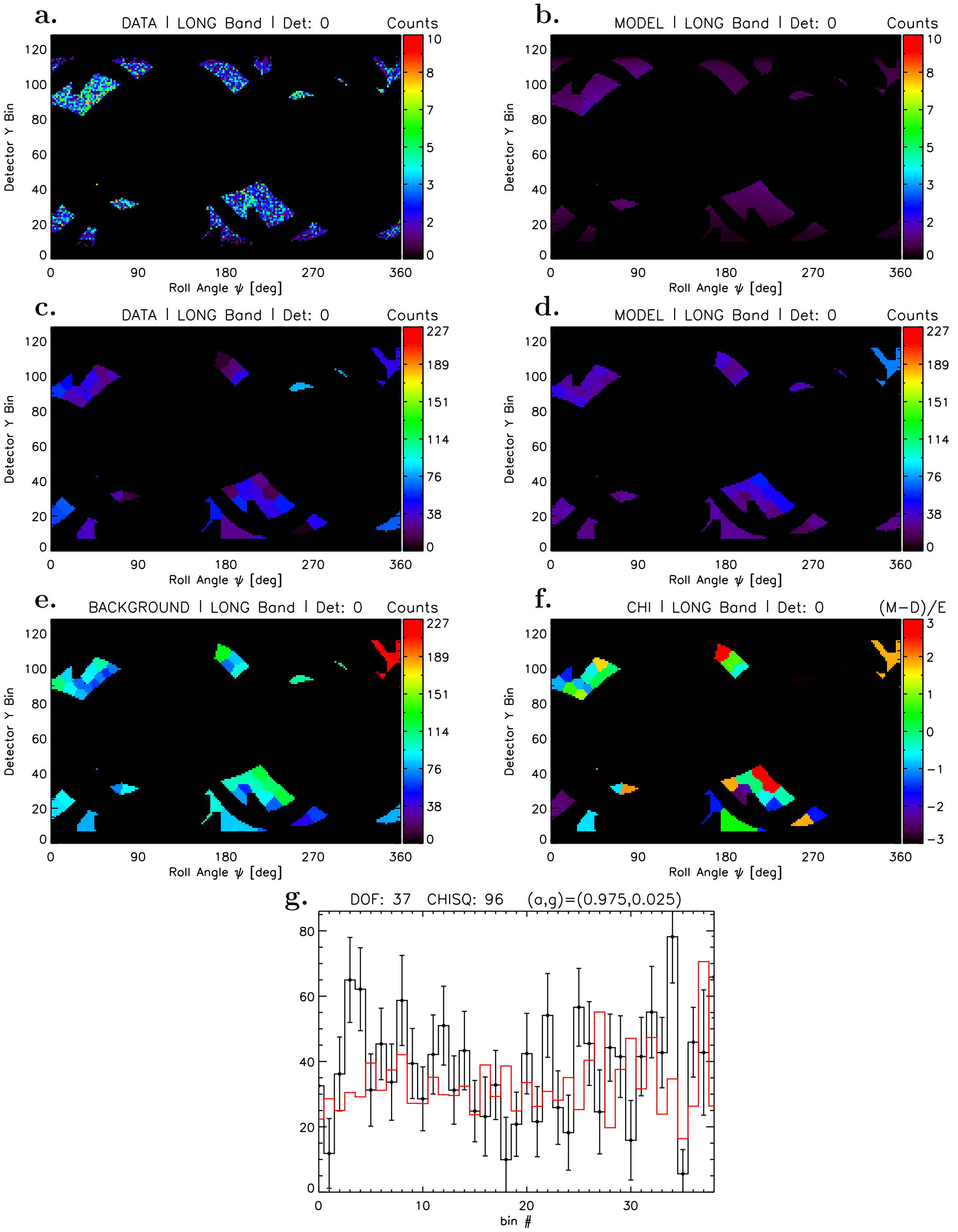

Figure 3.11: Best-fit, long-band, detector 0 model. **a.** Raw-data (unbinned). **b.** Best-fit model (unbinned). **c.** Background-subtracted data (binned). **d.** Best-fit model (binned). **e.** Background (binned). **f.** χ^2 elements (Data-Model)/Error. **g.** Binned count values for the data (*black*) and model (*red*). The degrees of freedom, non-reduced $\chi^2$and best-fit ($\boldsymbol{a}$,$\boldsymbol{g}$) values are shown along the top.

3.8.2 Background Dust Model 2

Model Description

In the previous model, each star was assigned its observed brightness. This choice carried the implicit assumption that the OMC receives approximately the same amount of FUV radiation from the star field as is received by an observer on Earth. To build the first limiting model, the question is asked: *what is the maximum amount of radiation that could reach the OMC from the foreground star field?* The amount of dust behind each star is unconstrained. To reach the limiting case, it is assumed that no dust sits between the stars and the OMC. The stars are now assigned their dereddened luminosity, which is calculated by multiplying each observed (reddened) brightness by e^{τ}, where τ is the optical depth of the star. As stated, Theta^1 Ori C is not dereddened. All other parameters from model 1 are preserved. The model geometry is presented in Figure 3.12.

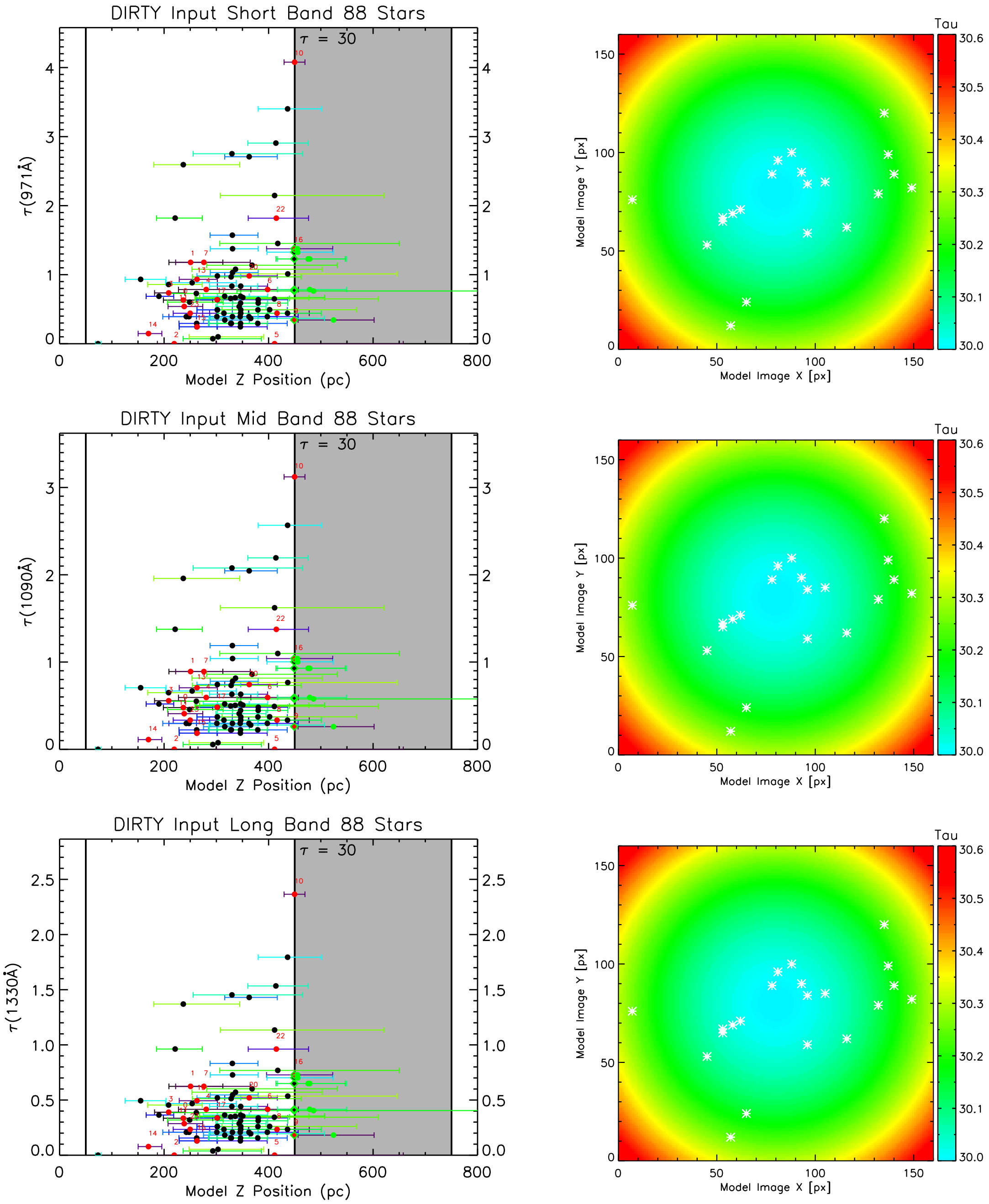

Figure 3.12: Background dust model 2. *Left:* Stellar distance vs. optical depth in each SPINR band. Black dots mark the position of each star in the model. Stars with measured spectra are shown in red. Green dots show the original position of stars that have been moved to a new position marked by a green diamond. *Right:* Optical depth maps of each dust distribution from the observer's point of view. The bright Orion stars are shown in white.

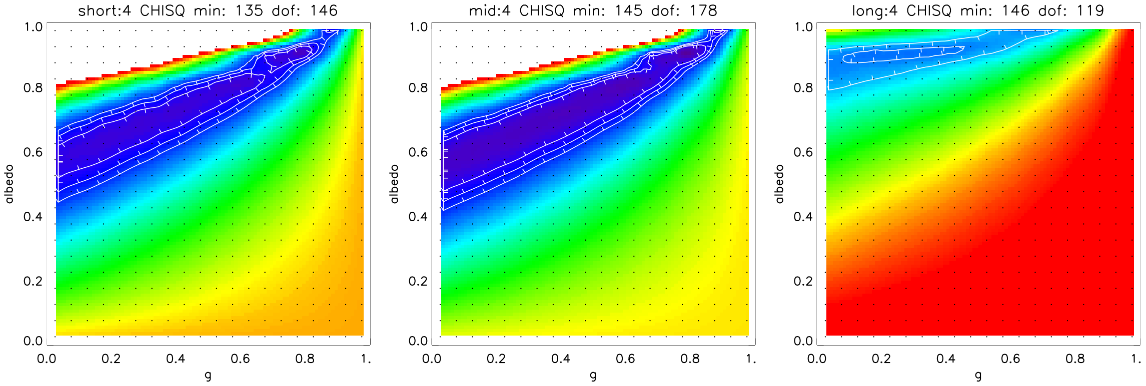

Figure 3.13: Background dust model 2: $(\boldsymbol{a},\boldsymbol{g})$ χ^2 confidence contours (68%, 95%, 99.7%). *Left:* Short band. *Middle:* Mid band. *Right:* Long band.

Model Results

The $\boldsymbol{a}$ and $\boldsymbol{g}$ results for background dust model 2 are shown in Figure 3.13. The best-fit model sinograms are compared to the data in Figures 3.14, 3.15 and 3.16.

The $(\boldsymbol{a},\boldsymbol{g})$ contours for this background-only model are very similar to those of the previous model. The allowed albedos have been slightly reduced due the additional starlight added to the model. Again, if previous $(\boldsymbol{a},\boldsymbol{g})$ measurements are considered, for $\boldsymbol{g}$ values greater than 0.75, only albedos > 0.8 are allowed for the short and mid bands and an albedo ~1 is required for the long band. This entire model class is also rejected in the highly forward-scattering limit.

As with the previous model, if prior measurements of $\boldsymbol{g}$ are disregarded and an isotropic value of $g = 0$ is considered, the best fit albedo values are 0.58 ± 0.05 at 971 Å, 0.55 ± 0.08 at 1090 Å, and 0.85 ± 0.05 at 1330 Å. These albedo values approach, but still exceed previous measurements.

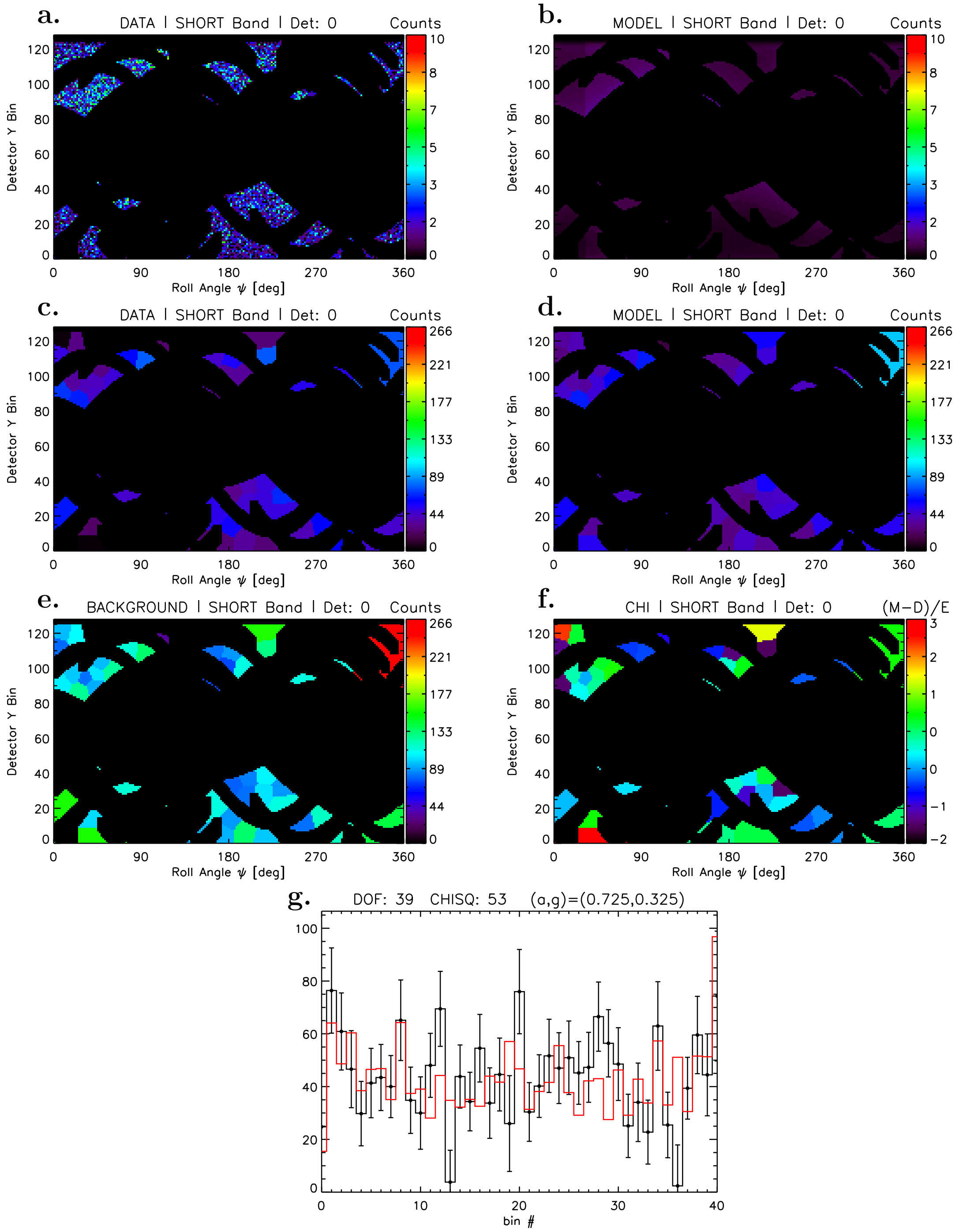

Figure 3.14: Best-fit, short-band, detector 0 model. **a.** Raw-data (unbinned). **b.** Best-fit model (unbinned). **c.** Background-subtracted data (binned). **d.** Best-fit model (binned). **e.** Background (binned). **f.** χ^2 elements (Data-Model)/Error. **g.** Binned count values for the data (*black*) and model (*red*). The degrees of freedom, non-reduced $\chi^2$and best-fit ($\boldsymbol{a}$,$\boldsymbol{g}$) values are shown along the top.

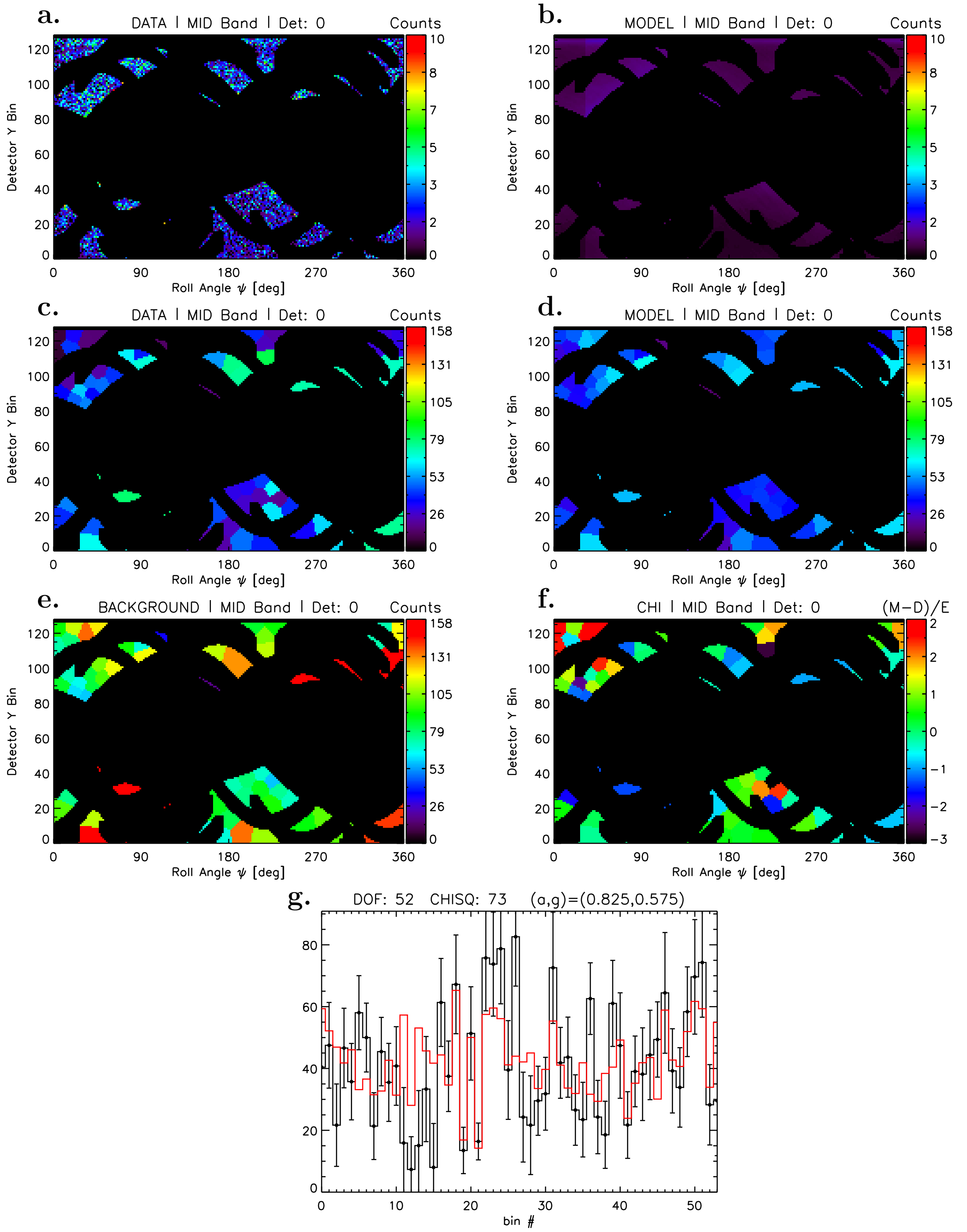

Figure 3.15: Best-fit, mid-band, detector 0 model. **a.** Raw-data (unbinned). **b.** Best-fit model (unbinned). **c.** Background-subtracted data (binned). **d.** Best-fit model (binned). **e.** Background (binned). **f.** χ^2 elements (Data-Model)/Error. **g.** Binned count values for the data (*black*) and model (*red*). The degrees of freedom, non-reduced $\chi^2$and best-fit ($\boldsymbol{a}$,$\boldsymbol{g}$) values are shown along the top.

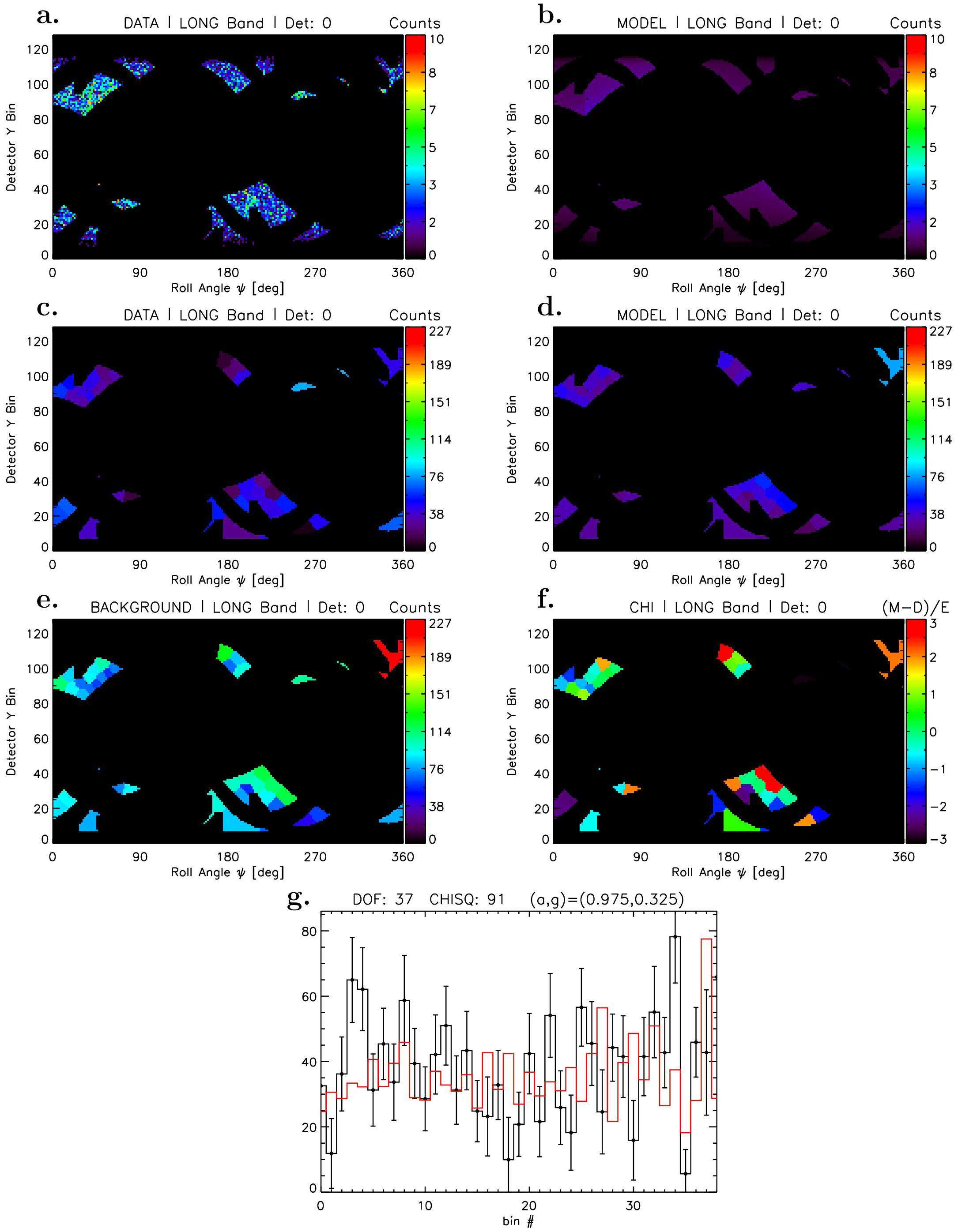

Figure 3.16: Best-fit, long-band, detector 0 model. **a.** Raw-data (unbinned). **b.** Best-fit model (unbinned). **c.** Background-subtracted data (binned). **d.** Best-fit model (binned). **e.** Background (binned). **f.** χ^2 elements (Data-Model)/Error. **g.** Binned count values for the data (*black*) and model (*red*). The degrees of freedom, non-reduced $\chi^2$and best-fit ($\boldsymbol{a}$,$\boldsymbol{g}$) values are shown along the top.

3.8.3 Background Dust Model 3

Model Description

Given that the two previous models are incapable of producing enough scattered light for forward-scattering dust grains, a final limiting model is constructed to produce the maximum amount of reflected light. This is accomplished by pushing the stars closer to the slab. Each star is placed as close as possible to the slab, but is forced to remain within the 1 σ uncertainty in its measured distance. Each star is assigned its dereddened luminosity.

One additional change is made to maximize the amount of reflected light. Some amount of scattered light is lost within the stellar mask. For a given mask diameter, a critical star-to-slab separation exists for which the maximum amount of light is reflected beyond the shadow of the stellar mask. Figure 3.17 plots this relation for a typical stellar mask diameter of 10 sinogram pixels or $\sim 1^\circ$. The critical separation for this mask size is 5 pc. In this model, no star is placed closer than 5 pc from the slab surface – including the Theta^1 Ori C object. The model geometry is presented in Figure 3.18.

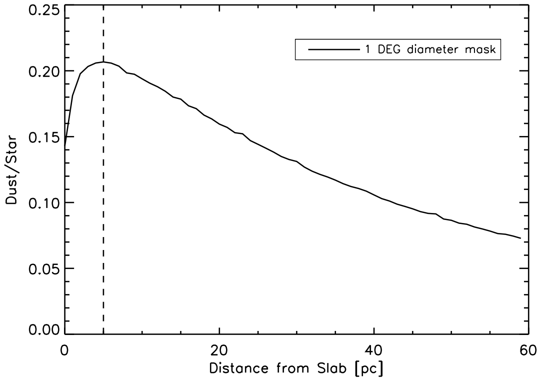

Figure 3.17: Reflected light measured outside a 1° stellar mask as a function of the distance between a star and the slab.

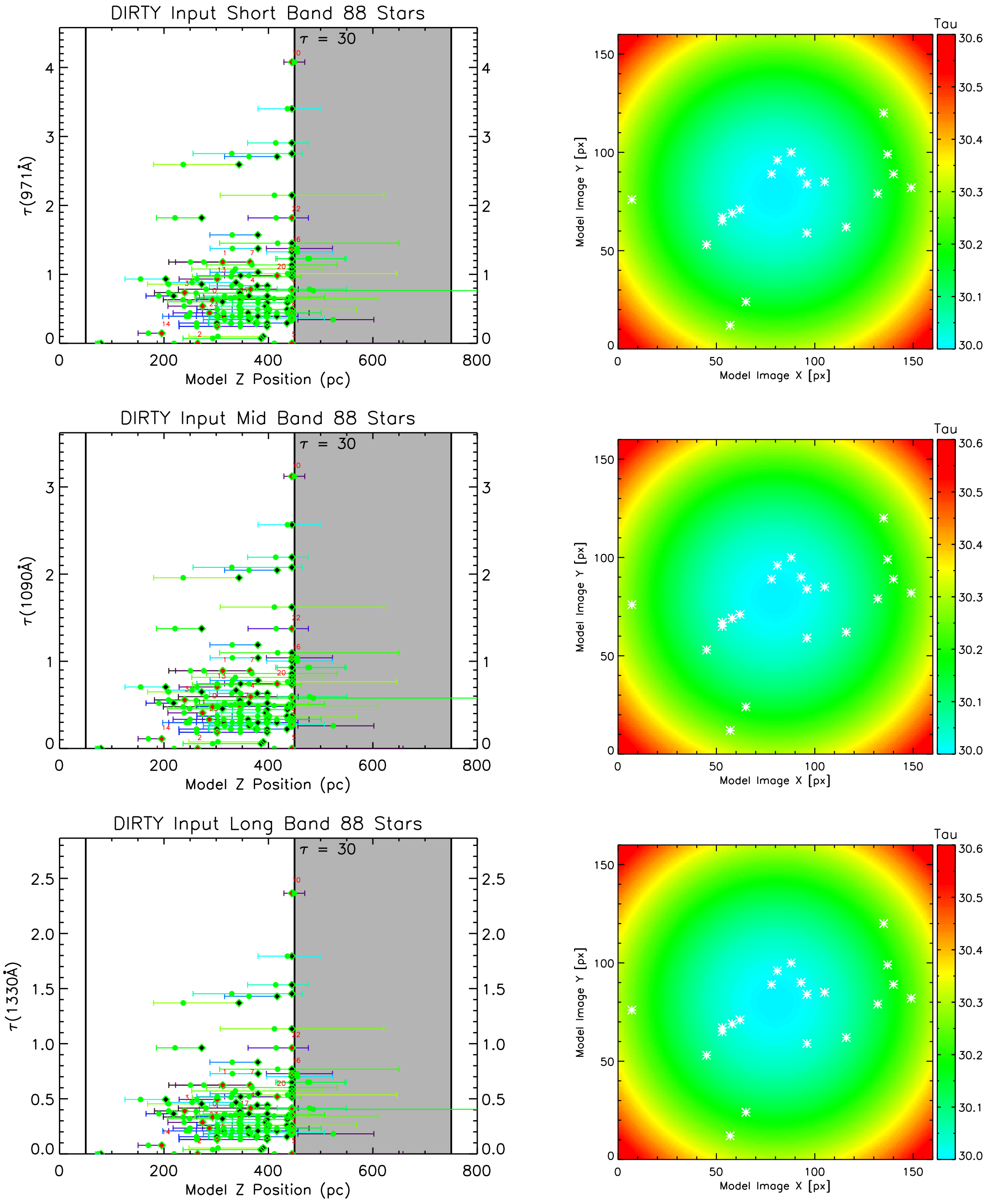

Figure 3.18: Background dust model 3. *Left:* Stellar distance vs. optical depth in each SPINR band. Black dots mark the position of each star in the model. Stars with measured spectra are shown in red. Green dots show the original position of stars that have been moved to a new position marked by a green diamond. *Right:* Optical depth maps of each dust distribution from the observer's point of view. The bright Orion stars are shown in white.

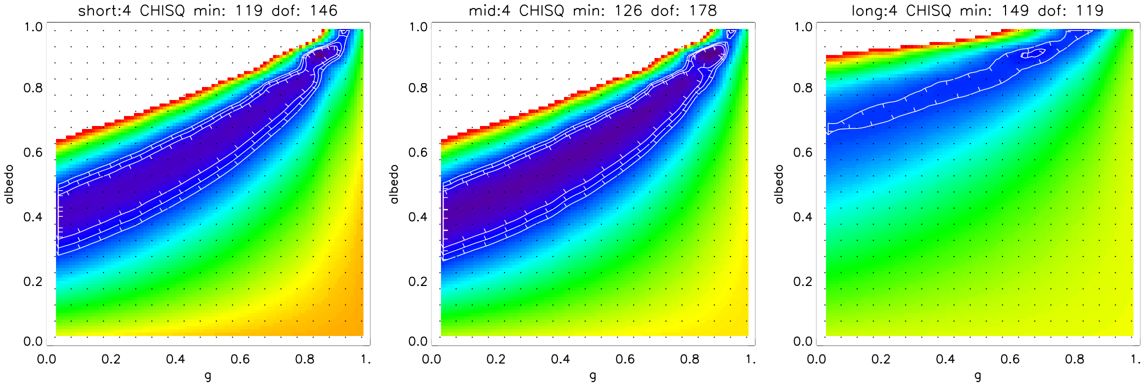

Figure 3.19: Background dust model 3: ($\boldsymbol{a}$,$\boldsymbol{g}$) χ^2 confidence contours (68%, 95%, 99.7%). *Left:* Short band. *Middle:* Mid band. *Right:* Long band.

Model Results

The $\boldsymbol{a}$ and $\boldsymbol{g}$ results for background dust model 3 are shown in Figure 3.19. The best-fit model sinograms are compared to the data in Figures 3.20, 3.21 and 3.22.

By pushing the stars closer to the slab, a stronger scattered light signal is produced. This allows the albedo values to continue to fall, however marginally. For this absolute limiting case model, and for $\boldsymbol{g}$ values greater than 0.75, only albedos ~0.7 are allowed for the short and mid bands and an albedo ~0.9 is required for the long band. This entire model class is also rejected in the highly forward-scattering limit and therefore, all background-only models are rejected. If the dust grains in Orion are highly forward-scattering, the background OMC cannot be responsible for producing all of the scattered light.

If, on the other hand, a value of $g = 0$ is considered, the best fit albedo values are 0.40 ± 0.08 at 971 Å, 0.40 ± 0.08 at 1090 Å, and 0.68 ± 0.02 at 1330 Å. These albedo values are consistent with previous measurements and cannot be statistically rejected by the data.

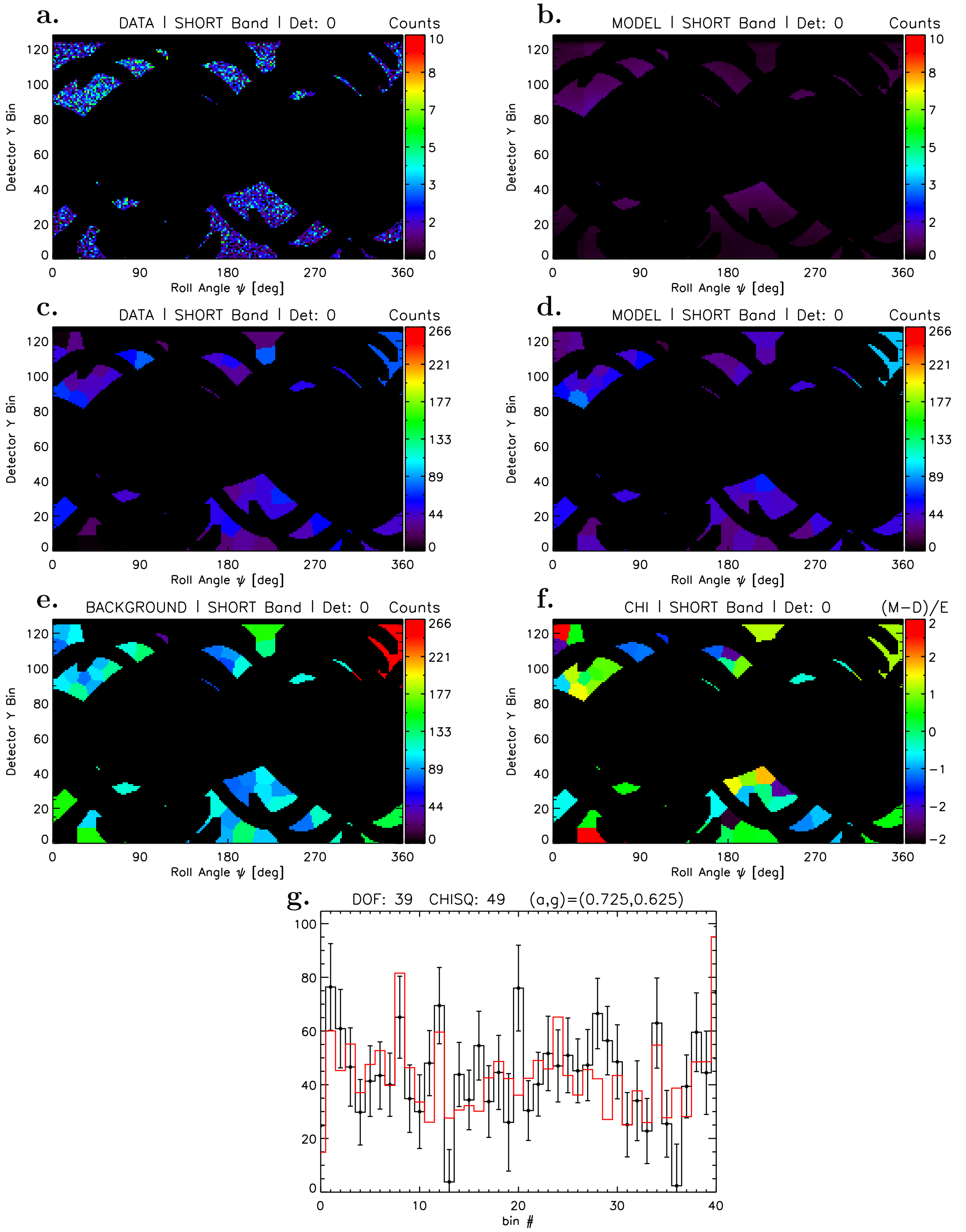

Figure 3.20: Best-fit, short-band, detector 0 model. **a.** Raw-data (unbinned). **b.** Best-fit model (unbinned). **c.** Background-subtracted data (binned). **d.** Best-fit model (binned). **e.** Background (binned). **f.** χ^2 elements (Data-Model)/Error. **g.** Binned count values for the data (*black*) and model (*red*). The degrees of freedom, non-reduced $\chi^2$and best-fit ($\boldsymbol{a}$,$\boldsymbol{g}$) values are shown along the top.

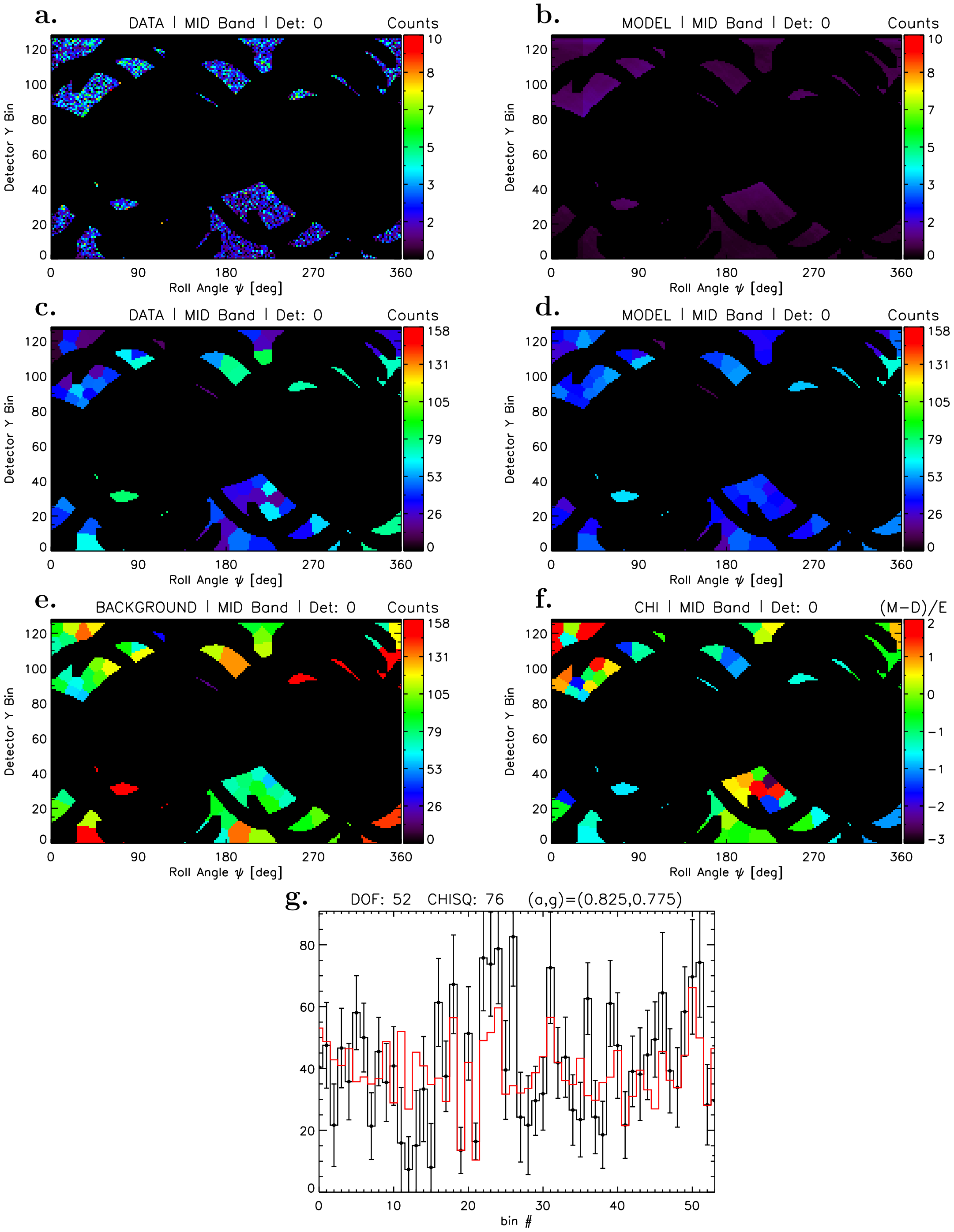

Figure 3.21: Best-fit, mid-band, detector 0 model. **a.** Raw-data (unbinned). **b.** Best-fit model (unbinned). **c.** Background-subtracted data (binned). **d.** Best-fit model (binned). **e.** Background (binned). **f.** χ^2 elements (Data-Model)/Error. **g.** Binned count values for the data (*black*) and model (*red*). The degrees of freedom, non-reduced $\chi^2$and best-fit ($\boldsymbol{a}$,$\boldsymbol{g}$) values are shown along the top.

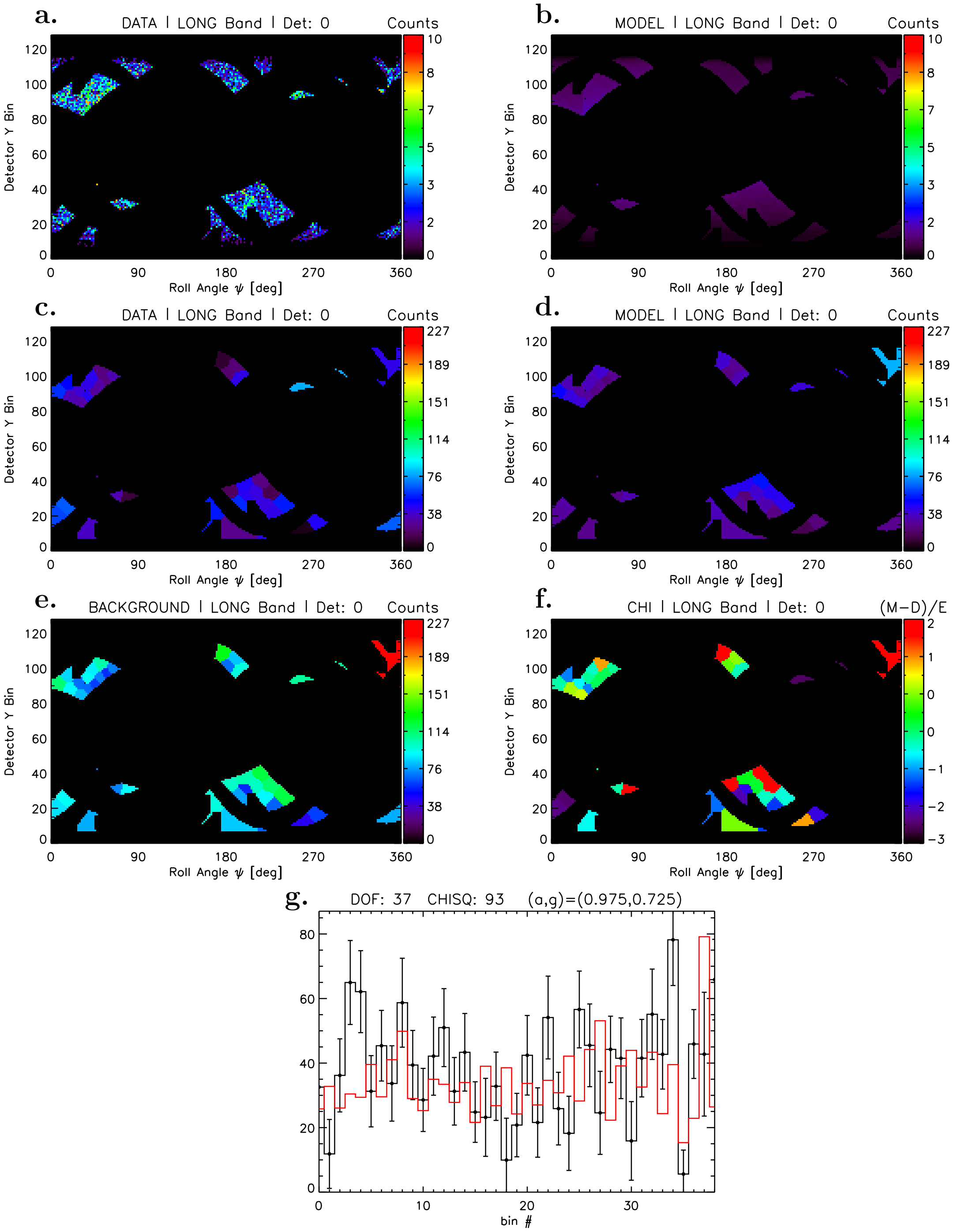

Figure 3.22: Best-fit, long-band, detector 0 model. **a.** Raw-data (unbinned). **b.** Best-fit model (unbinned). **c.** Background-subtracted data (binned). **d.** Best-fit model (binned). **e.** Background (binned). **f.** χ^2 elements (Data-Model)/Error. **g.** Binned count values for the data (*black*) and model (*red*). The degrees of freedom, non-reduced $\chi^2$and best-fit ($\boldsymbol{a}$,$\boldsymbol{g}$) values are shown along the top.

3.8.4 Foreground Dust Model

Model Description

This model consists of foreground dust only. The dust distribution is created using the iterative routine outlined in Section 3.7.4. The optical depth of Theta^1 Ori C is not used to constrain the foreground dust distribution. Upon completion of the model grid, the Theta^1 Ori C object is placed at its normal position and is dereddened only by the optical depth calculated through the foreground distribution along its line of sight. The model geometry is presented in Figure 3.23.

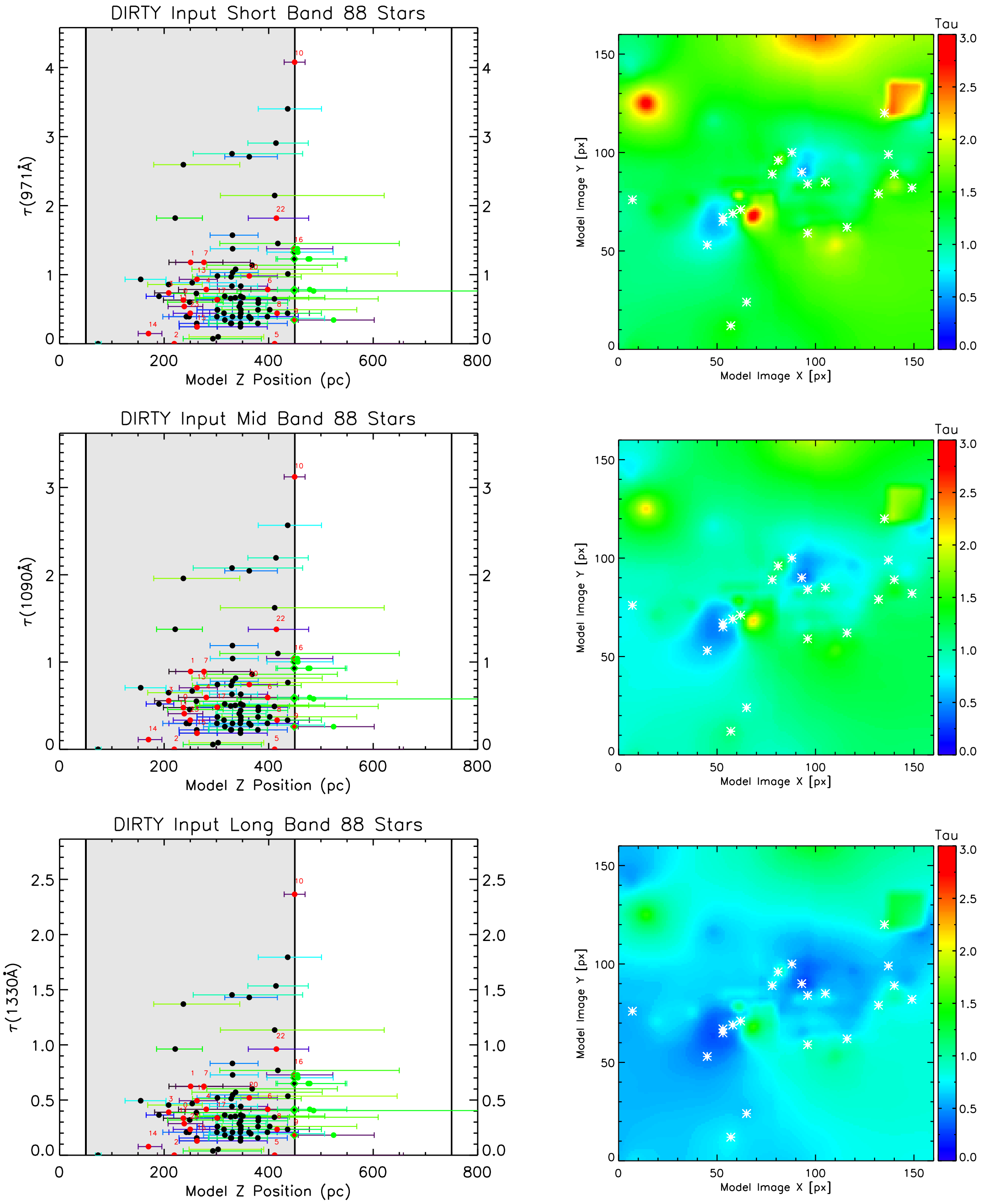

Figure 3.23: Foreground dust model. *Left:* Stellar distance vs. optical depth in each SPINR band. Black dots mark the position of each star in the model. Stars with measured spectra are shown in red. Green dots show the original position of stars that have been moved to a new position marked by a green diamond. *Right:* Optical depth maps of each dust distribution from the observer's point of view. The bright Orion stars are shown in white.

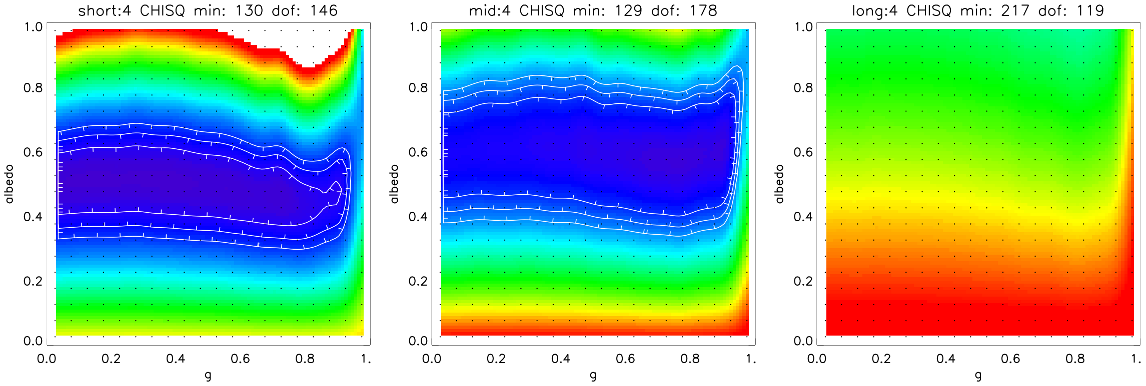

Figure 3.24: Foreground dust model: ($\boldsymbol{a}$,$\boldsymbol{g}$) χ^2 confidence contours (68%, 95%, 99.7%). *Left:* Short band. *Middle:* Mid band. *Right:* Long band.

Model Results

The $\boldsymbol{a}$ and $\boldsymbol{g}$ results for the foreground dust model are shown Figure 3.24. The best-fit model sinograms are compared to the data in Figures 3.25, 3.26 and 3.27.

This model shows little sensitivity to the $\boldsymbol{g}$ parameter in the short and mid bands. This is attributed to multiple scattering within the foreground dust distribution. When photons are multiply scattered, the scattered light distribution becomes more and more diffuse and the angular information carried by the photons is lost.

This foreground-only model allows for lower ($\boldsymbol{a}$,$\boldsymbol{g}$) values in the short and mid bands at all $\boldsymbol{g}$ values; however, the long-band model is statistically rejected. As can be seen in Figure 3.23, the projected optical depth through the long-band model is <1 for most sightlines. The stellar optical depths in the long band are, on average, a factor of two smaller than in the short band. This is simply due to the increased extinction efficiency at shorter wavelengths. The reduced optical depth of dust in the long-band model cannot produce enough scattered light. This model must then be rejected as a whole for its inability to reproduce the long-band data.

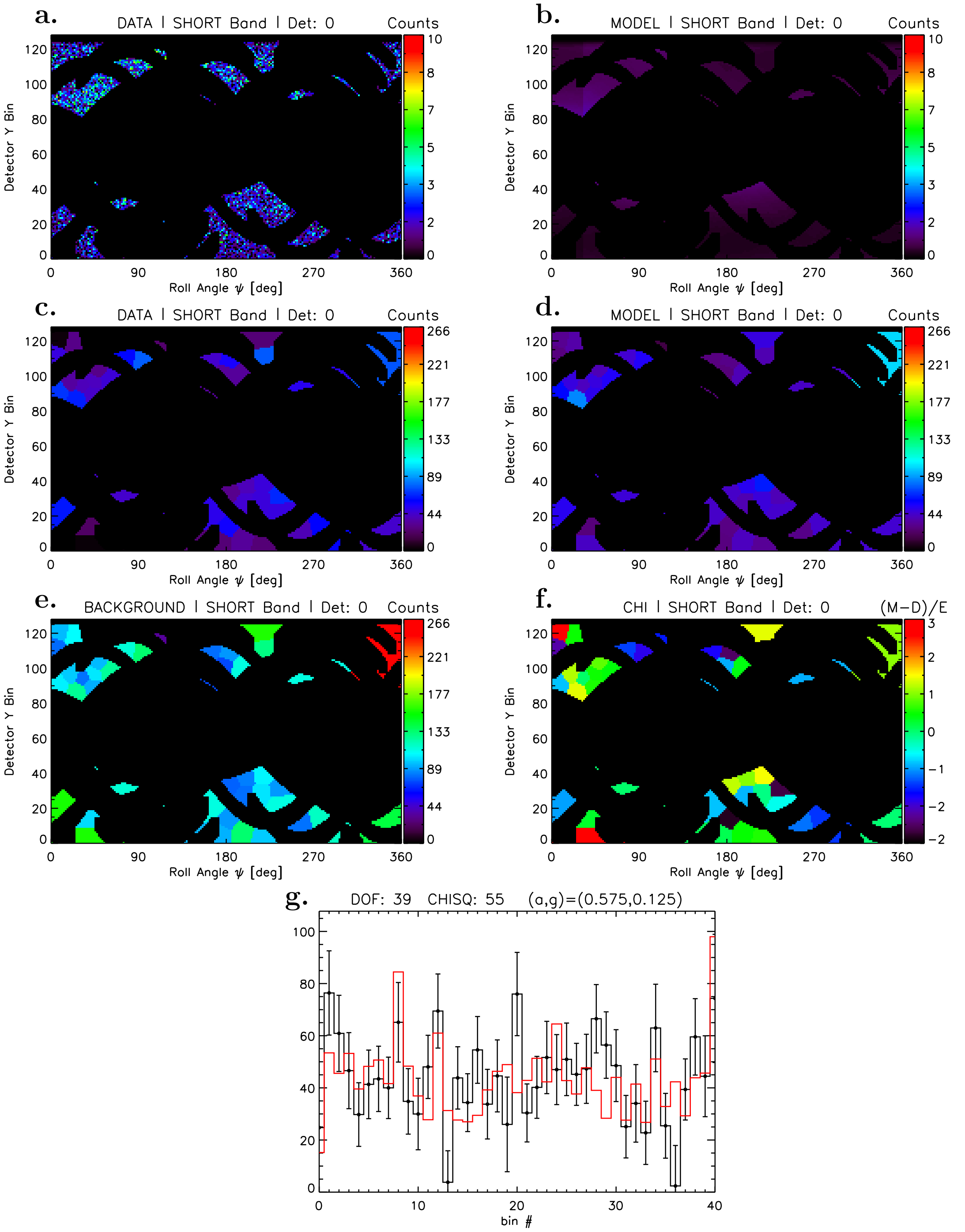

Figure 3.25: Best-fit, short-band, detector 0 model. **a.** Raw-data (unbinned). **b.** Best-fit model (unbinned). **c.** Background-subtracted data (binned). **d.** Best-fit model (binned). **e.** Background (binned). **f.** χ^2 elements (Data-Model)/Error. **g.** Binned count values for the data (*black*) and model (*red*). The degrees of freedom, non-reduced $\chi^2$and best-fit ($\boldsymbol{a}$,$\boldsymbol{g}$) values are shown along the top.

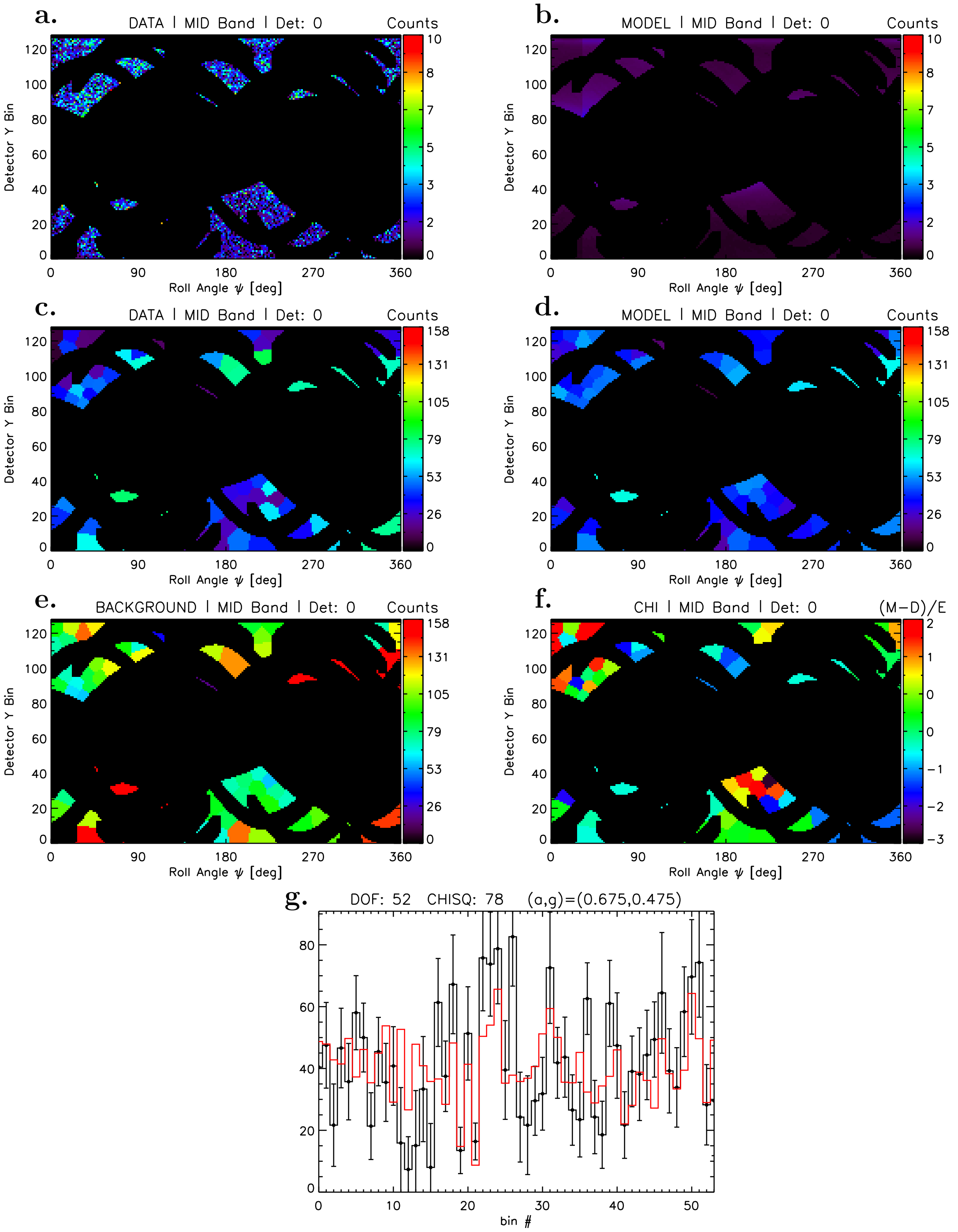

Figure 3.26: Best-fit, mid-band, detector 0 model. **a.** Raw-data (unbinned). **b.** Best-fit model (unbinned). **c.** Background-subtracted data (binned). **d.** Best-fit model (binned). **e.** Background (binned). **f.** χ^2 elements (Data-Model)/Error. **g.** Binned count values for the data (*black*) and model (*red*). The degrees of freedom, non-reduced $\chi^2$and best-fit (***a***,***g***) values are shown along the top.

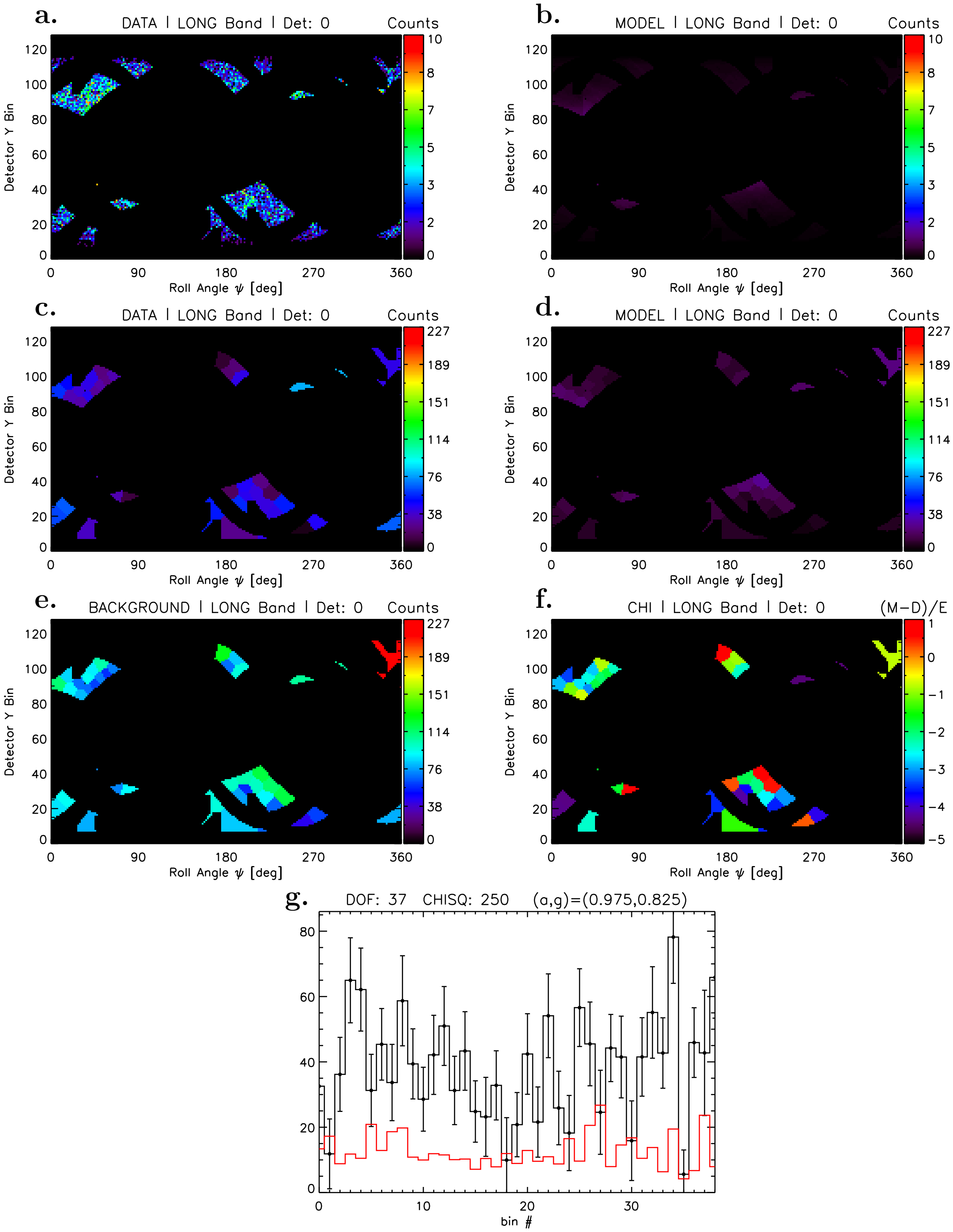

Figure 3.27: Best-fit, long-band, detector 0 model. **a.** Raw-data (unbinned). **b.** Best-fit model (unbinned). **c.** Background-subtracted data (binned). **d.** Best-fit model (binned). **e.** Background (binned). **f.** χ^2 elements (Data-Model)/Error. **g.** Binned count values for the data (*black*) and model (*red*). The degrees of freedom, non-reduced $\chi^2$and best-fit ($\boldsymbol{a}$,$\boldsymbol{g}$) values are shown along the top.

3.8.5 Hybrid Dust Model

Model Description

The final Orion model is a hybrid model consisting of both foreground and background dust. This is the most realistic dust distribution tested here. To the previous foreground-only model, the same $\tau = 30$ slab from the background-only models is added. All other model parameters are left unchanged. The model geometry is presented in Figure 3.28.

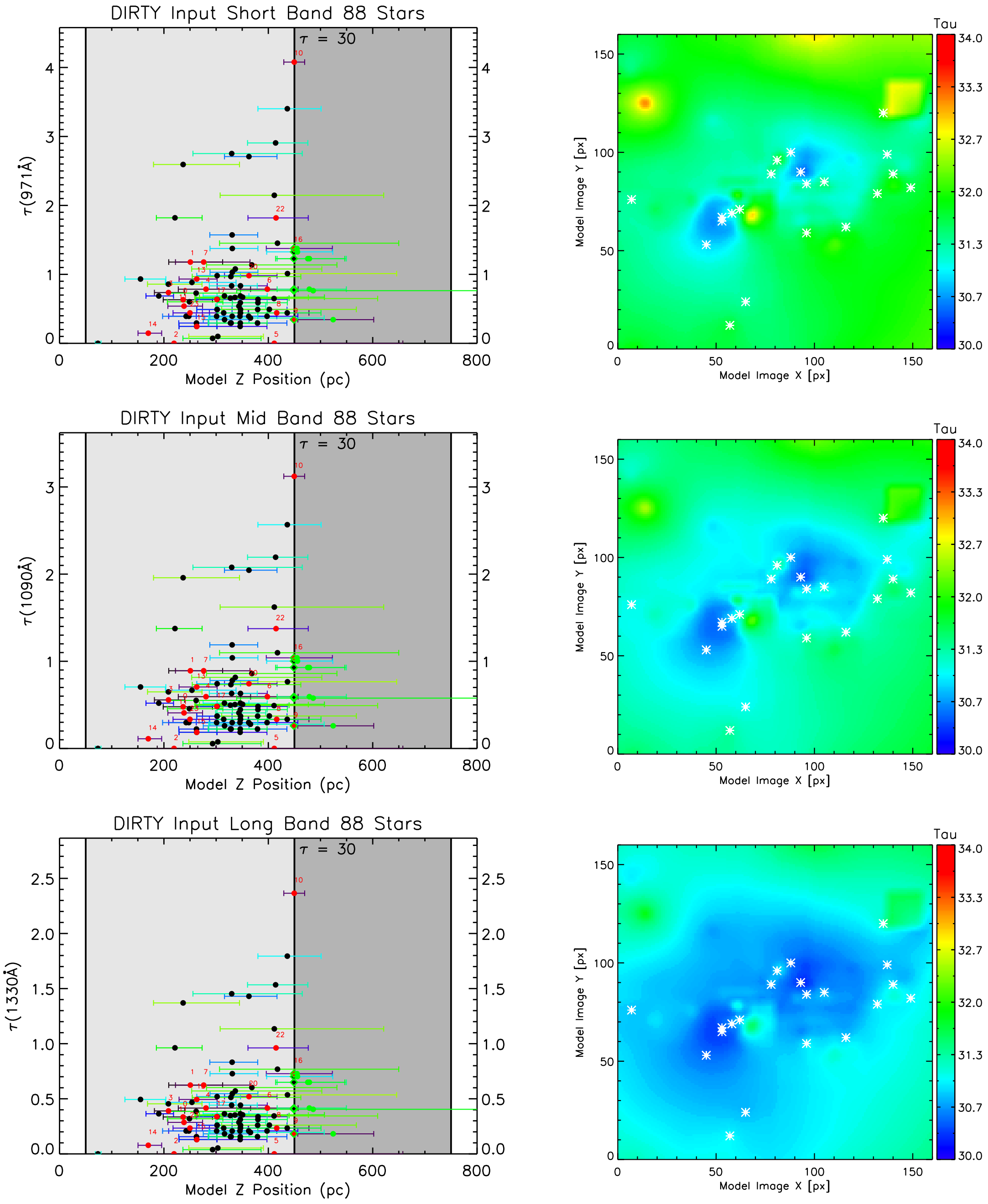

Figure 3.28: Hybrid dust model. *Left:* Stellar distance vs. optical depth in each SPINR band. Black dots mark the position of each star in the model. Stars with measured spectra are shown in red. Green dots show the original position of stars that have been moved to a new position marked by a green diamond. *Right:* Optical depth maps of each dust distribution from the observer's point of view. The bright Orion stars are shown in white.

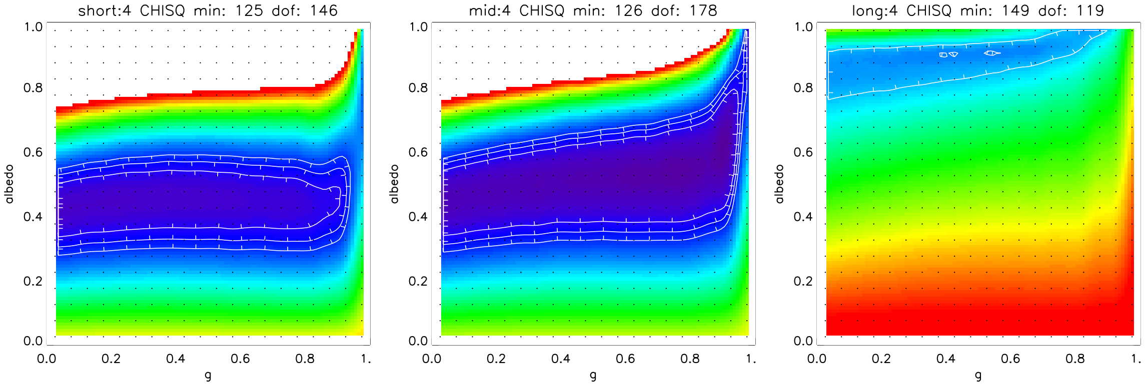

Figure 3.29: Hybrid dust model: ($\boldsymbol{a}$,$\boldsymbol{g}$) χ^2 confidence contours (68%, 95%, 99.7%). *Left:* Short band. *Middle:* Mid band. *Right:* Long band.

Model Results

The $\boldsymbol{a}$ and $\boldsymbol{g}$ results for the hybrid model are shown in Figure 3.29. The best-fit model sinograms are compared to the data in Figures 3.30, 3.31 and 3.32.

This hybrid model is capable of reproducing the data in all three SPINR bands. The model retains the low-$\boldsymbol{g}$ dependence of the foreground-only model, which allows for low albedos and highly forward-scattering grains in the short and mid bands. The ($\boldsymbol{a}$,$\boldsymbol{g}$) contours overlap well with those of the foreground-only model. In the long band, backscatter from the slab adds enough additional scattered light to match the data.

The hybrid model is by no means unique. It is, however, the most realistic model constructed here. Assuming a value of $g = 0.75$, the model is capable of reproducing the data with albedo values of 0.45 ± 0.08 at 971 Å, 0.53 ± 0.15 at 1090 Å, and 0.93 ± 0.05 at 1330 Å. These albedos change only slightly with varying $\boldsymbol{g}$.

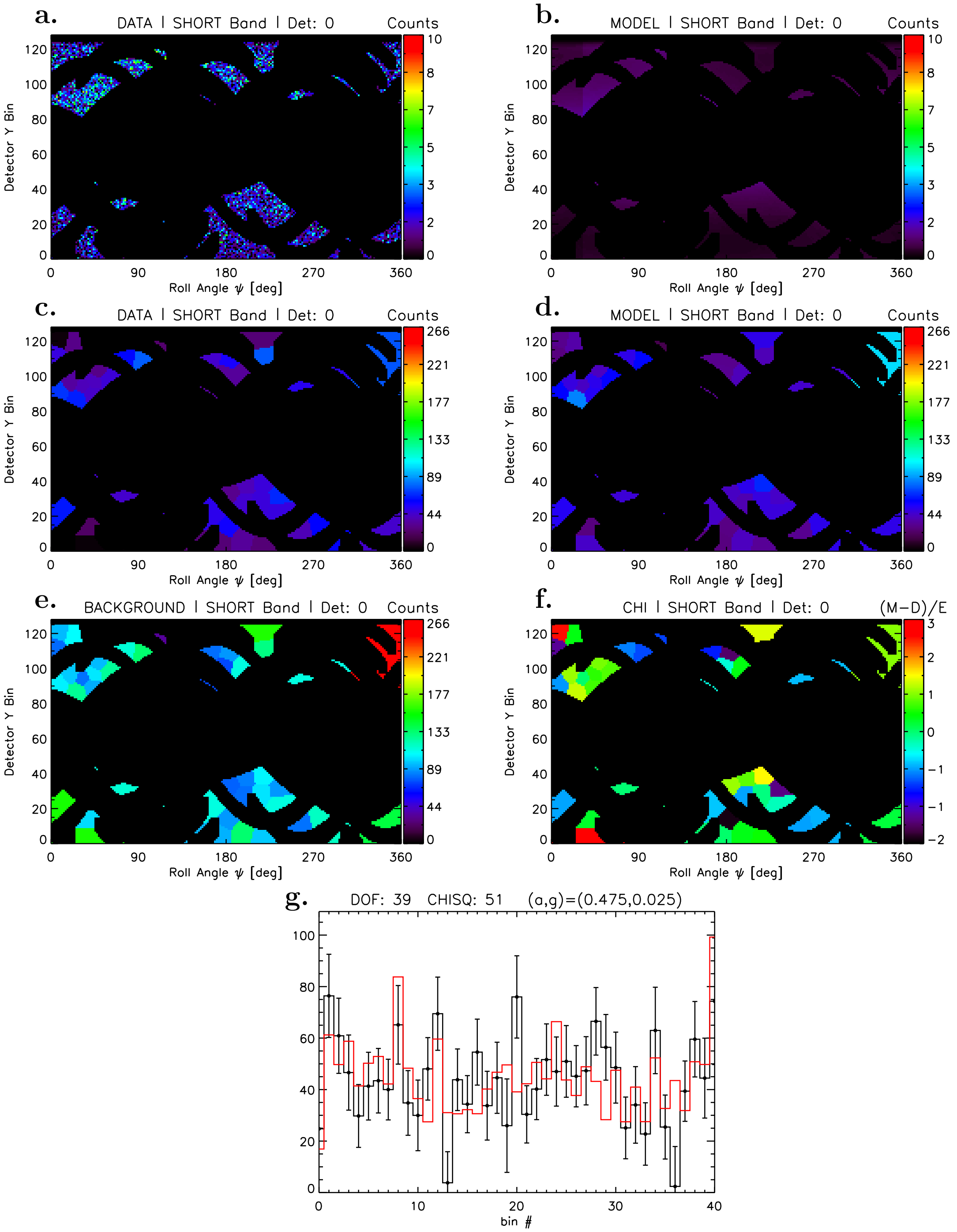

Figure 3.30: Best-fit, short-band, detector 0 model. **a.** Raw-data (unbinned). **b.** Best-fit model (unbinned). **c.** Background-subtracted data (binned). **d.** Best-fit model (binned). **e.** Background (binned). **f.** χ^2 elements (Data-Model)/Error. **g.** Binned count values for the data (*black*) and model (*red*). The degrees of freedom, non-reduced $\chi^2$and best-fit ($\boldsymbol{a}$,$\boldsymbol{g}$) values are shown along the top.

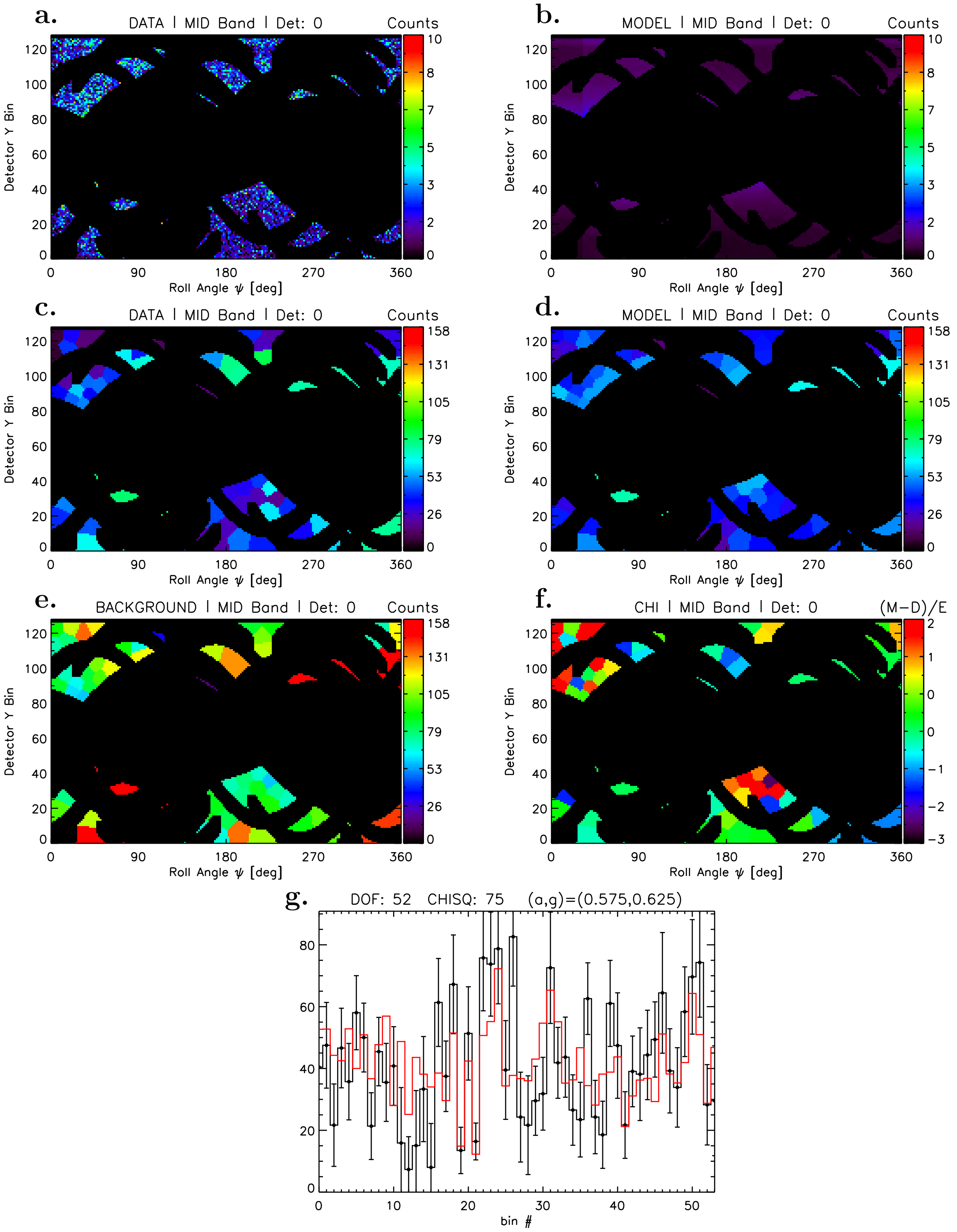

Figure 3.31: Best-fit, mid-band, detector 0 model. **a.** Raw-data (unbinned). **b.** Best-fit model (unbinned). **c.** Background-subtracted data (binned). **d.** Best-fit model (binned). **e.** Background (binned). **f.** χ^2 elements (Data-Model)/Error. **g.** Binned count values for the data (*black*) and model (*red*). The degrees of freedom, non-reduced $\chi^2$and best-fit ($\boldsymbol{a}$,$\boldsymbol{g}$) values are shown along the top.

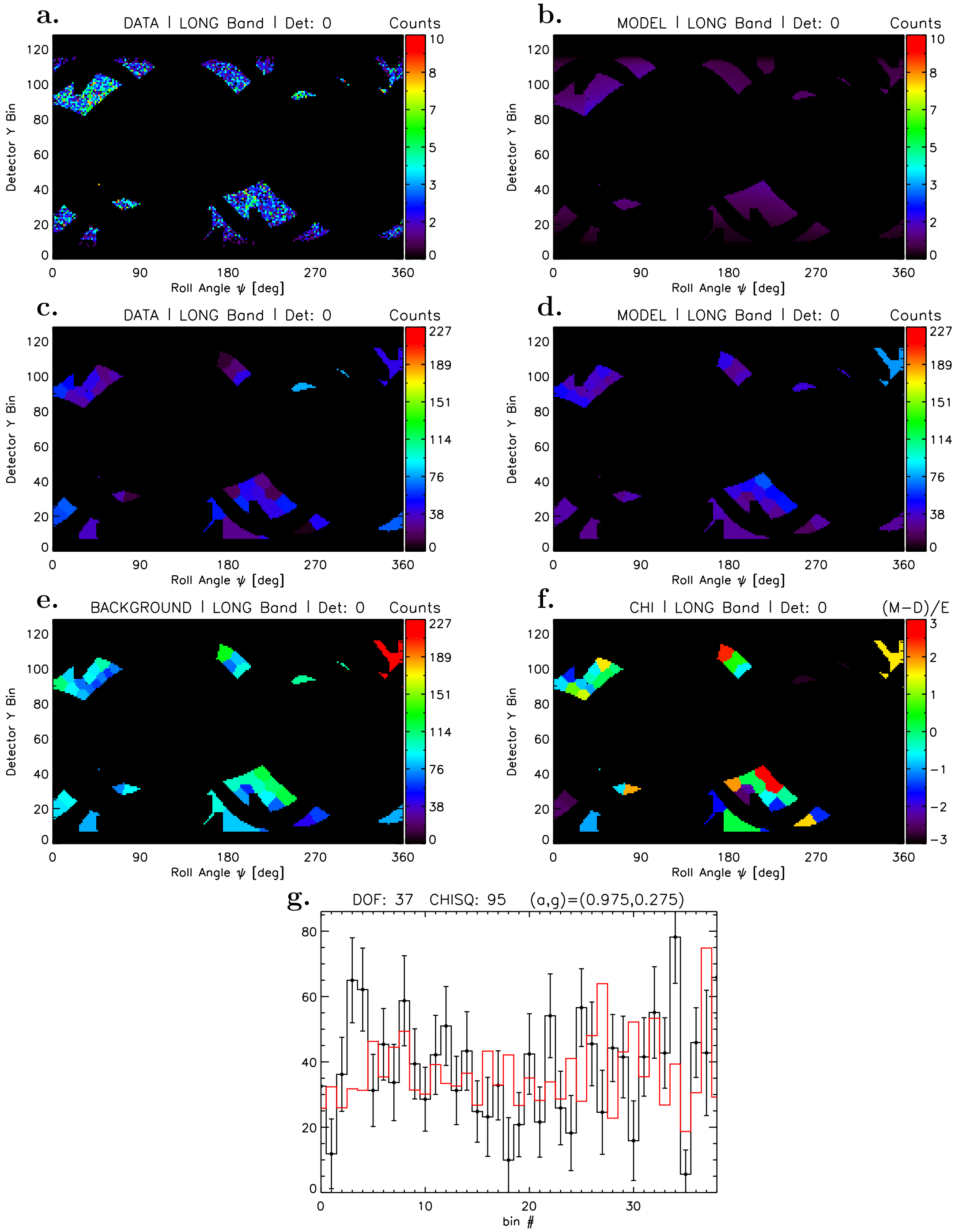

Figure 3.32: Best-fit, long-band, detector 0 model. **a.** Raw-data (unbinned). **b.** Best-fit model (unbinned). **c.** Background-subtracted data (binned). **d.** Best-fit model (binned). **e.** Background (binned). **f.** χ^2 elements (Data-Model)/Error. **g.** Binned count values for the data (*black*) and model (*red*). The degrees of freedom, non-reduced $\chi^2$and best-fit ($\boldsymbol{a}$,$\boldsymbol{g}$) values are shown along the top.

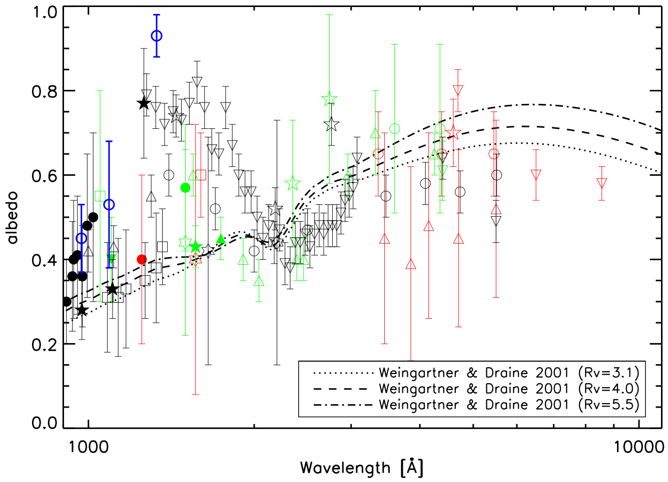

Figure 3.33: Previous measurements of grain albedo are plotted against the grain model predictions of Weingartner & Draine (2001). For data sources, see Table 1.1. The allowed albedo values from the hybrid model are overplotted as blue circles.

3.9 Discussion of Results

3.9.1 Albedo Measurements

The best-fit albedo values for the hybrid model with $g = 0.75$ are 0.45 ± 0.08 at 971 Å, 0.53 ± 0.15 at 1090 Å, and 0.93 ± 0.05 at 1330 Å. These values are plotted in Figure 3.33 along with the previous measurements discussed in Section 1.1.3. The data sources are listed in Table 1.1. The hybrid model values are 15-30% larger than previous measurements at similar wavelengths. However, given the uncertainty and scatter in the measurements, these values are not inconsistent with previous measurements. In the long-band, the measured albedo is the least consistent with previous measurements.

Much of the data-point scatter observed in Figure 3.33 is likely due to real differences in the dust populations for each sightline. The SPINR albedo measurements towards Orion agree well in the short and mid bands with the previous measurements of Shalima et al. (2006), which were taken near the Orion Nebula.

The previously observed rise in albedo near 1300-1500 Å is reproduced by the SPINR measurements. This rise is not explained by the grain models of Weingartner & Draine (2001). The observed increase in the dust reflectivity at 1330 Å is a more robust and model-independent result than the albedo measurements themselves. A sharp increase in the ratio of dust surface brightness to stellar flux is seen directly in the long-band data. These ratios are listed in Table 3.1. A factor of ∼3 increase is seen in the relative dust brightness from the short band to the long band.

The measured increase in nebular brightness in the SPINR long band is attributed here to a rise in the grain albedo at these longer wavelengths. An attempt has been made to remove all background sources that are not the result of dust scattering. If the increased brightness is the result of an emission process other than dust scattering, this process must produce broadband continuum emission in the FUV. Any additional spectral feature in the long band would have been identified in the nebular spectrum.

3.9.2 Dust Distribution

The results from the limiting background-only model suggest that a background slab alone cannot produce the observed scattered light distribution. This conclusion is based upon the assumption that the grains are highly forward scattering, $g \sim 0.75$. This assumption is supported by many previous measurements and grain models. Backscatter from isotropically scattering grains with $g = 0$ cannot, however, be statistically ruled out.

If the hybrid model is a good representation of reality, it implies that the foreground dust, which is responsible for reddening the Orion stars, contributes significantly to the scattered light distribution in the short and mid bands (971 Å, 1090 Å). The results for these two bands are very weakly dependent on the existence of a background slab. In the long band (1330 Å), the background slab is required to reproduce the data. This reality would imply that observations of Orion at shorter FUV wavelengths do not see through to the background molecular cloud; the foreground dust dominates in this spectral range. Only at longer wavelengths does the foreground dust become transparent revealing the molecular cloud.

To confirm this result, the next step would be to compare the observed morphology of scattered light in the SPINR measurements with previous wide-field observations at infrared wavelengths where the molecular cloud is visible. If the hybrid model does represent reality, one might expect the infrared morphology to correlate well with the long-band data and poorly with the short and mid bands.

3.10 Summary

A number of dust distribution models have been examined in this chapter. Models that include only the background dust of the OMC exhibit a strong linear relationship between $\boldsymbol{a}$ and $\boldsymbol{g}$. These models demand extremely high albedos > 0.7 to match the SPINR data in the mid and short bands. This is true even in the most limiting case where the amount of FUV radiation incident on the cloud is likely over-exaggerated. These models can comply only with previous measurements of low albedo *or* high $\boldsymbol{g}$, but not both simultaneously. The background OMC cannot alone produce the scattered light distribution observed in the short and mid bands.

The most realistic model tested here is a hybrid model consisting of both foreground dust and a background slab. The foreground dust distribution is constrained by the physical distance and optical depth to each star. This model exhibits little correlation between $\boldsymbol{a}$ and $\boldsymbol{g}$. The allowed albedo values are consistent with previous measurements in all three SPINR bands and are especially similar to albedo measurements near the Orion Nebula (Shalima et al. 2006).

Chapter 4

PICTURE: Experiment and Payload

4.1 Science Goals and Instrument Requirements

The primary science objective of the Planetary Imaging Concept Testbed Using a Rocket Experiment (PICTURE) mission was to obtain a direct, visible-light image of exozodiacal dust around the nearby sun-like star ϵ Eridani (K2V, 3.22 pc). Exozodiacal dust is the continually replenished population of dust grains that form due to asteroid and planetesimal collisions and shedding comets in the inner 50 AU of stellar systems. PICTURE sought a direct image of visible starlight reflecting off of these dust grains. The formation processes of exozodiacal dust are discussed in greater detail in Chapter 1.

4.1.1 The Problem: Diffraction

The most fundamental challenge associated with directly imaging exozodiacal dust or extrasolar planets in the interior of their host systems derives from the fact that the angular resolution of a telescope is limited by optical diffraction. Just as the angular resolution of a radio interferometer is limited by the longest baseline between any two dishes, the angular resolution of a single telescope is limited by the longest baseline that can be drawn between any two points on the surface of the primary mirror. This is, by definition, the diameter of the mirror. The diffraction-limited angular resolution of a telescope is $\sim \lambda/D$, where λ is the wavelength of light and D is the diameter of the telescope.

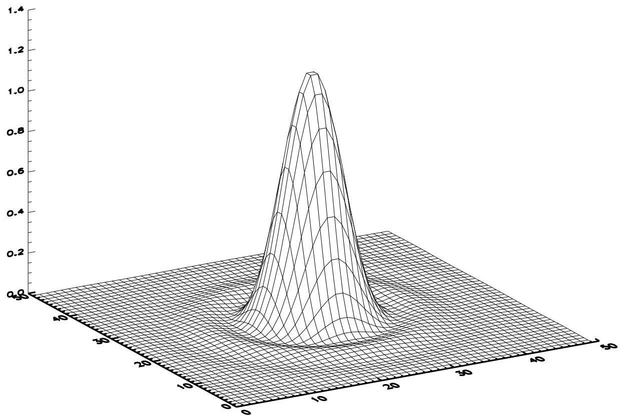

Figure 4.1: The Airy Function is the idealized PSF for a circular aperture telescope.

The vast majority of stars can not be resolved by the largest ground-based or space-based telescopes. If the Sun were placed at a distance of 10 pc, it would subtend ∼1 milliarcsecond (mas) on the sky. To resolve this stellar disk in the visible would require a telescope many hundreds of meters in diameter. Instead of producing a sharp image of a stellar disk, a diffraction limited telescope spreads the light from a star over a much larger area on the detector. The shape of this distribution, the point spread function (PSF) of the telescope, can be found by computing the two-dimensional Fourier transform of the aperture response. For an idealized circular aperture with no obscuration from the secondary mirror or its support structure, the PSF takes the form of the Airy function (Figure 4.1). The angular radius of the Airy spot, the distance between the peak and the first minimum, is $\sim 1.22\lambda/D$. This is the angular resolution of the telescope.

Figure 4.2 illustrates the problem imposed by optical diffraction when attempting to directly image an extrasolar planet next to an extremely bright star. As an example, we choose a planet that is a factor of 10^{-7} times dimmer than its host star

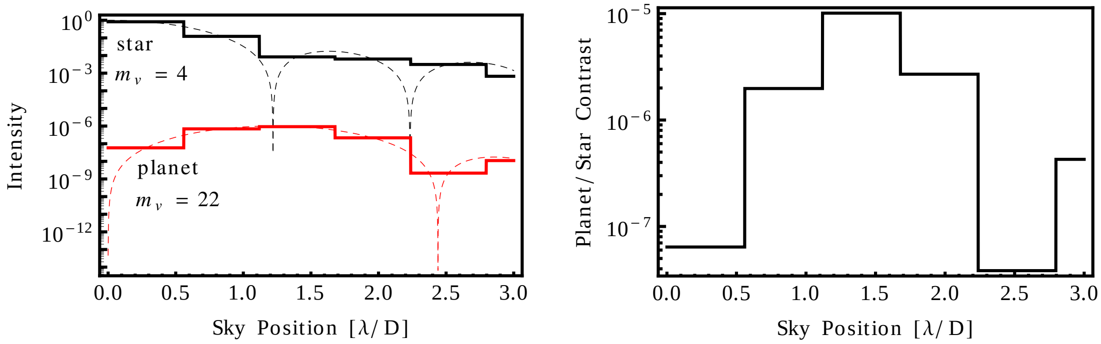

Figure 4.2: *Left:* The overlapping Airy function PSF of a star and planet with a peak-to-peak contrast ratio of 10^{-7}. Each signal is integrated into a series of pixels to show the real detector signal. The planet is placed at an angular position of 1.22 λ/D, the location of the first Airy minimum of the stellar PSF. *Right:* The planet-to-star contrast ratio as measured on the detector. The angular location of the planet improves the contrast ratio by a factor of 100.

in reflected visible light – a difference of roughly 18 magnitudes. This contrast ratio is representative of a system very similar to ϵ Eridani, one with a Jupiter-sized planet orbiting within 1 AU of its host star. Earth-sized exoplanets, due to their decreased cross section for reflection, have much less favorable contrast ratios, approaching 10^{-10} in reflected light.

Figure 4.2 shows the overlap of the stellar and planetary signals and the contrast between them at each point on the sky. The signals have been quantized into pixels that adequately sample the separation between the two sources. We can see that a factor of 100 can be gained in contrast by choosing to image the planet when it is located at the first minimum of the stellar PSF; a contrast of 10^{-7} becomes 10^{-5}. However, the problem remains despite this significant gain. The diminutive planet signal must be pulled out of the overwhelming background signal of the stellar PSF. It is the noise introduced by the large stellar signal that makes this task so difficult.

In our planet and star example, imagine a system where the telescope records 1 photon from the planet per second. If there were no star, and we consider only the Poisson noise associated with photon counting, a 10 second exposure would yield a signal-to-noise ratio (SNR) of $10/\sqrt{10} = 3.2$ for the planet – a positive detection. Turn on the star, and now for each planetary photon there are 100,000 stellar photons. Over the same 10 second exposure, the SNR would be $10/\sqrt{10^6} = 0.01$. As the SNR scales with the square root of the exposure time, it would require $\sim 1 \times 10^6$ seconds (11.6 days) to reach the same 3.2σ detection level for the planet.

One well-developed solution to this problem is to use a high-contrast coronagraph that is capable of attenuating the stellar signal before it reaches the detector. The planetary signal must be left unchanged to reap the benefits of this approach. The highest performance coronagraphs are currently approaching contrast factors of 10^{-10} (Trauger et al. 2011; Guyon et al. 2011). These coronagraphs are being designed for use in space, where there is no added blurring of the image from the Earth's atmosphere and the environments are thermally and vibrationally stable enough to support such high-level starlight suppression.

Large ground-based telescopes have made significant progress toward the goal of routinely imaging exoplanetary environments using state of the art adaptive optics in the infrared. At these longer wavelengths, the self-luminous planet to star contrast ratio is more favorable than the reflected signal. The upcoming Gemini Planet Imager combines state of the art coronagraph technology with adaptive optics to achieve extreme high-contrast imaging from the ground. The instrument has already demonstrated raw contrast levels of 1×10^{-6} and 2×10^{-7} after image processing (Macintosh et al. 2012).

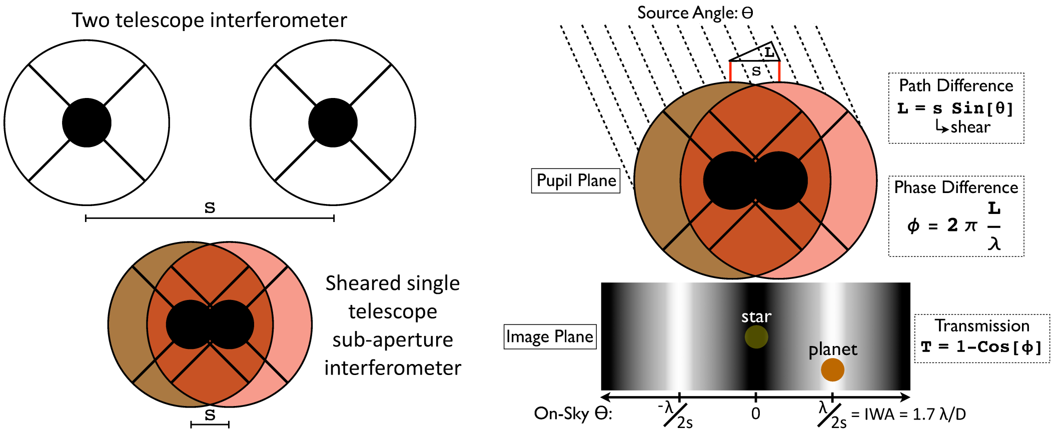

Figure 4.3: *Left:* Sub-aperture nulling interferometry can be performed using a single telescope by splitting and shearing the telescope beam to mimic a two-telescope system. *Right:* The single-aperture nulling interferometer produces a one-dimensional sinusoidal transmission pattern on the sky along the shear direction. The IWA ($1.7\lambda/D$) is defined as the location of the first maximum in the transmission pattern.

4.1.2 The Visible Nulling Coronagraph

The PICTURE mission incorporates a coronagraph design called the Visible Nulling Coronagraph (VNC, nuller). The PICTURE VNC was built at Jet Propulsion Laboratory (JPL) (Rao et al. 2008; Samuele et al. 2007; Shao et al. 2006) as a design candidate for the Terrestrial Planet Finder Coronagraph (TPF-C) mission. This design uses interferometry to destructively cancel the light from a star while allowing the off-axis planetary signal to pass through. A key figure of merit for coronagraphs is the inner working angle (IWA), the innermost angle that can be probed at a given contrast level. With a small IWA of 1.7 λ/D ($0.5''$) and a measured suppression factor of 3×10^{-4}, the PICTURE VNC can probe the ϵ Eri dust distribution down to an inner radius of 1.5 AU.

The optical theory employed by the VNC is nulling interferometry. This concept, which is illustrated in Figure 4.3, is analogous to a two-dish radio interferometer. Two radio dishes separated by a baseline (s) observe a relative phase delay in the measured signal of a source on the sky. The phase delay is a function of the source position angle and the baseline between the dishes. When the signals from the two dishes are combined, constructive and destructive interference fringes form. These fringes act as a transmission pattern on the sky. Sources at angles corresponding to constructive interference are transmitted and sources at angles corresponding to destructive interference are attenuated.

The radio interferometer concept holds true for two optical telescopes as well. The PICTURE VNC design takes this one step further. Instead of combining the beams of two telescopes, sub-apertures of a single telescope are interfered. This is accomplished by splitting the telescope beam into two identical copies and shearing them laterally with respect to each other by a distance s. This distance s, the "shear", is equivalent to the radio interferometer baseline. The sheared beams are recombined in a pupil plane where interference fringes form. The VNC must accomplish the task of creating complete destructive interference between these two beams. This destructive interference can only hold for a single angle on the sky; the shear (s) relates the position angle of a source (θ) to the relative phase difference (ϕ) between the recombined beams.

$$\phi(\theta) = 2\pi \frac{s \sin\theta}{\lambda} \tag{4.1}$$

This relationship superimposes a one-dimension sinusoidal transmission pattern (T) on the sky.

$$T(\theta) = 1 - V\cos(\phi(\theta)) \tag{4.2}$$

The fringe visibility (V) relates the balance of intensities between the two recombined beams in the nuller (I_1 and I_2).

$$V = \frac{2\sqrt{I_1 I_2}}{I_1 + I_2} \tag{4.3}$$

To act as a coronagraph, the VNC must be pointed such that the signal from the bright host star is attenuated by the destructive (null) fringe. The planetary source lies off-axis to the star and the phase difference induced by this angular offset allows the planetary signal to pass through the nuller to the image plane. The depth of the null fringe depends on the ability of the nuller to achieve zero phase error and unity visibility between the recombined beams. Mechanical control limitations and optical fabrication errors lead to small deviations from these idealized conditions. These errors determine the real performance of the nuller.

4.1.3 Pointing Requirements

Space and balloon mission designs that, like PICTURE, employ an internal coronagraph to directly image exoplanetary environments require milliarcsecond-level pointing stability. The principle of operation is very similar for most coronagraph designs; a star is placed behind a precisely tuned “mask” that attenuates the stellar PSF. In the case of the VNC, the coronagraphic “mask” is a dark interference fringe. The angular size of the mask must approach that of the stellar disk in order to detect planets and dust at small inner working angles. The angular diameters of nearby stars range from 0.1-10 mas. A Solar diameter star placed at a distance of 10 pc subtends 1 mas. The position of a star on the mask must be stabilized to a similarly small angle to prevent stellar leakage around the mask that would overwhelm the planetary signal.

Figure 4.4 shows the ideal transmission pattern for the PICTURE VNC. It can been seen clearly that for a given attenuation level, the null has a finite width. In the bottom panel of Figure 4.4, stars of three different angular diameters are multiplied by the nuller transmission pattern and the total starlight suppression is integrated across the face of the stellar disk. The angular diameter of ϵ Eridani is $\sim$2 mas, however, pointing jitter acts to enlarge the effective diameter of a star. The deepest

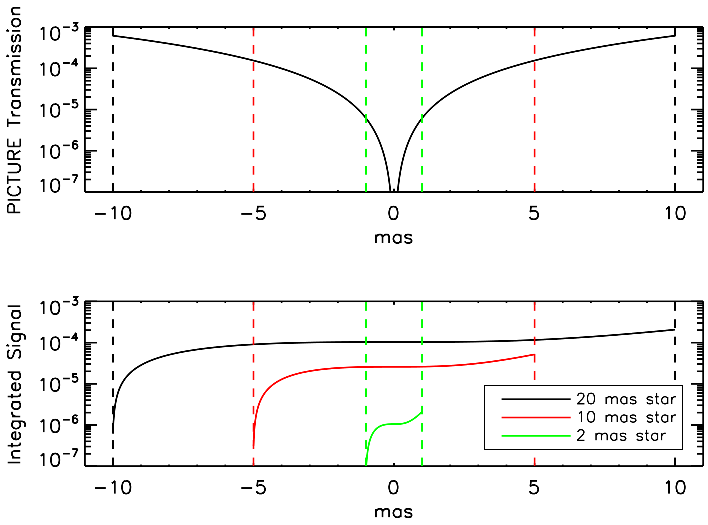

Figure 4.4: *Top:* The inner 20 mas of the idealized PICTURE nuller transmission pattern. *Bottom:* The cumulative integral of three stellar disks multiplied by the transmission pattern. The rightmost value of each curve is the total suppressed signal.

total psf suppression achieved with the PICTURE flight nuller at JPL was 3×10^{-4}. The stellar diameter corresponding to this suppression level for the ideal nuller is ∼20 mas. Based on this analysis, the PICTURE mission pointing requirement was set to 10 mas RMS. Below this limit, the nuller performance is limited by its internal optical properties.

The sounding rocket Attitude Control System (ACS) controls the pointing of the payload in space using high-pressure gas thrusters. This system is capable of delivering ∼1″ peak-to-valley (P-V) body pointing. The PICTURE instrument uses an active optical control system, the Fine Pointing System (FPS), to further stabilize the telescope beam. The FPS is similar to the image stabilization system found in a hand-held digital camera. The FPS incorporates an angle tracker camera and fast steering mirror (FSM) to actively sense and correct the residual ACS pointing jitter and stabilize the angular position of the star within the coronagraph. Similar systems

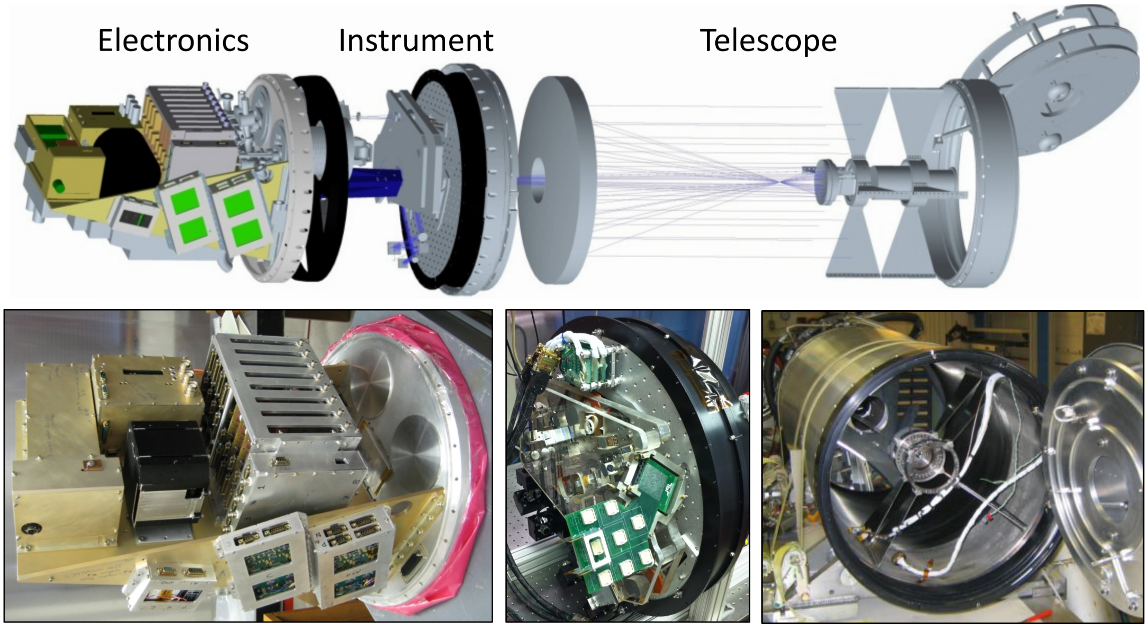

Figure 4.5: The PICTURE payload: the telescope, the instrument section and the electronics section. The flight electronics control the active optics and cameras inside the instrument section. The telescope is 0.5 m in diameter.

have been proposed for future exoplanet imaging missions (e.g. Brugarolas et al. 2010; Bryden et al. 2011; Schneider et al. 2012; Shao & Levine 2010; Matsuo et al. 2011; Liu et al. 2004). The FPS design is very similar to the image stabilization system flown onboard the Hinode (Solar-B) satellite (Shimizu et al. 2008).

4.2 Payload Design

The PICTURE payload consists of the three distinct sections: the telescope, the instrument and the electronics. A mechanical model of the payload and photographs of each section are shown in Figure 4.5. The telescope and instrument sections are evacuated for flight. All electrical connections pass from the electronics section to the instrument through a vacuum bulkhead, which serves as the mount point for the electronics support structure.

The PICTURE 0.5 meter telescope is built inside a carbon fiber tube (not shown in Figure 4.5) for a high strength-to-weight ratio and low thermal expansion. The primary mirror is an ultra-lightweight 4.5 kg ($\sim$20 kg/m^2 areal density) design with ultraviolet grade surface quality (Antonille et al. 2008). The mirror was built originally for the Solar High Angular Resolution Photometric Imager (SHARPI) mission (Rabin et al. 2002) and was contributed to this program by the Goddard Space Flight Center (GSFC) group for testing and flight verification onboard PICTURE.

The PICTURE instrument section contains the VNC, the FPS, an acquisition camera, the science camera (SCI) and the wavefront sensor (WFS) camera. The VNC is constructed from approximately 30 individual optical elements epoxied between two $\sim$1 inch thick ultra-low expansion (ULE) glass plates. It contains three piezoelectric transducer (PZT) tip-tilt-piston (TTP) mirrors and a 32×32 element Microelectromechanical Systems (MEMS) deformable mirror (DM) (manufactured by Boston Micromachines (BMC)) for use in active wavefront control. The SCI and the WFS cameras are cryogenically cooled (-70 C), 1024x1024 pixel, back-illuminated CCDs built originally for the Astro-E2 X-ray mission (Bautz et al. 2004). The FPS uses a high-speed angle tracker camera and a PZT-driven FSM to optically stabilize the telescope beam at the milliarcsecond level.

The flight electronics control the instrument's four PZT mirrors, the 1024 element MEMS DM and three CCD cameras. Each 3-axis PZT requires three independent low-noise amplifiers. The DM controller addresses each actuator individually through a set of 16 flex cables. Three single-board computers acquire images from the instrument cameras, send control signals to the active elements and communicate with each other autonomously over an on-board ethernet.

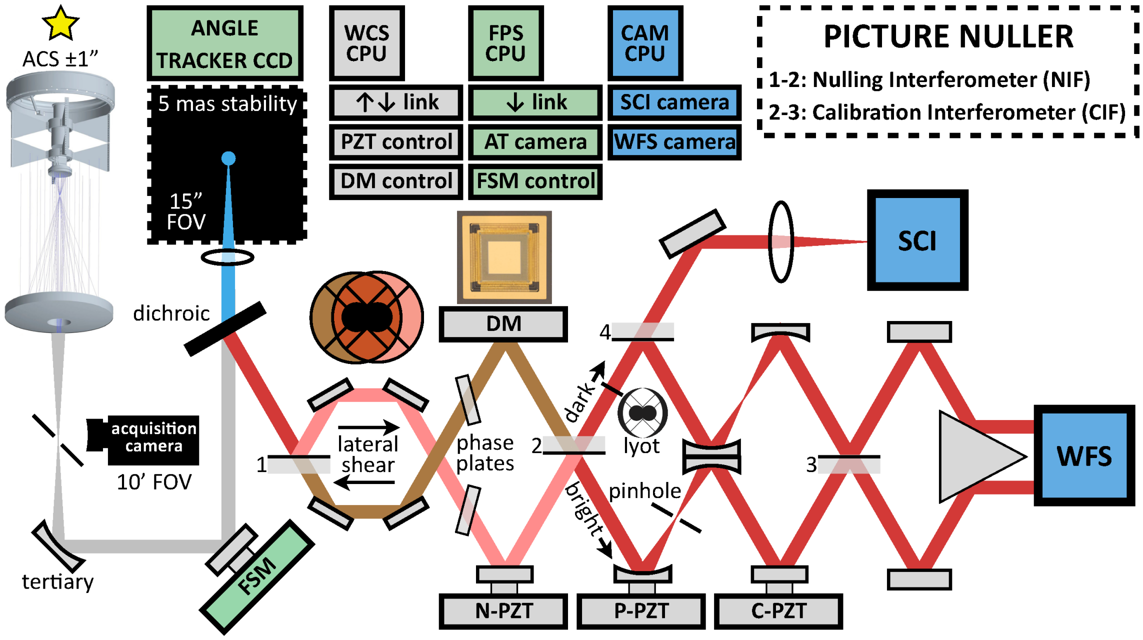

Figure 4.6: The PICTURE optical layout. The nuller beam splitters are numbered 1-4. The Nulling Interferometer (NIF) exists between beam splitters 1 and 2. The Calibration Interferometer (CIF) exists between beam splitters 2 and 3. A set of four mirrors within the NIF introduce the lateral shear which creates the baseline for nulling. The dispersive phase plates introduce a broadband π phase shift between the two arms of the NIF. A Lyot stop, which is shaped to match the sheared telescope aperture, is placed in the dark output of the NIF. Beam splitter 4 passes 50% of the dark output to the science camera (SCI) and reflects 50% into the CIF where it forms interference fringes with the bright output. Either of the two images that fall on the wavefront sensor camera (WFS) can be used for wavefront measurement.

4.3 Instrument Design

Design concepts for single and multi-aperture planet-imaging nullers have been developed at JPL over the past decade (Serabyn & Colavita 2001; Mennesson et al. 2003; Levine et al. 2003; Shao et al. 2006). The PICTURE nuller is a somewhat simplified single-aperture JPL design that demonstrates many of the design elements needed for larger missions. The nuller operates over a 20% bandpass in the visible spectrum (600-750 nm). The beamsplitters are arranged in a modified Mach-Zehnder

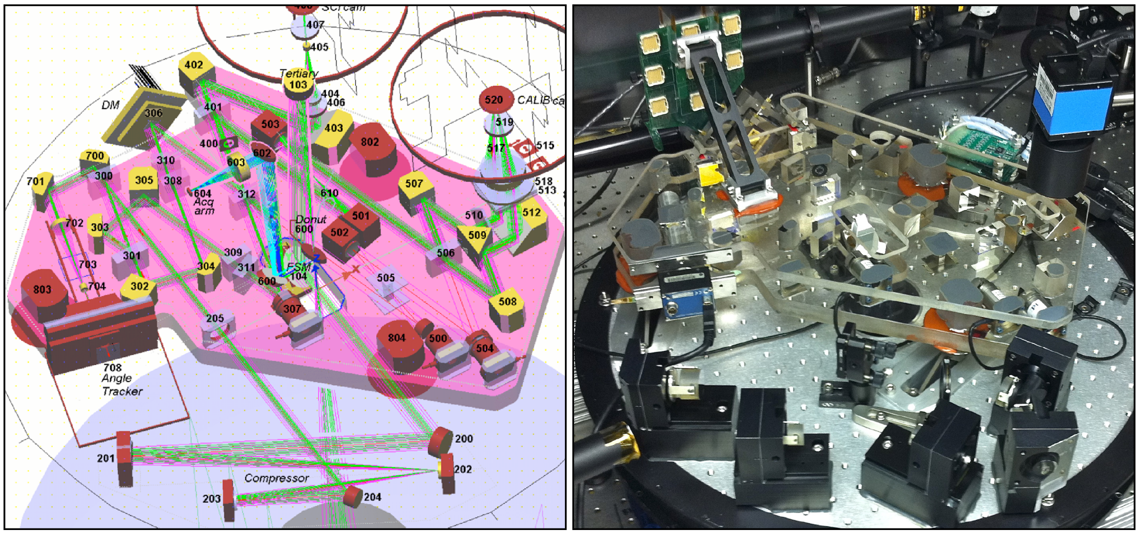

Figure 4.7: The PICTURE nuller. *Left*: 3D model and ray-trace. *Right*: Flight nuller during final alignment.

configuration, where two separate beamsplitters are used for beam separation and recombination.

The optical layout of the PICTURE experiment is shown in Figure 4.6. A 3D model and a photograph of the flight nuller are shown side-by-side in Figure 4.7. The VNC actually contains two interferometers: the nulling interferometer (NIF) functions as the coronagraph and the calibration interferometer (CIF) provides post-coronagraph wavefront sensing. A design similar to the PICTURE calibration system is being implemented on the Gemini Planet Imager (Wallace et al. 2010).

4.3.1 The Nulling Interferometer

The NIF contains two active elements, the Nuller PZT (N-PZT) and a 32×32 actuator MEMS DM. These elements are used by the Wavefront Control System (WCS) to remove optical path difference (OPD) between the two NIF arms at each point in the split/sheared/recombined pupil. These elements are responsible for minimizing the static phase errors which, as discussed in Section 4.1.2, limit the overall nuller performance.

If the NIF contained no dispersive elements, its physical path would match its optical path and it would only null at a single wavelength. To create a quasi-achromatic null, the NIF uses a pair of fused-silica dispersive phase plates to introduce a broadband (20%) π phase shift between the two arms (Morgan et al. 2000; Shao et al. 2004). The NIF does not actively control amplitude, rather the reflective optics are match-coated to within 1%. Eq. 4.2 and Eq. 4.3 can be used to show this places a hard lower limit of $T_{min} = 1 - 2\sqrt{0.99}/1.99 \simeq 1 \times 10^{-5}$ on the nuller contrast performance. To conserve energy, the NIF must have a bright and dark output. When nulling, the dark output is passed to the SCI camera.

4.3.2 The Calibration Interferometer

The CIF uses the Pinhole PZT (P-PZT) to pass the bright output of the NIF through a 5 μm pinhole, which acts as a spatial filter to create a reference beam that is re-interfered with the NIF dark output to measure the stellar leakage wavefront properties. If a small amount of starlight leaks into the NIF dark output, it will form interference fringes with the reference beam. These can be used to correct the DM in order to fix the leak or to simply monitor the leakage. The Calibration PZT (C-PZT) is used to control the optical path length through the reference arm of the CIF. Both the CIF and NIF operation will be discussed further in Section 4.7.

4.3.3 The Science and Wavefront Sensor Cameras

The WFS camera collects images of interference fringes in the recombined pupil to provide feedback to the WCS. The WFS is focused to the surface of the DM, which sits in a system pupil. Imaging optics re-focus the pupil to form images of the

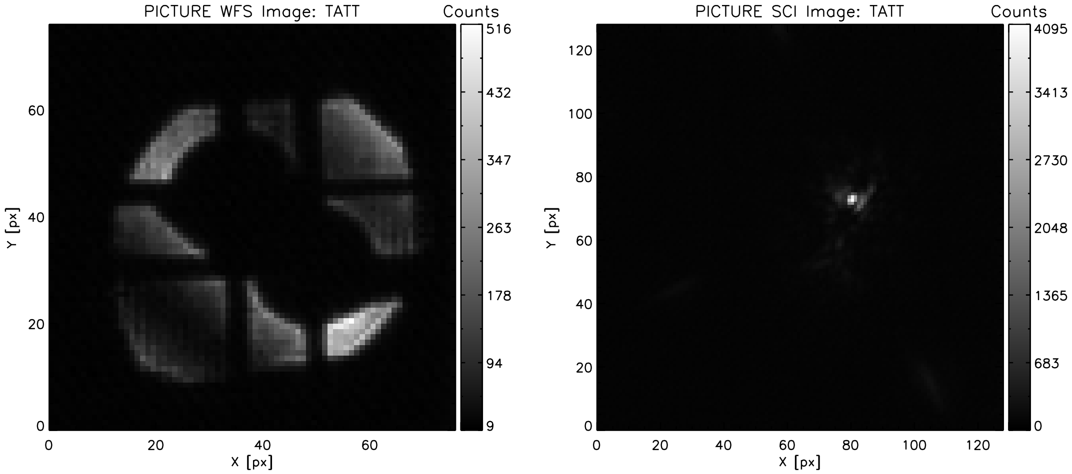

Figure 4.8: *Left:* An image of white-light interference fringes on the WFS camera. *Right:* An image of the instrument PSF on the SCI camera.

sky on the SCI camera. Example images of white-light interference fringes on the WFS and the focused instrument PSF on the SCI camera are shown in Figure 4.8.

4.3.4 Flight Observation Plan

The rocket ACS is capable of pointing the payload at a target star with ~1″ P-V stability. At telescope focus, a circular pick-off mirror reflects a 10′ field of view to an acquisition camera. This is shown in Figure 4.6. The live signal from this camera is used to manually drive the rocket ACS from the ground to send the stellar spot through a 15″ hole in the center of the mirror. The stellar beam drops down into the FPS, which actively stabilizes the input pointing to the nuller. A dichroic beam splitter is used to pass only the blue (<600 nm) light to the angle tracker camera. The red science light is reflected into the nuller.

The first ~60 seconds of the 320 second observation window are spent pointed at a bright calibration star while the WCS aligns the NIF active elements to produce a coronagraphic null. Here the NIF functions as its own wavefront sensor, stepping the N-PZT through a full wave to generate alignment phase maps. The design and functionality of the WCS is described further in Section 4.7. On completion of alignment, the NIF is placed in "nulling" mode with the N-PZT set to the bottom of the central dark fringe. Reference exposures of the system PSF are taken on the dust-free calibration star for use in data post-processing. The payload then slews to the dimmer science target to collect science exposures. During this phase, the CIF is used to monitor the null and maintain alignment. Science exposures are taken at two roll angles to enable angular differential imaging (see Marois et al. (2006)).

4.4 Telescope Design and Alignment

The PICTURE telescope (Figure 4.9) is a Gregorian design consisting of a f/1.26, 0.508 m clear aperture (0.559 m physical diameter), ultra-lightweight (4.54 kg, 19.75 kg/m^2 aerial density) primary mirror and a 0.102 m clear aperture secondary. The primary is mounted on three bipods (shown in Figure 4.11). The mounting procedure must exert minimum stress to avoid deforming the lightweight and flexible mirror. This procedure is discussed at length in Antonille et al. (2008).

The f/12.3 telescope is collimated to an 18.4 mm beam by a tertiary mirror that reimages the system pupil to the FSM. A set of beam-compressor mirrors further reduce the beam diameter to 12.5 mm to match the format of the 32×32 actuator DM. The compressor mirrors also reimage the system pupil from the FSM to the DM.

To align the secondary mirror, the telescope was mounted horizontally as seen in Figure 4.10. A phase-shifting Fizeau interferometer was built and used with the telescope in a double pass arrangement. The interferometer beam was passed backwards though the telescope. A 0.5 m flat mirror was positioned at the entrance aperture to return the collimated beam back through the telescope to the interferometer. Wave-

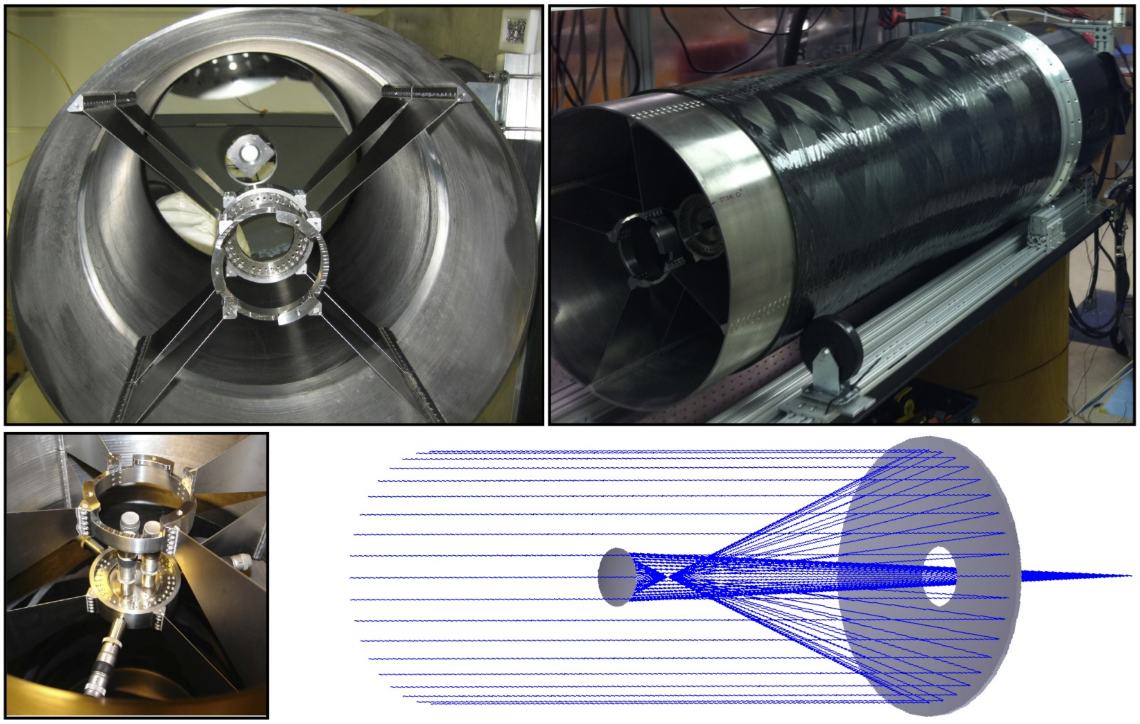

Figure 4.9: *Top Left:* The 0.5 m primary mirror and secondary support structure. The outer support holds the ST5000 star tracker camera (Percival et al. 2007), which feeds the ACS with pointing data based on the position of the observed star field. *Top Right:* The telescope is housed within a carbon fiber tube (black) with a titanium insert at the entrance aperture. *Bottom Left:* 6 manual drive actuators are used to align the secondary mirror. They are removed for flight after the circular ring of bolts has been used to clamp the mirror in place. *Bottom Right:* The PICTURE telescope is a Gregorian design; the primary focus is between the primary and secondary mirrors and the secondary has a concave figure.

front error (WFE) maps of the returned telescope beam were generated using the Durango software package (www.diffraction.com). In rolling the telescope, aberrations introduced by non-common path elements could be isolated from the telescope. At each roll angle, six actuators (shown in Figure 4.9) were used to manually set tip, tilt, focus and decenter of the secondary mirror in order to minimize the measured WFE. A best alignment position was chosen based on an average of the secondary actuator settings from each roll angle.

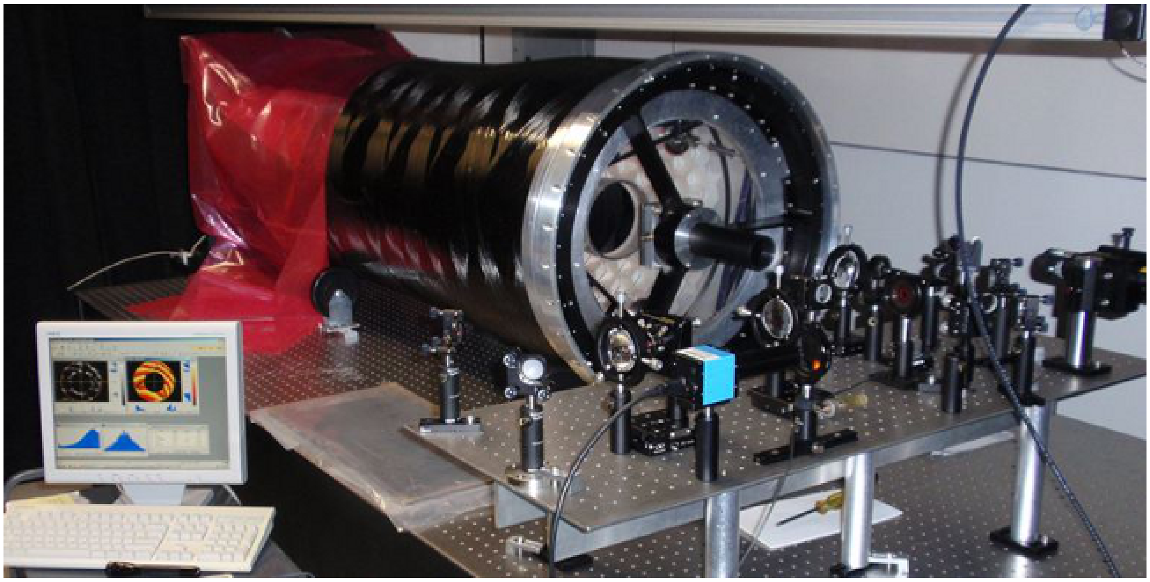

Figure 4.10: The telescope is shown along with the phase-shifting interferometer built for aligning the secondary to the primary in double pass.

A characteristic figure error map of the final telescope alignment is shown in Figure 4.11. The error is dominated by gravity sag on the primary mirror. The low-spatial-frequency figure error due to primary sag alone is modeled at 215 nm P-V (Antonille & Content 2008) and measured at 361 nm P-V for the complete telescope. Print-through deformations from the primary mounting bipods are apparent, as is a cylinder-like fold that varied in amplitude depending on the roll angle.

The figure error of the aligned telescope is 502 nm P-V at 1-g (measured in a horizontal configuration). Vertical and horizontal measurements were combined by Antonille et al. (2008) to predict that the primary would gravity-release in space to a 9 nm RMS figure. This error combined with the measured alignment errors would leave approximately 54 nm RMS (150 nm P-V) of residual telescope error.

The challenges associated with testing a $\sim\lambda/1$ telescope on the ground with the expectation of a $\sim\lambda/4$ telescope in space are discussed further in Chapter 5. Both

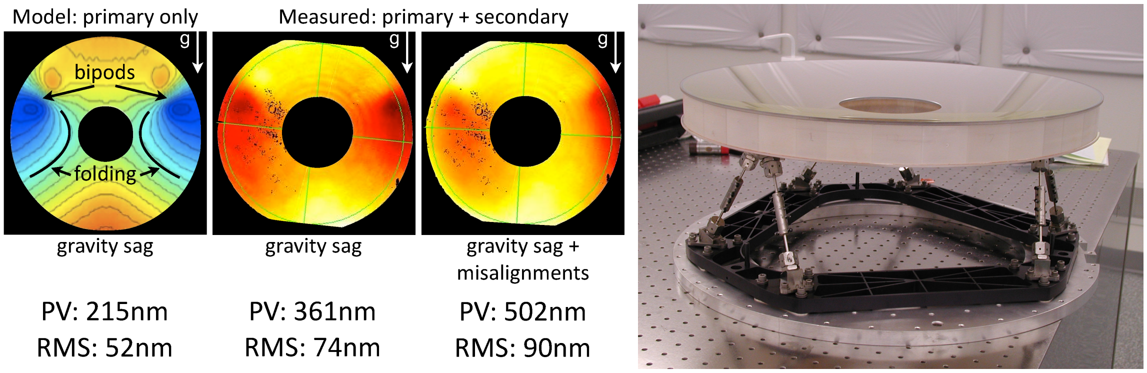

Figure 4.11: *Left panel*: The modeled primary sag (Antonille & Content 2008) and bipod print-through surface errors in a horizontal configuration (*left*), the measured gravity sag (*center*) and the final telescope figure error, which includes the combination of alignment errors and gravity sag (*right*). *Right panel*: The primary mirror bipod mounting fixture.

the measured 1-g and projected 0-g errors are within the capture range of the DM, which was measured to have 1.6 μm of stroke (Rao et al. 2008). Based on these considerations, it was determined that the final telescope alignment was sufficient for integration with the instrument.

4.5 Electronics Section

A block diagram of the PICTURE electronics section is shown in Figure 4.12. The task of operating the FPS, WCS and the SCI and WFS cameras is split between three flight computers. All three computers are built upon the PC-104 standard, utilizing off-the-shelf single board computers stacked with various analog-to-digital converter (ADC), digital-to-analog converter (DAC), field-programmable gate array (FPGA), fiber-link and power boards to perform the necessary data acquisition and hardware control. The flight computers run an embedded Linux operating system. The FPS and WCS computers both implement a hard real-time layer for performing time-critical functions. The nuller PZTs and DM are controlled by JPL designed

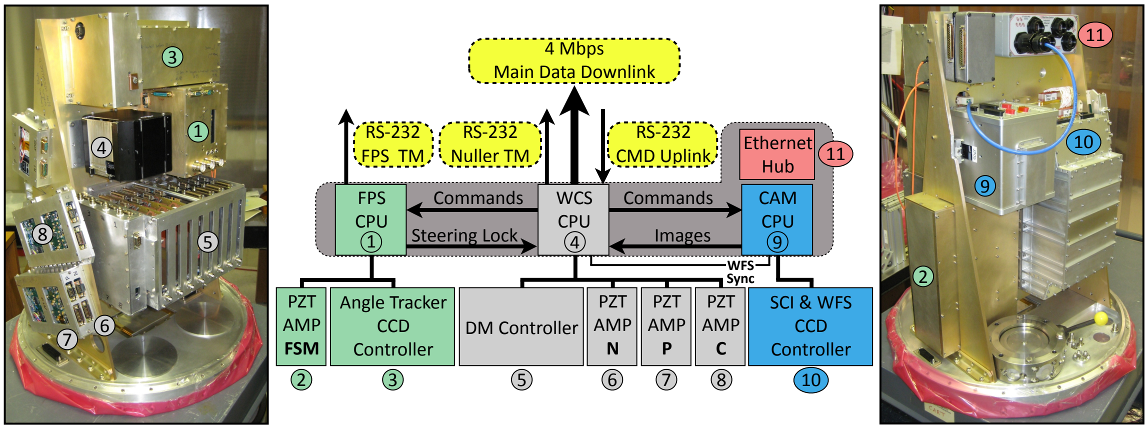

Figure 4.12: PICTURE electronics section block diagram. Each item is identified by number in the photographs of the flight electronics.

driver electronics. They receive digital commands from the WCS computer via two digital input/output (DIO) boards in the PC-104 stack. Along with the CCD chips, the SCI and WFS camera controller was also manufactured originally for the Astro-E2 mission.

4.6 Flight and Ground Support Software

As the project's primary software engineer, I developed all flight and ground-support software for the mission. This includes software to operate the FPS and WCS (to be described in later sections), software to provide on-board communications between the flight computers and software to pass all of the science and housekeeping data to the Wallops Flight Facility (WFF) telemetry system.

The WCS computer provides a system-wide command interface to receive, interpret, and pass commands from the ground to the appropriate system over an on-board ethernet. The ethernet provides a critical communication layer between the flight computers. SCI and WFS images are passed over ethernet from the camera computer to the WCS for processing and eventual transmission to the ground

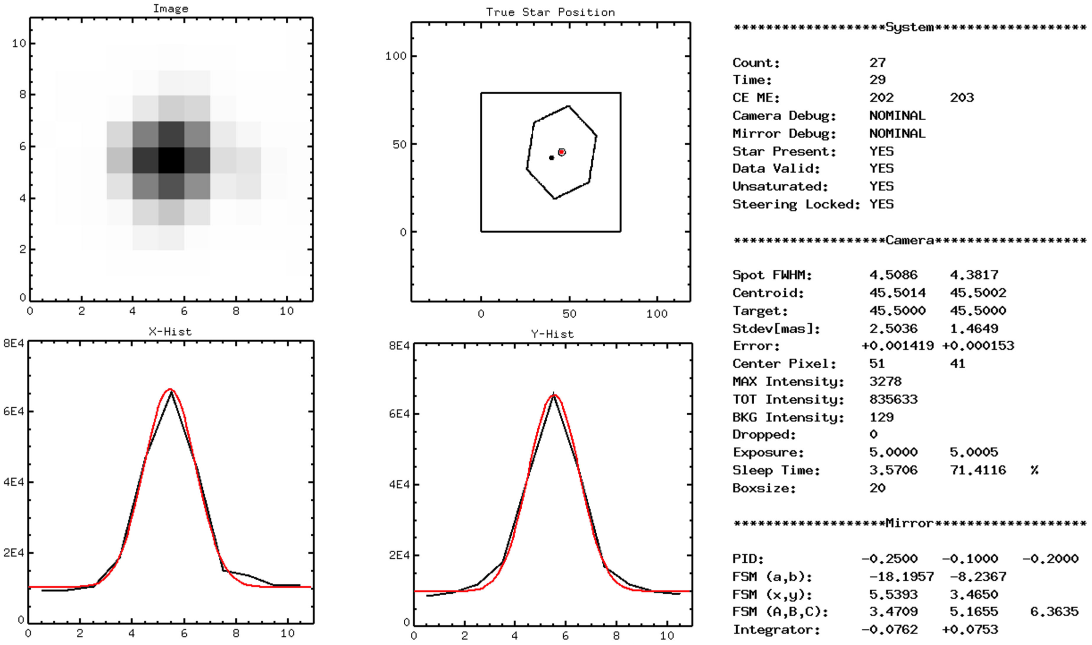

```
*******************System*******************

Count:           27
Time:            29
CE ME:           202       203
Camera Debug:    NOMINAL
Mirror Debug:    NOMINAL
Star Present:    YES
Data Valid:      YES
Unsaturated:     YES
Steering Locked: YES

*******************Camera*******************

Spot FWHM:       4.5086    4.3817
Centroid:        45.5014   45.5002
Target:          45.5000   45.5000
Stdev[mas]:      2.5036    1.4649
Error:          +0.001419 +0.000153
Center Pixel:    51        41
MAX Intensity:   3278
TOT Intensity:   835633
BKG Intensity:   129
Dropped:         0
Exposure:        5.0000    5.0005
Sleep Time:      3.5706    71.4116   %
Boxsize:         20

*******************Mirror*******************

PID:            -0.2500   -0.1000   -0.2000
FSM (a,b):       -18.1957  -8.2367
FSM (x,y):       5.5393    3.4650
FSM (A,B,C):     3.4709    5.1655    6.3635
Integrator:     -0.0762   +0.0753
```

Figure 4.13: PICTURE FPS real-time display. *Top-left*: 15×15 pixel postage stamp telemetry image from the angle tracker. *Top-right*: The inner square represents the full 80×80 pixel angle tracker CCD. The hexagon represents the capture range of the FSM. The black dot shows where the star would land if the mirror was not tilted. The red dot shows the true measured position of the star. The tracking target is marked with a circle. The rocket ACS is used to manually drive the black dot inside the hexagon. At this point, the FPS automatically tracks the star (red dot) to the target. *Bottom*: X and Y profiles of the stellar PSF. Gaussian fits are overlaid in red. *Far-right*: Live telemetry showing the status of the tracking system.

over the high-bandwidth 4 Mbps parallel downlink. The FPS computer uses the ethernet to inform the WCS that the pointing is locked and it may proceed to iterate through the nuller alignment sequence. The FPS computer is also given its own serial downlink for transmitting housekeeping and pointing status data. These data were displayed in real time during flight. The measured position of the star on the angle tracker was used to issue manual ACS commands to drive the star into the capture range of the FSM. The FPS real-time display is shown in Figure 4.13.

4.7 Wavefront Control System

The PICTURE WCS is used to manipulate the N-PZT and the DM to minimize OPD between the sheared and recombined telescope beams. Two modes of WCS operation are performed in flight. The "alignment" mode quickly removes static OPD between the two beams using the NIF as its own wavefront sensor. The "nulling/calibration" mode uses the CIF to improve the NIF alignment and to monitor and correct slow thermal drifts in the telescope, PZT actuators and nuller components while the system is nulling and collecting science exposures.

4.7.1 Operational Design

The "ABCD" phase measurement method (Wyant 1975; Colavita et al. 1999) forms the operational backbone of the WCS. This technique is used to measure the relative phase between recombined beams in both the nulling and calibration interferometers. When two wavefronts interfere, the relative phase between them can be reconstructed by stepping one beam through a full wave of phase delay and observing the induced change in the fringe pattern. The ABCD phase measurement method, a simple implementation of this technique, uses 1/4 wave steps.

The WFS camera continually generates sets of 4 (A,B,C,D) images. At the start of each "A" image, a WFS sync pulse is sent from the camera computer to the WCS to signal that an exposure set has begun. The WCS software runs in two layers: a real-time hardware interaction layer and a non-real-time user space layer. The software architecture is illustrated in Figure 4.14. The two software layers communicate using a bank of shared memory where the ABCD positions of each active element are held. The user space layer calculates the next set of ABCD positions from the WFS images. These positions are asynchronously copied to shared memory as they are calculated. The time-critical matter of applying the updates to the active elements in sync with

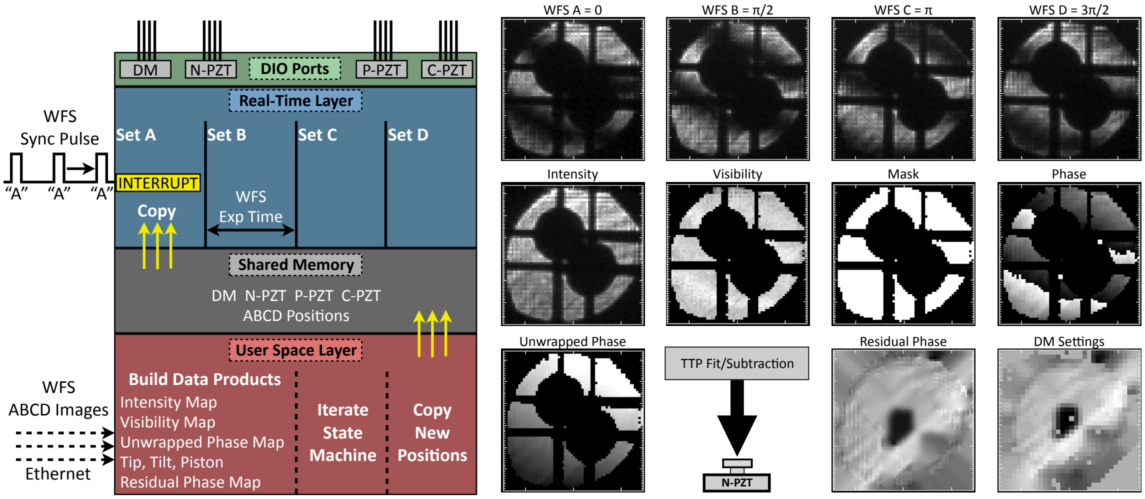

Figure 4.14: *Left*: WCS software architecture. *Right*: WCS data products. (*See text for details*).

the WFS images is handled by the real-time layer. The WFS sync pulse generates an interrupt that triggers the code to sequence through the 4 ABCD positions of each element – timed to match the exposure cadence of the WFS. This design creates a flexible system that can operate the WCS in a variety of modes.

4.7.2 Data Products

ABCD image sets are collected by the WCS computer and processed into several data products. First, the images are corrected for background counts, dark counts, and flat-field effects. Then, intensity (I), visibility (V) and phase (ϕ) maps are calculated using Equations (4.4, 4.5, 4.6). A pixel selection mask is also defined to include all pixels with intensity and visibility above a pre-defined threshold.

$$I = A + B + C + D \tag{4.4}$$

$$V = 2\sqrt{\frac{(A-C)^2 + (B-D)^2}{I^2}} \tag{4.5}$$

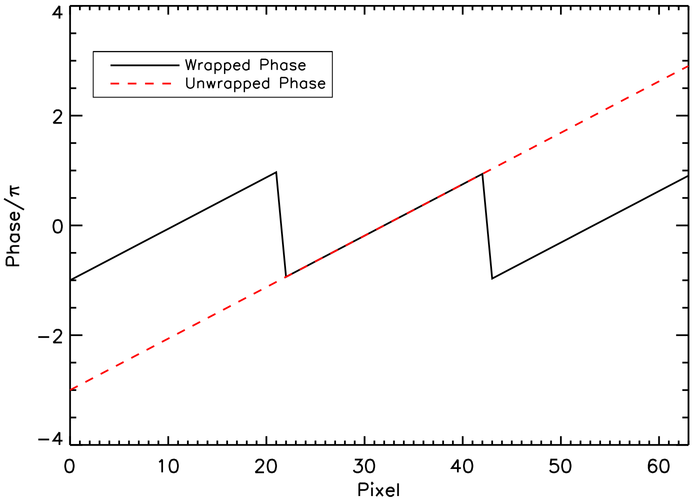

Figure 4.15: Phase unwrapping. The measured phase (*solid black line*) is wrapped over a ±π interval. The phase unwrapper calculates the absolute phase error (*dashed red line*).

$$\phi = ArcTan\left[\frac{B-D}{A-C}\right] \tag{4.6}$$

Next, a test is run on the phase map to determine if there is more than one fringe of OPD across the pupil. The phase map is limited to values between $\pm\pi$, multiple fringes cause the phase map to wrap over from $+\pi$ to $-\pi$ or vice versa. If these phase wraps exist, the iterative Picard method (Ghiglia & Romero 1994) is used to construct an unwrapped phase map. The unwrapped phase map shows the full OPD without the $\pm\pi$ ambiguity. Figure 4.15 illustrates the phase unwrapping process.

In the next step, a tip-tilt-piston (TTP) plane is fit to the unwrapped phase map and subtracted off leaving a residual phase map. This residual phase map will be used to correct the DM. To prevent DM edge effects around the selection mask, the residual phase map is extrapolated and smoothed onto the pixels outside the selection region. An example set of these data products taken during WCS alignment mode is displayed in Figure 4.14.

4.7.3 Alignment and Calibration

The WCS alignment mode is used first to quickly drive out static OPD from figure errors on the optics and the incurred misalignments due to launch vibration and gravity release on the telescope. In this mode, the N-PZT is configured to make 1/4 wave ABCD steps such that the generated data products represent the OPD between the two arms of the NIF. The TTP error signal is applied to the N-PZT zero-point "A" position, processed first through a simple integral servo controller. This correction is superimposed on top of the continuous ABCD piston stepping. The residual error correction is applied to the DM, likewise through an integral controller.

The alignment mode is halted when the residual OPD is pushed below 10 nm RMS. At this point, the instrument is placed into "nulling/calibration" mode. With the N-PZT set to the $C=\pi$ "null" position, the nuller dark output is now sent to the science camera. The once highly saturated science images drop well below the saturation limit and the WFS images go dark. With the system nulling, calibration can begin. The P-PZT is tilted to pass the nuller bright output through the calibration pinhole to create a reference beam that is interfered with the NIF dark output. The C-PZT begins stepping at 1/4 wave (ABCD) intervals. The WCS data products now measure OPD within the calibration system. The calibration maps can be used to simply monitor the nuller performance or to provide fine-alignment error signals for null maintenance and improvement. To continue driving the DM, the N-PZT is dithered on either side of the null to measure the slope of the fringe visibility at each DM actuator. The DM actuators are set to minimize the calibration visibility. The dither pattern is required to measure the downhill direction for each actuator. This method was shown to achieve 2 nm RMS OPD across the full pupil using the flight DM (Rao et al. 2008).

The measured calibration maps can also be used in image post processing to further separate starlight from planetary light. This technique takes advantage of the fact that the stellar light is coherent in the CIF, while the planetary light is not. The calibration fringes are formed only by stellar photons and a reconstructed PSF from these fringes represents only the stellar component. This PSF can be subtracted from the science images to reveal the planetary signal. This technique is explained in Lane et al. (2006).

4.7.4 Flight Alignment Procedure

The discussed methods for nuller alignment and calibration fit into the larger schema of automated operation during flight. The flight alignment procedure is implemented as a simple state machine on the WCS computer. The flight states take the WCS data products as input and nominally follow a pre-determined order – each state exits to one and only one state. As a fail-safe, the operator can command the alignment procedure to either start over with the original startup conditions, or fall back to a saved state. The flight state machine is diagrammed in Figure 4.16. One iteration of the state machine is defined by one ABCD image set. For each iteration, the state decides whether or not to advance to the next state. This decision is based either on self-evaluation of its progress, or a pre-determined number of iterations. The flight states are as follows:

- LOST: The system begins here. The initial DM and PZT settings are set to their hard-coded defaults. The DM is set to a pre-defined flat pattern. The N-PZT is configured to make 1/4 wave ABCD steps. The P-PZT is tilted at an extreme angle to dump the NIF bright output. The C-PZT is frozen.

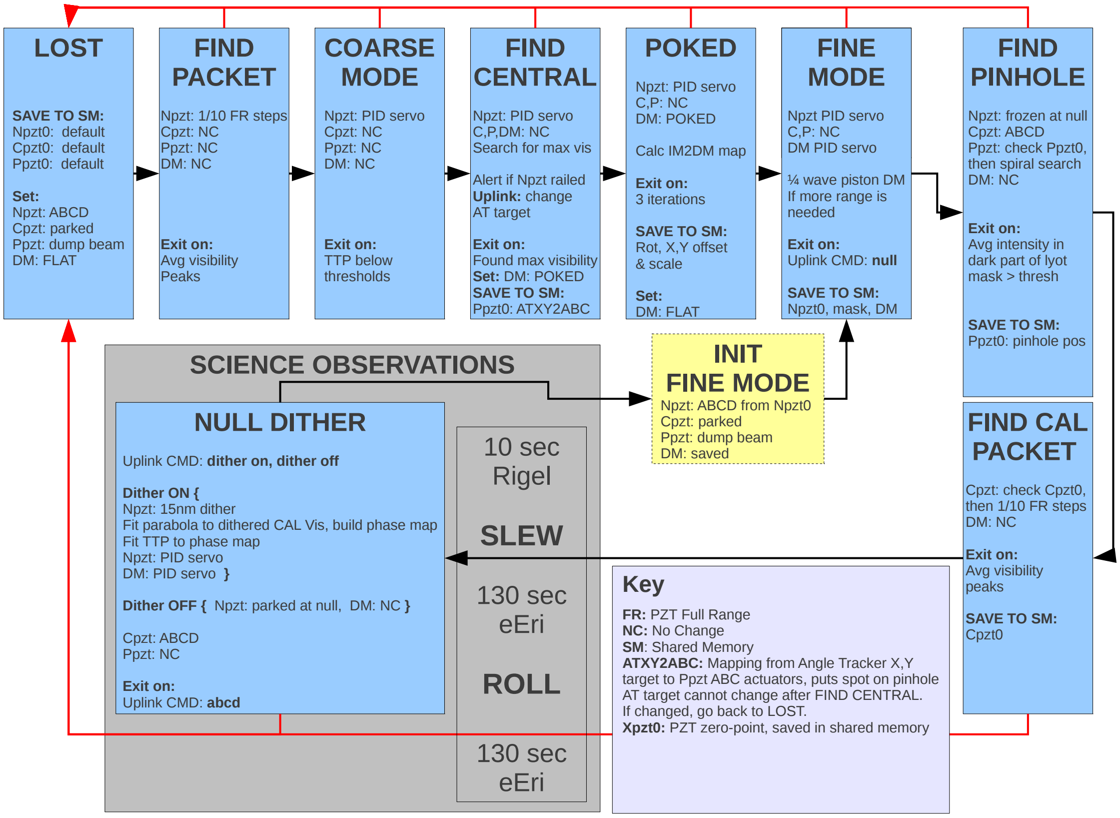

Figure 4.16: WCS flight software state machine layout (*see text for details*).

- FIND PACKET: The N-PZT zero-point "A" position is stepped in 0.8 μm intervals over its 8 μm range until the measured average visibility across the pupil passes through a maximum. As seen in Figure 4.17, these steps are small enough to catch some part of the white-light fringe packet, which is approximately 3 μm wide. The N-PZT begins at the position where the central fringe packet was last measured on the ground. If no packet is found, the stepping program wraps around to the low end of the PZT stroke and continues stepping. If the fringe packet is out of range, another ± 2 μm of delay can be

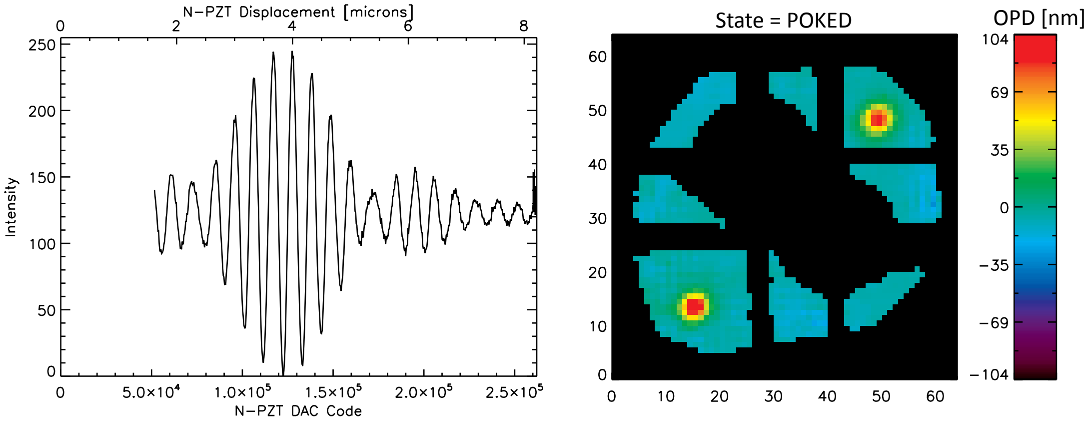

Figure 4.17: *Left*: A scan of the N-PZT through the white-light fringe packet. The fringes are measured at a fixed pixel in the WFS image. *Right*: A residual OPD map of the pupil in the POKED state.

accessed by shifting the angle tracker target position laterally in the shear direction. This is equivalent to changing the delay between the two NIF arms.

- COARSE MODE: An integral servo controller is run to minimize the measured TTP using the N-PZT. The DM remains static. This state advances when these values drop below a pre-defined threshold.
- FIND CENTRAL: Here the N-PZT makes single fringe hops in either direction to locate the central fringe. The search routine uses the average visibility across the pupil to climb uphill to the central fringe.
- POKED: The DM is registered to the WFS image. The DM pokes up two actuators creating two "bright" spots in the calculated phase map (Figure 4.17). These spots are located and centroided. They are used to calculate the rotation and scale mapping between the WFS coordinates and the DM coordinates. This state is necessary to correct for any shifts in the WFS position from launch vibration.

- FINE MODE: Now both the N-PZT and DM servo controllers are operational. The TTP error signal is sent to the N-PZT and the residual errors are mapped onto the DM. The WCS works to push each pixel in the C=π WFS image to the bottom of the central dark fringe. To exit this state requires user interaction. An operator on the ground watches the RMS OPD fall towards zero. When the decision is made that the OPD is no longer improving, an uplink command is sent to begin nulling. At this point the WCS switches from "alignment" mode to "nulling/calibration" mode. The N-PZT is set to the C=π position, and the calibration interferometer is activated.

- FIND PINHOLE: Before flight, the pinhole position and the P-PZT range of motion are registered to the angle tracker to aid the P-PZT in quickly locating the pinhole based on the current angle tracker spot position. If the pinhole is not found immediately, a spiral search is implemented. The spiral step size is set at 1/5 the pinhole diameter. When the pinhole is found, the WFS lights up dramatically and the C-PZT begins 1/4 wave ABCD stepping.

- FIND CAL PACKET: This state is identical to the "FIND PACKET" state except here the system is searching for the CIF fringe packet.

- NULL DITHER: This state requires three iterations to make one measurement. For each iteration, the N-PZT cycles though the following dither pattern with respect to the null: -15 nm, 0 nm, +15 nm. The C-PZT continues ABCD stepping to generate a calibration visibility map for each of the three N-PZT positions. A parabola is fit to the 3-point visibility curve for each DM actuator and the measured null offset is fed into the DM servo. The dither size can be reduced as the system walks onto the null as described in Rao et al. (2008).

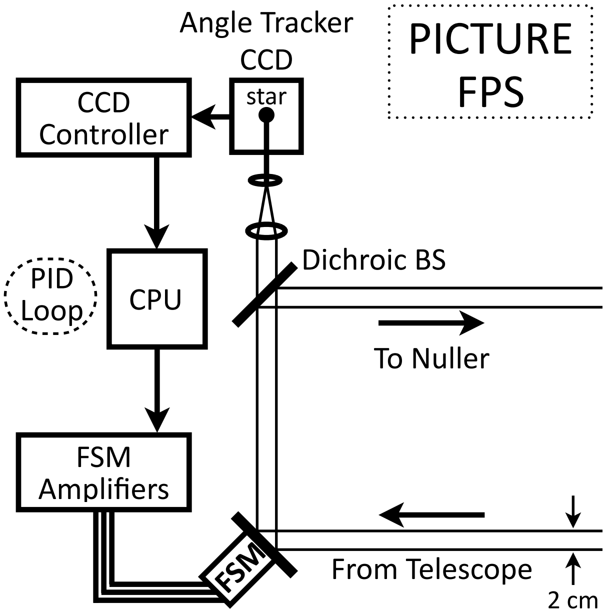

Figure 4.18: FPS diagram.

4.8 Fine Pointing System

The FPS actively stabilizes the input pointing to the nuller. A diagram of the FPS is shown in Figure 4.18. The system includes a high-speed angle tracker camera for stellar position measurement, a fast steering mirror (FSM) for tip-tilt corrections and a flight computer to close the Proportional + Integral + Differential (PID) feedback loop between the camera and the FSM. The f/12.3 telescope is collimated to a ∼2 cm beam by a tertiary mirror that reimages the system pupil to the FSM. A dichroic beam splitter picks off the blue (<600 nm) light for tracking and passes the red science light into the nuller. The angle tracker camera is hard-mounted to the glass nuller optical bench to minimize differential motion between the two. This ensures that the pointing measured on the angle tracker is the pointing into the nuller.

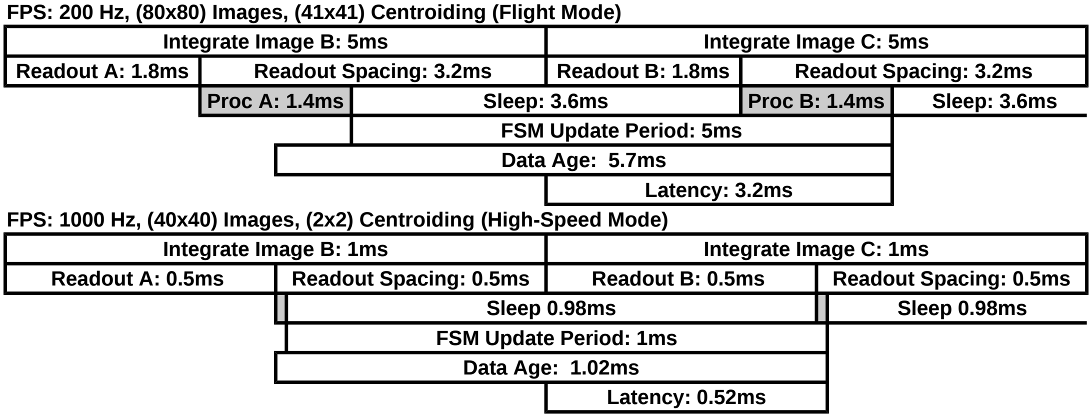

Figure 4.19: Timing diagrams for the PICTURE FPS. The flight mode (*top*) uses a 200 Hz system rate with full chip (80×80) readout. The frame transfer nature of the angle tracker camera allows the slow analog-to-digital conversion to proceed while the next image is integrating. The data age at the time of each FSM update is 5.7 ms and the controller latency, defined as the sum of the readout and image processing time, is 3.2 ms. The image processing stage (*shaded*) includes centroiding and PID calculation. The FPS high-speed 1 kHz mode is diagrammed in the lower chart. This mode was also available in flight to prevent CCD saturation. The image processing time, which scales as the number of centroiding pixels, is dramatically reduced in the 1 kHz mode through the use of a 3×3 or 2×2 centroiding box. In either mode, the centroid box size can be adjusted on the fly to accommodate any spot size.

For each exposure cycle, the FPS computer acquires an image from the angle tracker, calculates the stellar centroid and passes the measured pointing offset to a software PID controller. The PID output control signals are sent to the FSM to correct the offset. The mirror is updated once per camera exposure; this allows the FPS timing to be described by a single "system rate." During flight, the system rate was 200 Hz. A second 1 kHz mode was also available to prevent CCD saturation. Timing diagrams for these two FPS modes are shown in Figure 4.19.

High speed optical image stabilization systems that incorporate a fine guidance camera and a tip-tilt steering mirror are being used today in many functioning ground-based adaptive optics (AO) and high resolution imaging systems (e.g. Dekany et al. 1997; Wizinowich et al. 2006; Vogt et al. 2010; Close & McCarthy 1994; Olivier et al. 1993; Taylor et al. 1999; Warner et al. 2010; Stein & Neufeld 2004; Glindemann et al. 1997). These systems all employ fast tip-tilt correctors to remove high-bandwidth, low-order aberrations. Rocket-borne tip-tilt systems have been flying for decades (Bottema et al. 1969). The FPS design is very similar to the image stabilization system onboard the Hinode (Solar-B) satellite (Shimizu et al. 2008). The Hinode system tracks resolved features on the surface of the Sun instead of a single unresolved star.

4.8.1 Hardware Components

The angle tracker CCD is an e2v CCD39 (www.e2v.com) – an 80×80 pixel frame-transfer chip that operated at 200 Hz with full-frame readout during flight. The high-speed, low-noise performance of this chip has made it a popular choice for AO sensing applications (DuVarney et al. 2000; Dekany et al. 1997; Thompson et al. 2002). The CCD full-well limit is 3×10^5 e-/px. The average dark rate is 58×10^3 e-/px/s at room temperature. The optical train upstream from the camera produces a plate scale of $0.19''$/px and a $15''$ field of view on the sky. The camera is controlled by an Astronomical Research Cameras (ARC) GEN III controller (www.astro-cam.com). ARC controllers are widely used in ground-based AO systems (Thompson et al. 2002; Brummelaar et al. 2005). The GEN III delivers ∼12 e-/px RMS read noise with no measurable periodic readout variations across the chip. With 16-bit analog-to-digital conversion, the controller can operate over a range of gains from 0.22-1 ADU/e-.

The FSM components are manufactured by Physik Instrumente (PI) (www.physikinstrumente.com) and have been used in similar ground-based applications (Glindemann et al. 1997). The mirror actuator is a PI S-316 three-axis PZT stage. It is operated by three low-noise (1.6 mV RMS) PI E-610 amplifiers, which are fed by 16-bit DACs. The mirror itself is a 25 mm elliptical flat.

4.8.2 Pointing Control Limitations

The performance of the FPS is limited by its subsystems for centroid measurement and FSM control, and by the interaction between the PID controller and the ambient pointing environment. The absolute performance limit of the FPS is set by the FSM response to amplifier noise. This limit is ∼0.5 mas and will be discussed in Section 4.8.4. Above this limit, the pointing control noise floor is determined by the statistical uncertainty of the centroid measurement – a product of the CCD noise properties, the brightness of the star and the centroid algorithm. The tracking deadband is set by both the FSM control resolution and the centroid sensitivity to small-angle excursions. The frequency characteristics of the ambient ACS pointing environment must be understood relative to the independent sensing and control bandwidths of the FPS to determine what fraction of the total pointing error is sensed but not corrected and what fraction is not sensed at all. Both contributions must be accounted for to accurately determine the pointing error into the coronagraph.

4.8.3 Centroid Measurement Sensitivity & Noise

The FPS uses a simple center-of-light centroid calculation to measure the stellar position on the angle tracker camera.

$$\langle x \rangle = \frac{\sum_i^N x_i C_i}{\sum_i^N C_i} \tag{4.7}$$

Here, x_i is the X coordinate of the i^{th} pixel and C_i is the number of counts or analog-to-digital units (ADU) in that pixel. The $(\langle x \rangle, \langle y \rangle)$ centroid is calculated over a square region containing N pixels. To improve centroid accuracy and remove any time dependence in the thermal background, an average background value is calculated over a one-pixel perimeter surrounding the centroid region and is subtracted from each of the N pixels. This centroiding method offers a linear response to sub-pixel motion and is robust against imperfections in the telescope PSF.

The calculated centroid of an infinite illumination pattern over a finite number of pixels necessarily carries a reduced sensitivity to the true stellar position (Helstrom 1964; Down 1992; Ma et al. 2009). The centroid measurement sensitivity, defined here as the ratio of measured position to true position, is plotted as a function of the centroiding box width in Figure 4.20. Sensitivity increases with the size of the centroiding box at the cost of added noise from additional pixels. For a given illumination pattern, a box size can be chosen to optimize the sensitivity and noise. Figure 4.20 shows that for an Airy spot, the centroid box should extend at least to the first Airy minimum for >95% sensitivity.

A star of fixed brightness and location will still exhibit a time varying centroid measurement due to the influence of detector noise and the Poisson statistics of photon counting. The centroid measurement variance is a function of the noise in each pixel. The relevant noise sources are uncorrelated; the variance of Eq. (4.7) can be expressed as follows:

$$\begin{aligned} \sigma^2_{\langle x\rangle} &= \sum_i^N \sigma^2_{C_i} \left(\frac{\partial \langle x\rangle}{\partial C_i}\right)^2 \\ &= \frac{\sum_i^N \sigma^2_{C_i} \left(x_i - \langle x\rangle\right)^2}{\left(\sum_i^N C_i\right)^2} \end{aligned} \tag{4.8}$$

$$\sigma^2_{C_i} = \sigma^2_{RN} + GD_i + GP_i + \frac{1}{12} \tag{4.9}$$

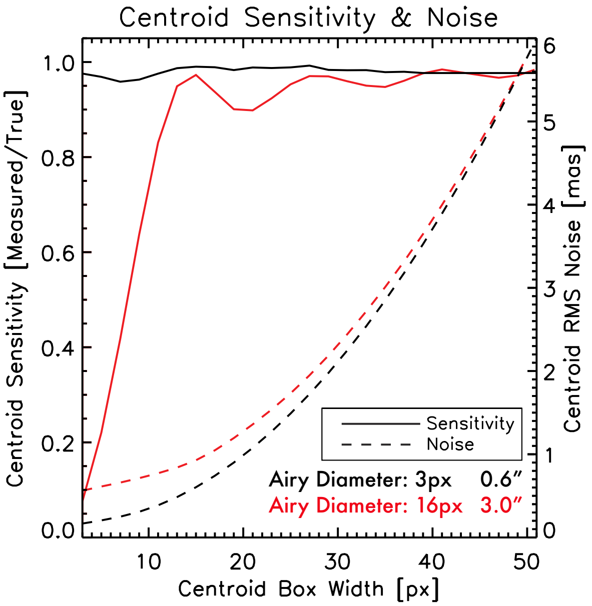

Figure 4.20: The modeled FPS centroid measurement sensitivity and noise as a function of centroid box size for two different Airy spots. A $m_v = 2$ star is used with a 5 ms exposure time and typical angle tracker CCD noise values. In this simulation, the star is positioned at the center of a pixel and the minimum box width is 3 px.

where σ_{RN} is the RMS read noise per pixel, D_i is the number of dark counts in the i^{th} pixel, P_i is the number of photon counts in the i^{th} pixel, G is the analog-to-digital conversion gain in (ADU/e-) and 1/12 is the digitization noise (Buil 1991). Eq. (4.8) shows that for a star of a given brightness, the centroid measurement noise grows with the size of the PSF because the noise in pixels farther from the centroid is given more weight. The noise also increases with the number of pixels used in the calculation – as seen in Figure 4.20.

The angle tracker plate scale ($0.19''/px$) was chosen to pair well with the $0.26''$ diffraction limit of the 0.5 m PICTURE telescope to produce a minimal centroid calculation box of 2×2 or 3×3 pixels for low noise and high sensitivity. For targets near the full-well brightness limit of the angle tracker CCD, the centroid noise equivalent angle (NEA) can approach 0.1 mas RMS at 95% sensitivity.

4.8.4 Fast Steering Mirror Resolution & Noise

The characteristics of the FSM electronics limit the system's ability to stabilize the stellar pointing. The least significant bit (LSB) of the 16-bit 20V DAC that controls the FSM amplifiers defines the absolute lower limit of the control authority. The 1.1 mV amplified DAC LSB provides a projected FSM tip-tilt beam-control resolution of 0.22 mas on the sky.

FSM jitter induced by amplifier noise at frequencies greater than the angle tracker Nyquist frequency (half the system-rate) does not couple well to the centroid measurement. At frequencies much greater than the system rate, the effect is a slight, sub-pixel blurring of the stellar spot. This adds a negligible amount of variation to the calculated centroids. These high-frequency errors pass straight through to the nuller and limit its performance. The FSM amplifiers are specified to deliver 1.6 mV RMS noise (0.42 mas NEA) integrated from 0-100 kHz. To calculate the true high-frequency mirror jitter, the amplifier noise spectrum should be multiplied by the FSM response function and integrated over frequencies above the angle tracker Nyquist frequency. In the context of the PICTURE flight, which performed at 5.1 mas RMS, this is a small effect; however, I will consider this noise term for future flights in Section 6.4.

4.8.5 Spacecraft Environment

The performance of the FPS is ultimately limited by the environment in which it operates. Characterizing the ambient pointing environment over a wide spectral range is a necessary step in the design of any image stabilization system. The NASA sounding rocket ACS mixes on-board gyroscope rates with the output of an ST-5000 star tracker camera (Percival et al. 2007) to measure the fine-scale body pointing of the payload at the sub-arcsecond level. The ACS controller uses these measurements to command the linear thrust modules, which control the rocket attitude. The ACS attitude measurement becomes noise limited at a level of $\sim$30 mas RMS. To estimate the true high-frequency ACS response below the noise floor, the ACS engineers have developed a flight dynamics simulator that operates the flight thrust commands on a computer model of the payload. Simulations of previous flights were used to develop two FPS flight modes capable of delivering $<$10 mas RMS residual pointing error from the rocket ACS platform. The 200 Hz and 1 kHz modes are diagrammed in Figure 4.19. The 200 Hz FPS mode operates with a $\sim$5 Hz closed-loop bandwidth (see Section 6.4). A well-tuned PID controller acts as a high-pass filter; pointing jitter below the bandwidth frequency is greatly attenuated and jitter at higher frequencies passes through. The ACS simulator predicted no resonances and $\sim$1 mas RMS residual jitter above the FPS $\sim$5 Hz bandwidth. ACS flight dynamics simulations of the PICTURE flight will be compared to flight data in Section 6.3.1.

Chapter 5

PICTURE: Pre-Flight Testing

5.1 Introduction

The following sections will present a number of pre-flight tests that were performed on the various PICTURE subsystems to verify their performance.

5.2 Fine Pointing System Gain Tuning

The PICTURE Fine Pointing System (FPS) employs a Proportional + Integral + Differential (PID) closed-loop servo controller to stabilize the stellar spot on the angle tracker camera using a fast steering mirror (FSM). The PID loop provides negative feedback to the FSM based on the error between the stellar centroid and a predefined target. The details of the FPS system as a whole are given in Section 4.8.

The response of the PID loop is determined by three gain parameters: K_P, K_I and K_D. The jth mirror position (FSM_j) is calculated as

$$FSM_j = FSM_{j-1} + K_P P_j + K_I I_j + K_D D_j, \tag{5.1}$$

where,

$$\begin{aligned} P_j &= e_j \\ I_j &= I_{j-1} + e_j \\ D_j &= \frac{e_j - e_{j-1}}{\Delta t}, \end{aligned} \tag{5.2}$$

and e_j is the error signal – the measured offset between the stellar spot and the target. By convention, to provide negative feedback the K_P, K_I and K_D gains are assigned negative values between 0 and -1.

The general role of the proportional term in Eq. 5.1 is to increase the system response to transient events. The integral controller removes the steady-state error and the derivative controller reduces the correction over-shoot and increases stability.

The PID gains must be tuned to provide optimal tracking performance. Gain values that are too large can cause the system to become unstable and oscillate. Gain values that are too small give a weak response. The system stability will be quantified in the following section. A simple technique was devised to tune the FPS gain parameters for flight. Instead of tracking a moving star to a stationary target, the FPS is reconfigured to track a stationary star to a moving target. The tracking error is computed as the offset between the moving target and the stellar centroid. Any user-defined target pattern can then be tested.

To find the highest performance gain values, a grid of test gain values is defined that spans the $K_P \times K_I \times K_D$ space. A 30 second tracking test is run for each gridpoint. The target pattern used for each test is a $1''$ amplitude sine wave with a maximum drift rate of $0.2''$/s. This test pattern approximates the typical sounding rocket Attitude Control System (ACS) response.

A small sample of gain-tuning test results is shown in Figure 5.1. These plots show the power spectral density (PSD) of the measured pointing error. The mid-frequency (1-10 Hz) response is seen to increase with increasing proportional gain. The integral controller is implemented to remove the steady-state error and low-frequency disturbances. As expected, a large increase in the low-frequency performance is seen when the integral term is enabled. The effect of the derivative controller

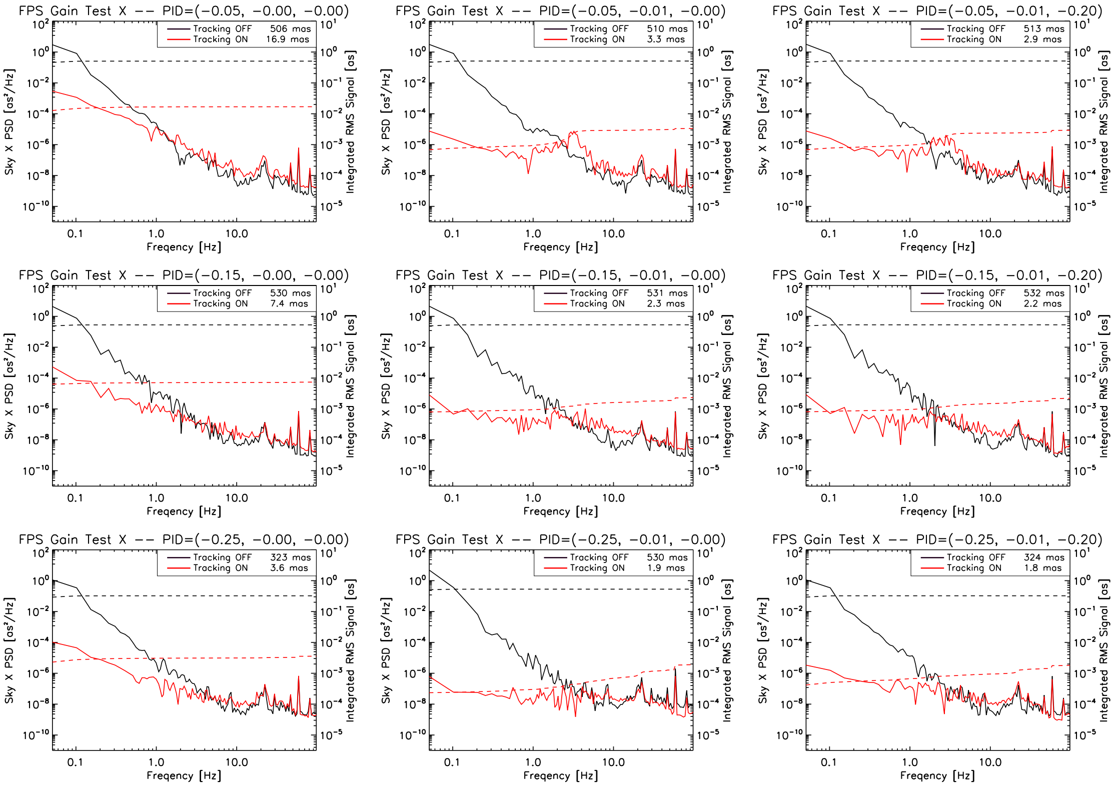

Figure 5.1: FPS gain-tuning power spectra are plotted over a grid of (K_P,K_I,K_D) values. The gain values are given at the top of each plot. The black line represents the moving target – the tracking “OFF” response. The red line represents the stabilized spot position. The dashed lines plot the cumulative integral of the PSD on the right-hand Y-axis. The integrated RMS error is shown in each plot legend. The first column shows tests with only K_P gain. The second shows tests with K_P and K_I gain. The third shows tests with all three gains enabled.

is the most subtle. Increased derivative gain only marginally improves performance. It is likely this term increases the stability of the controller.

Using gain tests similar to the one shown in Figure 5.1, flight gain values of $K_P = -0.25$, $K_I = -0.1$ and $K_D = -0.1$ were chosen. Analysis of the FPS flight performance is presented in Chapter 6.

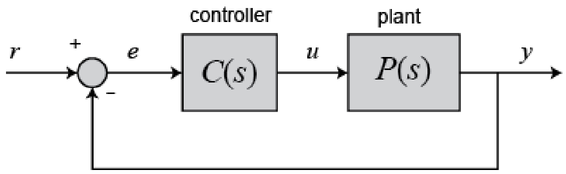

Figure 5.2: FPS control system block diagram.

5.3 Fine Pointing System Performance and Stability

To analyze the performance and stability of the FPS servo controller, a model of the system was constructed using the Matlab control systems package. A block diagram of the FPS control system is shown in Figure 5.2. This block diagram is constructed using the conventional language and mathematics of control theory. The components of the system are the plant $P(s)$ and the controller $C(s)$. These concepts require some introduction.

5.3.1 Building the Model

The plant $P(s)$ is the object the operator wishes to control. The plant has an input u and output y. The circle represents the "adder" or "combiner." Its function is to calculate the error signal e from the measured plant output y and a reference value r. The error signal is the input to the controller $C(s)$. The job of the controller is to calculate the plant input u that reduces the error signal to zero. This is accomplished using negative feedback.

In the model of the FPS, the plant represents the FSM and the angle tracker camera. The plant uses the FSM to move the stellar spot on the angle tracker. That is its only function. To maintain consistency with Eq. 5.1, the plant input u is defined as the differential change to the current FSM position. The position corrections are integrated within the plant to arrive at the current FSM position. The plant output

y is the measured spot centroid on the angle tracker. The error signal, $e(t) = y(t) - r$, is the difference between the measured spot position and the fixed target position r.

The next step is to construct the plant transfer function $P(s)$. A transfer function is defined as the ratio between the output and input of any system. In control theory, transfer functions are written not in the time domain, but in the Laplace transform of the time domain. The Laplace transform operates on a function of a real variable $f(t)$ to produce a function of a complex variable $F(s)$. When t represents time, s represents the complex frequency

$$s = \sigma + i\omega. \tag{5.3}$$

The Laplace transform $F(s)$ of a function $f(t)$ is defined as

$$F(s) = \int_0^\infty e^{-st} f(t)\,\mathrm{d}t. \tag{5.4}$$

The first component of the plant transfer function represents $q(t)$, the integral of the commanded position updates.

$$q(t) = \int u(t)\,\mathrm{d}t, \tag{5.5}$$

The transfer function ($Q(s)$) is found by taking the Laplace transform of Eq. 5.5.

$$Q(s) = \frac{1}{p\,s} \tag{5.6}$$

Here, p is the FPS update period. The 200 Hz FPS mode has a value of $p = 0.005$ seconds.

The second component of the plant transfer function is a model of the FSM open-loop response. The mirror actuator is a Physik Instrumente (PI) S-316 three-axis piezoelectric transducer (PZT) stage. The actuator loaded with a 1-inch mirror has a resonant frequency of $f_0 = 3.4$ kHz. The PZT resonant frequency is analogous to the harmonic frequency of a mass hanging from a spring. It is a function of the mass of the system and the stiffness of the material. The time τ taken by the actuator to reach a commanded position is approximately one third the resonant period. This is given as a rule of thumb by the manufacturer.

$$\tau = \frac{1}{3f_0} = 9.8 \times 10^{-5} \text{ seconds} \tag{5.7}$$

PZT actuators are capacitive devices. The displacement function $z(t)$ of a PZT follows the same form as a charging capacitor,

$$z(t) = 1 - e^{\frac{-t}{t_0}} \tag{5.8}$$

where, t_0 is the characteristic rise time, or "e-folding" time for the actuator expansion. Recasting the rule of thumb given in Eq. 5.7, the rise time can be written

$$t_0 = \frac{\tau}{6} = 1.6 \times 10^{-6} \text{ seconds.} \tag{5.9}$$

The PZT transfer function is found by taking the Laplace transform of Eq. 5.8.

$$Z(s) = \frac{1}{t_0\, s + 1} \tag{5.10}$$

The PZT step-function response is plotted in Figure 5.3. The PZT model does indeed reach full extension in the correct time, $\tau = 9.8 \times 10^{-5}$ s.

The last component of the plant transfer function represents the latency of the system. In Laplace space, delays are written as exponential functions of s. The delay associated with the 200 Hz FPS is $\Delta t = 0.0057$ s. This represents the age of the measured centroid at the time when the FSM is updated. This value is defined as

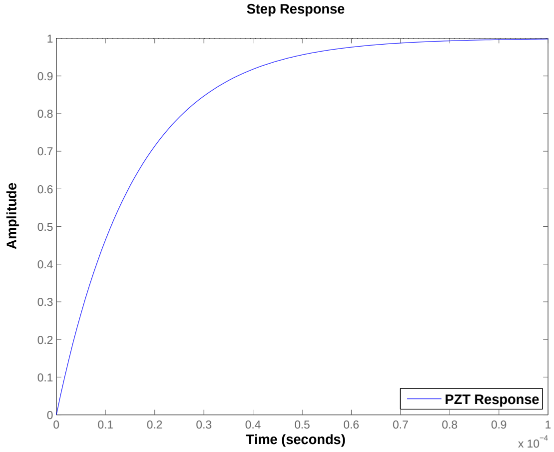

Figure 5.3: Model PZT step-function response. The PZT reaches its commanded position in a time τ equivalent to approximately one third the resonant period, a value of 9.8×10^{-5} s for the FSM PZT.

the "data age" in Figure 4.19. The delay transfer function is then

$$D(s) = e^{-\Delta t\, s}. \tag{5.11}$$

The complete plant transfer function is then the product of these three components.

$$\begin{aligned} P(s) &= Q(s) \times Z(s) \times D(s) \\ &= e^{-\Delta t\, s} \frac{1}{p\, t_0\, s^2 + p\, s} \end{aligned} \tag{5.12}$$

The system controller $C(s)$ is a PID controller. The PID output $c(t)$ is

$$c(t) = K_P\, e(t) + K_I \int e(t)\, \mathrm{d}t + K_D \frac{\mathrm{de}}{\mathrm{d}t}. \tag{5.13}$$

In reference to Figure 5.2, $c(t) = u(t)$, the controller output equals the plant input. The PID transfer function $C(s)$ is the Laplace transform of Eq. 5.13.

$$\begin{aligned} C(s) &= K_P + \frac{K_I}{s} + K_D\, s \\ &= \frac{K_D\, s^2 + K_P\, s + K_I}{s} \end{aligned} \tag{5.14}$$

The transfer function of the entire system $S(s)$ is the product of the controller and plant transfer functions

$$\begin{aligned} S(s) &= C(s) \times P(s) \\ &= e^{-\Delta t\, s} \frac{K_D\, s^2 + K_P\, s + K_I}{p\, t_0\, s^3 + p\, s^2} \end{aligned} \tag{5.15}$$

where, Δt is the system delay, p is the system update period, t_0 is the characteristic rise time of the PZT, and K_P, K_I and K_D are the PID gains.

5.3.2 Model Performance Analysis

With a model transfer function for the entire FPS, the Matlab control systems toolkit can be used to calculate the expected performance and stability of the system. To begin, the flight PID gains are plugged into the modeled transfer function. This will be referred to as the "flight" model. For comparison, the transfer functions of two other systems are also calculated. The first system is the FPS model with optimized PID gains determined by the Matlab *pidtune()* function. The optimized values are $K_P = -0.42$, $K_I = -0.02$ and $K_D = 0$ compared to the flight values of $K_P = -0.25$, $K_I = -0.1$ and $K_D = -0.1$. This will be referred to as the "optimized" model. The second system uses a modified model of the plant that does not included the integrator defined in Eq. 5.6. Since the PID controller already includes an integrator, a second integrator in the plant is not necessary for closed-loop control. The "single-

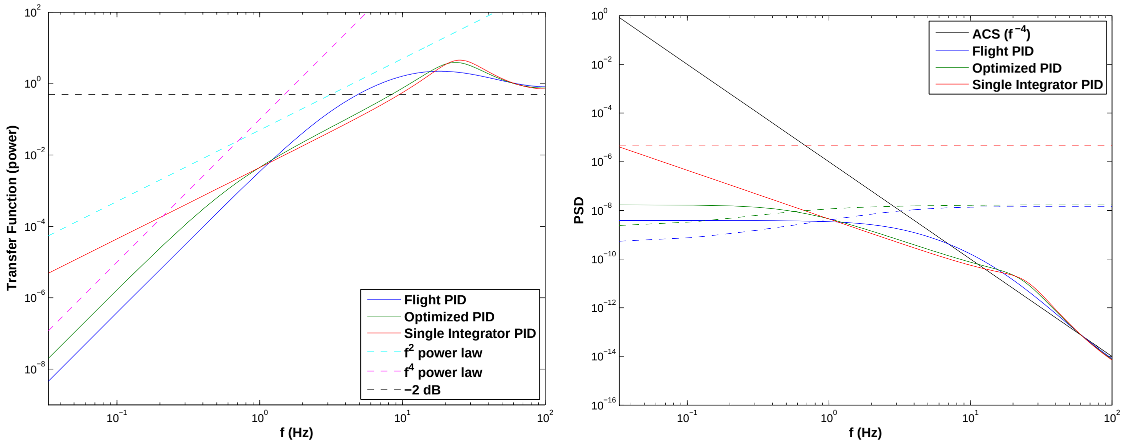

Figure 5.4: Closed-loop transfer functions (*left*) and power spectra (*right*) for the modeled PID controllers. A horizontal dashed-line is drawn at -3 dB in the transfer function plot to define the tracking bandwidth. Dashed lines in the PSD plot show the cumulative integral of the pointing error. The PSD of the ACS pointing is modeled as an f^{-4} power law.

integrator" model transfer function is

$$\begin{aligned} S_1(s) &= C(s) \times Z(s) \times D(s) \\ &= e^{-\Delta t\, s} \frac{K_D\, s^2 + K_P\, s + K_I}{t_0\, s^2 + s}. \end{aligned} \tag{5.16}$$

The described model transfer functions are open-loop transfer functions. The Matlab *feedback()* function is used to calculate the closed-loop transfer function of each model in feedback. The closed-loop transfer function describes the disturbance attenuation as a function of frequency. These curves are plotted for each model in Figure 5.4.

Examination of Figure 5.4 reveals many important characteristics of the different controllers. The flight controller follows an f^4 power law and provides the best low-frequency attenuation. The single-integrator controller follows an f^2 power law and provides better high-frequency performance. The optimized controller looks like a hybrid of the two; it follows an f^4 power law at low frequencies and an f^2 power law at high frequencies.

The closed-loop bandwidth of each controller is also shown in Figure 5.4. The bandwidth is defined as the frequency range over which the attenuation is less than -3 dB. The flight controller has an estimated bandwidth of 5 Hz. The optimized and single-integrator controllers have 9 Hz and 10 Hz bandwidths respectively.

The flight controller sacrifices bandwidth to provide better low-frequency attenuation. This is an appropriate trade-off given that the rocket ACS pointing environment exhibits very little high-frequency noise. The PSD of the ACS is shown to follow an f^{-4} power law in Chapter 6. To calculate the PSD of each controller in the flight environment, their respective closed-loop transfer functions are multiplied by an f^{-4} model of the ACS. These power spectra are also shown in Figure 5.4. The integral of the power spectrum is the RMS pointing error. The flight PID controller offers the best RMS performance. Relative to the flight controller, the RMS pointing errors from the optimized and single-integrator controllers are 1.1 and 18 times worse respectively.

5.3.3 Model Stability Analysis

The stability of a control system is commonly expressed in terms of two numbers, the gain margin and the phase margin. Treating the FPS system as a simple amplifier with one input and one output, an input wave is amplified by the open-loop gain factor G_{OL} and experiences a phase delay ϕ. Both of these numbers are combined to form the complex open-loop gain A_{OL}

$$A_{OL} = G_{OL} + i\phi \tag{5.17}$$

The complex closed-loop gain A_{CL} of the system in feedback is written

$$A_{CL} = \frac{A_{OL}}{1 + A_{OL}}. \tag{5.18}$$

This expression has one point of instability, or “pole” where $A_{OL} = -1$. If this condition is satisfied, the closed-loop gain becomes infinite and the system becomes unstable. In the FPS, instability is seen as the rapid oscillation of the FSM between its minimum and maximum tilt angles.

An important tool for examining the stability of a control system is the Bode diagram. A Bode diagram plots both components of the complex open-loop gain, the scalar gain G_{OL} and the phase delay ϕ, as functions of the system input frequency. The Bode diagrams and step response functions for the three modeled controllers are displayed in Figure 5.5.

Two characteristic frequencies are defined from the Bode diagram. The phase crossover frequency f_{180} marks the frequency at which the phase delay reaches exactly -180°. At this point, the output signal is exactly one half wave out of phase with the input signal. The gain crossover frequency f_{0dB} marks the frequency at which the gain reaches unity (0 dB). The instability condition $A_{OL} = -1$ is satisfied if $f_{180} = f_{0dB}$.

Two numbers are defined to gauge how far the system is from becoming unstable. At the gain crossover frequency, the phase margin PM defines the distance between the phase and -180°. At the phase crossover frequency, the gain margin GM defines the distance between the gain and unity. The larger both of these margins are, the more stable the system is.

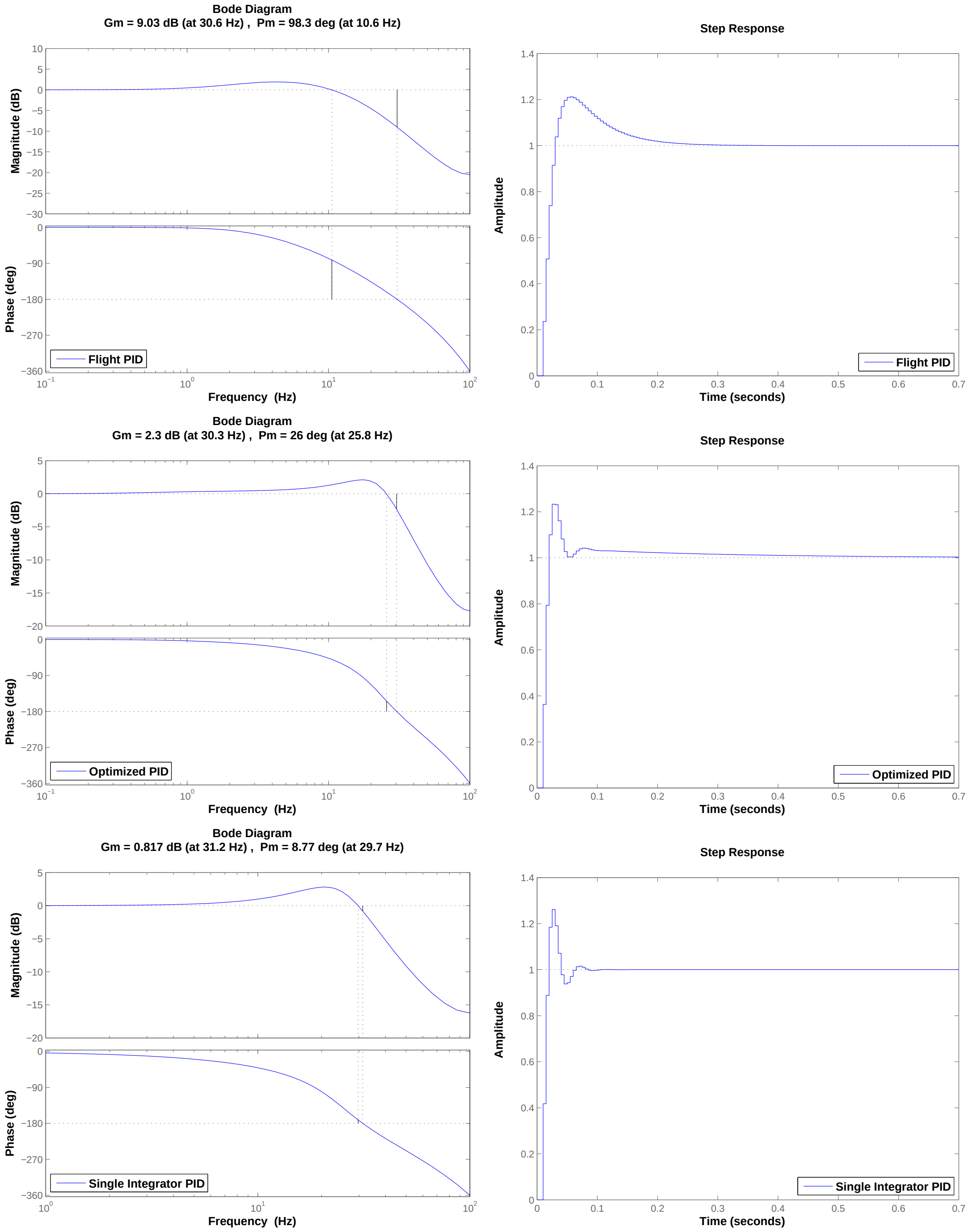

Figure 5.5: Bode diagrams (*left*) and step response functions (*right*) for the modeled PID controllers.

From Figure 5.5, we see the estimated gain margin of the flight system is GM=9.0 dB at the phase crossover frequency $f_{180} = 30.6$ Hz. The phase margin is PM=98.3° at the gain crossover frequency $f_{0dB} = 10.6$ Hz. These values represent a very stable system. Rules of thumb for stability are GM>8 dB and PM>45°(Phillips & Harbor 1991).

The optimized gains provide a much smaller stability margin, GM=2.3 dB at 30.3 Hz and PM=26.0° at 25.8 Hz. The single-integrator stability margins are also much smaller than the flight system, GM=0.8 dB at 31.2 Hz and PM=8.7° at 29.7 Hz. The discussed parameters for all three modeled controllers are summarized in Table 5.1.

Controller	BW	Rel. RMS	GM	PM
Flight PID	5 Hz	1	9.0 dB at 30.6 Hz	98.3° at 10.6 Hz
Optimized PID	9 Hz	1.1	2.3 dB at 30.3 Hz	26.0° at 25.8 Hz
Single-Int. PID	10 Hz	18	0.8 dB at 31.2 Hz	8.77° at 29.7 Hz

Table 5.1: The bandwidth (BW), relative RMS tracking error (Rel. RMS), gain margin (GM) and phase margin (PM) are listed for each modeled controller.

5.4 Wavefront Control System Noise Analysis

As discussed in Section 4.7.2, the Wavefront Control System (WCS) phase measurement is made using 4 ABCD images at 1/4 wave spacing. The phase is calculated using the equation

$$\phi = ArcTan\left[\frac{B-D}{A-C}\right]. \tag{5.19}$$

The ability of the nuller to remove phase errors depends on the influence of image noise on this calculation. The phase measurement is averaged over the number of wavefront sensor (WFS) image pixels (N) that span each deformable mirror (DM) actuator. For the PICTURE WCS, $N = 4$. The statistical error in the the phase measurement for each actuator is calculated from Eq. 5.19.

$$\begin{aligned}\sigma_\phi &= \frac{1}{\sqrt{N}}\sqrt{\left(\frac{\partial\phi}{\partial A}\sigma_A\right)^2 + \left(\frac{\partial\phi}{\partial B}\sigma_B\right)^2 + \left(\frac{\partial\phi}{\partial C}\sigma_C\right)^2 + \left(\frac{\partial\phi}{\partial D}\sigma_D\right)^2} \\ &= \frac{1}{\sqrt{N}}\frac{\sqrt{(B-D)^2\left(\sigma_A^2+\sigma_c^2\right)+(A-C)^2\left(\sigma_B^2+\sigma_D^2\right)}}{(A-C)^2+(B-D)^2} \end{aligned} \tag{5.20}$$

The noise in each image pixel represents contributions from Poisson counting noise, read noise and dark current.

$$\begin{aligned}\sigma_A &= \sqrt{A+\sigma_{RN}^2+\sigma_{DC}^2} \\ \sigma_B &= \sqrt{B+\sigma_{RN}^2+\sigma_{DC}^2} \\ \sigma_C &= \sqrt{C+\sigma_{RN}^2+\sigma_{DC}^2} \\ \sigma_D &= \sqrt{D+\sigma_{RN}^2+\sigma_{DC}^2}\end{aligned} \tag{5.21}$$

Here the pixel values (A,B,C,D) express the number of photo-electrons in each pixel. The average WFS read noise is $\sigma_{RN} = 3$ e-/px and the noise contribution from the dark current is $\sigma_{DC} = 1$ e-/px for one 0.25 s exposure.

Using flight WFS data, an accurate calibration of the system throughput was made for the calibration target, Rigel. This calibration is used to plot the WCS phase measurement error as a function of stellar brightness in Figure 5.6. Using 0.25 s exposures, the bright signal from Rigel limits the phase measurement to ∼1 nm RMS (0.009 rad). This places a limit on the null depth N_D, which can be calculated from the nuller transmission function (Eq. 4.2). The null depth is defined as the ratio between the dark transmission fringe and the bright transmission fringe.

$$N_D = \frac{1-cos(\sigma_\phi)}{1-cos(\sigma_\phi+\pi)} \tag{5.22}$$

The null depth limit imposed by a $\sigma_\phi = 0.009$ rad RMS phase error is $\sim 2\times10^{-5}$.

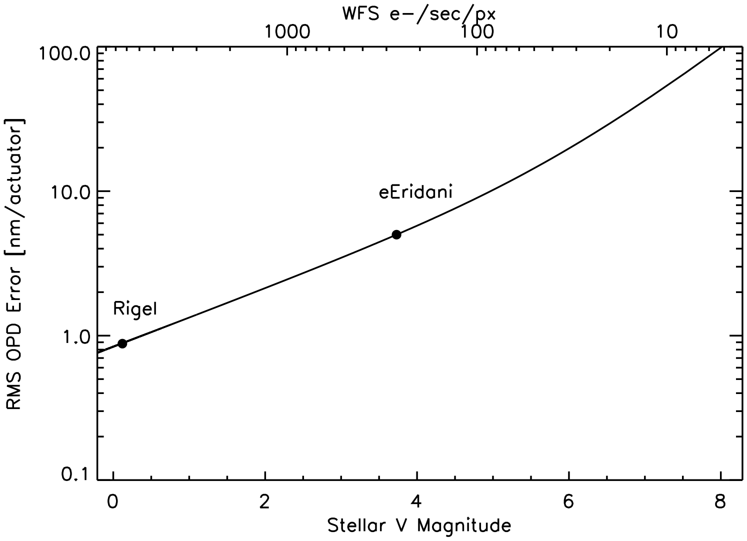

Figure 5.6: WCS phase measurement error as a function of stellar brightness.

5.5 Deformable Mirror Surface Effects

Deformable mirrors suffer from surface deformations on sub-actuator size scales. The effect of these surface errors, which are at the ∼10 nm RMS level for the Boston Micromachines (BMC) MEMS mirrors, is to place a lower limit on the corrected phase error. A simple limit to the null depth can again be calculated using Eq. 5.22. The null depth limit for a 1 nm RMS phase error was $\sim 2\times10^{-5}$. The limit for a 10 nm RMS phase error (0.09 rad) is $\sim 2\times10^{-3}$. As shown in Serabyn (2000), the null depth limit scales as the phase error squared. The spatial variance of the null limit, however, is lost in this RMS calculation. It is important to understand how these sub-actuator phase errors propagate to the image plane in order to find the angular region on the sky with the highest contrast.

To estimate the effects of DM surface errors in the nulled image, a simple model of the nuller is constructed. First, a model of the DM surface is required. The PICTURE DM is a 32×32 actuator BMC MEMS device. Two DM models will be

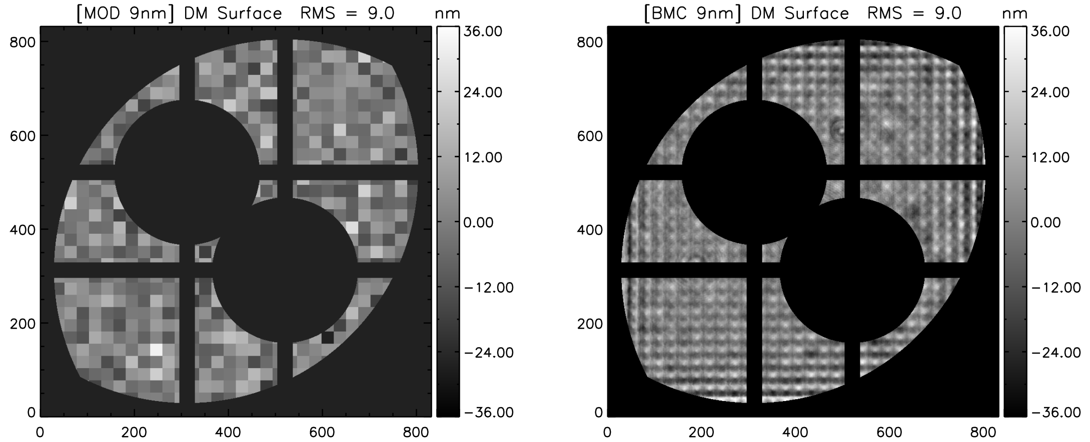

Figure 5.7: Two models of the deformable mirror surface error. *Left:* The simple DM model with 9 nm RMS surface error. *Right:* The realistic BMC model with 9 nm RMS surface error.

compared. The first is a simple 32×32 grid where each actuator is perfectly square and decoupled from its neighboring actuators. This model will be denoted by the abbreviation MOD in all subsequent figures. The second model is generated from a high resolution surface displacement map of a real 32×32 BMC DM. This map was provided by BMC and figures associated with this model will be denoted by the abbreviation BMC.

The typical DM surface error is 9 nm RMS. A version of each DM model is generated with this amount of surface error. These models are shown in Figure 5.7. The BMC map shows the characteristic sub-actuator "scalloping" effect, which is caused by surface constraints from the mirror substrate.

The nulling interferometer (NIF) has two arms, the DM arm and the Nuller PZT (N-PZT) arm. The purpose of the two active elements is to remove optical path difference (OPD) between the two arms at each point in the pupil. To construct a model representation of the two nuller arms, the complex aperture function is first

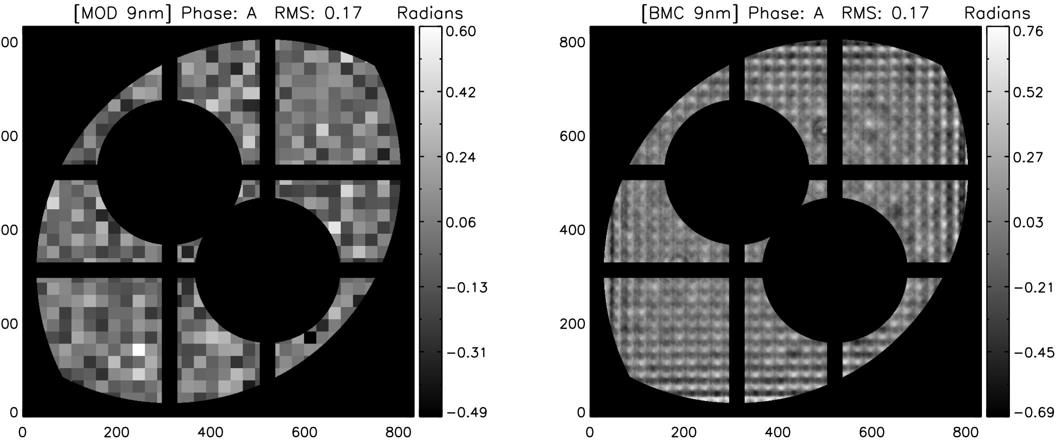

Figure 5.8: Phase errors in the DM arm for both the MOD and BMC models.

defined. The wavefront in a pupil plane can be parametrized by the complex aperture function

$$\Psi = A + i\phi \tag{5.23}$$

where, A is the electric field amplitude and ϕ is the phase of the wavefront. The aperture functions Ψ_{DM} and Ψ_{PZT} are defined for each arm. The phase components of the DM aperture functions are, accounting for reflection, twice the surface error. These components are shown in Figure 5.8. No amplitude errors are included in these models. The amplitude function for each arm is set to 1 everywhere within the pupil mask.

The combined system aperture function $\Psi = \Psi_{DM} + \Psi_{PZT}$ is the sum of the aperture functions of each arm. The illumination pattern in the image plane is found by taking the square of the Fourier transform of the aperture function. Images of the bright and dark outputs are created using PZT phase values of $\phi_{PZT} = 0$ and $\phi_{PZT} = \pi$ respectively. The simulated bright and dark images for both DM models

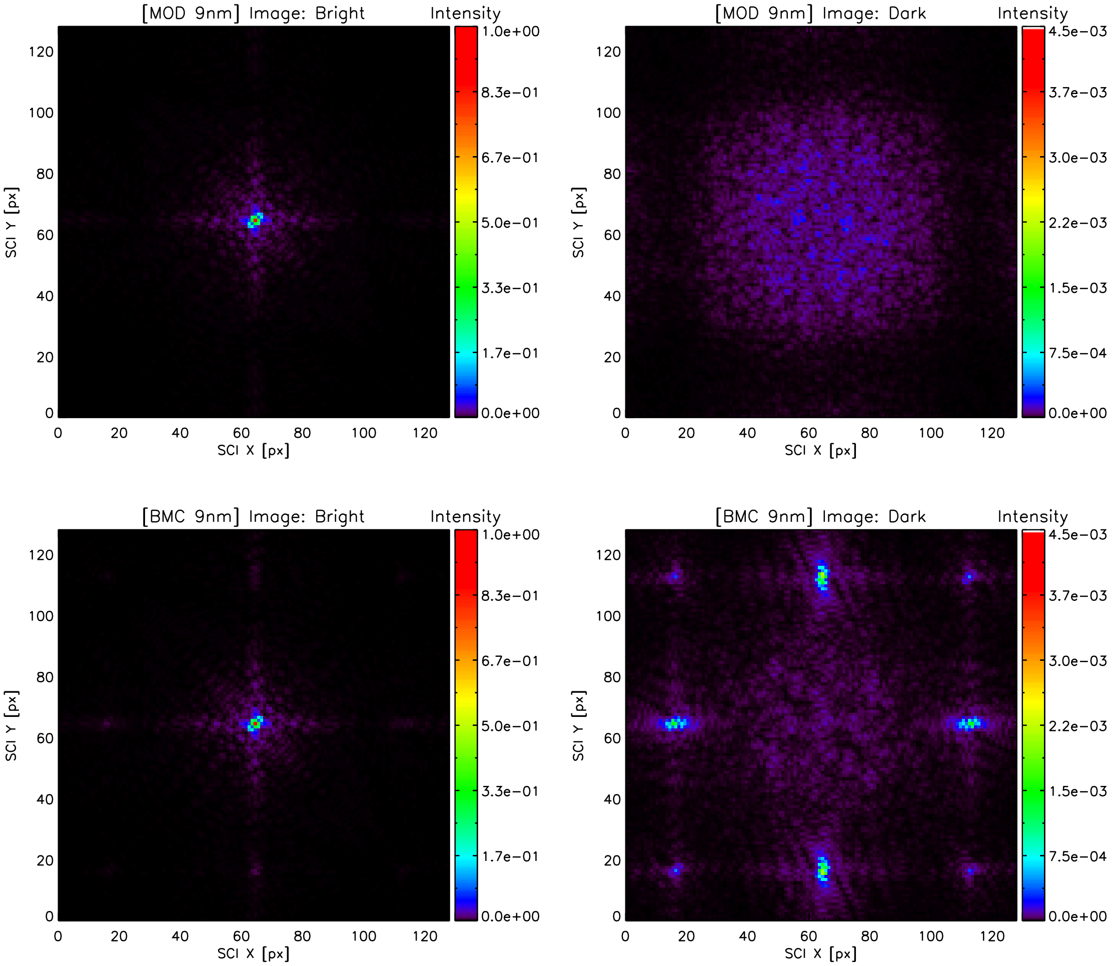

Figure 5.9: Simulated bright and dark science camera images

are shown in Figure 5.9. These images are presented in the correct PICTURE science camera plate scale of $0.18''$/px.

The bright images for both models in Figure 5.9 appear nearly identical – the small phase errors have little effect. Comparing the dark images of both models, strong symmetric peaks are seen in the BMC dark image that correspond to the characteristic angular spacing of $32\,\lambda/D = 8.9''$ (45 px). These features are created by the periodic scalloping pattern in the BMC DM model. A spatially periodic phase error in the pupil projects light into a specific angle in the image. The MOD dark image is much more uniform. There is no spatial coherence in the random errors of the MOD DM. This white-noise error leads to evenly distributed speckles across the image. Although the BMC dark image contains 8 bright speckles, the center is darker than the MOD image.

To gauge the effect of DM surface errors on the performance of the nuller, two measurements of contrast are made from the models. First, the pixel-to-pixel contrast is calculated by dividing the dark image by the bright image. These contrast maps are shown in Figure 5.10. For comparison, an additional set of models are created with 1 nm RMS surface errors. The null depth has been shown to vary proportional to the phase error squared. Indeed, the 1 nm errors produce, on average, 100 times higher contrast. Due to the darker central region of the BMC image, the contrast in this region is slightly higher.

The inner working angle (IWA) of the PICTURE nuller is 1.77 $\lambda/D = 0.48''$. At a distance of 3.2 pc to ϵ Eridani, this corresponds to a projected length of 1.5 AU. The target science region in the PICTURE field of view extends to ∼3 times the inner working angle, 4.5 AU. The science region is drawn on each contrast map in Figure 5.10. The most realistic model of the PICTURE DM is the BMC 9 nm model. In this contrast map, the starlight suppression ranges from 10^{-2} to 10^{-3} within the science region.

The second type of contrast map is created by dividing the dark image by the total of the bright image. These are shown in Figure 5.11. These maps are useful for calculating the expected signal-to-noise ratio (SNR) of a science detection. The total number of photons expected from a star during an exposure can be multiplied by these contrast maps to predict the number of stellar photons in each pixel of the dark image. These leaked stellar photons are the dominant source of noise against which dust and planets must be detected. For the BMC 9 nm model, one out of every 10^5-10^6 stellar photons lands in the science region.

The presented contrast maps are monochromatic and do not include the effects of amplitude error. They serve as upper limits to the nuller performance. In Section 4.3.1, the contrast limit imposed by the $\sim$1% reflectivity errors was estimated to be 1×10^{-5}. This contribution to the stellar leakage is greatly outweighed by the contribution from DM surface errors, which are the greatest source of stellar leakage in the system.

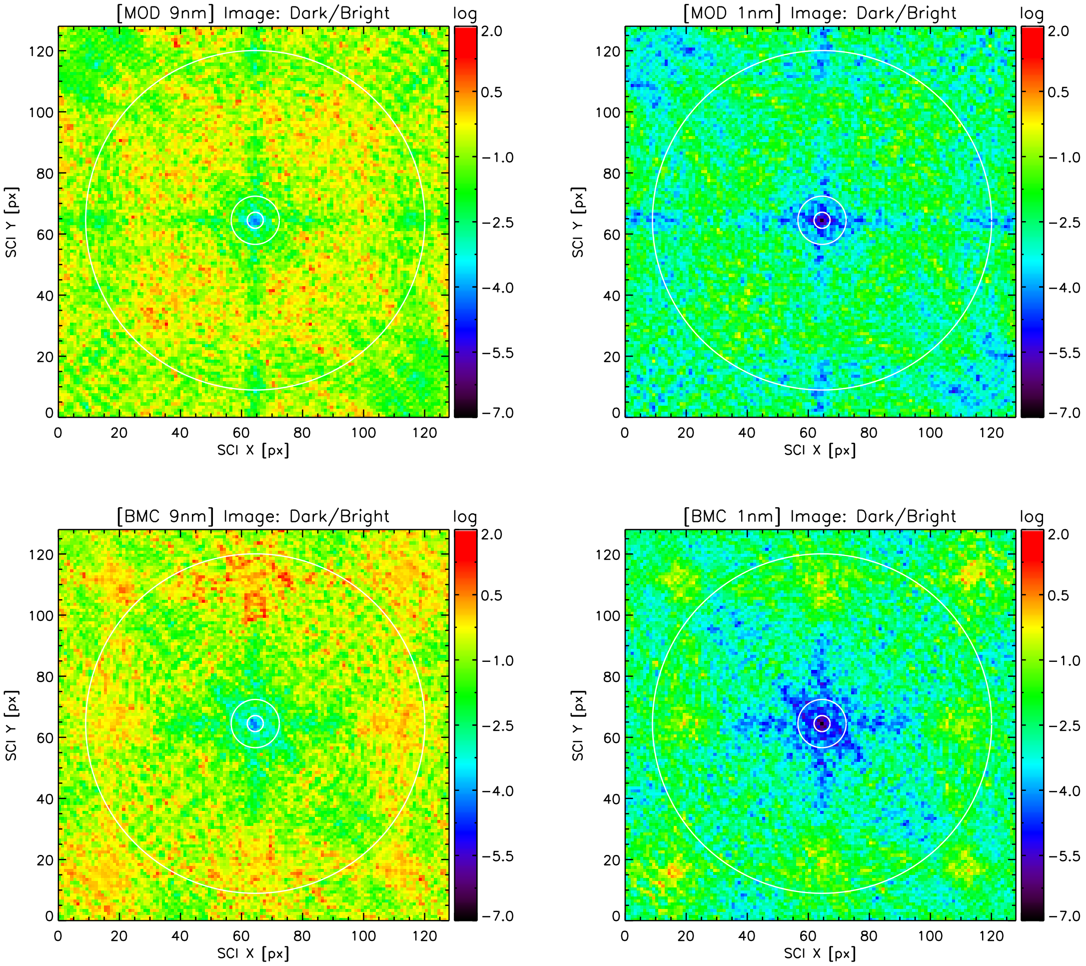

Figure 5.10: Simulated pixel-to-pixel contrast between the bright and dark images. *Left:* The BMC and MOD contrast maps for a DM with 9 nm RMS surface error. *Right:* The same for a DM with 1 nm RMS surface error. The inner white circle marks the inner working angle of the nuller ($1.77\ \lambda/D = 0.48''$). The middle circle positioned at $1.5''$ defines the outer edge of the target science region. The outer white circle is positioned at a radius of $10''$.

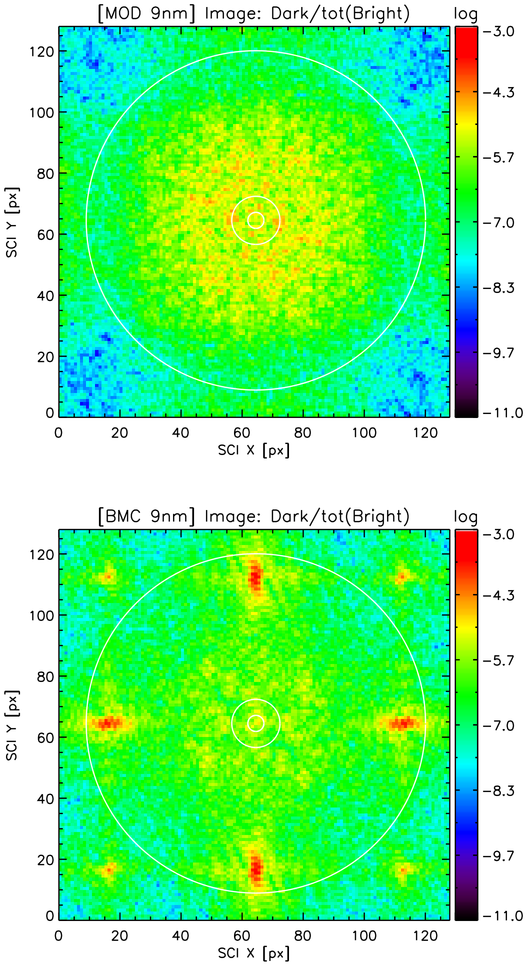

Figure 5.11: Simulated contrast between the dark image and the total of the bright image. The inner white circle marks the inner working angle of the nuller (1.77 λ/D = 0.48″). The middle circle positioned at 1.5″ defines the outer edge of the target science region. The outer white circle is positioned at a radius of 10″.

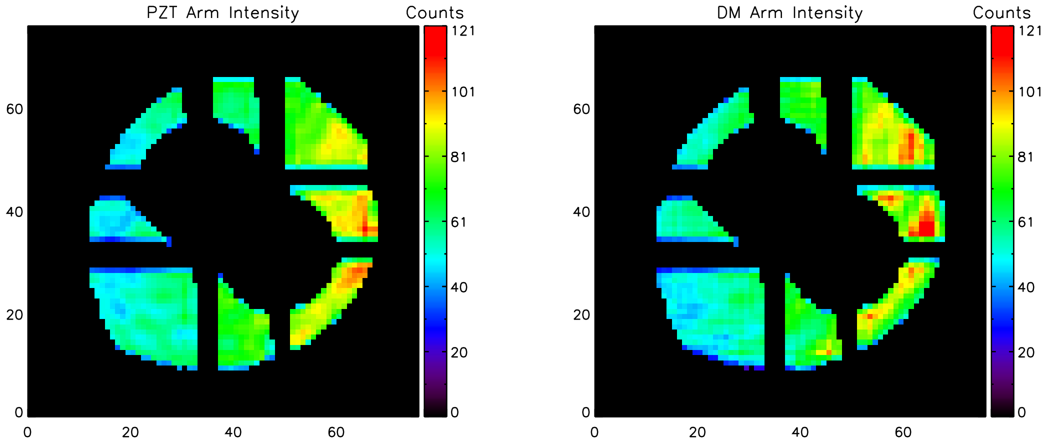

Figure 5.12: DM and N-PZT beam amplitude.

5.6 Nuller Amplitude Measurements

An attempt was made to measure the relative amplitude of the nuller DM and N-PZT arms. Measurements of each beam were made independently with the opposite beam blocked. An average intensity map for each arm is shown in Figure 5.12. It was later discovered that the aperture illumination pattern was not uniform during these tests. Since the beams are sheared with respect to one another, the input beam must be uniform to measure a uniform amplitude in each arm. The effect of non-uniform illumination can be seen in Figure 5.12. The DM illumination pattern resembles the PZT illumination, except it is shifted to the upper left along the shear direction. This effect invalidates the test results. The illumination pattern is shown to be much more uniform in the flight data in Chapter 6.

5.7 Nuller and Telescope Temperature Dependence

During integration, both the telescope and DM arm of the nuller were found to exhibit strong temperature dependence. The physical position of the telescope

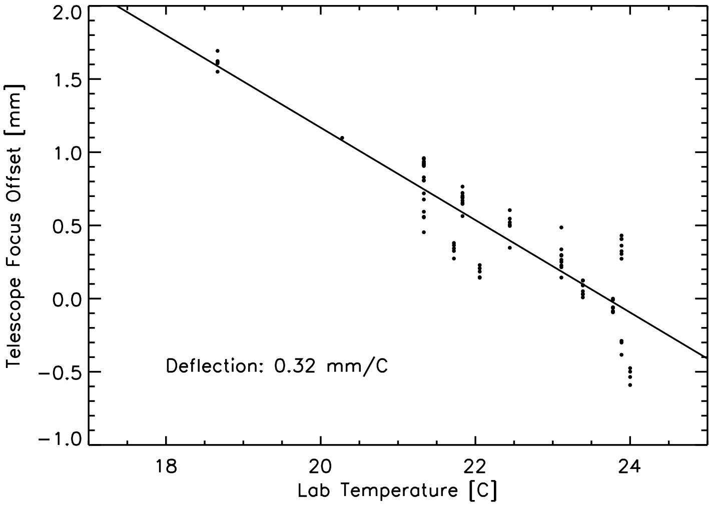

Figure 5.13: Telescope focus thermal dependence. The position of telescope focus shifts along the optical axis 0.3 mm per degree Celsius.

focus is plotted with respect to the laboratory temperature in Figure 5.13. The focus position was found to change by 0.3 mm/°C. The cause of the telescope temperature dependence is likely the bipod mounting structure for the primary mirror.

The path length of the nuller DM arm was found to change with temperature by ∼700 nm/°C. This temperature dependence was observed directly by watching the nuller fringes drift back and forth as the temperature in the lab changed. To measure this effect, the N-PZT was scanned through its full range to measure the position of the white-light fringe packet along the delay line. This was performed at two different temperatures. The results are shown in Figure 5.14. The cause of this temperature dependence has been confined to the DM. It is either the DM mount or the DM chip carrier. Further tests will be performed in the future to isolate the problem.

Given the temperature sensitivity of both the telescope and DM, an alignment temperature of 70° F was chosen for the entire optical system and a launch temper-

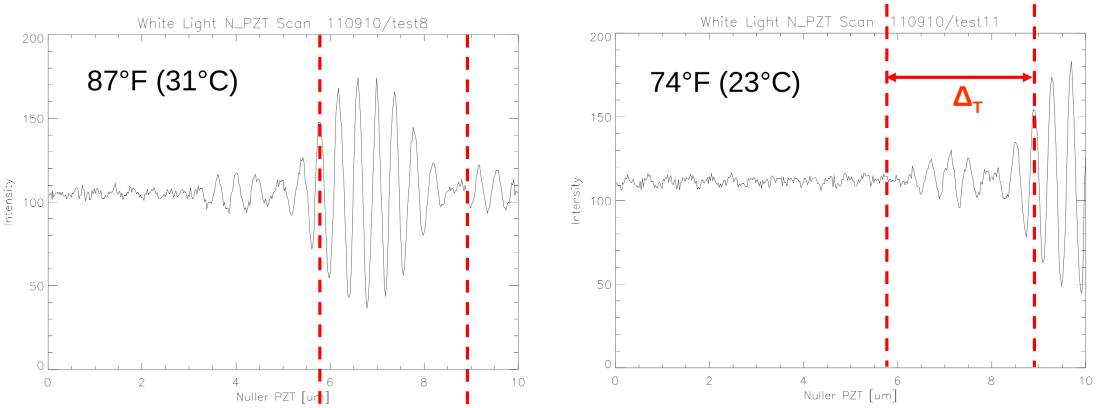

Figure 5.14: Nuller thermal dependence. The position of the white-light fringe packet is observed to shift along the nuller delay line as the temperature of the instrument changes. This is due to a change in physical length of the delay line. The measured deflection is ~700 nm/°C.

ature constraint was established. An environmental enclosure was built around the payload to control the temperature to $70 \pm 5^\circ$ F. The payload was also evacuated prior to launch to maintain thermal stability. Internal temperature sensors were used to monitor the temperature of the nuller and telescope.

5.8 Nuller Alignment

The final flight alignment of the nuller was performed at Boston University after the nuller was delivered by Jet Propulsion Laboratory (JPL). A number of constraints needed to be met during final nuller alignment. First, the nuller input beam was aligned along the correct vector in three-dimensional space. This input vector is the one which hits the center of the angle tracker camera and centers the telescope secondary obscuration behind the Lyot mask. This vector constrains both the tilt and translation of the beam. All of the optics leading up to the nuller were aligned to achieve this input vector while also fully illuminating the pupil. The beam could not be allowed to walk off the edge of any of the optics. With this accomplished, the internal nuller alignment could begin.

The job of the N-PZT is to remove all tip-tilt-piston (TTP) OPD between the two nuller arms. To do this, it must be mounted within 10 μm of the zero OPD location; the PZT stroke is 10μm. Given the temperature sensitivity of both the telescope and DM, this alignment was performed at 70° F. The Pinhole PZT (P-PZT) was then aligned to place the nuller pinhole within its tip-tilt range of motion. The discussed alignment constraints are projected into the image plane in Figure 5.15.

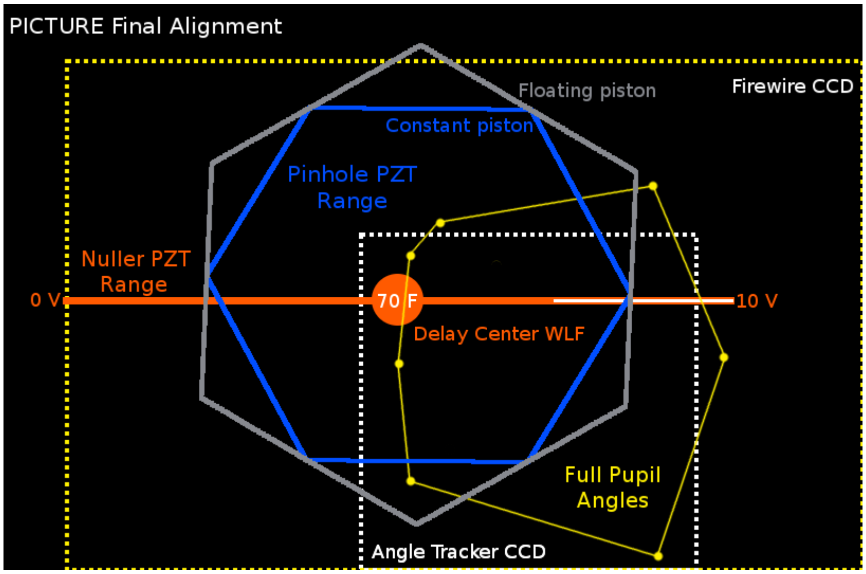

Figure 5.15: Nuller final alignment. All alignment parameters are projected into the image plane and must overlap within the box representing the Angle Tracker CCD. The yellow outline represents those input angles that pass through the instrument and result in a fully illuminate pupil. The orange line represents the range and center of the N-PZT delay line at 70° F (21° C). The angle of the source on the sky (in the shear direction) is equivalent to delay between the nuller arms. The orange line gives the range of angular source positions for which a null can be achieved. The white inset line represents the width of the white-light fringe packet. The blue hexagon represents the angular range of the P-PZT. Input angles falling within this range can be redirected to the pinhole by the P-PZT. The FPS target position was placed inside the overlap region of these constraints.

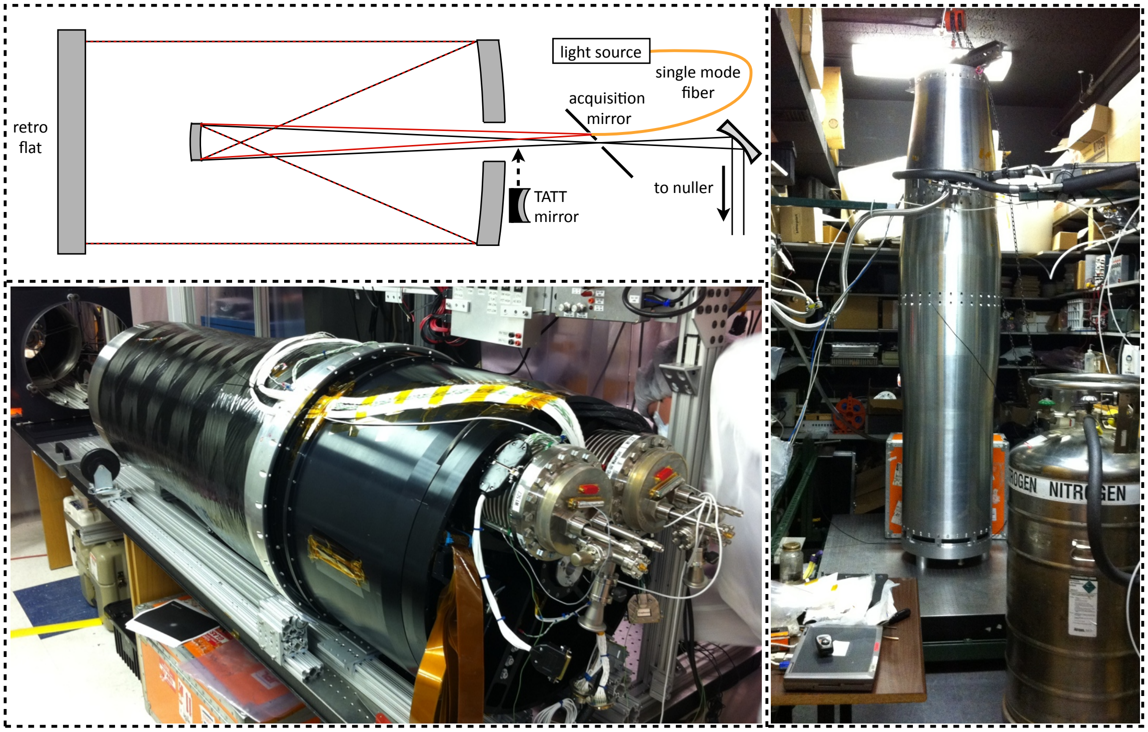

Figure 5.16: PICTURE payload test configurations. Optical layout (*top-left*). Horizontal test configuration (*bottom-left*). Vertical test configuration (*right*). In the vertical configuration, the 0.5 m retro mirror is held inside the endcap fixture. Three jack screws positioned on the bottom of the endcap are used to adjust tip and tilt. The entire payload stands freely on-end atop a floating optical bench.

5.9 End-to-End Payload Testing

End-to-end testing of the payload was conducted in both horizontal and vertical configurations. The testing was performed to demonstrate functionality of the WCS alignment procedure on the full-up payload and to determine if the combined telescope and instrument aberrations were within the capture range of the DM. The test configurations are shown in Figure 5.16 along with a simplified drawing of the optical layout. A single mode fiber was used to inject a test beam at telescope focus through a fiber ferrule that is built into the back of the acquisition mirror and projects back towards the secondary mirror. The test beam runs backwards through the telescope and is retro-reflected with a slight tilt to pass the return beam through

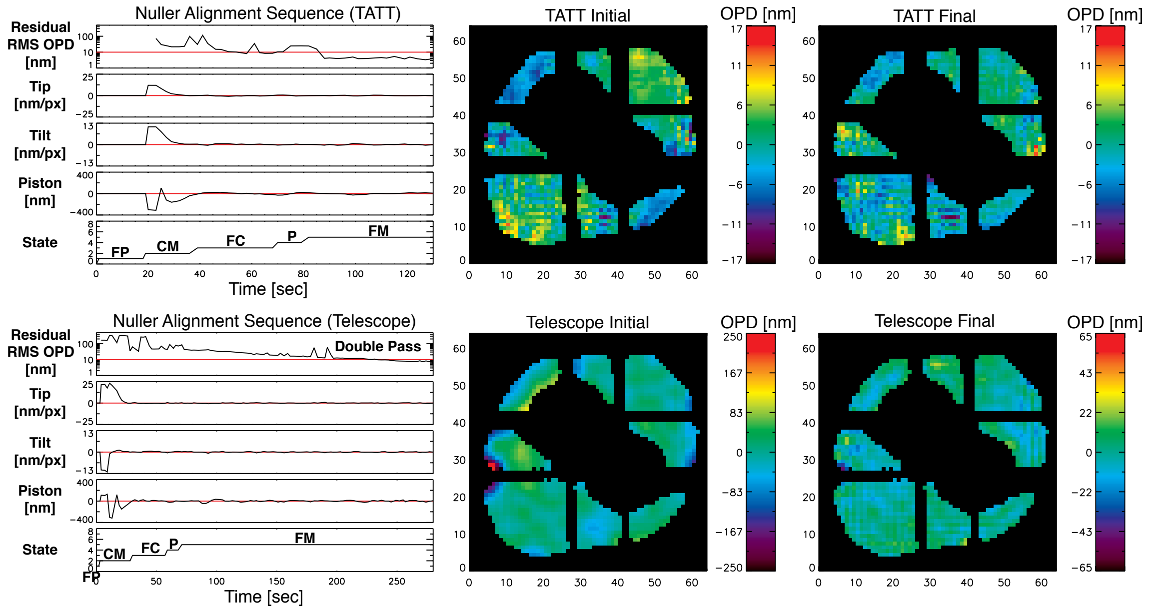

Figure 5.17: The progression of the flight alignment state machine on both the TATT and telescope in double pass. The telescope test was conducted in the vertical configuration (see Figure 5.16). Initial and final residual OPD maps are taken at the beginning and end of FINE MODE (FM). Note that the OPD map color scale varies between images.

the acquisition mirror pinhole and down into the instrument. In this configuration, the telescope is used in double pass; the wavefront error (WFE) introduced by the telescope and thus the stroke required by the DM is doubled. Before integration with the telescope, WCS testing was performed using the Telescope Alignment Transfer Tool (TATT) spherical mirror as a telescope simulator. This mirror is also shown in Figure 5.16.

During the functionality test, the alignment state machine operated as it would in flight. The residual RMS OPD and TTP values for the TATT and telescope are plotted through the progression of the state machine in Figure 5.17. The telescope test results are from the more environmentally stable vertical configuration. The initial and final residual OPD maps, taken at the beginning and end of FINE MODE, are also shown. In both tests, the WCS was able to push the residual OPD below 10 nm RMS.

Both tests used the same initial DM settings, which were established from earlier TATT tests. This explains the longer telescope alignment time; the 1-g primary figure imparted nearly a full wave of OPD. Extra time was required to remove this error. As discussed in Section 4.4, the telescope was expected to produce a wavefront more similar to that of the TATT in space. The TATT test completed alignment in 85 seconds, an acceptable amount of time for a 5 min observing window. In the telescope test, the DM was shown to have adequate stroke to remove most of the low-frequency OPD down to the $\sim$10 nm level – a positive result given that the tests were conducted in double pass with a 1-g primary. Environmental effects from air currents and vibration further limited the telescope tests.

The TATT setup reached 4 nm RMS residual OPD. The final TATT OPD map clearly shows the high-frequency, sub-actuator scalloping effect from the DM, which appears as a checkerboard pattern. To push the lower spatial frequency performance down into the 1 nm RMS regime, the calibration system is needed. Unfortunately, a fabrication error in the nuller prevents calibrator operation across the full pupil. A portion of the pupil is obscured by the calibrator pinhole mount. This can be fixed for a future flight to restore full nuller operation.

5.10 Summary of Test Results

The measured and modeled performance was examined for many of the PICTURE subsystems. The FPS PID controller was shown to be a stable system ideally suited for the sounding rocket ACS environment. The calibration star, Rigel was shown to provide an adequate SNR to perform phase measurements down to the 1 nm RMS level. The effects of high-spatial frequency surface errors on the DM were modeled and shown to limit the nuller contrast to 10^{-2}-10^{-3} over the science region of interest. Amplitude mismatch was investigated between the two nuller arms. A result could not be found due to the effects of non-uniform pupil illumination. The telescope and nuller were shown to exhibit strong temperature dependencies and a mitigation strategy was implemented. The nuller alignment procedure was described. Finally, end-to-end test results were shown for the entire payload in a vertical configuration. The internal nuller OPD resulting from the combined alignment and optical surface errors within the system was shown to be within the correction authority of the DM and N-PZT.

Chapter 6

PICTURE: Flight Results

6.1 Flight Observations

The PICTURE sounding rocket launched from White Sands Missile Range (WSMR) at 4:25 MDT on October 8th, 2011. The PICTURE flight plan allocated 320 seconds of total observing time that was to be divided into two phases: an instrument alignment phase targeted on the calibration star, Rigel ($m_V = 0.12$), and a science observation phase targeted on ϵ Eri ($m_V = 3.73$).

During the alignment phase, the Visible Nulling Coronagraph (VNC) would be aligned to produce a coronagraphic null. This procedure is explained in Chapter 4. Rigel was chosen as the alignment star for two reasons. First, it is ~30 times brighter than ϵ Eri in the PICTURE science band (600-750 nm). As shown in Section 5.4, this extra signal produces more accurate phase measurements in the Wavefront Control System (WCS), which allow for faster nuller alignment. Second, Rigel has no detectable dust signature. Its lack of dust would provide a clean measurement of the instrument point spread function (PSF), which could be used in data post-processing to help reveal the dusty excess around ϵ Eri. A timeline for the nominal PICTURE mission is shown in Table 6.1.

The PICTURE flight did not follow the nominal timeline. Following launch and booster separation, the rocket Attitude Control System (ACS) successfully maneuvered the payload to point towards the alignment star, Rigel. The ACS acquired its target on schedule at T+105 seconds; however, a failure of the on-board 4 Mbps

Event	Time [+ sec]	Altitude [km]
Terrier (1st stage) burnout	6	3
Black Brant (2nd stage) ignition	12	6
Black Brant burnout	46	42
Black Brant separation	65	77
Shutter door open	75	93
ACS on Rigel	105	138
Nuller alignment complete	165	201
ACS on ϵ Eri	186	207
Apogee	250	234
Shutter door close	425	73

Table 6.1: PICTURE nominal flight timeline.

telemetry transmitter, which occurred ~70 seconds after launch, resulted in near-total science data loss. Figure 6.1 shows the telemetry transmitter power during flight. The lost data channel carried the wavefront sensor (WFS) and science camera (SCI) images, and the WCS data products. It also carried positional data from the deformable mirror (DM) and the three nuller piezoelectric transducer (PZT) mirrors. These data were not stored onboard the payload. For the remainder of the observing window, the payload held pointing on Rigel until an on-board timer triggered the shutter door to close as the payload began to reenter Earth's atmosphere.

Approximately 15 seconds of flight data were recovered from the SCI and WFS cameras. These data were recorded very early in the flight, before the WCS had begun its alignment sequence. Although the recovered data are of limited scientific significance, they provide a number of flight diagnostics that will be discussed in the following section.

The most valuable result returned from the PICTURE flight was the successful demonstration of the Fine Pointing System (FPS). Upon ACS acquisition of Rigel, manual ACS uplinks were sent to drive the star into the acquisition mirror pinhole

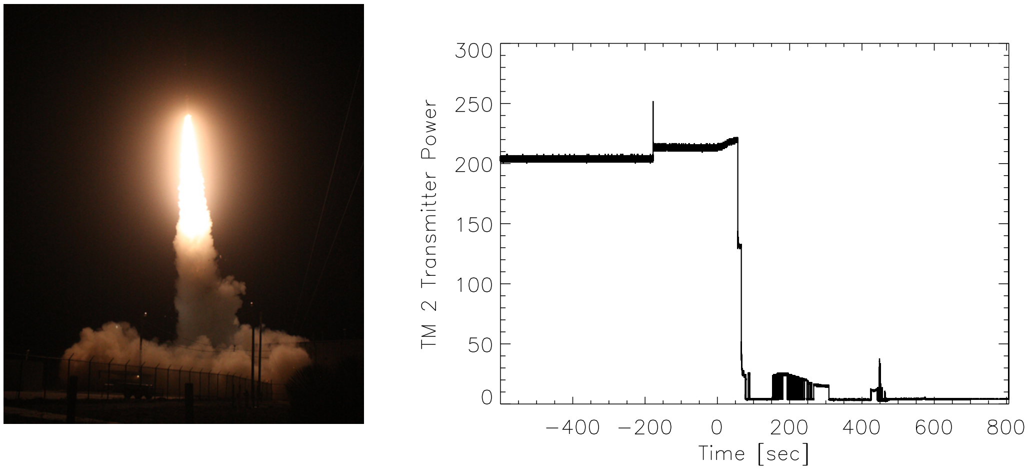

Figure 6.1: *Left:* PICTURE launch. *Right:* Telemetry failure. The main science data telemetry transmitter (TM 2) failed ∼70 seconds after launch.

(see Section 4.3). The functioning FPS telemetry link showed the star appear on the live angle tracker display (shown in Figure 4.13). A measured offset was calculated on the fly and an additional ACS uplink command was sent to drive the star into the capture range of the fast steering mirror (FSM). At this point the FPS immediately locked on and stabilized the beam pointing. The raw 200 Hz pointing data were stored onboard the payload. These data will be presented in Section 6.3.

6.2 Nuller Data

Approximately 180 seconds into the PICTURE flight, the failing telemetry transmitter regained somewhat nominal operation for 15 seconds and a small number of SCI and WFS images were successfully transmitted to the ground. A WFS image taken during flight is compared to a pre-flight laboratory testing image in Figure 6.2. A number of simple diagnostic conclusions can be inferred from these images. First, the instrument pupil was fully illuminated during flight. This confirms that the telescope survived launch and did not shift with respect to the instrument. This second point is known because the secondary obscuration remained hidden behind the pupil

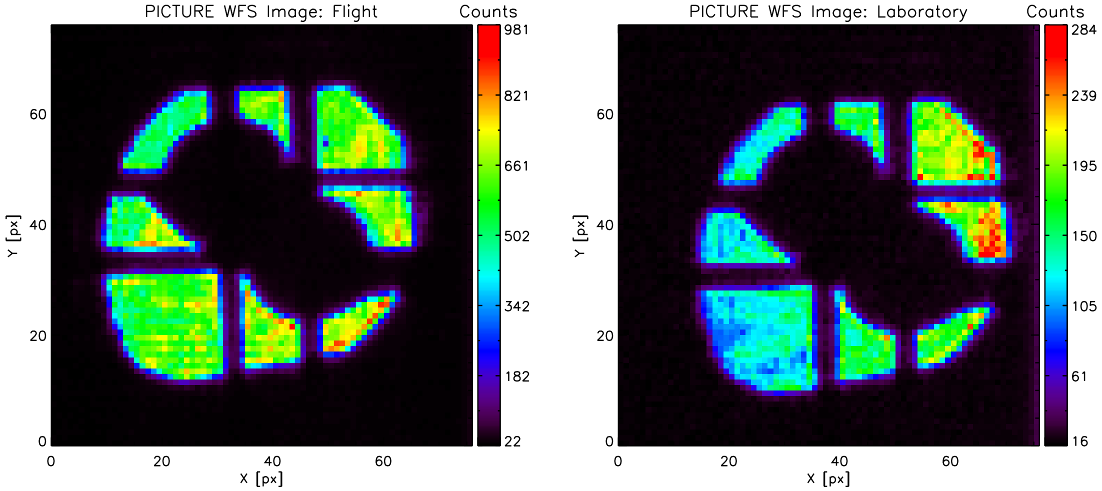

Figure 6.2: Flight *(left)* and laboratory *(right)* wavefront sensor images. The apparent shift in image location is due to a deliberate change in the readout pattern, not a shift during launch.

plane mask. Note that the large apparent shift between the WFS images in Figure 6.2 is due to a deliberate change in the camera readout pattern that was applied before flight, not a mechanical shift during launch.

Another piece of diagnostic information that can be drawn from the WFS images is that the pupil illumination was much more uniform in flight than in the lab. This confirms that, as discussed in Section 5.6, the intensity gradient seen to stretch from bottom left to top right in the laboratory image is in fact a product of the fiber input beam illumination pattern and not a reflectivity gradient across the nuller optics.

During this short window of valid data, a computer glitch in the FPS had caused a system reboot and the FPS was not yet tracking. Due to this fact, the WCS had not yet received its first notification of steering lock and had not yet applied power to the DM or the three nuller PZTs. The unpowered DM is not flat. The mirror forms a bowl shape that is approximately one wave deep and acts to defocus the DM arm of the nuller. The unpowered Nuller PZT (N-PZT) introduces some additional

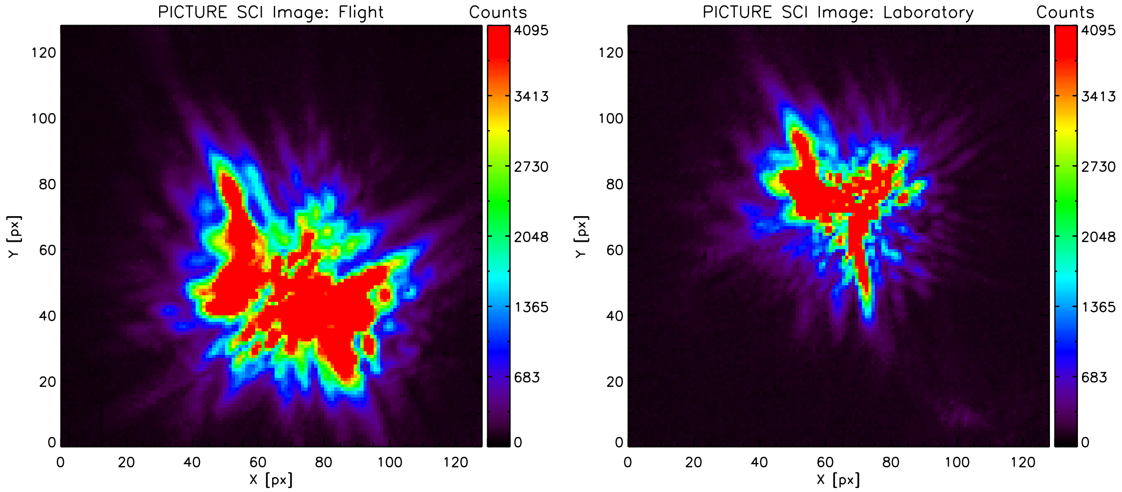

Figure 6.3: Flight *(left)* and laboratory *(right)* science camera images from the unpowered nuller.

tilt between the two nuller arms. Both of these effects combine to form a highly aberrated nuller PSF on the SCI camera. Added to these effects is the fact that the un-suppressed star greatly saturates the CCD. This was the state during the short window of flight where SCI images were recovered from the payload. One of these flight images is compared to a laboratory image in Figure 6.3. The laboratory image was taken with the nuller in the same unpowered state as in flight.

Despite the complexity of the unpowered nuller PSF, one important piece of information can be gained from the images in Figure 6.3: the telescope PSF was larger in space than it was on the ground. The telescope clearly suffered from a strong focus error during flight. Further evidence for this error, its possible causes and its effect on the FPS performance will be discussed in Section 6.4.5.

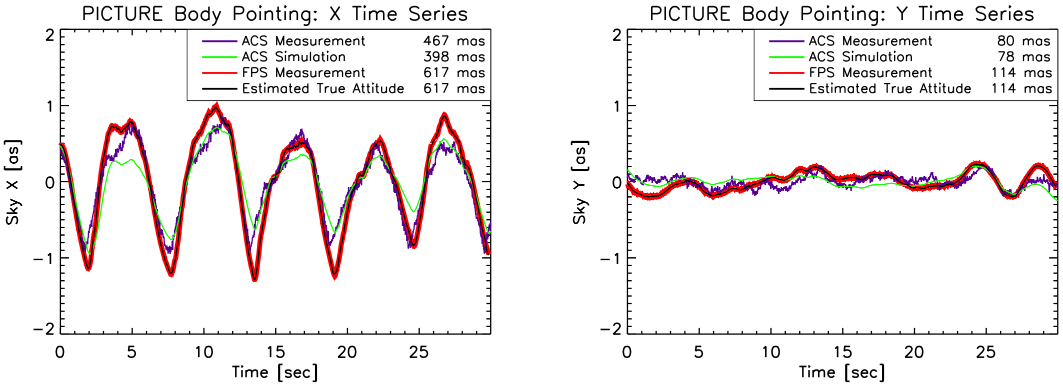

Figure 6.4: Body-pointing time series data from the PICTURE flight: X-axis (*left*), Y-axis (*right*).

6.3 Fine Pointing System Data

A computer glitch in the FPS, which caused a system reboot, reduced the overlap in time where both the ACS and FPS were tracking in steady-state. A 30 second window from this overlap region has been selected to analyze and evaluate the performance of both systems. This sample consists of 6000 contiguous angle tracker centroid measurements and completely describes the statistical characteristics of the steady-state pointing performance.

6.3.1 Rocket Body-Pointing Data

A convenient by-product of the closed-loop FPS tracking is a high-fidelity measurement of the payload pointing attitude. This measurement is simply the angular position of the FSM, which tracks the motion of the payload to hold the star stationary on the angle tracker. The on-board ACS sensors and the ACS flight dynamics simulation offer two additional estimates of the payload pointing. The ACS simulator was discussed in Section 4.8.5. These data sets are presented in time series format in Figure 6.4. The ACS simulator data presented here was generated using the recorded thrust commands from the PICTURE flight.

The ACS pointing sensors are noise limited at ∼30 milliarcsecond (mas) RMS. The effects of ACS sensor noise can be seen in Figure 6.4. The noise is most pronounced over the broad jagged peaks of the X attitude measurement, where the payload is moving more slowly. The morphology of the ACS flight simulator results matches the FPS measurement more closely; however, the simulated pointing amplitude is approximately 35% lower than the measured amplitude. This may be due to a miss-calibration of the ACS simulation. The ACS sensor data show a similar scale error. The ACS data are not simply the readout of a single sensor, they are a position solution calculated by the ACS on-board computer. The solution is based on a mixture of data from two sets of gyroscopes and the star tracker camera. The FPS on the other hand, offers a direct and absolute measurement of the payload pointing. Its calibration is pinned directly to the angle tracker plate scale and is accurate to within ±5%. For this reason, the FPS is believed to provide the most accurate measurement of the payload pointing.

The power spectral density (PSD) of the body-pointing data is plotted in Figure 6.5. The PSD shows the frequency response of the ACS. The FPS body-pointing measurement supports the ACS simulator prediction of the high-frequency ACS response, which follows an f^{-4} power law and carries much less power at high frequencies than the noise-limited ACS sensors would indicate. The FPS measurement begins to deviate from a simple power law near the ∼5 Hz tracking bandwidth, where the controller starts to lose its effectiveness. The bandwidth is calculated in Section 6.4. Above the bandwidth, the FPS measurement no longer reflects the true pointing of the payload.

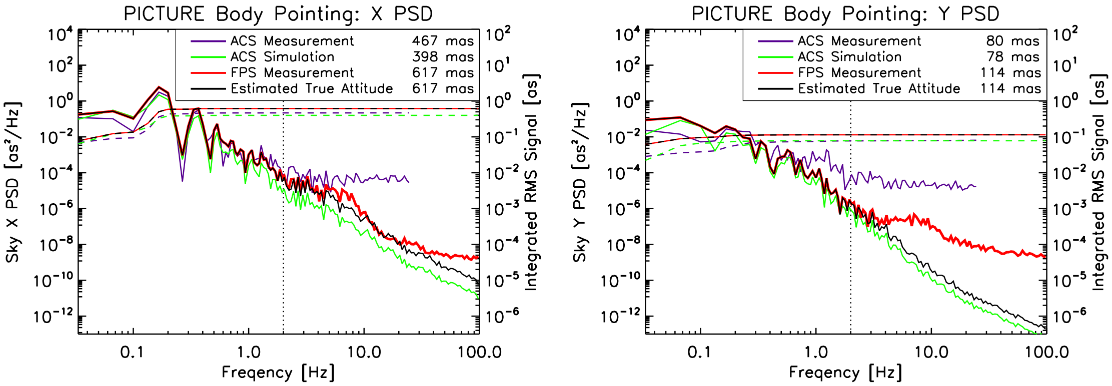

Figure 6.5: Body-pointing power spectra from the PICTURE flight: X-axis (*left*), Y-axis (*right*). These power spectra are calculated directly from the time series data shown in Fig. 6.4. The dashed lines show the cumulative pointing error on the right axis. The ACS attitude measurements are recorded at 50 Hz. This sets the 25 Hz Nyquist cut-off frequency. The vertical dashed line at 2 Hz shows the point where the FPS measurement is spliced with the ACS simulation to form the Estimate True Attitude (ETS).

From these data sets, a best estimate of the true rocket body-pointing is constructed. The FPS provides the most accurate measurement of the low frequency ACS response. At frequencies near and above the ∼5 Hz tracking bandwidth, the rocket pointing is assumed to follow the prediction of the ACS flight simulator. The Estimated True Attitude (ETA) is calculated by mixing the FPS measurement below 2 Hz with the ACS simulator results above 2 Hz. The ACS simulator results are scaled to match the FPS amplitude at 2 Hz before mixing. Since 99% of the power lies below 2 Hz, the ETA and the FPS measurement appear nearly identical in the time domain (Figure 6.4) and have the same RMS value. The difference at high frequencies is clearly seen in the power spectrum (Figure 6.5).

Both the ETA and the FPS measurement show the ACS stability was 5.4 times worse in X than in Y. Both axes did, however, meet the $\pm 1''$ flight requirement established to limit beamwalk on the telescope secondary and tertiary mirrors. The

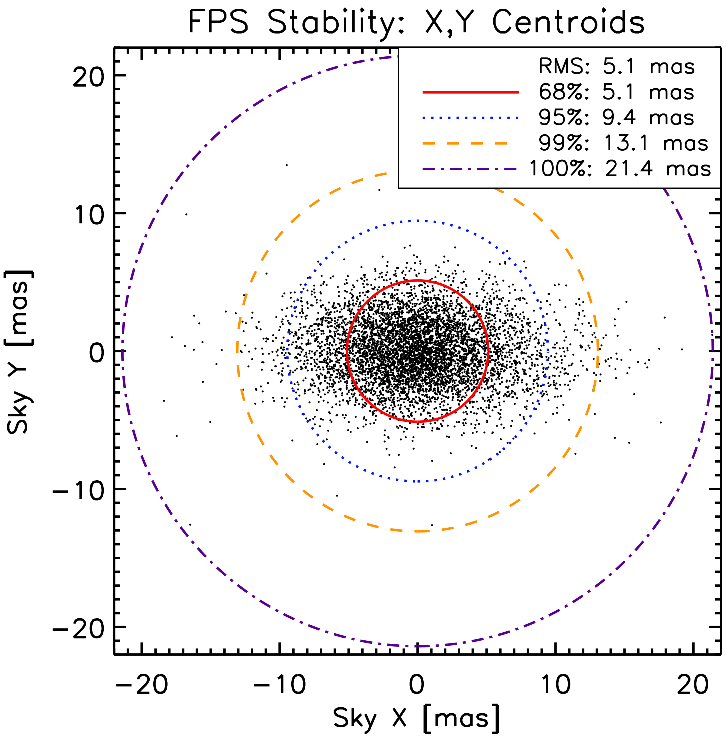

Figure 6.6: The 2D distribution of 6000 contiguous angle tracker centroids. These data points are concurrent with the body-pointing time series data from Fig. 6.4. Total enclosed error contours are overlaid.

ACS pointing error was 617 mas RMS in X and 114 mas RMS in Y. The radial pointing error was 627 mas RMS. In Section 6.4, the ETA will serve as the spacecraft environment model for FPS simulations of future PICTURE flights.

6.3.2 Pointing Stability Data

The angular distribution of the 200 Hz angle tracker centroids is presented in Figure 6.6 and Figure 6.7. These data are concurrent with the body-pointing data presented in the previous section. The tracking jitter is represented well by a Gaussian distribution. The X distribution is nearly twice as wide as as the Y distribution. This clearly results from the difference in ACS performance between X

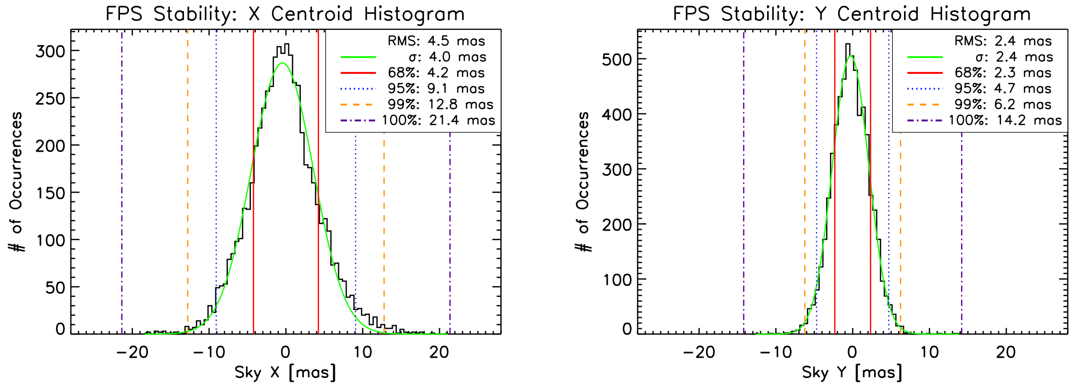

Figure 6.7: The angular distribution of centroids on the angle tracker camera: X-axis (*left*), Y-axis (*right*). These are the same centroid measurements as shown in Fig. 6.6. Gaussian fits and total enclosed error intervals are overlaid.

and Y. The ACS pointing error was reduced to 4.5 mas RMS in X and 2.4 mas RMS in Y. The radial pointing was stabilized to 5.1 mas RMS. The raw flight centroids have been scaled up by a factor of 1.67 to correct for the centroid sensitivity effects discussed in Section 4.8.3. The derivation of this factor will be shown in Section 6.4.2.

6.4 Fine Pointing System Performance Analysis

6.4.1 Fine Pointing System Simulator

I developed a FPS simulator to better characterize the in-flight performance and to predict the pointing stability for future flights. The simulator operates the FPS Proportional + Integral + Differential (PID) controller between models of the FSM and angle tracker to stabilize the input payload pointing. Details of the PID controller are given in Section 5.3. Effects from image latency, centroid noise and sensitivity, FSM tip-tilt resolution and FSM amplifier noise are included as adjustable parameters. A block diagram of the simulator components is shown in Figure 6.8. The simulator input is a time series representing the true payload pointing. The

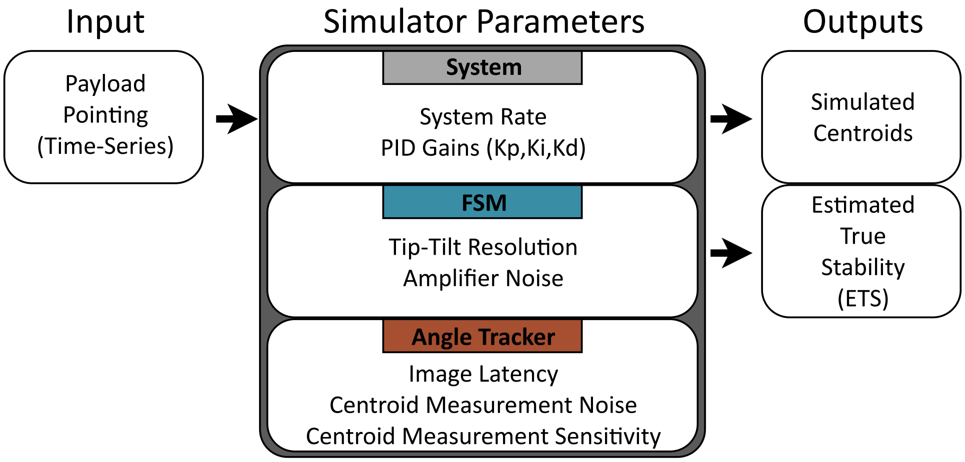

Figure 6.8: FPS simulator block diagram.

two outputs are the simulated angle tracker centroids and a related quantity, the Estimated True Stability (ETS). The ETS is an estimate of the true pointing into the nuller. This estimate is simply the offset between the input payload pointing and the FSM position (averaged over each time sample). The ETS represents the true pointing stability rather than the measured centroid stability. It is the best choice for evaluating the expected nuller performance.

To produce a time series of simulated flight centroids, the FPS simulator is fed with the ETA as the “true” angular pointing of the payload. The measured and simulated centroids are plotted alongside the ACS response in Figure 6.9. The ETS is plotted as well. The radial RMS ETS is 4.4 mas.

The periodic packets of centroid jitter seen in Figure 6.9 occur only during ACS motion in the positive X direction. They originate from a real narrow-band (3-8 Hz) feature in the ACS; they are present in both the ACS sensor data and the ACS flight simulations. These mid-frequency disturbances are less attenuated by the FPS PID controller and print through to the angle tracker camera. The residual disturbance in the centroids is reproduced at full amplitude by the FPS simulator.

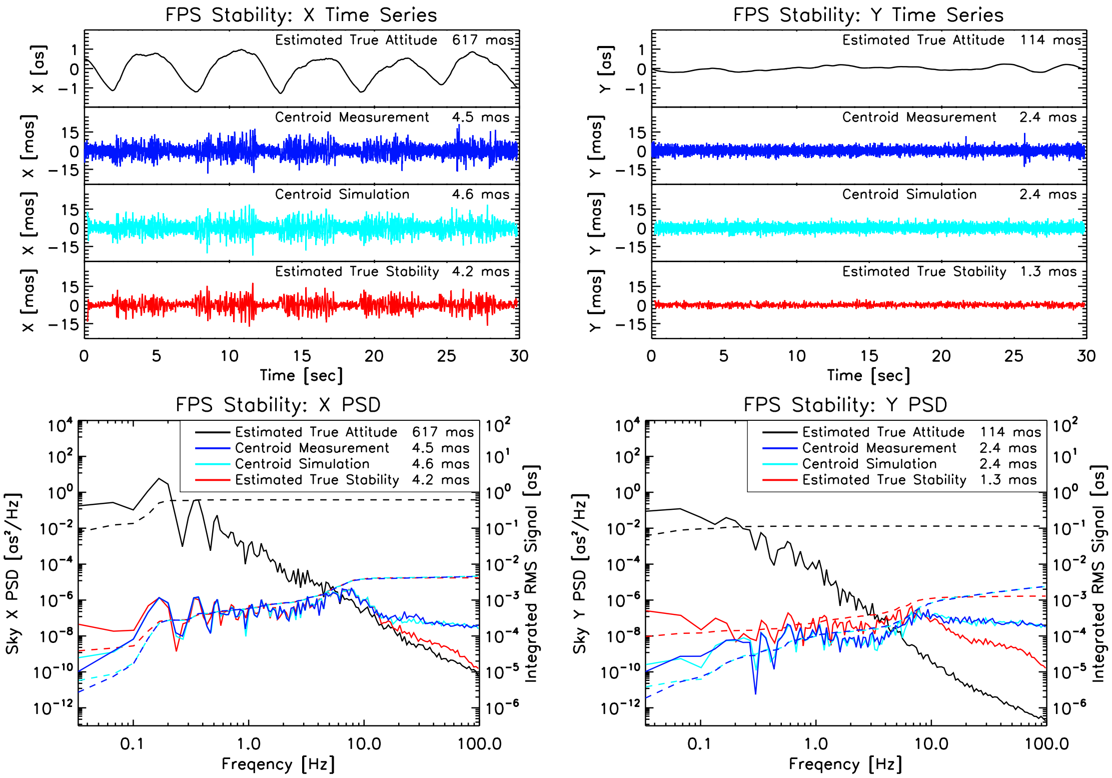

Figure 6.9: Measured and simulated FPS stability: X-axis (*left*), Y-axis (*right*). Time series data and simulations are shown across the top two panels. The power spectrum of each time series is plotted below. The dashed lines show the cumulative pointing error on the right axis. Simulated centroids are produced by running the ETA through the FPS simulator. The estimated true stability (ETS), a model of the true pointing into the nuller, is also plotted.

The power spectra of the centroid measurements and simulations are also plotted in Figure 6.9. The FPS operated very close to the modeled limit at most frequencies. The measured flight FPS transfer function is presented in Figure 6.10. The transfer function, the ratio of output power to input power, is defined here as the quotient of the measured centroid power spectrum and the ETA power spectrum. The closed-loop tracking bandwidth is defined as the range of frequencies over which there is at least a -3 dB suppression of the residual ACS pointing jitter. The bandwidth ranges

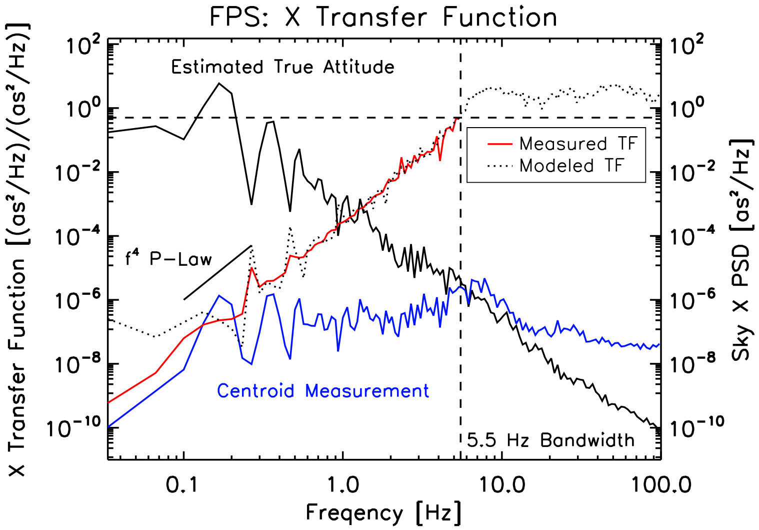

Figure 6.10: The in-flight X-axis FPS transfer function is the quotient of the measured centroid PSD and the ETA PSD. These power spectra are taken directly from Fig. 6.9; the PSD values are shown on the right axis. The 200 Hz FPS has a measured bandwidth of 5.5 Hz (*vertical line*), the frequency at which the transfer function crosses 1/2 (-3 dB) (*horizontal line*). Below the bandwidth frequency, the transfer function follows a f^4 power law. Above the bandwidth frequency, the measured transfer function becomes invalid due to centroid measurement noise and the modeled transfer function (*dotted-line*), the ratio of the ETS to the ETA, gives the best estimate of the FPS response.

from 0 Hz to 5.5 Hz, the frequency at which the transfer function crosses 1/2 (-3 dB). The transfer function follows a f^4 power law and shows that the FPS attenuated the ACS pointing error by several orders of magnitude over the tracking bandwidth. The PID controller was stable at all frequencies during steady-state tracking. The flight PID gains were tuned for stability and performance through repetitive testing prior to flight. This testing is described in Section 5.3. In the event of instability during flight, an uplink command was available to lower the gains and reset the controller.

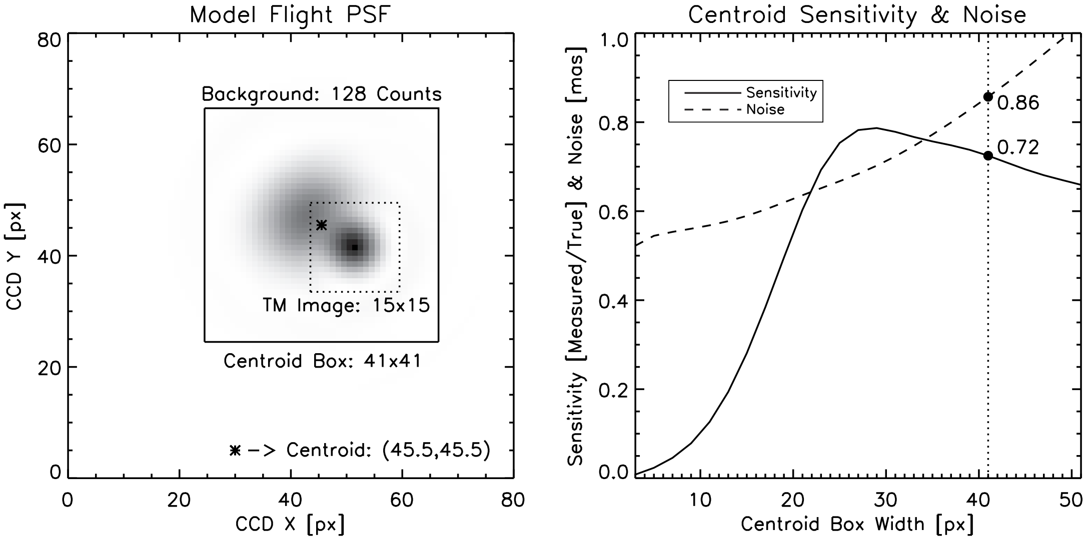

Figure 6.11: A model of the flight PSF (*left*) and the resulting centroid measurement sensitivity and noise curves (*right*).

6.4.2 Centroid Measurement Sensitivity

As discussed in Section 4.8.3, the measured centroids do not correspond exactly to the true position of the stellar spot on the angle tracker camera. A sensitivity factor relates the two quantities. To derive the flight centroid measurement sensitivity, a measure of the flight PSF is needed. However, the flight PSF was much larger than anticipated, nearly ten times the diffraction limit, and the true shape cannot be confirmed because full-chip images were not recorded during flight. Smaller 15×15 pixel images were transmitted to the ground over the functioning FPS telemetry channel. These images show a fragment of the large aberrated spot – they are not large enough to enclose the entire PSF. The PSF measured on the SCI camera within the nuller (Figure 6.3) cannot be used for this task either because it represents the overlapping beams from the two misaligned arms of the nulling interferometer (NIF). The SCI camera images are also extremely saturated.

Two approaches are taken to determine the centroid sensitivity. First, a model of the flight PSF is constructed that is constrained by a number of in-flight measurements. These include: the total number of counts inside the 15×15 pixel telemetry images, the number of counts in the brightest pixel, the calculated centroid position, the total number of counts inside the 41×41 pixel centroiding box and the measured background level. This model is presented in Figure 6.11. During post-flight analysis, a software bug was discovered in the flight code that prevented background subtraction during the in-flight centroid calculation. The ∼128 count background produces the sensitivity fall-off seen at large box sizes in Figure 6.11. This effect dominates over the shape of the PSF; however, the available data cannot rule out the presence of low-amplitude speckles near the centroid box perimeter that could have further reduced the in-flight sensitivity. The modeled centroid sensitivity of 0.72 is therefore taken as an upper limit.

In the second method, the FPS simulator is used to estimate the centroid sensitivity. The centroid sensitivity is an adjustable parameter within the simulator. Simulations are run over a range of sensitivities with all other parameters held constant. Figure 6.12 shows the resulting simulated centroid power spectra. The centroid sensitivity effectively acts as a scale factor for all three PID gains within the controller. The controller gain strongly affects the response through the bandwidth transition at 5.5 Hz. The FPS simulations best fit the measured PSD with a centroid sensitivity of 0.6. This value is consistent with the upper limit set using the model PSF; it is adopted as the best estimate of the true sensitivity. To correct for this decreased sensitivity, all centroid data presented in this work have been multiplied by the reciprocal of this value. Since the loss in sensitivity acts only to decrease the PID controller gain, the FPS measurements of the payload attitude are unaffected and do not require correction.

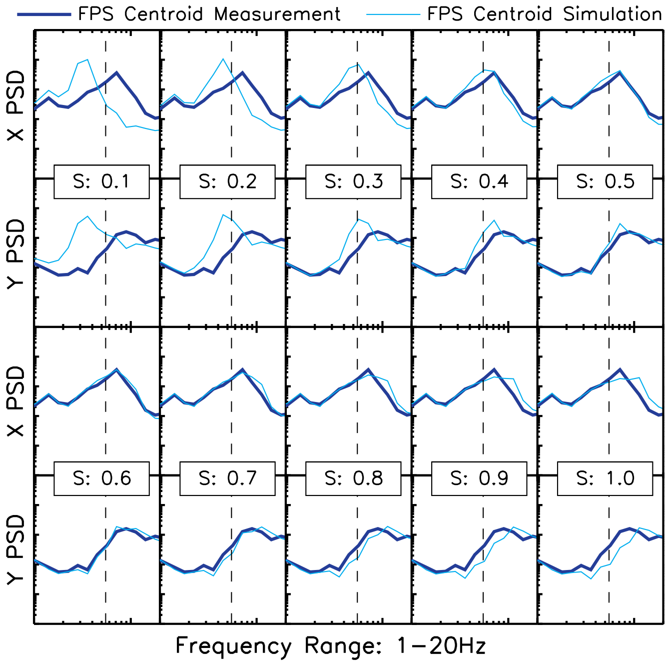

Figure 6.12: FPS simulator constraints on the flight centroid measurement sensitivity. Ten FPS simulations are plotted from left-to-right, top-to-bottom in order of increasing centroid sensitivity. The X and Y axes are stacked. The sensitivity is displayed for each X,Y pair. The simulated centroid PSD (*thin line*) is overplotted with the measured PSD (*thick line*). The transition across the 5.5 Hz bandwidth (*vertical dashed line*) is best fit by the simulation using a centroid sensitivity of 0.6.

6.4.3 Centroid Measurement Noise

The centroid measurement noise limit is observed as the flat tail at the high-frequency end of the centroid power spectrum. As seen in Figure 6.9, the flight centroid measurements become noise limited at a level of 1.4×10^{-8} as^2/Hz. The integrated RMS measurement noise is 1.2 mas. Although this noise is fed back to the FSM, it is greatly attenuated by the PID controller. As a result, much of the high-frequency power is not applied to the FSM and does not affect the nuller input pointing. The ETS is constructed to model this precise effect.

6.4.4 Pointing Error Budget

The FPS pointing error is separated into component parts in the error budget presented in Table 6.2. This table reports the measured pointing results on the calibration target, Rigel. High-frequency environmental jitter above the system Nyquist frequency (100 Hz) is not well sampled by the angle tracker. Estimates of the high-frequency jitter contributed by the ACS and the influence of amplifier noise on the FSM are listed in the error budget as well.

The jitter induced by FSM amplifier noise was discussed in Section 4.8.4. The FSM is responsive to signals up to 4 kHz. For simplicity, we assume that all of the 1.6 mV RMS (0.42 mas NEA) FSM amplifier noise occurs between 100 Hz and 4 kHz and translates directly into FSM motion (response function = 1).

Unlike the FSM, the ACS response has the benefit of a large control mass, which serves to greatly dampen vibrations at high frequencies. The rocket ACS is also a pure high-pressure gas system that contains no reaction wheels that might produce high-frequency resonances. The integrated ETA jitter above 100 Hz is predicted to be extremely small, approximately 0.05 mas RMS. Both of these high-frequency noise contributions are insignificant compared to the measured stability (5.1 mas RMS) and the ETS (4.4 mas RMS).

6.4.5 Telescope Point Spread Function Effects

Centroid measurement noise and decreased sensitivity, both resulting from the large telescope PSF, were the leading sources of in-flight tracking error. Sufficient data are not available to determine the root cause of the large flight PSF. Non-ideal gravity release on the primary mirror, thermal deformation of the telescope or perhaps an optical misalignment incurred from launch vibration are among the most likely possibilities.

	Value	NEA [mas]	Origin
Centroid			
Camera Rate	200 Hz		Defined: Section 4.8
Read Noise	12.5 e-/px		Manufacturer spec & confirmed
Dark Current	58×10^3 e-/px/s		Manufacturer spec & confirmed
Star	6.8×10^8 e-/s		Measured in flight
PSF Shape	Large, asymmetric		Modeled: Figure 6.11
# Centroid px	1681 px		Defined: Section 4.8
Sensitivity	60%		Modeled: Section 6.4.2
Modeled Noise	0.86 mas		Eq. (4.8) & Figure 6.11
Measured Noise	6.3×10^{-3} px	**1.2**	Measured: Section 6.4.3
FSM Resolution			
DAC LSB	1.1 mV	**0.22**	Manufacturer spec & confirmed
High Frequency			
FSM Amp Noise	1.6 mV RMS	**0.42**	Manufacturer spec
ACS	5×10^{-2} mas	**0.05**	Integrated ETA above 100 Hz
FPS Performance			
FSM Rate	200 Hz		Defined: Section 4.8
PID Bandwidth	5.5 Hz		Measured: Figure 6.10
ACS X	617 mas RMS	**4.5**	Measured: Figure 6.9
ACS Y	114 mas RMS	**2.4**	Measured: Figure 6.9
ACS Radial	627 mas RMS	**5.1**	$(X^2+Y^2)^{1/2}$

Table 6.2: FPS error budget. The in-flight FPS performance on the calibration target, Rigel is separated into component sources of error. Estimates of the high-frequency noise contribution from FSM amplifier noise and the ACS are also included.

The ultra-lightweight primary mirror experienced severe gravity deformation on the ground. The 1-g telescope was measured to have approximately one full wave of figure error (see Section 4.4). A mechanical model of the primary was used to predict that the telescope would relax to a $\sim \lambda/4$ figure in space (Antonille et al. 2008). It is possible that the primary mirror did not gravity release as predicted. Unfortunately, the primary mirror was destroyed upon landing ruling out the possibility of post flight alignment checks. All available temperature sensors reported that the telescope was within range at the time of launch.

A number of performance improvements flow down from tracking on a smaller spot. With a smaller spot, a high sensitivity centroid measurement can be made using fewer pixels, thereby reducing the effects of read and dark noise. The smaller centroiding region also allows for faster calculation, decreasing controller latency. As the spot becomes more concentrated, the weighted contribution from stellar shot noise in Eq. (4.8) decreases and the camera and steering mirror are allowed to run faster, increasing the tracking bandwidth.

The FPS simulator is used to model the optimal tracking performance as a function of PSF size and stellar brightness. As before, these simulations are run using the ETA time series as the "true" payload pointing. The simulations are system-rate-optimized to produce the best possible tracking on a star of a given brightness. The system rate describes both the camera exposure rate and the FSM update rate. The optimal system rate strikes a balance between the centroid measurement noise and the residual ACS jitter. The centroid box size for a given PSF is set as small as possible while maintaining >95% sensitivity. The PID gains are held constant at their flight values for all simulation runs. The resulting tracking curves are shown in Figure 6.13. These curves represent the ETS as discussed in Section 6.4.1.

The simulations suggest that with no modification to the pointing hardware, a future PICTURE flight could achieve sub-milliarcsecond pointing on a bright star ($m_v < 4$) simply by improving the optical quality of the telescope. The highest performance results shown in Figure 6.13 take advantage of the 1 kHz FPS mode, which uses only a single 40×40 quadrant of the angle tracker to decrease readout time and a 2×2 or 3×3 centroid calculation box. The high-frequency noise estimates from Table 6.2 are also included in the simulator results. The FSM amplifier noise, which dominates over the residual ACS jitter, produces a hard lower limit to the FPS pointing performance at 0.42 mas RMS.

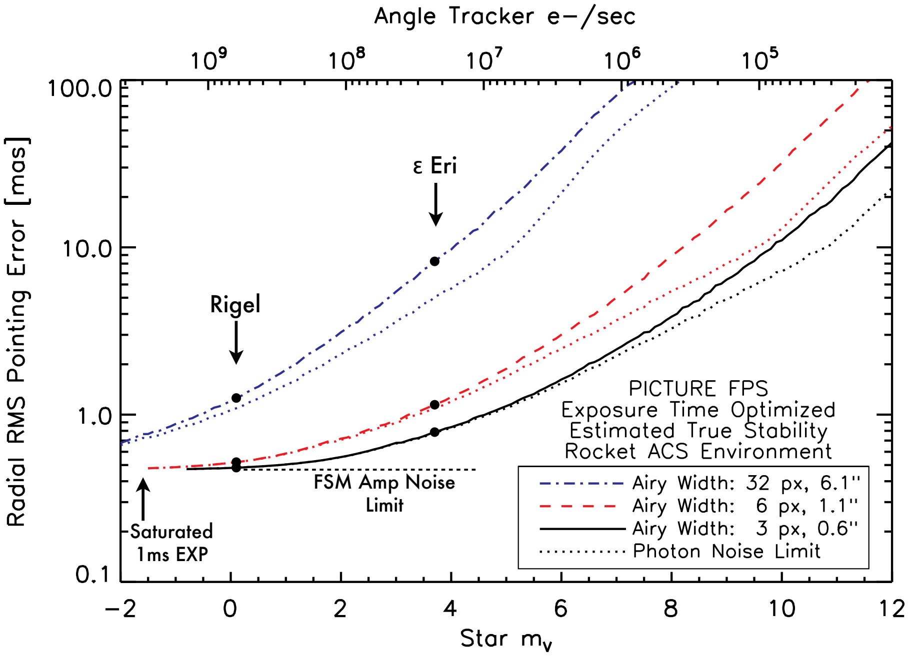

Figure 6.13: The simulated, system-rate-optimized, estimated true stability (ETS) is plotted as a function of stellar brightness for three different telescope spot sizes. The lower (*solid*) line represents the diffraction-limited performance of the PICTURE 0.5 m telescope. A 1 ms lower limit is imposed on the exposure time to illustrate the effects of CCD full-well saturation, which occurs at 3×10^5 e-/px. The dotted lines below each curve show the theoretical photon-noise-limited pointing performance in the absence of CCD dark current and read noise. The 0.42 mas RMS FSM amplifier noise level sets a lower limit on the system performance.

6.5 Summary of Flight Results

PICTURE was the first dedicated exoplanetary imaging mission to fly in space. Unfortunately, a telemetry failure onboard the payload resulted in near-total science data loss. Approximately 15 seconds of data were recovered from the SCI and WFS cameras. These data, combined with those from the FPS confirm that the overall alignment of the entire optical system, from the telescope down through the instrument, was not disturbed during launch. The telescope PSF, however, was much larger than expected.

The PICTURE FPS provided 5.1 mas RMS pointing stability onboard a NASA sounding rocket. This level of pointing stability is comparable to that of the Hubble Space Telescope, which nominally achieves 2-5 mas RMS stability over a single orbit (HST_MultiDrizzle_Handbook). It is also very similar to the performance achieved by the image stabilization system onboard the Hinode (Solar-B) satellite (Shimizu et al. 2008), which has demonstrated 9 mas RMS stability with a similar design. PICTURE marks the first flight demonstration of an active optical pointing control system for direct exoplanet imaging.

The PICTURE FPS has also made the most accurate measurement to date of the true sounding rocket ACS pointing performance. The body-pointing jitter was characterized at the ∼5 mas level, well below the ∼30 mas RMS noise floor of the ACS sensors. This measurement supports the predictions of the Wallops ACS flight dynamics simulator at frequencies above 1 Hz and identifies the sounding rocket platform as a suitable environment for future high-pointing-precision missions due to its lack of high-frequency vibration.

The sources of noise that limit tracking performance are presented in Table 6.2. The leading driver of tracking error for the PICTURE flight was the large and aberrated telescope PSF. The large PSF led to high centroid measurement noise (1.2 mas RMS) and decreased the centroid measurement sensitivity (60%). FPS simulations show that the system performed near its modeled limit during flight and that its performance can be optimized for future flights simply by improving the optical quality of the telescope. This would enable sub-milliarcsecond tracking on bright stars ($m_v < 4$).

Chapter 7

Summary and Conclusions

7.1 SPINR Summary and Conclusions

The SPINR sounding rocket was launched on February, 19th 1999. It recorded spectral-imaging data in the FUV (912-1450Å) over a 16° field of view, a region of sky containing the entire Orion constellation. These measurements were used to study the scattering properties of interstellar dust grains. Two key questions were addressed: *Where is the dust that produces the observed scattered light distribution, and what are the scattering parameters (**a**,**g**) of that dust?*

In Chapter 2, the SPINR instrument was introduced and the data analysis pipeline was described. The data were calibrated into physical units using IUE-calibrated Castelli & Kurucz (2003) model spectra and a model of the instrument response. The SPINR data were split into stellar and nebular components. A number of background sources were subtracted from the nebular signal to estimate the signal from dust-scattered starlight. These sources were: detector background, instrument-scattered Lyman-α and Lyman-β photons, telluric emission lines, fluorescent H_2 emission, undetected stars and the extragalactic background. Spatial sinogram maps were compiled in three photometric bands centered at 971 Å, 1090 Å and 1330 Å. These sinograms were the primary data product used to constrain the dust parameters.

In Chapter 3, the DIRTY radiative transfer model was introduced and a three-dimensional model of the Orion system was constructed. The model included two dust distributions: an amorphous foreground distribution to match the measured extinction toward the stars in Orion and a background slab to represent the Orion Molecular Cloud (OMC). The models were illuminated by a selection of 88 stars in the Orion OB association.

DIRTY models containing only the background dust distribution were unable to reproduce the data for strongly forward-scattering dust grains ($g > 0.75$). The results from a limiting-case background model imply that no model containing only background dust can reproduce the data. A physical interpretation of this model suggests that the background OMC cannot alone produce the observed scattered light distribution.

A model containing only foreground dust was able to reproduce the data in the short (971 Å) and mid (1090 Å) bands, but was statistically rejected in the long (1330 Å) band.

A hybrid model containing both foreground and background dust was able to match the data in all three bands. The best-fit albedo values for the hybrid model with $g = 0.75$ were 0.45 ± 0.08 at 971 Å, 0.53 ± 0.15 at 1090 Å, and 0.93 ± 0.05 at 1330 Å. These values are consistent with previous Orion measurements by Shalima et al. (2006). The observed fall-off in grain albedo at far-ultraviolet (FUV) wavelengths further confirms that dust grain absorption becomes more and more efficient at shorter wavelengths. The grain albedo observed at 1330 Å is much higher than predicted by grain models, but is consistent with many previous measurements. This further supports the possibility of a strong albedo feature at 1300-1500 Å.

The hybrid dust model was the most realistic model tested. It was constrained by the measured optical depth and physical position of each star and included a model of the background OMC. A physical interpretation of this model suggests a very different view of Orion in the three SPINR bands. In the short and mid bands, the foreground dust is optically thick and at least partially obscures the background OMC. In the long band, the foreground dust becomes optically thin and backscatter from the OMC dominates the scattered light distribution. If this is true, it has important implications for the interpretation of *all* FUV observations of Orion. Observations shortward and longward of 1090 Å may probe entirely different dust populations.

The significance of foreground dust along the line of sight to Orion may also carry important implications for the value of f_{esc}, the fraction of ionizing photons ($\lambda < 912$ Å) that escape the Galaxy and contribute to ionizing the intergalactic medium. Despite having extremely low visible extinction ($A_V \sim 0.3$), the Orion foreground region has a significant FUV optical depth. This indicates that Orion-like dust may make a significant contribution to the $\lambda < 912$ Å opacity even along nominally low extinction sightlines.

7.2 PICTURE Summary and Conclusions

The PICTURE sounding rocket was launched on October, 8$^{\text{th}}$ 2011. The goal of the mission was to obtain a direct image of exozodiacal dust within the ϵ Eridani exoplanetary system using a Visible Nulling Coronagraph (VNC) to attenuate the signal of the bright host star. Unfortunately, the main science telemetry transmitter on the payload failed ~70 seconds after launch and nearly all science data was lost. The mission did, however, successfully demonstrate a milliarcsecond-level pointing control system.

In Chapter 4, the hardware components of the PICTURE payload were presented and the principles of nulling interferometry were explained in the context of producing a coronagraphic null to directly image exoplanetary systems. The

PICTURE flight plan was defined and included an instrument calibration phase targeted on Rigel and a science observation phase targeted on ϵ Eri. The functionality and flight alignment sequence of the Wavefront Control System (WCS) was also described.

In Chapter 5, pre-flight test results from the different PICTURE subsystems were presented. The process of tuning the Fine Pointing System (FPS) PID controller gains for flight was described. A Matlab model of the FPS was also developed and used to show the system operates with a gain margin of 9.0 dB and a phase margin of 98.3°.

The noise properties of WCS "ABCD" phase measurement technique were also investigated. Using flight data to calibrate the throughput of the instrument, the RMS noise in the phase measurement was calculated as a function of stellar brightness. The calibration star, Rigel was shown to provide enough signal to measure phase errors at the ∼1 nm RMS level.

To estimate the influence of DM surface errors on nuller performance, a monochromatic model of the nuller was constructed. This model was used to show the 9 nm RMS surface scalloping of the Boston Micromachines (BMC) 32×32 MEMS DM limits the null depth (dark/bright) to 10^{-2}-10^{-3} over the science field of view ($0.5''$-$1.5''$).

Both the telescope and nuller were shown to exhibit strong temperature dependence. Test data of the telescope focus position taken at different laboratory temperatures was used to show the focal point changed by 0.3 mm/°C. Similar data was used to show the optical path length of the nuller DM arm changed by ∼700 nm/°C. These results were used to set a 70° F alignment temperature and a $70 \pm 5°$ F launch temperature constraint.

Finally, end-to-end tests of the entire payload in both horizontal and vertical configurations were presented. The WCS flight alignment sequence was able to remove optical path difference (OPD) between the nuller arms at the 10 nm RMS level for the telescope in double pass and at the 4 nm RMS level for a $2''$ telescope simulation mirror.

In Chapter 6, the PICTURE flight results were presented. A telemetry failure $\sim$70 seconds after launch caused near-total science data loss. Approximately 15 seconds worth of science camera and wavefront sensor images were recovered and used to perform basic flight diagnostics.

The primary result of the PICTURE flight was the successful demonstration of the FPS, which stabilized the stellar image to 5.1 milliarcseconds RMS. This pointing stability is equivalent to that achieved by the Hubble Space Telescope. The pointing system was also used to characterize the frequency response of the sounding rocket Attitude Control System (ACS). The ACS was shown to produce very little high-frequency vibration making it an ideal platform for future high-contrast imaging missions. The FPS demonstration marks an important technical achievement towards the goal of developing a dedicated exoplanet-imaging satellite mission.

List of Journal Abbreviations

A&A	Astronomy and Astrophysics
A&AS	Astronomy and Astrophysics Supplement Series
AJ	The Astronomical Journal
ApJ	The Astrophysical Journal
ApJS	The Astrophysical Journal Supplement Series
Appl. Opt.	Applied Optics
ARA&A	Annual Review of Astronomy and Astrophysics
ASPC	Astronomical Society of the Pacific Conference Series
BAAS	Bulletin of the American Astronomical Society
Geophys. Res.	Geophysical Research
IAU	International Astronomical Union
JOSAA	Journal of the Optical Society of America A
MNRAS	Monthly Notices of the Royal Astronomical Society
PASP	Publications of the Astronomical Society of the Pacific
Sol. Phys.	Solar Physics
SPIE	International Society for Optics and Photonics

References

Antonille, S., & Content, D. 2008, private communication

Antonille, S., Content, D., Rabin, D., Wake, S., & Wallace, T. 2008, Proc. SPIE, 7011, 70110Z

Aumann, H. H. 1985, PASP, 97, 885

Aumann, H. H., Beichman, C. A., Gillett, F. C., et al. 1984, ApJ, 278, L23

Backman, D., Marengo, M., Stapelfeldt, K., et al. 2009, ApJ, 690, 1522

Bautz, M. W., Kissel, S. E., Prigozhin, G. Y., et al. 2004, Proc. SPIE, 5501, 111

Beichman, C. A., Bryden, G., Gautier, T. N., et al. 2005, ApJ, 626, 1061

Benedict, G. F., McArthur, B. E., Gatewood, G., et al. 2006, AJ, 132, 2206

Bottema, M., Fastie, W. G., & Moos, H. W. 1969, Appl. Opt., 8, 1821

Bowyer, S. 1991, ARA&A, 29, 59

Brown, A. G. A., de Geus, E. J., & de Zeeuw, P. T. 1994, A&A, 289, 101

Brugarolas, P., Alexander, J., Trauger, J., et al. 2010, Proc. SPIE, 7731, 77314V

Brummelaar, T. A., McAlister, H. A., Ridgway, S. T., et al. 2005, ApJ, 628, 453

Bryden, G., Traub, W., Roberts, Jr., L. C., et al. 2011, Proc. SPIE, 8151, 81511E

Buil, C. 1991, CCD Astronomy: Construction and Use of an Astronomical CCD Camera (Willmann-Bell, Inc.)

Burgh, E. B., McCandliss, S. R., & Feldman, P. D. 2002, ApJ, 575, 240

Calzetti, D., Bohlin, R. C., Gordon, K. D., Witt, A. N., & Bianchi, L. 1995, ApJ, 446, L97

Cappellari, M., & Copin, Y. 2003, MNRAS, 342, 345

Cardelli, J. A., & Clayton, G. C. 1988, AJ, 95, 516

Cardelli, J. A., Clayton, G. C., & Mathis, J. S. 1989, ApJ, 345, 245

Cash, W. 1976, A&A, 52, 307

—. 1979, ApJ, 228, 939

Castelli, F., & Kurucz, R. L. 2003, in IAU Symp. No Piskunov et al. 2003, poster A20, Vol. Poster A20

Chakrabarti, S., Kimble, R., & Bowyer, S. 1984, J. Geophys. Res., 89, 5660

Chiang, E., Kite, E., Kalas, P., Graham, J. R., & Clampin, M. 2009, ApJ, 693, 734

Close, L. M., & McCarthy, Jr., D. W. 1994, PASP, 106, 77

Colavita, M. M., Wallace, J. K., Hines, B. E., et al. 1999, ApJ, 510, 505

Cook, T. A., Gsell, V. J., Golub, J., & Chakrabarti, S. 2003, ApJ, 585, 1177

Cotton, D. M., Cook, T., & Chakrarabarti, S. 1994, Appl. Opt., 33, 1958

Cotton, D. M., Stephan, A., Cook, T., et al. 2000, Appl. Opt., 39, 3991

de Geus, E. J., Lub, J., & van de Grift, E. 1990, A&AS, 85, 915

Dekany, R. G., Wallace, J. K., Brack, G., Oppenheimer, B. R., & Palmer, D. 1997, Proc. SPIE, 3126, 269

di Folco, E., Absil, O., Augereau, J.-C., et al. 2007, A&A, 475, 243

Down, D. 1992, Journal of the Optical Society of America A, 9, 700

Draine, B. T. 2003, ApJ, 598, 1017

—. 2006, ApJ, 636, 1114

Draine, B. T., & Li, A. 2007, ApJ, 657, 810

Dumusque, X., Pepe, F., Lovis, C., et al. 2012, Nature, 491, 207

DuVarney, R. C., Bleau, C. A., Motter, G. T., et al. 2000, Proc. SPIE, 4007, 481

Fischera, J., & Dopita, M. 2011, A&A, 533, A117

Fitzgerald, M. P., Stephens, T. C., & Witt, A. N. 1976, ApJ, 208, 709

Fitzpatrick, E. L. 1999, PASP, 111, 63

—. 2004, ASPC , 309, 33

Fitzpatrick, E. L., & Massa, D. 2005, AJ, 130, 1127

—. 2007, ApJ, 663, 320

France, K., & McCandliss, S. R. 2005, ApJ, 629, L97

Ghiglia, D. C., & Romero, L. A. 1994, JOSAA , 11, 107

Gibson, S. J., & Nordsieck, K. H. 2003, ApJ, 589, 362

Glindemann, A., McCaughrean, M. J., Hippler, S., et al. 1997, PASP, 109, 688

Golimowski, D. A., Ardila, D. R., Krist, J. E., et al. 2006, AJ, 131, 3109

Gordon, K. D. 2004, ASPC , 309, 77

Gordon, K. D., Cartledge, S., & Clayton, G. C. 2009, ApJ, 705, 1320

Gordon, K. D., Misselt, K. A., Witt, A. N., & Clayton, G. C. 2001, ApJ, 551, 269

Gray, D. F., & Baliunas, S. L. 1995, ApJ, 441, 436

Greaves, J. S., Holland, W. S., Moriarty-Schieven, G., et al. 1998, ApJ, 506, L133

Greaves, J. S., Holland, W. S., Wyatt, M. C., et al. 2005, ApJ, 619, L187

Guyon, O., Kern, B., Belikov, R., et al. 2011, Proc. SPIE, 8151, 81510H

Haikala, L. K., Mattila, K., Bowyer, S., et al. 1995, ApJ, 443, L33

Hatzes, A. P., Cochran, W. D., McArthur, B., et al. 2000, ApJ, 544, L145

Helstrom, C. 1964, Information Theory, IEEE Transactions on, 10, 275

Henyey, L. G., & Greenstein, J. L. 1941, ApJ, 93, 70

HST MultiDrizzle Handbook, www.stsci.edu/hst/HST_overview/documents/multidrizzle/ch42.html

Hurwitz, M. 1994, ApJ, 433, 149

Jo, Y.-S., Min, K.-W., Lim, T.-H., & Seon, K.-I. 2012, ApJ, 756, 38

Jo, Y.-S., Min, K.-W., Seon, K.-I., Edelstein, J., & Han, W. 2011, ApJ, 738, 91

Kalas, P., Graham, J. R., & Clampin, M. 2005, Nature, 435, 1067

Kuchner, M. J., & Brown, M. E. 2000, PASP, 112, 827

Kurucz, R. L. 1979, ApJS, 40, 1

Lagage, P. O., & Pantin, E. 1994, Nature, 369, 628

Lagrange, A.-M., Bonnefoy, M., Chauvin, G., et al. 2010, Science, 329, 57

Lane, B. F., Muterspaugh, M. W., & Shao, M. 2006, ApJ, 648, 1276

Laureijs, R. J., Mattila, K., & Schnur, G. 1987, A&A, 184, 269

Lawler, S. M., Beichman, C. A., Bryden, G., et al. 2009, ApJ, 705, 89

Levine, B. M., Shao, M., Liu, D. T., Wallace, J. K., & Lane, B. F. 2003, Proc. SPIE, 5170, 200

Lewis, N. K., Cook, T. A., Wilton, K. P., et al. 2009, ApJ, 706, 306

Li, A., & Draine, B. T. 2001, ApJ, 554, 778

Lillie, C. F., & Witt, A. N. 1976, ApJ, 208, 64

Liu, K.-C., Blaurock, C., & Mosier, G. E. 2004, Proc. SPIE, 5497, 437

Liu, W. M., Hinz, P. M., Hoffmann, W. F., et al. 2009, ApJ, 693, 1500

Lombardi, M., Alves, J., & Lada, C. J. 2011, A&A, 535, A16

Lub, J., & Pel, J. W. 1977, A&A, 54, 137

Ma, X., Rao, C., & Zheng, H. 2009, Optics Express, vol. 17, issue 10, p. 8525, 17, 8525

Macintosh, B. A., Anthony, A., Atwood, J., et al. 2012, Proc. SPIE, 84461U

Marois, C., Lafrenière, D., Doyon, R., Macintosh, B., & Nadeau, D. 2006, ApJ, 641, 556

Marois, C., Macintosh, B., Barman, T., et al. 2008, Science, 322, 1348

Marois, C., Zuckerman, B., Konopacky, Q. M., Macintosh, B., & Barman, T. 2010, Nature, 468, 1080

Martin, C., Hurwitz, M., & Bowyer, S. 1990, ApJ, 354, 220

Mathis, J. S. 1973, ApJ, 186, 815

Matsuo, T., Fukagawa, M., Kotani, T., et al. 2011, Advances in Space Research, 47, 1455

Mattila, K. 1970, A&A, 9, 53

www.astro-cam.com, Astronomical Research Cameras (ARC) website

McCaughrean, M. J., & Stauffer, J. R. 1994, AJ, 108, 1382

Mennesson, B. P., Shao, M., Levine, B. M., et al. 2003, Proc. SPIE, 4860, 32

Millan-Gabet, R., Serabyn, E., Mennesson, B., et al. 2011, ApJ, 734, 67

Misselt, K. A., Gordon, K. D., Clayton, G. C., & Wolff, M. J. 2001, ApJ, 551, 277

Morgan, D. H., Nandy, K., & Thompson, G. I. 1976, MNRAS, 177, 531

Morgan, R. M., Burge, J. H., & Woolf, N. J. 2000, Proc. SPIE, 4006, 340

Mouillet, D., Larwood, J. D., Papaloizou, J. C. B., & Lagrange, A. M. 1997, MNRAS, 292, 896

Murthy, J., & Henry, R. C. 1995, ApJ, 448, 848

Murthy, J., Im, M., Henry, R. C., & Holberg, J. B. 1993, ApJ, 419, 739

Murthy, J., Sahnow, D. J., & Henry, R. C. 2005, ApJ, 618, L99

O'Dell, C. R. 2001, ARA&A, 39, 99

Olivier, S. S., Max, C. E., Gavel, D. T., & Brase, J. M. 1993, ApJ, 407, 428

Onaka, T., Sawamura, M., Tanaka, W., Watanabe, T., & Kodaira, K. 1984, ApJ, 287, 359

Percival, J. W., Jaehnig, K. P., & Nordsieck, K. H. 2007, BAAS, 39, 976

Perryman, M. A. C., Lindegren, L., Kovalevsky, J., et al. 1997, A&A, 323, L49

Petersohn, J. 1997, MS Thesis, Univ. of Toledo, Ohio

Phillips, C. L., & Harbor, R. D. 1991, Basic feedback control systems (Prentice Hall)

Rabin, D., Davila, J., Content, D., Keski-Kuha, R., & Michael, S. 2002, BAAS, 34, 735

Rao, S. R., Wallace, J. K., Samuele, R., et al. 2008, Proc. SPIE, 6888, 68880B

Roques, F., Scholl, H., Sicardy, B., & Smith, B. A. 1994, ICARUS , 108, 37

Ryu, K., Min, K.-W., Park, J.-W., et al. 2006, ApJ, 644, L185

Samuele, R., Wallace, J., Schmidtlin, E., et al. 2007, Proc. IEEE Aerospace Conference, 1

Schiminovich, D., Friedman, P. G., Martin, C., & Morrissey, P. F. 2001, ApJ, 563, L161

Schlegel, D. J., Finkbeiner, D. P., & Davis, M. 1998, ApJ, 500, 525

Schneider, G., Guyon, O., Science Mission, E., & Technology Team. 2012, in American Astronomical Society Meeting Abstracts, Vol. 219, American Astronomical Society Meeting Abstracts, 155.13

Schneider, G., Weinberger, A. J., Becklin, E. E., Debes, J. H., & Smith, B. A. 2009, AJ, 137, 53

Schneider, G., Silverstone, M. D., Hines, D. C., et al. 2006, ApJ, 650, 414

Serabyn, E. 2000, Proc. SPIE, 4006, 328

Serabyn, E., & Colavita, M. M. 2001, Appl. Opt., 40, 1668

Shalima, P., & Murthy, J. 2004, MNRAS, 352, 1319

Shalima, P., Sujatha, N. V., Murthy, J., Henry, R. C., & Sahnow, D. J. 2006, MNRAS, 367, 1686

Shao, M., & Levine, B. M. 2010, ASPC , 430, 368

Shao, M., Wallace, J. K., Levine, B. M., & Liu, D. T. 2004, Proc. SPIE, 5487, 1296

Shao, M., Levine, B. M., Wallace, J. K., et al. 2006, Proc. SPIE, 6265, 626517

Shimizu, T., Nagata, S., Tsuneta, S., et al. 2008, Sol. Phys., 249, 221

Smith, B. A., & Terrile, R. J. 1984, Science, 226, 1421

Stark, C. C., & Kuchner, M. J. 2008, ApJ, 686, 637

Stein, J. T., & Neufeld, C. 2004, Proc. SPIE, 5495, 340

Su, K. Y. L., Rieke, G. H., Misselt, K. A., et al. 2005, ApJ, 628, 487

Su, K. Y. L., Rieke, G. H., Stapelfeldt, K. R., et al. 2009, ApJ, 705, 314

Sujatha, N. V., Shalima, P., Murthy, J., & Henry, R. C. 2005, ApJ, 633, 257

Taylor, J. R., Anderson, M. S., & Bunton, P. H. 1999, Appl. Opt., 38, 219

Thompson, G. I., Nandy, K., Jamar, C., et al. 1978, Catalogue of stellar ultraviolet fluxes. A compilation of absolute stellar fluxes measured by the Sky Survey Telescope (S2/68) aboard the ESRO satellite TD-1

Thompson, L. A., Teare, S. W., Crawford, S. L., & Leach, R. W. 2002, Publications of the Astronomical Society of the Pacific, 114, pp. 1143

Toller, G. N. 1981, PhD thesis, State University of New York, Stony Brook.

Trauger, J., Moody, D., Gordon, B., Krist, J., & Mawet, D. 2011, Proc. SPIE, 8151, 81510G

van de Hulst, H. C. 1981, Light scattering by small particles

Vogt, F., Martinache, F., Guyon, O., et al. 2010, Proc. SPIE, 7736, 773612

Wallace, J. K., Burruss, R. S., Bartos, R. D., et al. 2010, Proc. SPIE, 7736, 77365D

Warner, M., Heathcote, S., Schumacher, G., Cantarutti, R., & Parkes, E. 2010, Proc. SPIE, 7739, 77393D

Warren, Jr., W. H., & Hesser, J. E. 1977, ApJS, 34, 115

Weingartner, J. C., & Draine, B. T. 2001, ApJ, 548, 296

Whittet, D. C. B., ed. 2003, Dust in the galactic environment

Williams, J. P., & Cieza, L. A. 2011, ARA&A, 49, 67

Wilner, D. J., Andrews, S. M., & Hughes, A. M. 2011, ApJ, 727, L42

Wilner, D. J., Holman, M. J., Kuchner, M. J., & Ho, P. T. P. 2002, ApJ, 569, L115

Wilson, B. A., Dame, T. M., Masheder, M. R. W., & Thaddeus, P. 2005, A&A, 430, 523

Witt, A. N. 1968, ApJ, 152, 59

Witt, A. N., Friedmann, B. C., & Sasseen, T. P. 1997, ApJ, 481, 809

Witt, A. N., Oliveri, M. V., & Schild, R. E. 1990, AJ, 99, 888

Witt, A. N., Petersohn, J. K., Bohlin, R. C., et al. 1992, ApJ, 395, L5

Witt, A. N., Petersohn, J. K., Holberg, J. B., et al. 1993, ApJ, 410, 714

Witt, A. N., Walker, G. A. H., Bohlin, R. C., & Stecher, T. P. 1982, ApJ, 261, 492

Wizinowich, P. L., Le Mignant, D., Bouchez, A. H., et al. 2006, PASP, 118, 297

Woods, T. N., III, R. T. W., Rottman, G. J., & Haring, R. E. 1994, Appl. Opt., 33, 4273

www.diffraction.com, Durango website

www.e2v.com, e2v website

www.physikinstrumente.com, Physik Instrumente (PI) website

www.stsci.edu/∼kgordon, Karl Gordon's website

Wyant, J. C. 1975, Appl. Opt., 14, 2622

Wyatt, M. C., & Dent, W. R. F. 2002, MNRAS, 334, 589

Curriculum Vitae

[redacted]

[redacted]